UNIVERSITY OF
BIRMINGHAM

DEVELOPMENT AND OPTIMIZATION OF SMALL-SCALE AXIAL TURBINES FOR DISTRIBUTED CRYOGENIC ENERGY STORAGE SYSTEM

By

Khalil Mohammed Khalil

A Thesis Submitted to the University of Birmingham for the Degree of

Doctor of Philosophy

School of Engineering

Department of Mechanical Engineering

The University of Birmingham

Edgbaston, Birmingham, UK

August - 2018

ABSTRACT

Cryogenic energy storage (CES) is an innovative energy storage technology that uses low temperature cryogen liquids such as liquid air or liquid nitrogen as the energy storage vector. This technology is important for utilizing the intermittent renewable energy sources in local small power generation and supply through smart grids. Both small-scale generation and cryogenic energy storage technologies are still under research development and more efforts are required to transfer them to the full commercial stage. This research aims to study in a comprehensive way different power generation cryogenic energy storage cycles and different strategies for developing an efficient design and optimization of small scale nitrogen axial turbines as the expanders for these cycles within the capacities that can be used in small/medium size buildings, rural, and remote off-grid communities.

Based on thermodynamic modeling, four new cryogenic power generation cycles ranging from the basic cycle (open Rankine) to the complex combined one (combined power generation and cryogenic storage plant) were developed to predict the performance of a small scale power generation system. The hybrid open-closed Rankine (HOCR) cycle has been chosen as the case study for nitrogen turbine further analysis for expansion ratios ranging from 1.5 to 3 which is considered safe and convenient for small size building applications where the calculated cycle thermal efficiency ranged from 15.45% to 24.72 % respectively. New methodology has been developed to investigate the performance of small scale nitrogen axial turbines for hybrid open-closed Rankine cycle. This methodology integrates one dimension preliminary design method (mean-line method), three dimensional CFD simulations, and experimental validation testing, where the best design with isentropic efficiency 78.3% and power output of 4.6kW was achieved. This turbine methodology was expanded to include developing optimization parametrization technique which describes

blade geometry by using only 6 parameters and through ANSYS design exploration module to maximize the total efficiency and power output. A parametric study of four different blade configurations (lean, sweep, twist, and bow) was carried out with the aim of investigating the effects of these configurations on the turbine performance and identify the best blade configuration that enhances the turbine performance. A novel dual stage non-repeated annular area small-scale axial nitrogen turbine was also developed to handle higher expansion ratios up to 3, which enhanced the cycle efficiency. Results from these further modifications showed that the optimized model enhanced the efficiency performance from 78.3% to 84.88% and power output from 4.6 kW to 5.3 kW. Better performance was achieved using sweep blade configuration angle of 30 degrees while efficiency and power output were enhanced to 82.4% and 5.18 kW. Finally, results from the two non-repeated stages turbine has shown higher total efficiency of 81.4% compared to the two repeated stages of 78.2% and a single stage of 74.6%.

In order to validate the CFD simulation, and the design methodology, and to investigate the effects of blade height on small-scale axial turbines performance, a test rig using compressed air was developed. Three manufactured axial turbines with different blade heights (4mm, 6mm, and 8mm) were manufactured and tested at various operating conditions. The experimental results showed that the maximum power produced at expansion ratio around 1.75 and rotational speed around 16000 RPM were 630.75 W, 694.1 W, and 796.89 W for the blade height 4mm, 6mm, and 8mm turbines, respectively. While the maximum efficiencies for them at pressure ratio 1.3 were: 47.1%, 39.8%, and 38.83% respectively. Comparison with experimental results showed that the validity of the developed CFD models for the 4mm, 6mm, and 8mm turbines with deviation percentage in terms of efficiency were +16%, +15%,+13% respectively while in terms of power output were +14.5%, +14%,+12% respectively.

بِسْمِ اللَّهِ الرَّحْمَٰنِ الرَّحِيمِ

(وَنُرِيدُ أَن نَّمُنَّ عَلَى الَّذِينَ اسْتُضْعِفُوا فِي الْأَرْضِ وَنَجْعَلَهُمْ أَئِمَّةً وَنَجْعَلَهُمُ الْوَارِثِينَ)

صَدَقَ اللَّهُ العَلِيُّ العَظِيم

ACKNOWLEDGMENTS

I would like to express the deepest gratitude to my supervisor Dr Saad Mahmoud who provided me with scientific guidance, constructive advice, and encouragement especially through clear-cut reviewing of my thesis and the scientific papers.

I would also like to express my thanks to Dr Raya Al-Dadah who mentored and trusted me during the whole period of this project.

I would very much like to thank Mr. Simon Rowan, senior laboratory technician, for his helping during constructing my test rig and manufacture turbines. I want to say to my mother's soul this achievement is a small gift to your glory in the heaven.

Last but not least, thanks to my brother Mr. Asaad M. Khalil, also all brothers, friends and colleagues for supporting me spiritually throughout writing this thesis and my life in general.

Khalil Mohammed Khalil

2018

CONTENTS

LIST OF FIGURES

LIST OF TABLES

NOMENCLATURE

Symbols	Description	Unit
A	stage loss parameter	[-]
A_{an}	annular area	[m2]
B	exit loss parameter	[m]
b	chord length	[m]
C	loss parameter	[-]
cp	specific heat at constant pressure	[J/kg K]
D	diameter	[m]
D_s	Specific diameter	[-]
E	squared ratio of stage	[-]
Er	Expansion ratio	[-]
F	weighting factor	[-]
G_k	Turbulent kinetic energy generation term	[kg/m s^3]
G_ω	Dissipation generation term	[kg/m^3 s^2]
H	blade height	[m]
h	specific enthalpy	[J/kg]
Δh	specific turbine work	[J/kg]
K	turbine loss coefficient	
k	turbulent kinetic energy	[m^2/ s^2]
l	blade Chord length	[m]
M, M_a	mach number	
ṁ	mass flow rate	[kg/s]
N	rotational speed	[RPM]
p	pressure	[Pascal]
Pr	Pressure ratio	[-]
q	specific heat	[J/kg]
R	universal gas constant	[J/kg K]
Re	Reynold number	
r	radius	[m]
S	Blade pitch length	[m]

S_k	turbulent kinetic energy source terms	kg/m s^3
S_ω	dissipation source terms	kg/m^3 s^2
t	time	(s)
t_{max}	maximum trailing edge thickness	(m)
T	temperature	(K)
R	universal gas constant	(J/kg K)
Re	Reynold number	[-]
r_t	Tip radius	
r	radius	(m)
T	temperature	(K)
u	mean flow velocity	(m/s)
U	blade vleocity	(m/s)
V	absolute velocity	(m/s)
w	specific work	(J/kg)
w	relative velocity	(m/s)
XRe	correction factor	[-]
y+	near wall non-dimensional distance	[-]
Y_k	the turbulent kinetic energy fluctuating dilation of compressible turbulence	kg/m s3
Y_ω	the dissipation fluctuating dilation of compressible turbulence	kg/m3 s2
Y	loss coefficient	[-]
Zw	Zweifel's coefficient	[-]

Greek symbols	**Description**	**Unit**
α	absolute flow angle (degree)	[degree]
β	relative flow angle (degree)	[degree]
γ	ratio of specific heats	[-]
μ	viscosity	[m^2/s]
η	efficiency	[%]
θi	incident angle	[degree]
ρ	fluid density	[kg/m^3]
λ	stage speed-work parameter	[-]

ω	Rotational speed	[rad/sec]
Γ	effective diffusivity term	[kg/m s]
Δτ	variation of tip clearance	[m]
ψ	Loading coefficient	[-]
ν	velocity ratio	[-]
φ	flow coefficient	[-]
ε	blade deflection angle	[degree]
ζ	stagger angle	[degree]
τ	Torque	[N.m]

Subscripts	Description
1-5	stations within the cycle respectively
1-3	inlet and outlet station to the turbine blades respectively
Cs	Cooling system
comp.	Compressor
R	closed Rankine cycle
N	nitrogen open cycle
st	stator
h	hub
o	Stagnation or total thermodynamic status
ro	rotor
x	axial
S,is	isentropic
ex	exit
in	input
u	circumferential direction
ev	exit vanes
ts	total to static
t	total to total
a	first stage
n	last stage
m	mean line

p	profile
se	secondary
Te	trailing edge
Tl	tip leakage

Acronyms	Description
ATM	Automatic topology method
CAES	compressed air energy storage
CCD	Central composite design
CES	cryogenic energy storage
CFD	Computational Fluid Dynamics
DEO	Deasign exploration optimization
DM	Design modular
DOE	Design of experiments
DPG	Distribution power generation
FEA	Finite element analysis
HOCR	Hybrid Open-Closed Rankine
HX	Heat exchanger
LASE	liquid air storage energy system
LNG	Liquid natural gas
LN2	Liquid nitrogen
LAir	Liquid air
MOGA	Multi objective genetic algorithm
OR	Open Rankine
ORC	Organic Rankine Cycle
PSH	pumped storage hydropower

RANS	Reynolds averaged Navier-Stokes
RA	Rotor angle
RTD	Resistance temperature detector
RT	Rotor blade thickness
RSM	Response Surfaces meta-model
RC	Rotor chord length
RN	Rotor number of blades
SST	Shear stress transport
SA	Stator angle
SX	Stator blade peak location
ST	Stator blade thickness
SC	Stator chord length
SN	Stator number of blades

LIST OF PUBLICATION

I. Journal papers

1- Khalil, K.M., Mahmoud, S. and Al-Dadah, R.K., 2018. Development of innovative non-repeated annular area dual stage small-scale nitrogen axial turbine for hybrid open-closed Rankine cycle. Energy Conversion and Management, 164, pp.157-174.

2- Khalil, K.M., Mahmoud, S., Al-Dadah, R.K. and Fadhel, A.M., 2017. Parametric analysis of blade configurations for a small-scale nitrogen axial expander with hybrid open-Rankine cycle. Energy Conversion and Management, 142, pp.82-94.

3- Khalil, K.M., Ahmad, A., Mahmoud, S. and Al-Dadah, R.K., 2017. Liquid air/nitrogen energy storage and power generation system for micro-grid applications. Journal of cleaner production, 164, pp.606-617.

4- Khalil, K.M., Mahmoud, S., Al-Dadah, R.K. and Ennil, A.B., 2017. Investigate a hybrid open-Rankine cycle small-scale axial nitrogen expander by a camber line control point parameterization optimization technique. Applied Thermal Engineering, 127, pp.823-836.

5- Khalil M. K, A., Mahmoud, S. Al-Dadah, R. off- design performance prediction for cryogenic small scale axial turbine using CFD simulation. International Journal of Mechanical and Production Engineering. 2015 June; 3:92-95.

II. Conference papers

1- Khalil, K.M., Mahmoud, S., Al-Dadah, R.K., Al Jubori, A. and Rahbar, K., 2016, June. Impact of Skin Friction, Tip Clearance and Trailing Edge Losses on Small Scale Cryogenic Axial Turbine Performance. In ASME Turbo Expo 2016: Turbomachinery Technical Conference and Exposition (pp. V008T23A033-V008T23A033). American Society of Mechanical Engineers.

2- Khalil, K.M., Mahmoud, S. and Al-Dadah, R.K., 2016, October. Impact of advanced blade configuration on small scale cryogenic axial turbine performance. In Students on Applied Engineering (ICSAE), International Conference for (pp. 248-253). IEEE.

3- Al Jubori, A., Al-Dadah, R.K., Mahmoud, S., Khalil, K.M. and Ennil, A.B., 2016, June. Development of efficient small scale axial turbine for solar driven organic Rankine cycle. In ASME Turbo Expo 2016: Turbomachinery Technical Conference and Exposition (pp. V003T25A011-V003T25A011). American Society of Mechanical Engineers.

CHAPTER 1

INTRODUCTION

1.1 Background

Today's critical challenge is to ensure that the speed of the progress for the energy sector transformation can achieve the sustainable development goals which address climate change and other environmental and economical world concerns. The world population is growing steadily where according to the United Nations and World Bank statistics it will be about 10 billion in 2050 [1]. This global growth will be associated with rapid development in some economies like China and India; which will have a major impact on the energy sector. Such expansion in the energy sector needs to deliver affordable and secure energy services by reducing the emissions to minimum levels. In this regard, the International Energy Agency (IEA) suggested effective three pathways for future energy technology development. The first one is Reference Technology Scenario (RTS) which is based on current energy policies and commitments outlined by the Paris agreement; therefore, this scenario can be a reference point of worldly ambitions. The second scenario (2DS) aims to limit the future temperature increases to 2 ^{o}C by 2060. The third scenario is beyond 2 ^{o}C (B2DS) which is looking at how far the clean energy technologies can achieve with their practical limits. The IEA reports showed that the demand for electricity in transportation sector will double from today 18% to 35% in 2DS and 41% in the B2DS as the electricity will become the main means for the future transportation. This transformation to the electrification in 2DS and B2DS will require

a change in the carbon declining traditional rates to be -3.9% for the 2DS and -4.5 for the B2DS compared with -0.5 for the past decade. This reduction in the 2DS scenario can be achieved by generating 98% of the electricity from sources that have low carbon emission by 2060 as shown in Figure 1-1. This 2DS generation rate reduces the emissions by two-thirds for renewable, 18% for fossil with Carbon Capture and Storage (CCS), and 16% for nuclear [2].

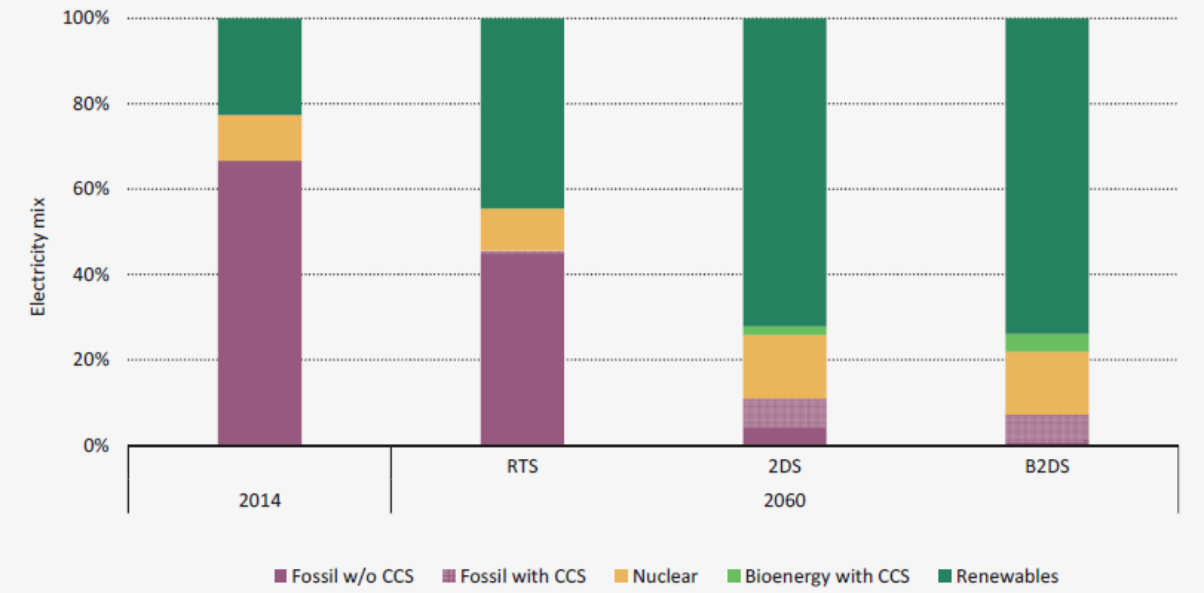

Figure 1-1 Power generation fuel mix by IEA scenarios [2]

With these predicted demands for energy generation, the technologies that can efficiently harness renewable energy sources will play a major role in the future energy industry. The renewable energy sources exist in nature in many forms such as geothermal energy, solar energy, wind energy and the low-temperature waste heat. Most of these renewable sources are intermittent by nature and often available when demands are low. This stimulates the need to develop cost effective energy storage technologies, where surplus energy can be efficiently stored and then recovered when needed. As the cost for renewable energy generation continues to fall down especially for regions with weak grid infrastructure, the

need of energy storage increases. The use of energy storage technologies is increasing where it is expected to increase energy storage capacity over 40% annually in the next decade which adds about 80GW of storage capacity to 2GW that currently exist [3]. There are many types of energy storage technologies and they are classified according to the form that energy is stored. Based on this classification, the energy storage technologies are divided into four main categories: (mechanical energy storage) such as pumped storage hydropower (PSH), compressed air energy storage (CAES), and flywheels; (thermal energy storage) such as cryogenic energy storage (CES) and latent heat energy storage; (chemical energy storage) such as batteries and fuel cell; (electrical energy storage) such as super capacitors (SC) and superconducting magnetic energy storage (SMES) [4]. Cryogenic energy storage (CES) is an innovative energy storage technology that has been developed as low-temperature thermal energy storage. This technology offers many advantages over the PSH and CAES technologies such as high volumetric energy density, not restricted by geological or geographical constrains, competitive capital cost, short start up time, and safe storing conditions. Such advantages increase the interest of developing successful systems to integrate with this storage technology for the better use of its potentials in many applications including power generation. Not only the storage energy technologies escort the renewable energy development, the distribution power generation (DPG) technology also escort it due to the distribution of renewable energy through large territories. There are many definitions for the DPG, but in general, they are about small-scale and decentralized power generation where power is generated near to the end user. There are also many benefits for using this technology in future power generation systems but the main advantage is their ability to reduce the thermal and transmission losses by 30% compared to centralized power generation [5]. Integrating the DPG and energy storage systems in smart grids will make the future energy sector sustainable, renewable, smarter, well regulated, integrated and more

distributed. The integrated smart grid option can effectively regulate the small amount of power generation because it can schedule the supply and demand based on the consumer's requirements. This integration between distributed power generation and storage energy technology within smart girds will increase the development of innovative technologies such as micro or small-scale turbines as power generating tools. The turbine is the device that converts the working fluid potential energy to mechanical shaft power; therefore, it is considered a significant component in any power cycle. The conventional way to design any turbine is summarized in Figure 1-2, where in each step there is an iterative design analysis process until reaching the best results. The turbine operating conditions specified after thermodynamic cycle analysis are completed to be input data to the first turbine design step. In the preliminary 1D design the set of stations are chosen for a specific inlet and outlet for each turbine component.

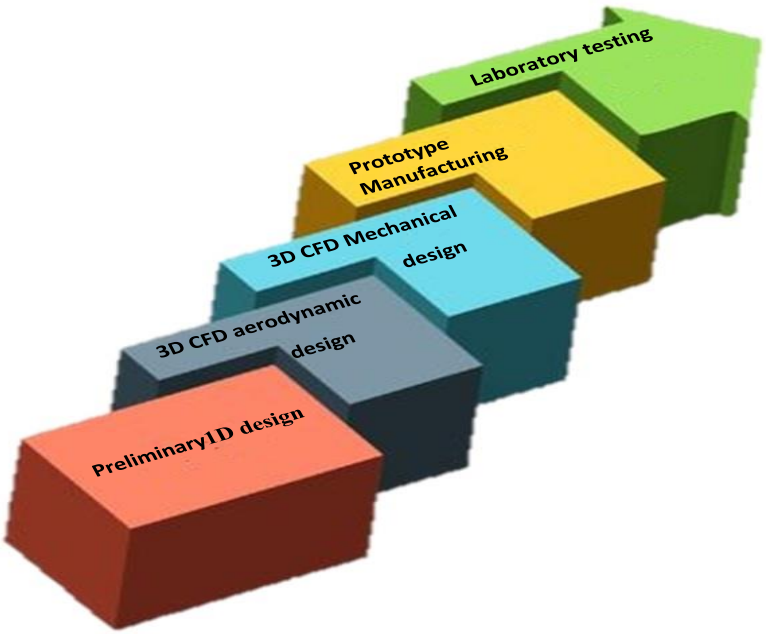

Figure 1-2 Turbine design methodology process

Then the thermodynamic properties and basic geometries calculated by an iterative process based on efficiency and losses parameterizes. Following this, the full 3D design geometry is defined by using preliminary design outputs as inputs for 3D CFD aerodynamic design analysis. The mechanical structural analysis evaluates the 3D geometry output from aerodynamic design analysis to ensure their durability for the operating conditions. The prototype can be manufactured after full stage design is completed and the laboratory test is usually done to ensure design performance and the design tool validation.

1.2 Motivation and contribution

Globally there are around 1.3 billion humans who do not connect to the main electricity grid especially in the developing countries [6]. This disconnection is combined with extreme weather conditions which makes life very difficult. These areas or countries have renewable energy sources like solar energy, wind and geothermal energy which can provide sustainable energy supplies. Therefore smart grids integrated with distributed power generation and energy storage systems can address this problem with low cost and good quality. Cryogenic energy storage (CES) technology offers the advantages of relatively large volumetric energy density, ease of storage and offers the potential to overcome the other energy storage systems drawbacks in terms of high capital costs, geographical restrictions and environmental impacts. The effective designs for small-scale turbines can play a major role for these systems performance in term of improved work output and round-trip efficiency.

Most of the published work on cryogenic combined cycles is concerned with large scale system for power ratings from 2 to 20 MW and expansion ratios ranging from 100 to 300. Therefore, there is a knowledge gap in developing small-scale CES systems with good performance and simple structure, where this study is aiming to address. There are also limited research related to small-scale turbines (below 10 kW), especially with axial turbines.

Therefore, the second knowledge that this study is trying to address is the development of a novel methodology for integrating the 1D mean-line design with 3D CFD design and then validate this methodology by experimental work. Further contributions regarding small-scale axial turbines are: developing 3D optimization parametrization technique which describe the blade geometry in an effective way by using chord length and blade profile parameters; investigating the four axial turbine advanced blades configurations (lean, twist, sweep, and bow) on the small scale turbine by comprehensive study to enhance the turbine performance and show the configurations effects; developing the dual stage axial turbine non-repeated annular area to overcome the over speeding problem in the second stage, experimentally investigating the effects of blade heights (4mm, 6mm, and 8mm) on the turbine performance and show that the blade height of 4mm can work normally where it is tested for the first time.

1.3 Objectives and scope

As was discussed in previous sections the cryogenic energy storage is a promising technology and there is an urgent need to improve their small-scale systems overall performance by enhancing the expansion process in the recovery part. The key component in the expansion process is the small-scale turbine which affects the overall system performance. This research aims to develop successful small-scale cryogenic energy storage power cycle and efficient nitrogen small scale axial turbine working in this cycle based on 1-D mean line design, 3-D CFD design and experimental work with further modifications for enhancing the performance taking into account: 3D design optimization, advanced blade configurations, and non-repeated annular area dual stage turbine. This can be achieved by the following objectives:

1. Detailed thermodynamic modeling by using MATLAB/REFPROP software for four new cryogenic power generation cycles ranging from the simple basic cycle to the

complex combined one which is developed to analysis the performance of small scale power generation system.

2. Developing the small scale axial turbine by using one-dimensional mean-line method for preliminary design based on cycle thermodynamic outputs.
3. Integrated design methodology to make one-dimensional design outputs as input for the three dimensional CFD analyses by using ANSYS CFX software to predict the turbine performance.
4. Improving the turbine performance by developing new optimization method based on camber line control point's parameterization technique which describes blade profile, thickness and chord length by only six parameters to seek for optimum design geometry based on turbine efficiency and power output.
5. Investigate four axial turbine advanced blades configurations (lean, twist, sweep, and bow) on the small-scale nitrogen turbine with the aim of enhancing the turbine performance and show the effect of these configurations on the small-scale turbine performance.
6. Apply the integrated methodology to develop a novel two stage non repeated annular area axial nitrogen turbine in order to handle higher expansion ratios which enhance the cycle performance. This new configuration overcomes the problem of over speeding which appears in the second stage with high expansion ratios.
7. Develop an experimental test rig using compressed air to investigate the performance of three small scale axial turbines with different blade heights (4mm, 6mm, and 8mm) to show the importance of blade heights on turbine performance, particularly the small height of 4 mm, and validate the methodology procedure.

1.4 Thesis outlines

This thesis has been organized in seven chapters as follows:

Chapter one: provides introduction and background for the research and thesis objectives.

Chapter two: presents the literature review for energy storage technologies, distributed power generation, expansion machines, and axial turbine design with optimization analysis.

Chapter three: shows the thermodynamic analysis and parametric studies of four new cryogenic power generation cycles ranging from the basic cycle to the complex combined one.

Chapter four: presents the methodology for developing nitrogen driven small-scale axial turbine which includes modelling one-dimensional preliminary design and modelling three dimensional CFD analyses. Further modifications presents such as three dimensional CFD optimization with developed camber line control point parametrization technique procedure, developing axial turbine advanced four blade configurations (lean, twist, sweep, and bow), and the advantage and disadvantage of turbine number of stages with design concept.

Chapter five: describes the CAD modeling, manufacturing method and test rig facilities for three axial turbines with different blade heights (4mm, 6mm, and 8mm) and describes, in some detail, the components and the instrumentations that had been used.

Chapter six: provides the results and discussions for the preliminary Design 1D, CFD 3D analysis, 3D optimization analysis, blade configuration analysis, dual-stage small-scale analysis, and experimental and CFD model validation.

Chapter seven: summarises the most remarkable findings and conclusions in the preceding chapters and outlines the recommendations for potential future developments for the current work.

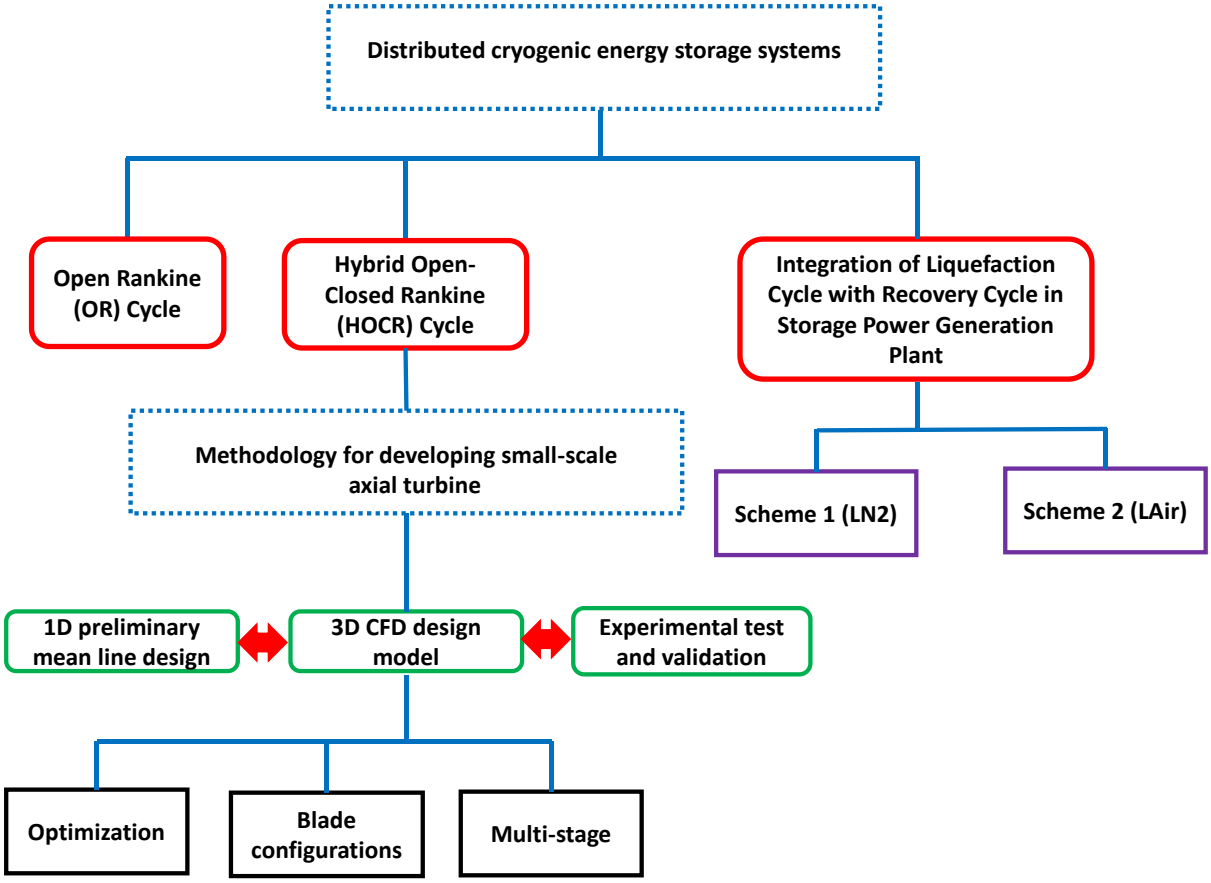

Figure 1-3 Thesis outlines flow chart

CHAPTER 2

LITERATURE REVIEW ON ENERGY STORAGE GENERATION SYSTEMS TURBINES

2.1 Introduction

The increased use of renewable energy sources such as wind and solar energy will lead to a reduction in fossil fuel consumption, and CO2 emission and improve energy supply security. Renewable energy sources are intermittent in nature, producing energy peaks at times when demands are low, thus energy storage systems are needed to store this surplus energy, smooth out energy production, reduce energy production cost, and increase the use of green power [7]. This chapter presents a comprehensive literature review of the storage energy generation systems as a new technology in energy generation integrated with renewable or low-grade heat resources. The literature review in this chapter will include the storage energy generation systems, modeling in different applications and the recent state of the art of investigated turbines.

2.2 Energy storage technologies

The history of the energy storage goes back to the turn of the 20th century where most of the power stations were shut down overnight while the lead-acid accumulators supplying direct current for residual loads [8, 9]. The development of the energy storage technologies has continued since then with the aim of enhancing capacity and decreasing the cost and environmental impact until relatively recent years. The big economies of the USA [10-12],

Australia [13], EU [14, 15], and Japan [16], all have funded national programmes on developing energy storage technologies.

The expected storage level has increased by 10-15% from the current delivered inventory in the near future in these countries [13, 15]. The energy storage technologies can be classified according to form that energy storage is accomplished. In this context, four main categories are classified [17] corresponding to: mechanical, electrical, thermal, and chemical as shown in Figure 2-1.

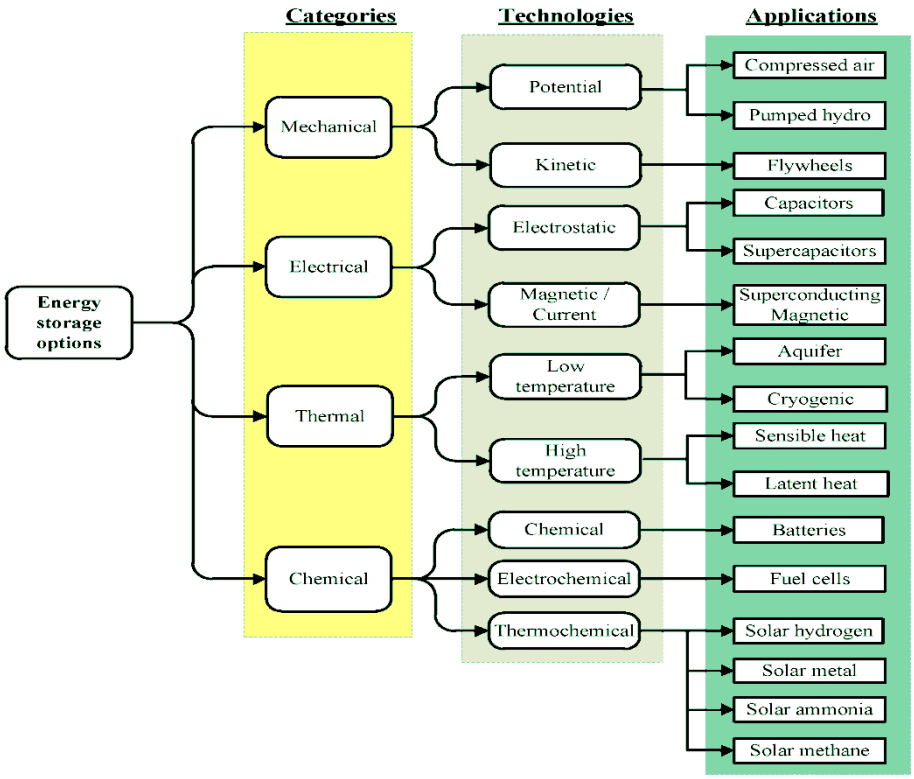

Figure 2-1 Energy storage technologies categorization of options and applications [17]

The electrical energy production, transmission, and distribution for the end user are a one-way system, which means that the supply rate needs to be the same as the demand rate. However the demand rate is not always constant as the supply as it varies over the year, month, or day, which will lead to designing expensive power plants according to maximum

required load. Integrating energy storage capacity with the power generation system can optimize the supply and demand fluctuation as shown in Figure 2-2 [8].

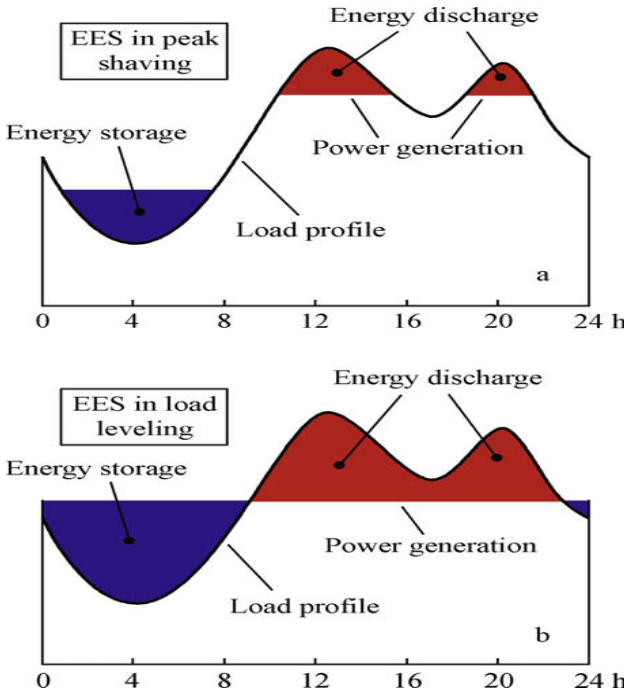

Figure 2-2 Electricity plant load profile of the storage system. (a) Peak shaving; (b) load leveling [8]

The other classification criteria for energy storage technologies are based on their applications as clarified in Figure 2-3. It can be noticed from this figure that the importance of storage technologies are in the services they provide in various locations through the energy production cycle. These storage methods can be used in the electricity grid, cooling, and heating network, distribution system, and in the off-grid electricity applications. The thermal and cryogenic storage technologies have a long span of applications where they can provide support through supply, transmission, distribution, and demand sides of the energy production cycle. Broadly speaking, the storage systems or technologies are a significant tool for energy production technologies with supply-demand variability [18]. For energy management application many energy storage technologies exist such as compressed air energy storage (CAES), pumped storage hydropower (PSH), and cryogenic energy storage

(CES). For example, the McIntosh site in Alabama uses CAES to produce 226MW of electricity while the PSH technologies already exist and add 95 GW to worldwide productions [13].

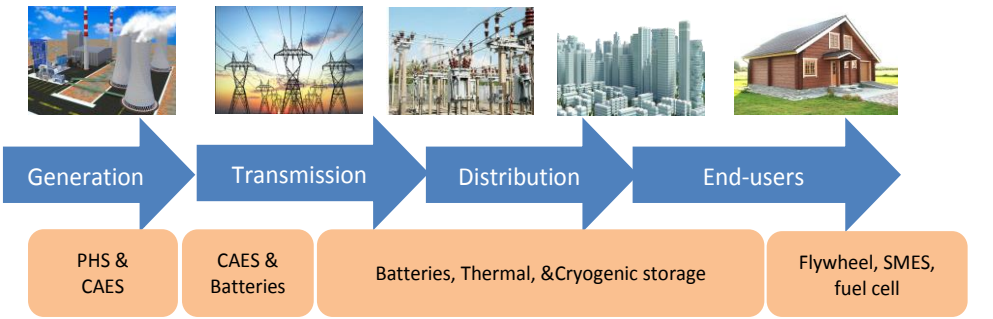

Centralized storage	Renewables integration	T& D Network storage	Distribution energy storage	Backup & power quality	Residential & commercial storage
Large centralized energy storage for ancillary services and energy management	Large centralized/ decentralized energy storage for time-shifting renewable generation	Energy storage at T&D network that support grid stability. Could be stationary or portable	Energy storage at distribution network providing small scale energy generation and energy management	Energy storage used for providing backup or high quality power for commercial and industrial consumers	Small scale energy systems at residential and commercial node for backup, time-shifting and act as micro generation

Figure 2-3 energy storage technologies classification according to applications [18]

2.2.1 Pumped storage hydropower (PSH)

The pumped storage hydropower (PSH) is a type of energy storage technology which stores the energy in the form of water in the upper reservoir with high elevation after being pumped from the lower reservoir with low elevation as shown in Figure 2-4. In the periods of energy demand, the stored water is released from high level to low level through turbines to work as hydro station [19]. This technology is the only current commercially proven as large-scale storage system to work with storage capacity bigger than 100MW and a discharge time reaching up to 100 hours depending on the volume of the upper and lower reservoir. It is one

of the oldest and most separated over the world representing 3% of the worldwide generation capacity [4].

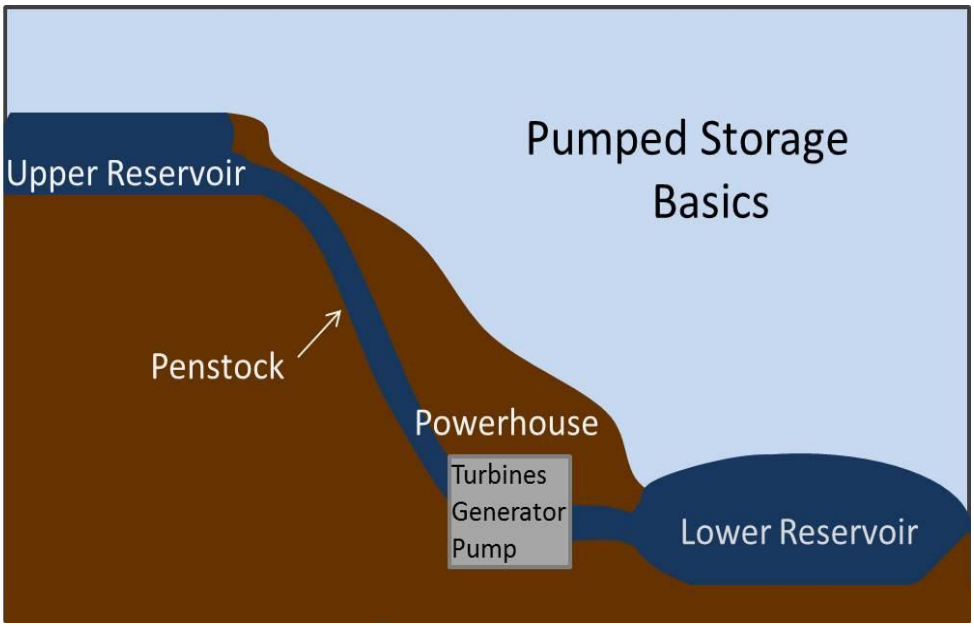

Figure 2-4 The pumped storage hydropower (PSH) basic system

However, there are drawbacks to this technology such as the high capital cost for new sites, difficulties of dynamic characteristics of the turbines-pumps system, and the restriction of the earth terrains with environmental impact on these terrains in some cases. Some of the published studies aim to address these issues such as Pérez-Díaz et al. [20] which studied reducing the scheduling costs in isolated power systems integrated with wind power by using the unit commitment mathematical model which is based on mixed integer linear programming. Results showed that the constant start-up costs can be 7% to 21% more expensive than the developed one which considers variable start-up costs as functions of wind power. Petrakopoulou et al. [21] simulated and evaluated the pumped storage hydropower integrated with renewable energies (solar and wind) by using exergy analysis as an evaluation parameter. Simulation outputs showed that hydropower hybrid plant generated 48% of its power by the photovoltaic part and 52% from the wind turbines, and has total

annual mean efficiency of 14.4%. When the lower reservoir is at underground levels, this will give the pumped storage hydropower system the advantages of not being limited by the topography and can produce power at the flat ground area. However, Pujades et al. [22] investigated the environmental consequences for such an underground pumped storage hydropower system, and showed that when the water releases in the underground reservoir the oxygen partial pressure increases which in turn decreases the water PH with time to reach around 5 after 15 days.

2.2.2 Compressed air energy storage (CAES)

In this energy storage technology, the air serves as suitable storage media where it is compressed to high pressure by using compressors which use surplus electricity or renewable energy. Later at peak times, the stored compressed air can be released through turbine-generator to reconvert the high-pressure energy to electricity. In this technology there are three main components for the compressed air energy storage, these are: compressors, turbines, and storage volumes. These storage volumes usually are located in underground large salt or rock caverns as shown in Figure 2-5 [23]. This kind of energy storage technology can create effective large-scale CAES plants which are capable of providing power reaching 100 MW in a single generation [24]. This technology dates back to the early 1940s but its development did not start until 1960s due to the lack of necessity of energy storage systems to connect to the national grid [25]. Nowadays there are a large variety of CAES types and concepts at different applications and level of developments, Figure 2-6 classifies the CAES concepts based on the idealized change of state, where the main criterion of this classification is the question of how the generated heat during and after compression process will be handled. In the D-CAES concept the heat generated cool down to ambient temperature by external heat source while in the A-CAES concept the heat of compression is captured by thermal energy storage arrangement to use it again in the discharge process. In

contrast to the previous two concepts, the I-CAES concept of the heat of compression is minimized or even prevented by using isothermal compression process [26].

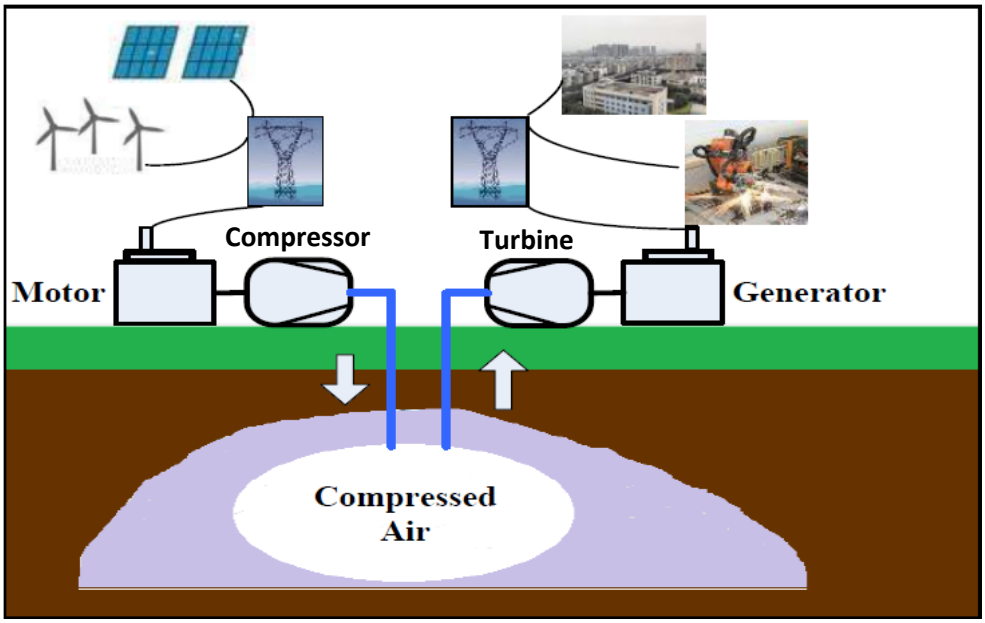

Figure 2-5 Illustration of a compressed air energy storage process [23]

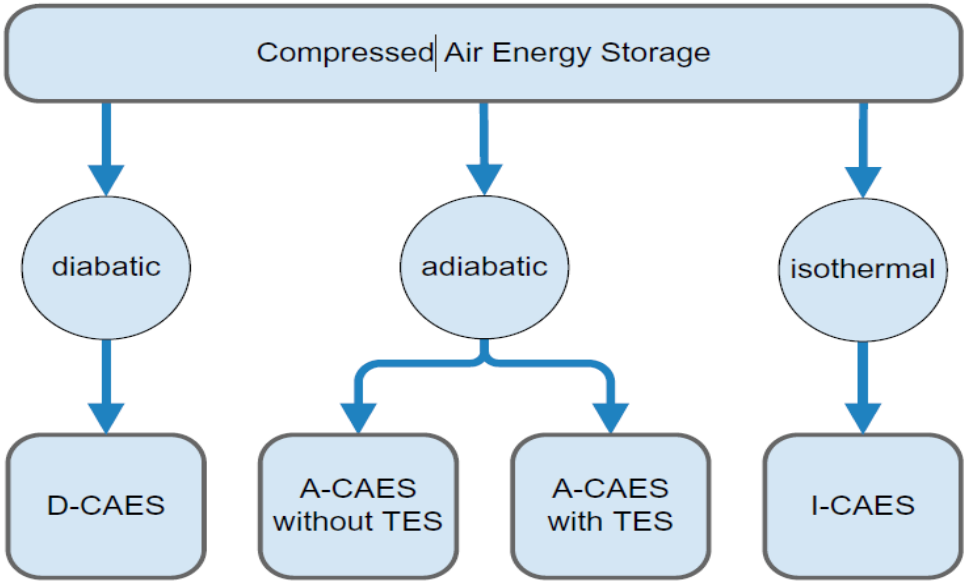

Figure 2-6 conceptual classification for CAES based on the idealized change of state [26]

With the advantages of this technology in terms of safety, life cycle, and construction investment cost [27], there are several disadvantages such as compression heat losses, low stored energy density, geological environmental impact, and geographical limitation [28, 29]. In this regard, various attempts have been reported to improve compressed air energy storage process efficiency and structure. He et al. [30] compared the compressed air energy storage (CAES) system and the supercritical compressed CO_2 energy storage (SC-CCES) system by using conventional and advanced exergy analysis. Results clarified that the SC-CCES system had better performance compared to the CAES where its exergy and round-trip efficiencies are 57% and 73% respectively. This is better than those of CAES where the exergy and round-trip efficiencies are 50.86% and 60.65% respectively. Optimization of a connected grid power of integral wind power with low temperature A-CAES system was studied by Tong et al. [31]. Results showed the possibility of smoothing out the fluctuation of wind power and reducing the power demands for the compressors train of a storage system where the wind power reaches to the utilization rate of 95% in better ideal condition. In the adiabatic compression process, approximately half of the energy is converted to heat and exhausted to the environment due to poor heat transfer which in turn decreases the CAES turnaround efficiency (electricity to electricity). In order to overcome this problem Guanwei et al. [32] invented a quasi-isothermal compression process by injecting water spray of micron-sized (10–100 μm) into the compressed air that would enhance the heat transfer and cool down the compressed air. Their measurements showed that the heat transfer rate for the water spray case ranged from 10-120 W/m^2K and for the compression power decreased from 73.8 J in the adiabatic cycle to 69.0 J in the quasi-isothermal cycle.

2.2.3 Cryogenic energy storage (CES)

Cryogenic energy storage (CES) is interesting energy storage technology that has been developed as low-temperature thermal energy storage. This approach involves two processes

the first one is the charging process where the surplus electricity or renewable energy used to liquefy a gas which in consequence is stored by a storage tank at low temperature (lower than -150^{o}C) near to environmental pressure. During the demand period, the second process, discharge process starts where the liquefied gas (cryogen) is pressurized to the required pressure and then evaporated and superheated to expand through the turbine and generate power as shown in Figure 2-7. The cryogen is a term that refers to the liquid state of the gas which has its boiling temperature lower than -150^{o}C at an environmental pressure such as liquid nitrogen, liquid hydrogen, and liquid air [33]. The use of cryogen as an energy carrier in energy storage system is more efficient than other energy carriers since the energy is stored by decreasing the internal energy while increasing the exergy of the cryogen. However, despite the high energy density, safety, availability and very low environmental impacts, the use of liquid air/nitrogen as an energy carrier has not been extensively exploited [34].

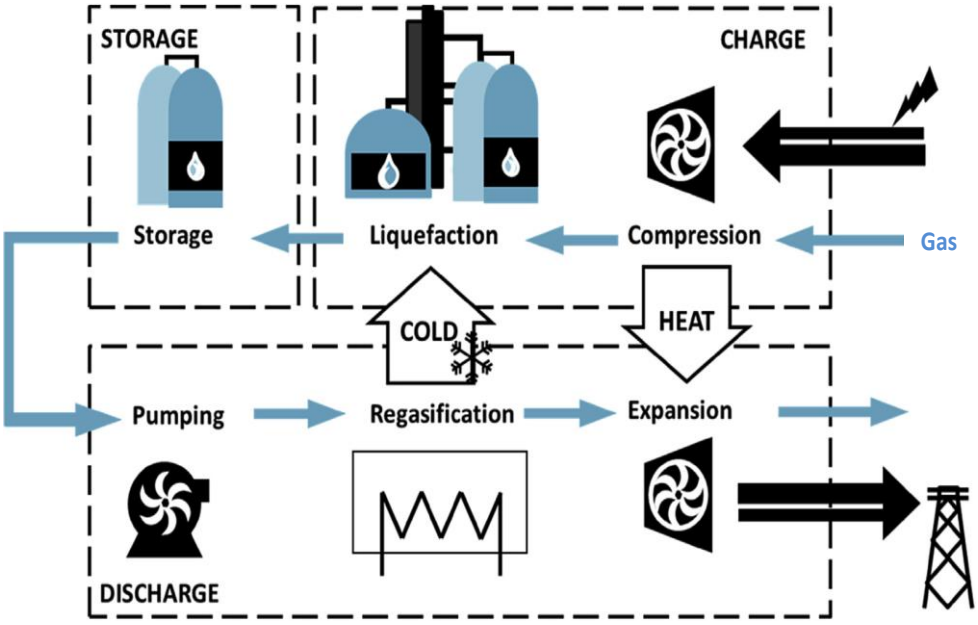

Figure 2-7 The concept of cryogenic energy storage overall system configuration [33]

The idea of CES technology dates back to 1900s where the company (Tripler Liquid Air) tried to use cryogen as a car fuel in order to compete with other car engines types such as electric and steam of those days [35]. During the crisis of oil in 1970s, the interest in the cryogenic car engine was renewed with idea of using liquid air as energy storage media in energy storage system [36].

Cryogenic energy storage is the promising energy storage technology because it offers many advantages over the PSH and CAES technologies such as (a) high potential of its relatively large volumetric energy density (100-200 Wh/kg)[37, 38], (b) no geological or geographical constraints [8], (c) no limited number of system charge and discharge, (d) competitive capital cost compared with other technologies (3-30 $/kW h) [8, 39], (e) storing time period relatively long, and (f) storing at ambient pressure which is considered as safe. Moreover, the CES startup time is just a few minutes, with 150 second as reported by the Alyami, et al. [40]. All these advantages have led to increase in the expected investment capital per plant capacity ranging from 840 to 1400 Euro/kW especially for large-scale plants [41].

2.2.3.1 Large-scale cryogenic energy storage systems

Increased interest in CES systems for large-scale applications have recently been reported and a few pilot plants have been invented by people like Guizzi et al. [42] which performed the thermodynamic analysis for a standalone combined air liquefaction and power recovery plant (hundreds of MWh) electric energy storage. Propane and methanol were used as cold storage fluid while essotherm650 was used as the hot storage fluid. The compressor pressure was 180.98 bar, the pump pressure was 6500 kPa, and the maximum temperature before entering to the turbine was 616.42 K. Results showed that such a system can achieve round-trip efficiency of (50-60%). Kishimoto et al. [43] proposed the liquid air storage energy system (LASE) as a power generating pilot plant which was developed by Mitsubishi Heavy Industries Ltd. (MHI). This plant was based on rocket liquid fuel engine technology through a

joint research project with the Chubu Electric Power Company. The system combines a gas turbine plant with LASE system to use surplus energy during the night for liquid air production. This energy is then recovered by burning the fuel and pressurized and evaporated liquid air then expands through the turbine. The LASE tank capacity was 13 m^3 with the operation time of 30 min which produced power output of 2.6 MW, with results showing the system achieved a high efficiency of approximately 77%. Feifei et al. [44] proposed two power cycle schemes, the first scheme combined the open expansion LNG, nitrogen Brayton, and water ammonia Rankine cycles while the second scheme combined open expansion LNG, Rankine propane, and Rankine ammonia cycles. Results showed that the thermal efficiency of scheme 1 was 60.94%, exergy efficiency was 53.08%, the thermal efficiency of scheme 2 was 60% and exergy efficiency was 52.31%. Ameel and De Paepe [45] made the efficiency analysis of combined Linde liquefaction cycle for air as working fluid and direct expansion cycle for energy recovery. Results showed that with waste heat temperature of 300 K in an open Rankine cycle evaporator the calculated efficiencies reached up to 36.8%.

Using a cryogen as an energy carrier in a combined simple cascading Rankine cycle with a Brayton cycle was reviewed and assessed by Li Y. et al. [46]. The conclusion from this study was that if a high grade waste source of heat is used then the combination of direct-expansion and Brayton cycles will be the good and efficient way of extracting the cryogenic exergy. While If only environmental and/or a low grade waste heat source is the option then the combining of direct-expansion and Rankine cycle will be more efficient choice because of its low power consumption in the pumping process. Integration between solar renewable energy and cryogenic storage system have been investigated by Li Y. et al. [47], where in this solar-cryogen hybrid power system there are two cycles, namely liquid nitrogen direct expansion cycle and a closed Brayton cycle to extract maximum cryogenic energy. These cycles were optimized using sequential quadratic programming (SQP). The results showed that this

integrated system can increase the power by 30% compared to the option of each cycle acting separately without the combination. Chino and Araki [48] proposed a new system which combined a steam-gas turbines cycle with a liquid air storage system. Results for this two-stage system showed that when the temperature difference between the compressed air at inlet of expansion valve and the cryogen was 20K the energy storage efficiency reached 74% which was considerably better than the 70% efficiency of a typical pumped-up hydroelectric power system. Li et al. [49] introduced a cryogen-based energy storage technology system for peak-shaving and CO_2 capture. In this technology the surplus electricity is used to produce oxygen and nitrogen as the air was separated in a liquefaction plant. Results showed that when helium was mixed with oxygen the performance for exergy efficiency improved from 64% to approximately 70%.

Employing new energy storage technology consisting of a compressed air energy store (CAES) integrated with a liquid air energy store LAES was proposed by Kantharaj et al. [50]. Results showed that the forward conversion system reached an efficiency of 63% with air pressures starting at 5000 kPa while the reverse conversion system reached an efficiency of 67% for the same air starting pressure. As the CES successfully integrated with other applications Li et al. [51] proposed the integration of nuclear power generation with the cryogenic energy storage CES subsystem. Propane and methanol were used for thermal energy storage between liquefaction and recovery cycles instead of pebbles which occupied larger space. The mass flow rate for air was 150 kg/s, the compression pressure during liquefaction was 13409 kPa and the pump pressure during recovery was 11385 kPa with a maximum temperature during recovery of 553 K. Results showed that CES round-trip efficiency of 71.2% and net power output in energy recovery mode of 687.51MW were achieved. Abdo et al. [36] evaluated various cryogenic energy storage CES systems using different liquefaction cycles. Results showed that the CES-Claude and CES-Collins systems

both had higher efficiency than CES-Linde-Hampson system because the bypass turbines provided part of the cooling load needed and generated work at the same time. The CES-Claude and CES-Collins systems had the same efficiency but, in terms of cost, the CES-Claude system was better because it used only one bypass turbine.

A combination of a Brayton cycle using natural gas as a fuel and a direct open nitrogen (cryogen) expansion cycle has been reported by Li et al. [52]. In this combined system the CO2 was captured in solid form as dry ice. The thermodynamic analysis was based on a natural gas flow rate of 1 kg/s, at inlet gas turbine pressure of 800 kPa and cryogen pressure of 10000 kPa. Results showed that the exergy efficiency of the combined system was 64% and the storage efficiency was about 54%. Smith [53] introduced for the first time an energy storage plant of 20 MW using liquid air as the energy storage medium. The compression status was 5000 kPa at 800 oC while the power generation operation status was 8106 kPa and 800 ^{o}C. Water and Freon 12 were used as working fluids for cooling the air in the liquefaction process. Each of three cryo-pumps was designed to deliver 8.6 kg/s of air in recovery mode which leaves the turbine at a temperature of 27 ^{o}C. The thermal efficiency for the cryogenic storage plant was 72%. Morgan et al. [41] presented a novel liquid air energy storage LAES energy generation concept and design at pilot scale. This pilot project is located at Scottish and Southern Energy's Slough Heat and Power station in Slough, United Kingdom. The optimum design results showed that the optimum pressure in the recovery part was between 15000 and 20000 kPa while it was 5400 kPa in the liquefaction part; and a round trip efficiency reached to 60%.

Integration of liquid air storage system with wind energy has been reported by Vandor [54], which integrated system produced and stored liquid air from wind turbine energy. The recovery part used the vaporized liquid air in a combustion chamber which burned natural gas as fuel to drive two gas turbines and used the heat from the flue gas and turbines bearings for

evaporating the liquid air. It has been pointed out from the previous review that most of the published work on cryogenic combined cycles are concerned with large-scale systems with power ratings from 2 to 20 MW and pressure ratios ranging from 100 to 300 resulting in high-efficiencies [55].

2.2.3.2 Small-scale cryogenic energy storage systems

The cryogenic energy technology offers high density of cold energy storage which in turn decreases the system size and the capital cost needed for construction. Moreover, CES systems have a long lifespan with low environmental impact. Such advantages have facilitated the improvement of CES systems for small scale applications. Very limited research work has been carried out in this regard such as Du et al. [56] who developed the feasibility of lab scale or a small scale CES system with power capacity of 5kW and a total storage capacity of electricity approximately 10kWh. The working fluid that exchanged the cold energy in the Rankine cycle was CO_2 and a reciprocating expander was used to convert the cold energy into electricity. The experimental results showed that using working fluid pressure of 10 bar to expand in the large reciprocating expander generated rotational speed of 60 RPM and efficiency of 24-44% for the small scale CES system. Preliminary study was performed for a micro grid scale air liquefaction plant of a liquid air energy storage system with flow rate (0.23 kg/s) by Borri et al. [57]. The software Aspen HYSYS was used for modeling and comparing three liquefaction cycles which were Claude, Linde, and Kapitza cycles. Results showed that the two compressors Kapitza cycle which works at pressure ratio of 40 was the best option in terms of performance and configuration, achieving specific work consumption of about 2519 kJ/kg. Moreover, adding pressurized phase separator decreased the specific work consumption by 21%. The limited published literature on small-scale CES systems indicates that there is a need for more research on this technology to enhance system performance through design and constructing simpler combined cycles.

In general, the published CES literature which described the selection of combined cycles, thermodynamic analysis, and optimization of the cryogenic energy storage combined cycles, shows that there have been relatively little-published works on modeling of cycle turbines which are key components of these cycles and has significant effect on size, cost, and performance.

2.3 Distributed power generation DPG

As the cost of the production of renewable energy continues to decrease, the utility companies around the world have the opportunity to decrease the energy access problems by using distributed power generation (DPG) approach. The DPG mainly dependents on the construction and operation of a compact, small, and clean power plant near or at the energy demand regions (customers) [58]. The DPG is also commonly called small-scale generation, embedded generation or decentralized generation [59]. Although the DPG concept was introduced more than a decade ago, there is still no universal agreement on its definition [60]. Table 2-1 presents the different DPG definitions based on literature survey from the two main perspectives of capacity and location.

Table 2-1 Different DPG definitions based on a literature survey

No.	Definition details	Perspective	Reference
1	The storage or generation typically ranging from 1kW to 100 MW and located close to the load	Location and Capacity	Dondi et al. [61]
2	The generation less than 30MW considers as small units and located close to the load	Location and Capacity	Chambers et al. [62]
3	The generation units which are connected directly to the distribution grid or load side.	Location	Ackermann et al. [5]

4	On-site generation units serving customers or support network	Location	IEA, [63]
5	The small generation units connected near to load or customers	Location	Borges et al. [64]
6	The generation units smaller than central generation units and allow to interconnection to any points in power system	Capacity	IEEE [65]

El-Khattam et al. [58] suggested new DPG calcification based on the capacity of DPG as shown in Figure 2-8. This classification is not restricted by the user or application where the level of capacity for DPG varies from 1kW as one unit to 300MW for multi-units connected in a modular form.

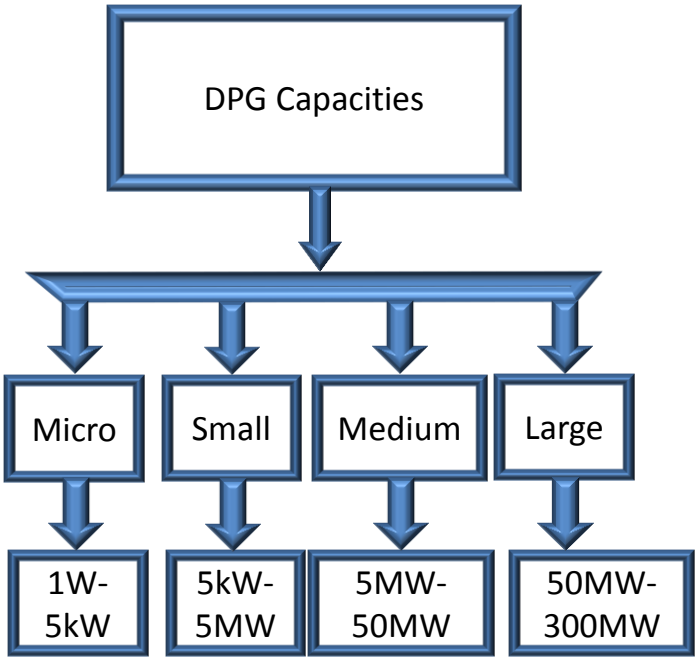

Figure 2-8 Distribution power calcification based on the capacity [58]

Historically the centralized energy generation system has been localized by the availability of natural resources such as coal, natural gas, and oil which is localized in certain territories. But recently the interest in DPG systems is growing with a strong diffusion of renewable energy resources such as wind, sun, hydro and biomass which are by nature distributed through large territories and consumers [66]. Parallel to the energy resource distribution as a driver for increasing interest in distributed power generation technology, there is the reform of energy sector legislative frameworks in many of industrial countries, which aims to make the energy market more environmently competitive [67]. However, the generated powers in developing countries are not utilized in proper grid management ways for most of the energy sources. Better grid management system can be achieved by using DPG through smart grid technology as shown in Figure 2-9. The smart grid technology can regulate effectively the micro and macro amount of power generation because it can schedule the supply and demand based on the consumer's requirements. Integrating distributed power generation with energy storage technologies, renewable energy resources, and centralized energy generation in the smart grid can create a self-healing grid capable of balancing the unstable supply and demand problem in an efficient way. The distributed generation which depends mainly on the renewable energy sources and their smart grid has eco-friendly nature with good impact on the environment. This complex integration between distributed generation and smart girds has increased the development of innovative technologies such as micro or small turbines, photocell, and fuel cell as power generation tools. Moreover it develops a new model for grid-integrated hybrid systems which are effective for energy management by using innovative ideas to integrate distributed generation with storage energy technologies [68]. The distributed power generation hybrid power systems can be based on the domestic capacity and household location as shown in Figure 2-10. Limited research have been done in this regard such as Wang et al. [69], who investigated the distributed power integrated with

energy storage unit to meet the domestic power demand. The generation unit used diesel engine generator and integrated fuel cell with an energy storage unit including a group of batteries and superconductors. This system was simulated and investigated using (Dymola) software where results showed that such a system can handle the household fluctuated demand. Moreover, the study showed that this system needs to be developed for a longer period of peak demand for different households.

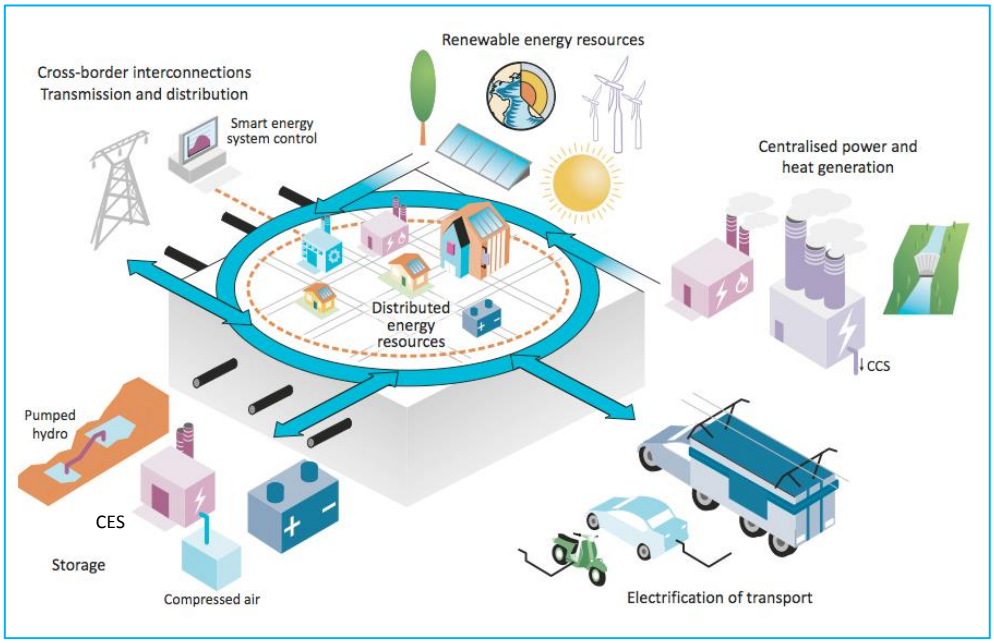

Figure 2-9 integrated smart grid power distribution at the transformed power system [70]

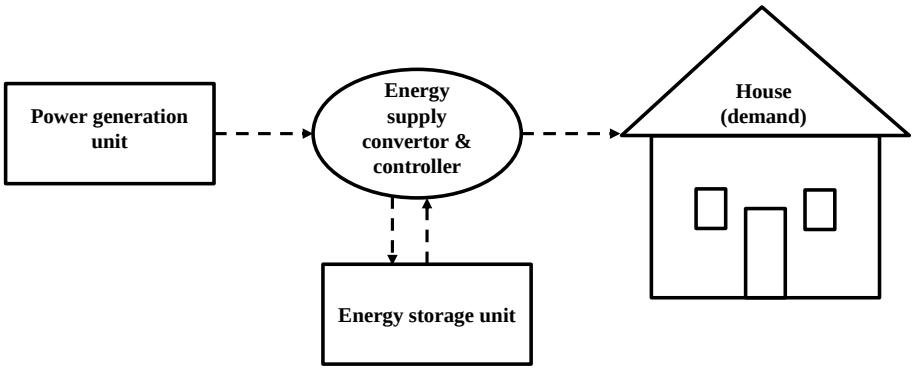

Figure 2-10 Domestic distribution power generation hybrid power system [69]

Bruni et al. [71] studied the hybrid power systems based on integrating photovoltaic panels and fuel cell as power generation sources with local energy storage unit to meet the power demand for a detached house. The Matlab/Simulink was used for simulating the model of hybrid power systems including fuel cells, PV, batteries, and supplying power to domestic load modules. Results showed that this system without long-term energy storage does not have significant renewable energy exploitation; moreover the system efficiency varies from a minimum of 9% to a maximum of 15.6%.

2.3.1 Distributed power generation DPG benefits

The DPG brings many benefits which have been mentioned in various research papers [58, 60, 72, 73]. These are summarised in coming subsections:

2.3.1.1 Technical benefits

- The DPG reduces the line losses when it is located at strategic locations.
- The voltage profile is improved by enhancing voltage support which is provided by the DPG unit.
- Quick installation time and quick change capacity by adding or removing generation units.
- The DPG improves the power quality.
- Enhances the DPG system reliability and security, as there are a lot of generation sites rather than only one centralized large generation.

2.3.1.2 Economic benefits

- Install the DPG in certain locations to provide the required demand can reduce the cost of constructing the new transmission and distribution lines also the cost of transporting fuel.
- The DPG increases the lifetime of grid components such as transformers.

- With lower losses, the generation rate and fuel savings will be more.
- Installing DPG decreases the constructing time and schedules which in turn decreases the cost.
- The DPG can diversify the type of energy sources and fuels which means that it is not restricted by the energy source or fuel type.
- The DPG has location flexibility which makes it not restricted by centralization power that has a great impact on energy production prices.
- The remote DPG and combined heat and power system can be more economical because it is using heating or cooling for improving system efficiency.
- The DPG plants have lower operation and maintenance costs.

2.3.1.3 Environmental benefits

- Encouragement of the green energy generation from renewable energy sources.
- Limiting emissions of greenhouse gas and optimum use of energy resource with simultaneous energy supply-demand.
- Avoidance of using more land for constructing new transmission grid and large generating stations.

2.4 Expansion machines

In the distributed power generation systems expansion devices are used for extracting the energy from the working fluid and convert it to useful mechanical power. The expanders are considered vital components in the cryogenic energy storage cycles due to their effectiveness on the cycle efficiency and performance [74]. In general, there are two types of expanders:

the first one is the positive displacement or volumetric type, such as reciprocating, screw, scroll, rotary expanders. The second type is the velocity type such as radial inflow and axial flow expanders [75].

2.4.1 Positive displacement expanders

The positive displacement expanders extract the work directly by changing the chamber volume of the working fluid. Therefore this kind of expanders deals with high pressure, small velocities, and high forces of the flow and expander parts. The main design parameters for this expander type are swept volume and the built-in volume ratio which usually specifies the suitable application for positive displacement expander type [76]. Despite the reasonable cost for this type of expanders, the main limitation is the internal volume where the maximum internal built-in volume ratio is 5 [77]. The coming subsections outline the types of positive displacement expander in literature.

2.4.1.1 Screw expander

The first steps toward using screw expanders date back to the early 1980s where they were designed as screw compressors with opposite rotational direction. The commercial manufacturing of screw machines was started by Lysholm company [78]. The screw expander has one helical grooved rotor in the case of single screw expander and two rotors connected with each other in case of twin screw expanders. Figure 2-11 shows the working steps of twin screw expander where at the inlet the high-pressure fluid enters the top of the screw and turns it, while the fluid keeps moving along the length of screw and the pressure decreases. The fluid static pressure on the screw blade surface makes it rotate. Finally at the outlet port when the tooth gap connects to it the fluid runs out and the volume decreases to zero [78, 79]. New thermodynamic calculations model for single screw expander includes frictional losses carried out by Shen et al. [80] for working fluid compressed air. The mathematical model is solved by MATLAB software and compressed air thermodynamic properties specified by the

REFPROP database which analysed results then compared it with experimental results. Results showed that in order to decrease the frictional losses and rotor wear, the fitting and meshing clearance height have to be in the range of 0.04mm to 0.02 mm.

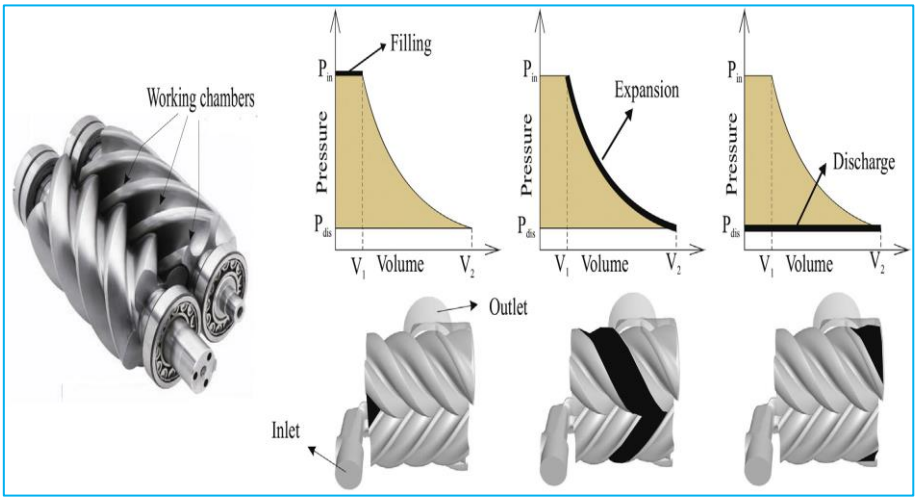

Figure 2-11 Screw expander working principle and steps [78]

Using a screw expander to replace throttle pressure valve to regulate natural gas pressure can harvest its potential pressure energy. Xiong et al. [81] proposed this screw expander with its dual tasks to keep the pressure constant and increase volume flow rate that in turn increase the expander rotational speed and influence the isentropic efficiency. Results showed that the stable pressure decreased from 0.6 MPa to 0.1 MPa with optimum isentropic efficiency reaching 25% and output electricity of 60 kWh. Bianchi et al. [82] investigated numerically the twin screw expander for power conversion applications at low heat source less than 100 °C by using commercial software (GT-SUITE^{TM}) which is the one-dimensional formulation of Navier–Stokes equations. Results for different inlet pressure of R245fa and rotational speed on the expander performance showed that at a pressure of 5 bar and a speed of 3750 RPM the volumetric efficiency was enhanced to 61.2%. The high-pressure screw expander has been investigated experimentally by Li et al. [83] for rotational speed from 1500 RPM to

3000 RPM and pressure ranging from 1.0 MPa to 5.0 MPa. Results revealed that at maximum operating conditions of 5.0 MPa and 3000 RPM the expander produced 56.55kW power output and the volumetric efficiency reduced to 46.9%. Hsieh et al. [84] examined experimentally an ORC with a screw expander working by R218 as the working fluid. The experiment evaluated the system performance at heat temperature ranging from 90-100 ^{o}C in both subcritical and supercritical states. The expander prototype dimensions were 171 cm high and 150 cm wide. Results disclosed that the heat source temperature produced 20 kW of power and 5.7% of gross thermal efficiency. Despite the advantage of the screw expander of handling high-pressure ratio reaching up to 7 [85], still there are main drawbacks that limit its performance such as the leakage through the clearance between the bottom of the screw groove and gate rotor tooth top and also the frictional losses between them [80, 86].

2.4.1.2 Reciprocating piston expander

This type of expander started as compression machine then with time it was adapted to be an expansion machine. As any expanders, this type use potential heat and pressure energy developed in combustion chamber by working fluid to produce useful mechanical shaft power. Figure 2-12 shows the two-stroke reciprocating piston expander cycle operational steps. Using this type of expander with cryogenic storage systems is still under development and little research has been done in this regard. In 2001, Peter Dearman [87] invented the Dearman engine which is cryogenic reciprocating piston expander using the vaporized liquid air or liquid nitrogen in the expander cylinder to push the piston and run the car with zero emissions. One of the significant options of this engine is using it in large refrigerated trucks where in this case it can at the same time provide both cooling and shaft power which might avoid 38 tonnes of CO_2 yearly. Tian et al. [88] studied two-stroke reciprocating piston expander driven by nitrogen as the working fluid, with inlet pressure and temperature at 1.1

MPa and 300 K, while the outlet pressure and temperature were 0.1 MPa and 268 K, and keeping the temperature of the cylinder walls at 294K.

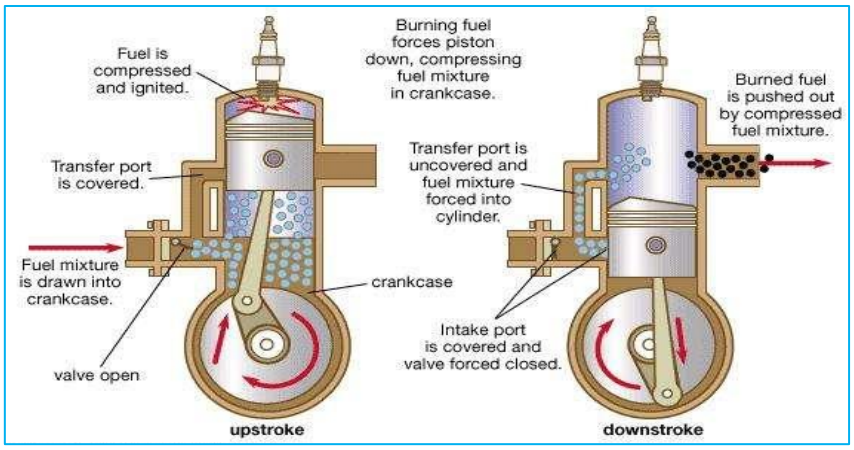

Figure 2-12 reciprocating piston expander operational steps [89]

Using STAR-CD software the cylinder flow simulation of the nitrogen engine was analyzed. Results showed that with engine speed of 1500 RPM the maximum intake speed was 122 m/s and the exhaust was 280 m/s while during the expansion the speed of the fluid inside the cylinder was 4.4m/s. The injection of cryogen in the engine needs a combination of swift injection duration and high mass transfer. To that end, Mutumba et al. [90] presented experimental set up of liquid nitrogen injecting system into an open vessel. The quasi-steady flow tests were utilized to analysis the direct cryogen injection process in the cryogenic engines. Results showed that using an electro-hydraulic valve actuation to control the injection process of liquid nitrogen could achieve high pressure reaching up to 94 bar, while observing the linear relationship between the valve lift and injected mass flow rate. The limitations of reciprocating piston expanders are leakage and friction between the piston and cylinder. As it has a large number of moving parts it needs a complex lubrication system.

2.4.1.3 Scroll expander

Work on the scroll expander machine had started in the 1970s as a compressor in refrigeration applications. Recently another potential application has emerged with the object of reusing it as a scroll expander to drive generators for power generation [91]. The construction of the scroll expander includes two major parts: the fixed scroll and the orbiting scroll where the combination between their spiral walls forms chambers trapping the gas as shown in Figure 2-13. As the working fluid expand in these chambers the orbiting scroll moves around a circular orbit and generates power [92].

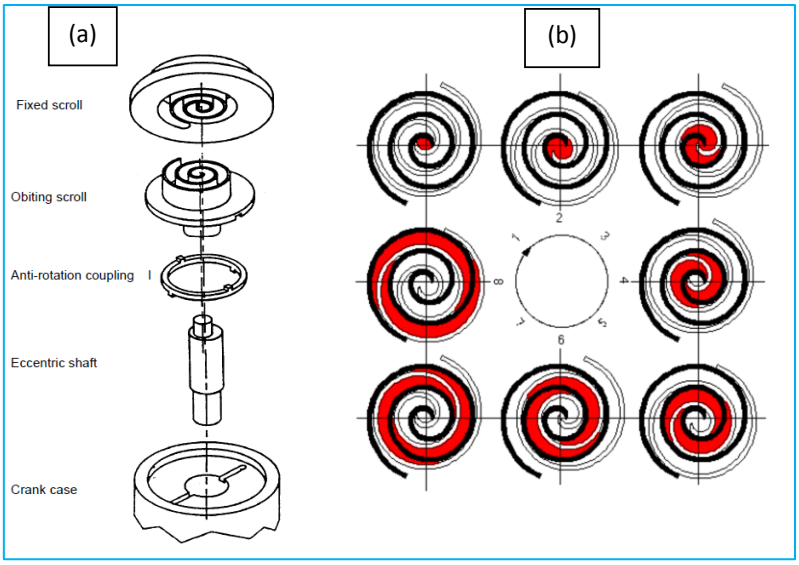

Figure 2-13 Scroll expander schematic (a) parts details, (b) operation steps [93]

A lot of research has been carried out for this type of expanders including the small-scale generation such as by Qiu et al. [94] which examined the viability of reusing the scroll compressor as expander in ORC system. The investigated geometry for the tested scroll compressors was: orbiting radius 11 mm, height of scroll vane 55 mm, and thickness of scroll vane 5 mm, using working fluid compressed air. Test results clarified that it was possible to

use the scroll compressor as an expander without major modifications, while changing the rotational speed from 1600 to 3995 RPM enhanced the adiabatic efficiency from 55.5% to 58.5% and power output from 449W to 965W. New scroll expander technology was proposed by Luo et al. [95] where he used permanent magnetic spirals to enhance the expander performance especially reducing the leakage at low-pressure supply conditions. The ANSYS Maxwell software was used to simulate the magnetic field distribution and MathWorks MATLAB for predicting the overall variation trend. Test results showed that at a supply inlet pressure of 2 bar and a flank leakage clearance of 0.06 mm the efficiency reached 15%. Lu et al. [96] presented a study to recover the waste heat from small engine coolant and exhaust by using ORC with scroll expander that differs from conventional engine ORC system which uses engine exhaust only. Results showed that when n-Pentane was used as the working fluid the scroll expander produced power output reaching 0.82 kW at inlet temperature of 90°C, and system efficiency reaching up to 12%. The efficiency and power evaluation for a scroll expander using compressed air has been studied by Zhang et al. [97]. Experimental testing and numerical modelling were carried out to evaluate the scroll expander performance. Results from experimental testing and theoretical models were in good agreement. The optimal expansion ratio was in the range of 3-4 which produced an isentropic efficiency of 66.2% and power output of 3.5 kW. The main advantages of the scroll expander are the low number of moving parts, low noise level, low flow rate, and the ability to work with two-phase conditions [91, 98]. While the main disadvantages are leakage and friction losses, addressing the leakage problem needs reliable and effective seals, while the friction needs lubricant compatible with working fluid [75, 99, 100].

2.4.1.4 Rotary vane expander

This kind of turbine type offers the potential of cost-effective solution in low power generation domain due to the simplicity of their structure [101]. Figure 2-14 shows the

operation steps and the parts details of rotary vane expander where the vanes are mounted on an eccentric rotor that drives the shaft. The vanes length keeps changing during rotor movement to contact with the housing wall and create the varying gas chambers sizes, while the vanes length is controlled by a spring or hydraulic pressure. The working fluid enters the small chamber with high pressure, and then drives the rotor to expand for larger chambers until exhaust.

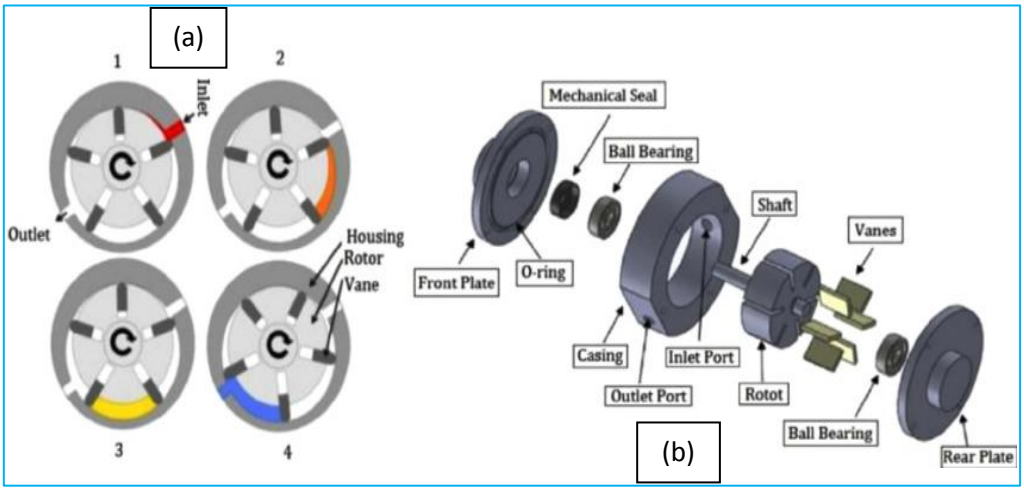

Figure 2-14 Schematic of rotary vane expander (a) operation steps, (b) parts details [102]

Various research work was carried out on this type of expander such as Kolasiński et al. [103] who presented experimental with numerical study for a rotary vane expander in small-scale ORC system. The numerical model was developed using ANSYS CFX commercial software and the experimental prototype was constructed with inner diameter of 37.5 mm and cylinder length of 22.0 mm. Results showed that the working fluid R123 produced power output ranging from 300W to 3kW, and overall efficiency from 7% and 12%. Mascuch et al. [101] tested rotary vane expanders as micro-unit for waste heat recovery (350°C inlet and 90°C outlet) for combined heat and power production with hexamethyldisiloxane (MM) as working fluid which mixed with 5% of lubricating oil in ORC system. Test results revealed that the rotary vane expanders have achieved isentropic efficiency ranging from 40% to 58%

and power output from 1kW to 8kW. Subiantoro et al. [104] has developed MATLAB computer models to simulate and compare the performance of four rotary vane expanders using inlet pressure ranging from 2 to 30 bars and rotational speed from 600 to 1800 RPM. Results showed that the optimum expander design produced power output of 160W and overall efficiency of 65%. The major problems facing the rotary vane expanders are: the complexity of the leakage problem between the inlet and outlet and between the chambers due to the contact delay between the vanes and the stator walls; and also the friction and wear that take place between the vanes and the stator walls [105].

2.4.2 Velocity expanders

The velocity expanders are also known as turbo-expander where the turbo word is of Latin origin meaning "that which spin". The turbo-expanders are devices that convert the fluid energy to kinetic energy and then extract the mechanical energy by the rotor part. Nowadays the turbo-expanders or turbines are at the heart of many industries such as turbo engine in aircraft and cars, the steam turbine in power plants, cryo-turbine in liquefaction plants, and gas turbine in petroleum plants [106]. The turbo-expanders are classified according to the most popular devices in the global market mainly to two types of radial turbines and axial turbines [107]. As the interest in renewable energy sources and waste heat recovery in industry is increasing, thus the interest in the development of small-scale turbo-expanders will increase.

2.4.2.1 Radial Turbines

This turbine type has had a long history of development where the first one was developed by Francis and Boyden in the United States in 1847, it is a hydraulic turbine and was used in a number of applications, it is now known as the Francis turbine [108]. As shown in Figure 2-15 the volute distributes the fluid flow to enter the stator blades in the radial directions, thus it is named as a radial turbine. Also, the flow enters the rotor in the radial

direction but leaves it in the axial direction after deflecting by 90 degrees. During the expansion from leading edges to the a trilling edges, the flow area changes significantly due to change in the mean radius from entry to exhaust [109].

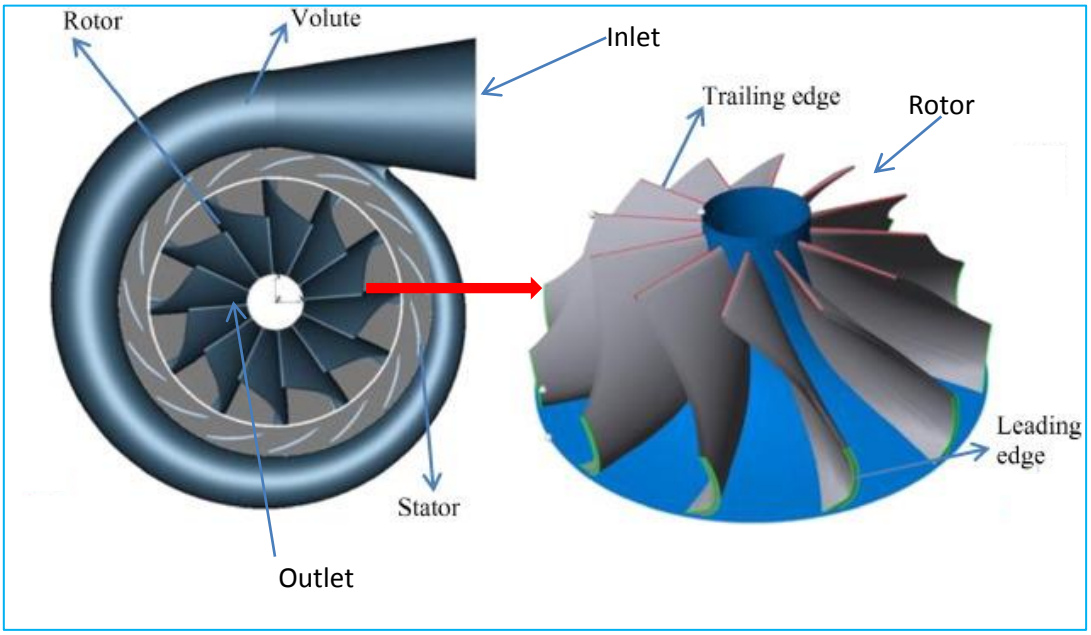

Figure 2-15 Schematic of radial turbines main parts [110]

Table 2-2 summarizes the recent important published literature regarding small-scale radial turbines for power generation application based on the: analyzing method, inlet condition, working fluid, and performance parameters.

Table 2-2 Radial turbine literature review summary

Authors	Analysing Method	Heat Source Temp. K	Inlet pressure MPa or expansion ratio	Working Fluids	Performance Parameters (Efficiency and Power)
Persky et al. [111]	1D mean line	943 -1073.15	10.69 to 39.59	CO_2, SF_6	84 kW 82.47%
Li et al. [112]	1D mean line and 3D CFD	1350	0.243	Combustion gas	71%

White et al. [113]	1D Baines model	353.15 - 633.15	2.87 to 4.17	R1234yf, Benzene	82.5% to 85.2% , 25 kW
Cerdoun et al. [114]	3D CFD	923.15	0.28	Air	80%
Mounier et al. [115]	1D Baines model	363-523	Er = 1.5-8.5	R134a	80%, 22kW
Kapoor et al. [116]	1D mean line and 3D CFD	373.15	0.15	Combustion gas	80%
Alshammari et al. [117]	1D mean line and 3D CFD	337-405	Er = 3.0-10.0	R245fa, R123	80%,18.6 kW
He et al.[118]	1D Wallace model	373	2.50	Air	82.34%, 225.2 kW
Ke et al.[119]	Experimental setup	233.7	0.36	Air	73.25%
Guillaume et al.[120]	Experimental setup	453	3	R245fa, R1233zd	28%, 3.5kW
Kim et al.[121]	1D Balje model and 3D CFD	413	5	R143a	79.56%, 400kW

It can be seen from this radial turbine review that there is limited work for turbine capacity less than 10kW with working fluid nitrogen, and the inlet pressure and temperature are higher than 300K and 0.3 MPa. This turbine is good for handling high expansion ratio per stage but still has startup and vibration drawbacks due to centrifugal forces effects.

2.4.2.2 Axial turbines

The earlier steam axial turbine was invented by the Swedish engineer Carl de Laval in 1883 which suffered from the technical problem of over speed. Sir Charles Parsons in 1891 overcame this problem by inventing his 15 stages axial steam turbine [108]. The one stage axial turbine mainly consisting of fixed guide blades which are called the stator and a row of moving blades called the rotor as shown in Figure 2-16.

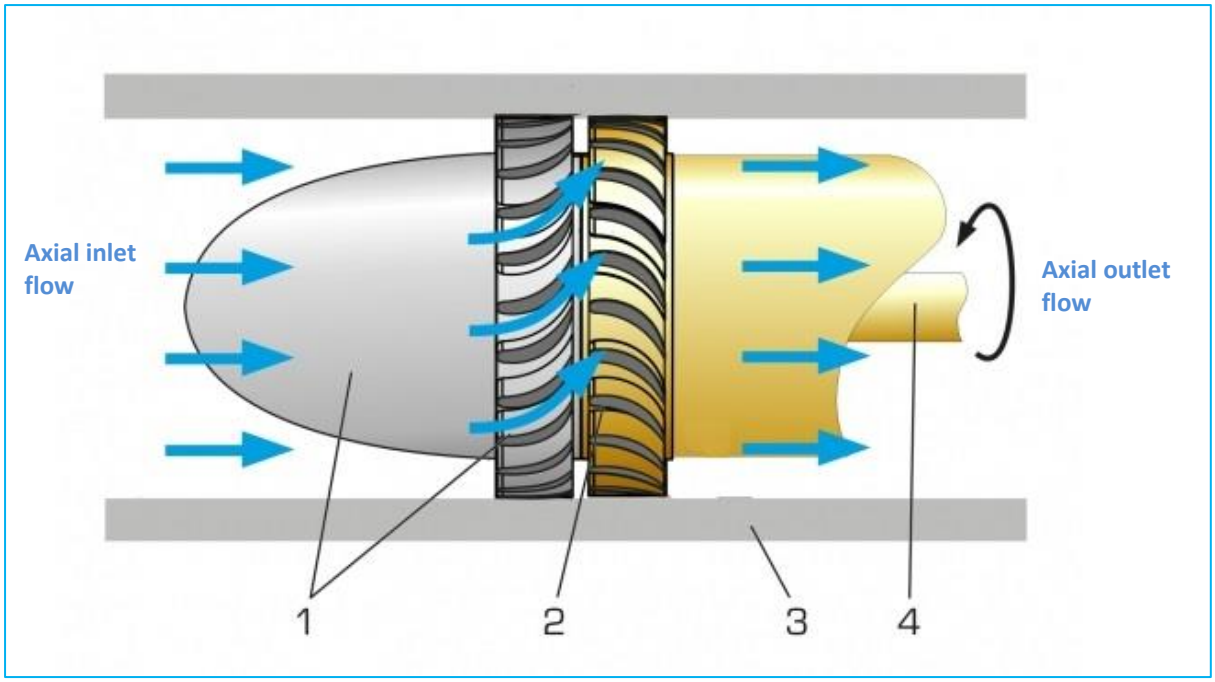

Figure 2-16 Axial turbine operation and parts: 1 stator, 2 rotor, 3 case housing, 4 shaft

The flow enters the stator in the axial direction to be accelerated to the required direction and speed then enters the rotor to provide the shaft power by moving the rotor rows. The stator and the rotor lay in the housing duct and the flow enters and leaves this duct in the axial direction which adds simplicity to the design and construction of this expander type. More attention has been paid recently to develop small-scale axial turbine design and Table 2-3 summarized published literature regarding small-scale generation based on the analyzing method, inlet conditions, working fluid, and performance parameters. The axial turbine provides significant advantages over the radial type such as it has better adiabatic efficiency for the same operation conditions, lower cost, easy to manufacture and maintain, lower vibration and fatigue failure risk. Moreover, the axial turbine partial admission configuration features can work with low flow rate operating conditions [122].

Table 2-3 Small-scale axial turbine literature review summary

Authors	Analysing Method	Heat Source Temp. K	Inlet pressure MPa or expansion ratio	Working Fluids	Performance Parameters (Efficiency and Power)
Weiß et al. [123]	Experimental setup	449	Er=12 - 24	Hexamethyl disiloxane (MM)	73.4%, 12 kW
Yue et al. [124]	Experimental setup	358	0.65	R245fa	59%, 5kW
Dumont et al. [125]	Experimental setup	493	0.5	Steam	41.5%, 1.5kW
Adnan et al. [126]	3D CFD	1200	0.33	Combustion gas	70 %, 155 kW
Di Battista et al.[127]	Experimental setup	566.5 - 766.8	1 - 2.2	R245fa	30-40%,2-5 kW
Varma et al.[128]	Experimental setup	353	0.51	Air	60%, 2.5kW
Zhang et al.[129]	1D analysis	420.15	3	R245fa	86.7%, 387.26 kW
Bahr Ennil et al.[130]	Experimental setup	307	0.16	Air	59.26 %, 0.7kW
Pu et al.[131]	Experimental setup	370	0.6	R245fa, HFE7100	59.7%, 1.979 kW
Sun et al.[132]	3D CFD	393.15	1.2	R245fa/R123 mixtures	55.3%, 8.13 kW
Heshmat et al.[122]	1D and 3D CFD analysis	349.4	0.655	R245fa	80%, 30kW

It can be concluded from above small-scale axial turbine literature review that: (1) there is limited research in this area, (2) turbines with power output less than 10kW suffer from low-efficiency performance, (3) the operating conditions in terms of inlet temperature and inlet pressure are often high (4) there is no published study that connected advanced analysis approach (which connect the 1D, 3D) and experimental testing, (5) there is no research to

investigate the nitrogen as working fluid and very little investigated air. For these reasons the current study aims to address such knowledge gap in the development of small-scale axial turbines.

2.4.3 Axial turbine optimization

Optimization of turbine blades has significant impact on turbine performance and cost in both industrial and aerospace fields. For the purpose of shaping the turbine blades with efficient geometry, the parameterization method needs to be created through an optimization procedure based on the CFD simulation analysis. Validating the CFD modelling with experimental results makes it a reliable and robust tool for optimizing turbine geometry to achieve best performance [133]. In the large scale, some research has been done to optimize axial turbine, So et al. [134] presented aerodynamic optimization design process for 2.2 MW axial turbine turbocharger single stage outlet casing geometry by using CFD numerical model ANSYS 14.5. The outlet casing geometry is controlled by a number of parameterized curves and the objective functions were the pressure coefficient and the isentropic total stage efficiency. The optimization results clarified that the turbine efficiency improved by 2.4% compared to the original design. Marchukov et al. [135] studied a multidisciplinary optimization for a three stage low pressure axial turbine in turbofan engine to improve turbine operation process of static and dynamic blade strength and turbine efficiency. The blade profile parametrization technique consisted of nine parameters which were the stagger angle and two thickness points for three blade sections hub, midspan, and shroud by using numeric software (Numeca FineTurbo) for aerodynamic analysis and (ANSYS Mechanical) for structural analysis. The optimization results showed that static and dynamic strengths were satisfied after reducing flow swirl at the low-pressure turbine outlet; however, that slightly decreased the turbine efficiency by 0.249%. Asgarshamsi et al. [136] considered 3D blade shape optimization for axial gas turbine to improve expansion ratio and efficiency of the axial

turbine. The 3D blade was shaped by redistributing the stagger angle along the spanwise sections and then solves the model using RANS 3D equations and steady state flow simulations. Results showed that optimizing the stagger angle can improve the turbine stage efficiency by 0.86%. Meroni et al. [137] presented preliminary design optimization for organic Rankine cycle and it featured four stage axial turbine with a selection of improved working fluid. The optimization task for the turbine is performed using the numerical software (TURAX) where the total number of turbine optimization input variables was 8 in addition for rotor rotational velocity and axial velocity for each stage. Results showed that the working fluid gave the best trade-off between turbine and cycle design where the optimum turbine design improved the turbine efficiency by 7%. Li et al. [138] optimized 600 MW seven stage axial steam turbine by using ANSYS CFX software. The stagger angles and stacking lines of the stator stages were changed to improve the turbine efficiency and power output. Results showed that the optimum design improved the turbine efficiency by 0.43% and power output by 0.72% while keeping the mass flow rate nearly unchanged. The previous large-scale axial turbine optimization process has a large number of optimization parameters which required very large computational time. Moreover, the improvement in the performance is little compared to these computational times efforts.

There is a very limited work for small-scale axial turbine optimization such as Ennil et al. [139] who developed compressed air small scale axial turbine (10kW) optimization by using ANSYS CFX software to improve the total efficiency and total pressure losses. The parameterization method was aerofoil with eleven parameters for the rotor blade only. The optimization results showed that the optimized turbine improved the total efficiency by 12.48%. However, this study are generated for the rotor only while any modification of the stator will directly influence the rotor entrance which means the stator is not less important than the rotor. The other issue is that the number of parameters used for the rotor only is high

without clarifying in which sections these parameters changed. Al Jubori et al. [140] investigated the optimization of small-scale axial turbine working in ORC low-temperature heat sources (<100^{o}C) by using ANSYS CFX software. The parametrization method was aerofoil with twelve parameters for each rotor and stator and the isentropic turbine efficiency and power output chosen as objective functions with two constraints mass flow rate and rotational speed. The author claimed that the optimized turbine produced an isentropic efficiency of 88% and power output of 6.3 kW for working fluid (R123). However, describing blade geometry by the aerofoil method is not recommended for small blades because the blade geometry changes when exports from BladeGen to DM modules and the stagger angle do not affect the geometry. Moreover, the rotational speed is an input parameter so it does not change during optimization while the study made it as a constraint parameter. Finally, the study did not clarify in which section the geometrical parameters changed. From the previous axial turbine optimization literature review, it can be seen that there is a need to develop new optimization parametrization technique with low parameters number which describes the blade geometry in an effective way. Therefore selecting the parameters needs to be wise; for example using chord length which is not used by any of the previous research could be very effective in representing the 3D blade geometry.

2.4.4 Axial turbine advanced blade configuration

When the layout of different sections within the blade is in the required direction, the stacked sections will form advanced three dimensional blade configurations as shown in the Figure 2-17 [141]. Such blade configuration can have positive effects on the flow vortices, the pressure, and the flow rate distribution along the blade [142].

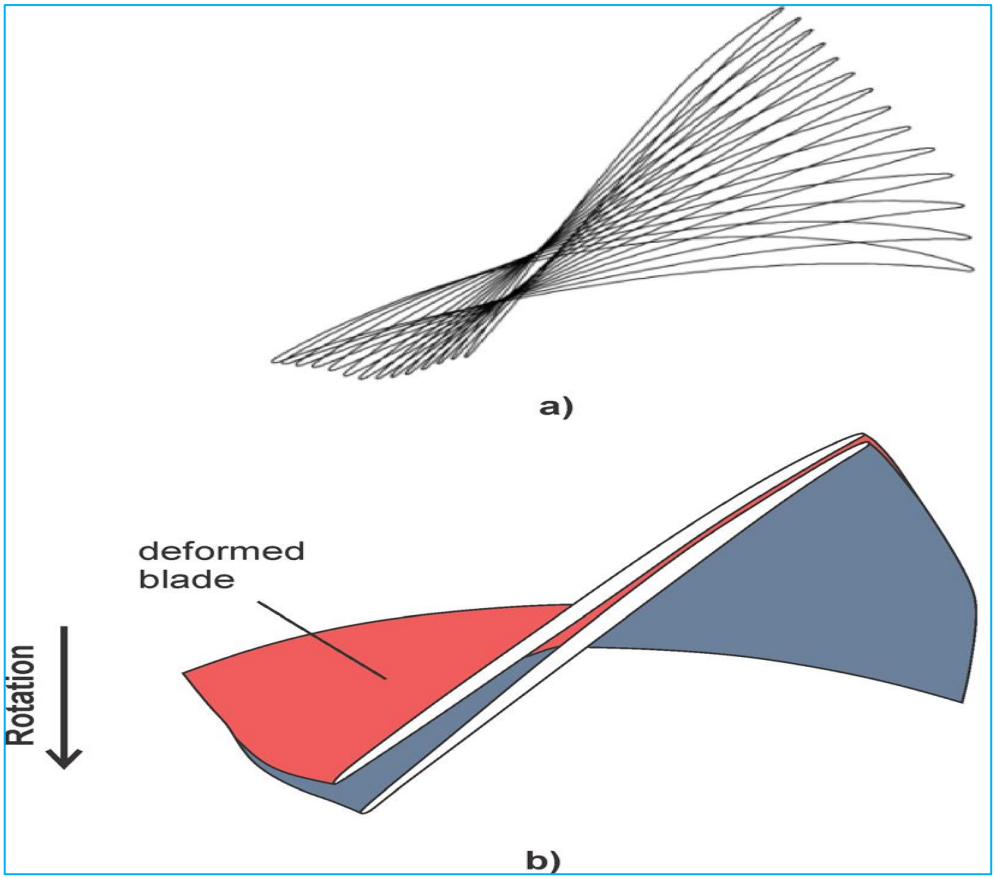

Figure 2-17 Blade configuration process (a) Rotated sections of axial turbine, (b) Blade configuration [141]

Some researchers have investigated the effects of these configurations on the performance of axial turbine such as Asgarshamsi et al.[143] who optimized the sweep and lean angles for the stator and rotor blades of axial gas turbine. The stator blade angle of sweep changed from 2.9 degrees to -5.9 degrees while rotor sweep angle changed from 2.0 degrees to -2.3 degrees in the same way the blade lean angle changed for the stator from -2.8 degrees to -4.3 degrees and for the rotor from 2.0 degrees to -1.5 degrees. Results showed that the change of the sweep and lean angles unloaded blade and improved the turbine total efficiency by 1.31% and 1.17% for design and off design conditions. The effect for negative bow stator blade for axial turbine with a blade height 0.36m was investigated by Shieh et al. [144]. The numerical finite-volume code of three dimensional Reynolds averaged Naiver-Stokes equations was

utilized for solving an axial turbine problem with bow blade. Results showed that the blade radial force increased when the bow negative angle increased and the aerodynamic loading decreased toward side walls. Karrabi et al. [145] study the significance of leaned, bowed, and twisted blade configuration on performance of single stage axial turbine. The twist angle varied from 3 degree to -3 degree, lean deviation stacking axis varied from -4mm to 4mm, and bow deviation stacking axis varied from -0.6mm to 0.6mm where the ANSYS CFX software has been used to analyze these cases. Results showed that the bow and lean configurations did not improve the turbine performance, while the twist configuration enhanced turbine performance. Dippolito et al. [146] detailed the flow field behavior through leaned axial turbine stator for lean angles 0,10,15, and 20 degrees. The experimental and numerical test is achieved in studying pressure contours through the turbine where the Fluent and ANSYS-CFX software were used in the numerical analysis and five holes probe used in the experimental tests for finding static and total pressure. Results showed that increasing the blade lean decreased the secondary vorticity at the tip section while increasing it at the hub section. On the contrary, the blade loading increased at tip section while decreasing it at the hub section. It is clear from the previous literature review of axial turbine advanced blade configurations that there is a need to investigate these configurations for small-scale axial turbines. Moreover there is a need to carry out a comprehensive study of four blade configuration (lean, sweep, twist, and bow) in one study.

2.4.5 Multistage axial turbine

Increasing the number of stages in axial turbine makes better exploitation of expansion enthalpy drop which in turn enhances the turbine power output and efficiency or could decrease the rotational velocity for the purpose of direct contact with the generator [147]. Recently several studies for multistage large scale axial turbines have been carried out such as that of Fuls et al.[148] who proposed a new methodology to model an impulse multistage

axial turbine by using a nozzle flow analogy which simulates the turbine stages as a series of nozzles. The three stages axial turbine is analyzed by (Mathcad) software with steam as the working fluid combined with (Flownex SE) software to interconnect various thermo-fluid components. Results showed that the validation for the numerical model has a maximum error of 6% at flow rate of 318 kg/s, and the turbine produced 5.63 MW. Partial admission features were used with a multistage axial turbine to have high power with low flow rate at the same time. Therefore Surwilo et al. [149] had investigated the effect of partial admission on a four stage axial turbine working with ORC which had MDM as the working fluid. The analysis was achieved by ANSYS Fluent and mesh generator ICEM–CFD which showed that the unsteady circumferential non-symmetry flow appeared in the first three stages due to partial admission features. Moreover, the efficiency of the turbine from stage 1 to 4 with a partial admission was 70%. Ghenaiet et al. [150] studied the characterization of steady and unsteady flows for the two-stage axial turbine which drove a high-pressure compressor in a turbofan engine. The ANSYS-CFX software and the Fast Fourier Transform FFT analysis were used to solve the two-stage axial turbine flow with outlet shroud diameter of 0.83 meters. Results clarified that the better turbine efficiency was 88.43% with a reduced mass flow rate of 113.5 kg/s; however, flow in the second rotor suffered from accumulated circumferential distortion. Ghoreyshi et al. [151] designed a three stage axial turbine with three stator pre-heaters to decrease fuel consumption and make uniform temperature distribution for high-performance multistage turbine. The analysis was done by preliminary design (mean line method) for each stage followed by 3D ANSYS CFX software to simulate the unsteady flow for ten total components. Results showed that the turbine power target of 200MW achieved with air flow rate of 150kg/s reduced engine emissions by creating rotors inlet uniform temperature distribution zones. One dimensional flow analysis for a two stage axial turbine are presented by Jouybari et al. [152]. The analysis was based on steady flow

conditions and a mean streamline method to test different losses models and compare them with experimental results. The comparison between theoretical and experimental results showed that good adaptations were obtained and the Soderberg losses model gave maximum error of 12.9% while Came & Dunham gave the lowest error of 10.3%.

In the small-scale case, very little literature has been done. Al Jubori et al. [153] compared small-scale axial turbine single stage with constant annular area two stage to show their effect on ORC system performance. The one-dimensional mean line method and 3D CFD ANSYS CFX software have been used to analyze the problem. The results for expansion ratios from 3 to 6 claimed that the better total turbine efficiency of 83.94% and output power of 16.037 kW for working fluid (n-pentane) was achieved for constant annular area two-stage turbines. However, the low expansion ratios were not included in this study to show clear advantage and disadvantage of the multi-stage design. Daabo et al. [154] compared small-scale radial turbine single-stage, axial turbine single-stage, and axial turbine constant annular area two stages to show their effects on the compressed air solar Brayton cycle. The one-dimensional mean-line method and 3-D CFD ANSYS CFX software were used to obtain their results. The authors argued that two stage axial turbine has better performance than the other two turbines at off design condition where at compressor efficiency 95% the cycle thermal efficiency was enhanced from 5% to 10%. However, this study did not include the expansion ratios as a design parameter, despite this being a critical parameter for choosing multistage turbine over the single stage. From the limited literature on small-scale multistage axial turbines, it is clear that a constant annular area multistage is the only configuration that has been investigated. The over-speed problem with high expansion ratios in the second stage needs to be investigated and solved by the new configuration.

2.5 Summary and conclusions from the literature review

From the above literature review the summary and conclusions can be outlined as below:

- The energy storage literature review explained and compared three storage technologies (PSH, CAES, and CES) which are important for energy management applications and the potential of CES technology over other technologies is presented.
- Most of the literature reviews of CES systems were concerned with large-scale systems and there is limited literature regarding small-scale especially for those ranging from 1 to 10 kW which is important for small/medium building, rural, and off-grid applications.
- The literature review for CES systems disclosed that most of the literature investigated thermodynamic modeling for combined cycles and optimization of this combination without attention to cycle expanders, which are considered as a key component in these cycles, and have significant impact on size, cost, and performance.
- The literature review for distributed power generation clarified the classifications for this power generation technology and the importance of its integration with storage systems within smart grid systems; and detailed benefits of this generation system were presented.
- The expansion devices are the main components in any power cycle therefore the types of expansion devices are obtained and the advantages and disadvantages of each expander type were explained and clarified.

- All previous studies regarding velocity turbines type (radial and axial) showed that there are limited published studies regarding small-scale turbines, especially within the range of 1 to 10 kW and CES applications.
- The majority of available literature for small-scale axial turbines are presented in Table 2-3 and it shows that the turbines with capacity less than 10 kW suffer from low-efficiency performance (less than 60%); the operating conditions were designed according to high value (pressure and temperature), while the working fluid nitrogen was not investigated, and no comprehensive study that includes 1D, 3D, and experimental analysis was carried out.
- In all previous studies regarding the optimization of the small-scale axial turbine, the aerofoil method was used. But because it is not suitable for small-scale, there is a need for developing a new optimization parameterisation technique with low parameters number which effectively describes the blade geometry.
- The literature review for advanced blade configurations showed that there is a need to investigate these configurations for the small-scale axial turbine. Moreover, there is a need to carry out a comprehensive study for all four blade configuration (lean, sweep, twist, and bow) in one study.
- The literature review for multistage axial turbines showed that there is limited work published regarding small-scale multistage axial turbines; where all investigate multistage constant annular area only, which in fact accelerates the flow until the over speeding problem appears in the second stage for high expansion ratios. This shows the need for developing new multistage turbine configurations to overcome this problem.

CHAPTER 3

CRYOGENIC DISTRIBUTED POWER GENERATION CYCLES AND SYSTEMS

3.1 Introduction:

The future of energy production faces many challenges such as sustainable energy supply, good management of energy demand and effective exploitation of renewable energy. The energy storage technology can play an important role in addressing all these challenges; therefore energy producers have a dramatic upsurge in attention for energy storage technologies. The significance of energy storage technologies is their ability to balance the fluctuation of energy supply and demand in addition to overcoming the intermittent nature of renewable energy sources. The cryogenic energy storage is one of the new energy storage technologies which have a high grade cold energy that is more valuable than hot grade according to the second law of thermodynamics [46]. Most of cryogenic combined systems modeling studies described in chapter two were related to large-scale cycles with power output ranging from 2 to 20MW and high turbine expansion ratios ranging from 100 to 300. However, the availability of studies related to small-scale generation for small buildings and small/medium buildings applications with power output ranging from 1 to 10 kW and turbine expansion ratios ranging from 1.5- to 3bar are very limited. In this chapter four new

cryogenic power generation cycles ranging from the simple basic cycle to the complex combined one are developed to predict the performance of a small-scale power generation system. Full thermodynamic analysis and parametric studies have been conducted to specify the turbine design and operation conditions. The work in the following sections has been already published in [7, 34, 55, 75].

3.2 Cryogenic Energy Cycles:

Cryogenic storage energy extraction has been studied from a theoretical prospective by using thermodynamic analysis. Four cycles has been proposed to utilize the stored energy from cryogen for generation of power and cooling applications.

3.2.1 Open Rankine (OR) Cycle:

The cryogen stored energy can be converted into useful work by using direct expansion in OR cycle expander as shown in Figure 3-1. This cycle has a simple design and a minimum number of components, and thus its manufacturing and installation become easy and cheap. In this cycle, the main parts of the system are the evaporator, the heat exchanger, the turbine, and the pump with the cryogen used in this cycle being liquid nitrogen. The low-temperature liquid nitrogen is drawn from a storage tank and pumped to the needed pressure by pump#1. Compressed liquid nitrogen is then passed to a heat exchanger HX#1 to evaporate by using the environmental temperature as the heat source, or by using a waste heat source to reach a temperature higher than the ambient temperature. Following that process nitrogen gas expands through the turbine#1. The exhausted gases from the turbine will have a temperature lower than the inlet temperature due to the expansion process through the turbine, which makes it useful for a cooling application. The saturated liquid nitrogen assumed to enter the heat exchanger HX#1 with heat and pressure losses through the cycle piping system are neglected. Moreover, the system is assumed to work under steady-state conditions.

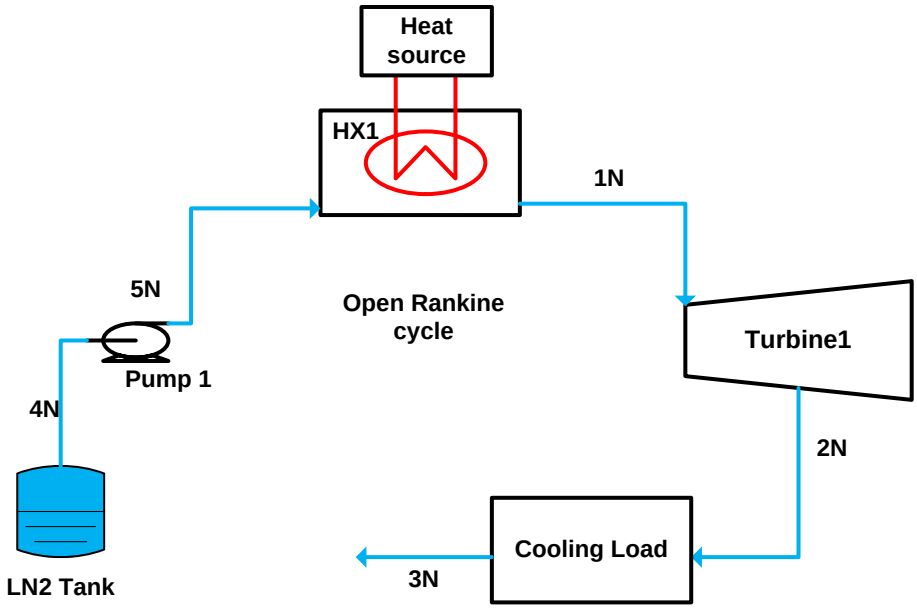

Figure 3-1 Schematic diagram of open Rankine (OR) cycle[55, 75]

The thermodynamic analysis for this cycle is summarized in equations 3-1 to 3-6 where the pump and turbine are modeled as:

$$h_{5N} = h_4 + \frac{h_{5Ns} - h_4}{\eta_{pump}} \quad 3\text{-}1$$

$$h_{2N} = h_{1N} - (h_{1N} - h_{2Ns})\eta_{expander} \quad 3\text{-}2$$

The added specific heat to the evaporator is calculated by:

$$q_{in} = h_{1N} - h_{5N} \quad 3\text{-}3$$

The net output specific work from turbine1:

$$W_{net} = (h_{1N} - h_{2N}) - (h_{5N} - h_{4N}) \quad 3\text{-}4$$

The specific cooling load extracted from the turbine exhaust is:

$$\text{cooling load} = h_{3N} - h_{2N} \quad (3\text{-}5)$$

The cycle's thermal efficiency is determined by:

$$\eta_{thermal} = \frac{W_{net}}{q_{in}} \quad (3\text{-}6)$$

3.2.2 **Hybrid Open-Closed Rankine (HOCR) Cycle:**

The cryogen has high-grade cold energy in the form of sensible heat and latent heat. This energy could only be efficiently exploited through effective thermodynamic arrangement based on the thermodynamic properties and operating conditions such as heat source temperature. Integration between closed Rankine cycle and open Rankine cycle in HOCR cycle theoretically is an attractive thermodynamic arrangement to extract the stored energy in the cryogen by the closed Rankine cycle working fluid which has a boiling temperature higher than that of the cryogen. Moreover, the HOCR cycle utilizes pumps to increase the fluids pressure that takes a small part of energy, so the cycle performance is not impacted so much by pumping losses. Figure 3-2 and Figure 3-3 show the schematic diagram of hybrid open closed Rankine cycle and pressure-enthalpy Gibb plot for cycle. The diagram in Figure 3-2 integrates two cycles, a closed propane Rankine cycle, which is denoted by (R), and a nitrogen open expansion, which is denoted by (N). The main parts of the cycle are the evaporator, the heat exchanger, the expanders, and the pumps. The propane Rankine cycle is the first operation stage; as shown in Figure 3-3. This cycle is driven by low-grade temperature source and cold energy from the cryogen in the open expansion cycle. The range of heat source temperature for solar thermal energy is from 323 K to 473 K with ETC

collector [155] and for geothermal from 373 K to 423 K [156]. A low-grade heat source temperature of 400 K was chosen for this study. The liquid propane pressure is increased by pump#1 and pumped to evaporator HX#1 for heating and steaming. After that, the propane hot gasses drive expander#1 to generate work output [55]. The low pressure propane gases flow through heat exchanger HX#2 for condensation by using a countercurrent liquid nitrogen cold energy.

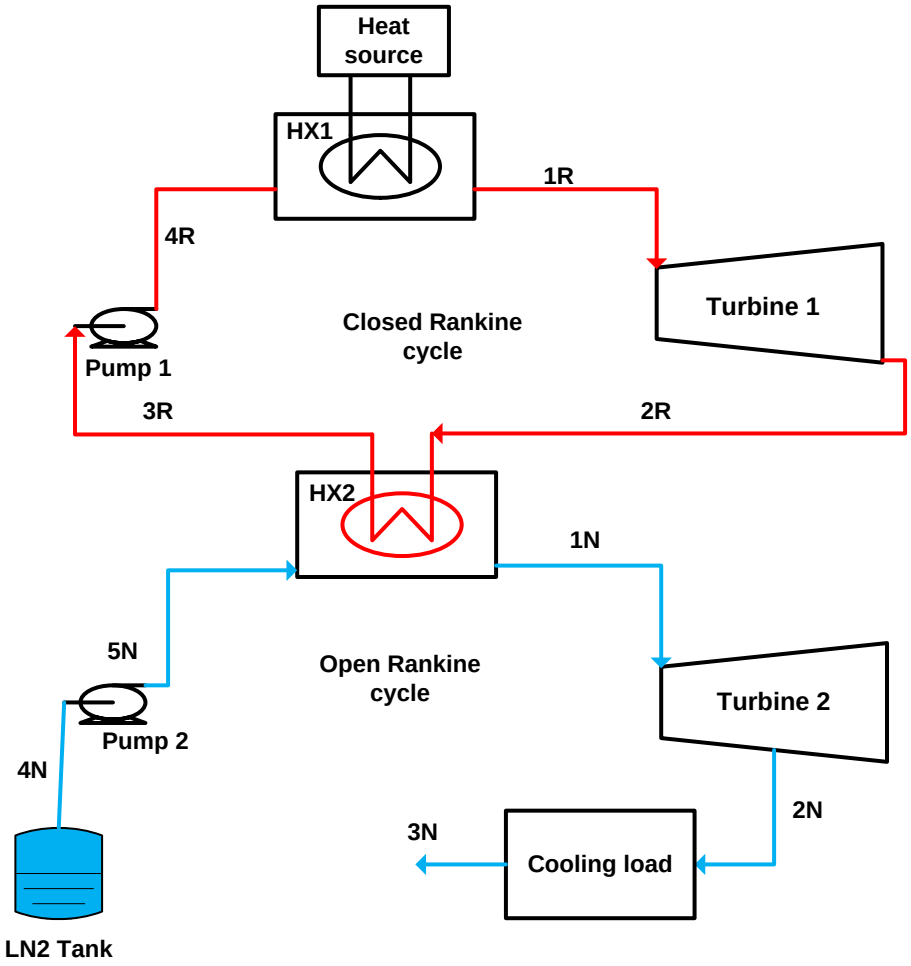

Figure 3-2 Schematic diagram of hybrid open-closed Rankine cycle [55, 75]

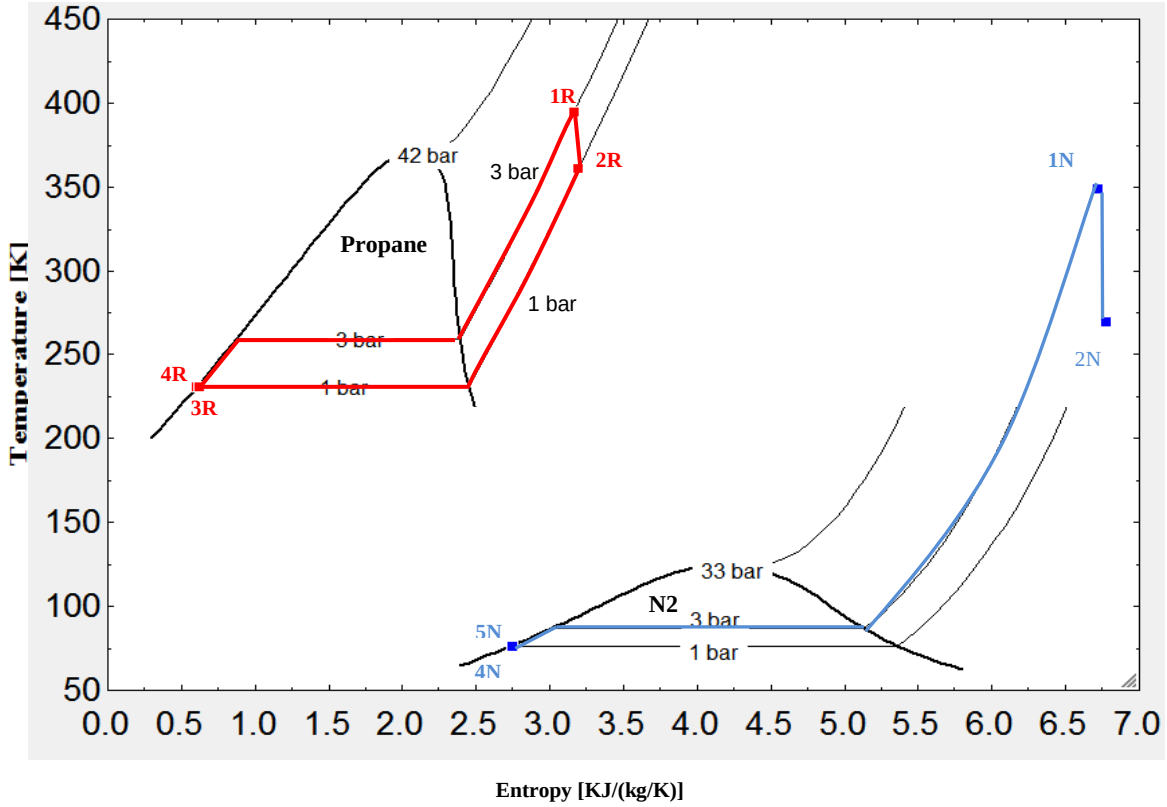

Figure 3-3 Gibbs plot for hybrid open-closed Rankine cycle for Propane (topping cycle) and nitrogen bottoming part[55]

The open expansion cycle nitrogen working fluid is driven by the propane closed Rankine cycle waste heat and it's cold energy. The cryogen liquid nitrogen is pumped to the required pressure by pump 2, as shown in Figure 3-2, and then flows to the heat exchanger HX#2. Heat exchanger pinch-points were set at the hot stream end of the heat exchanger and the minimum ΔT was taken as 5 K [42]. After waste heat from the closed Rankine cycle evaporates the liquid nitrogen, the nitrogen gas reaches a suitable pressure and temperature to produce work through expansion in expander#2. Following the expansion, the nitrogen gas has low-pressure and temperature which can be used for cooling applications. Subcritical cycles were used in this work to keep away from high pressures and so achieve certain safety issues and reduce the complexity of the system. In addition the saturated liquid going through

the heat exchangers and the connecting pipes were assumed to be perfectly insulated with no heat losses. Throughout steady-state conditions for the system were assumed. The thermodynamic analysis of hybrid open-closed Rankine cycle is summarized in equations 3-7) to 3-16) where the pumps are modeled as [55]:

$$h_{4R} = h_{3R} + \frac{h_{4R\_s} - h_{3R}}{\eta_{pump1}} \quad 3\text{-}7$$

$$h_{5N} = h_{4N} + \frac{h_{5N\_s} - h_{4N}}{\eta_{pump2}} \quad 3\text{-}8$$

For the expanders an isentropic efficiency was also used:

$$h_{2R} = h_{1R} - (h_{1R} - h_{2Rs})\eta_{expander1} \quad 3\text{-}9$$

$$h_{2N} = h_{1N} - (h_{1N} - h_{2Ns})\eta_{expander2} \quad 3\text{-}10$$

For the heat exchanger model:

$$(h_{1N} - h_{5N}) = \dot{m}_{ratio}(h_{2R} - h_{3R}) \quad 3\text{-}11$$

$$\dot{m}_{ratio} = \frac{\dot{m}_R}{\dot{m}_N} \quad 3\text{-}12$$

The added specific heat to the closed Rankine exchanger HX#1 is calculated by:

$$q_{in} = h_{1R} - h_{4R} \quad 3\text{-}13$$

The net specific work output from the combined system is:

$$W_{net} = (W_{expander1} + W_{expander2}) - (W_{pump1} + W_{pump2}) \quad 3\text{-}14$$

The specific cooling load produced by the nitrogen turbine is:

$$\text{cooling load} = h_{3N} - h_{2N} \quad 3\text{-}15$$

The system thermal efficiency is then calculated by:

$$\eta_{thermal} = \frac{W_{net}}{q_{in}} \quad 3\text{-}16$$

3.2.3 **Open Rankine and Hybrid Open-Closed Rankine Cycles Results:**

In sake of showing the potentials of the OR and HOCR cycles the ranges of inputs are analysed in a parametric study to disclose the thermodynamic performance and specify the significant impact of operating conditions. The default input operation conditions values for OR and HOCR cycles are shown in Table 3-1. Figure 3-4 presents the effects of nitrogen inlet pressure at the turbine on the cycle thermal efficiency and the net specific work output. It can be seen in both figures A and B that increasing the inlet pressure will increase the cycle specific power output due to higher expansion through the turbine. Increasing power output will increase the thermal cycle efficiency and enhance the cycle performance. The HOCR cycle performance is better than OR cycle where at pressure 50 bar the efficiency is 47.4 % and specific power is 249 kJ/kg for HOCR cycle while for OR cycle they are 43.5% and 227.5 kJ/kg respectively. The efficiency and power output trend for both cycles are constant with high pressure more than 50 bar. Both cycles worked with waste heat temperature of 400K but the OR cycle has the option to work with ambient temperature to evaporate the liquid nitrogen. Figure 3-5 shows the performance of OR with ambient temperature with a

trend similar to that of Figure 3-4 but the performance is lower, where at pressure of 50 bar the efficiency is 39 % and specific power is 156.5 kJ/kg.

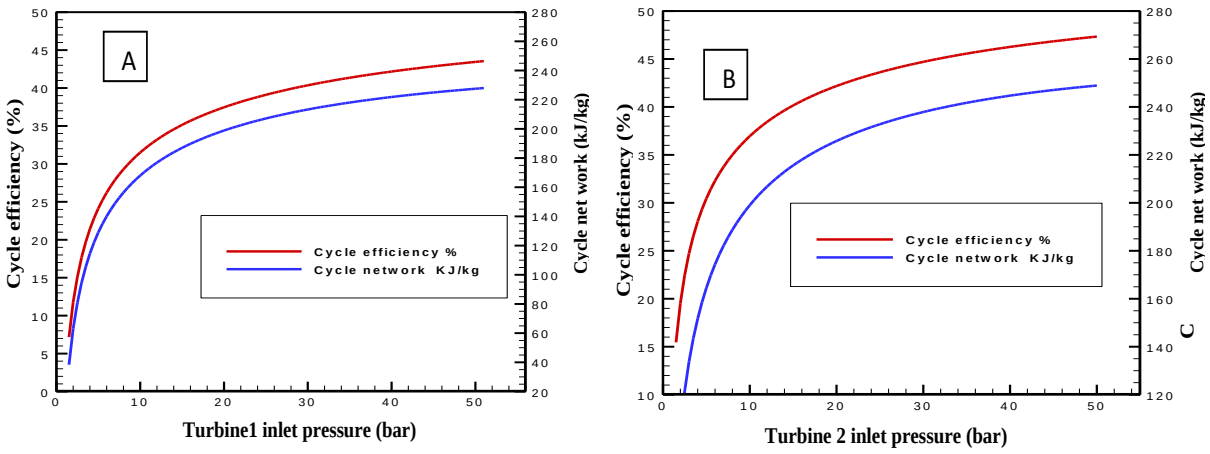

Figure 3-4 The nitrogen turbine inlet pressure effect on cycle efficiency and net specific power at a waste heat temperature 400 K: (A) OR cycle, (B) HOCR cycle.

Table 3-1 The OR cycle and HOCR cycle default input variables values [7]

Design parameter	Unit	Value
Temperature of the heat source	K	400
Propane turbine expansion ratio	__	3
Nitrogen turbine expansion ratio	__	1.5-3
Pumps efficiency	%	85
Turbine efficiency	%	85
HX pinch-point ΔT	K	5

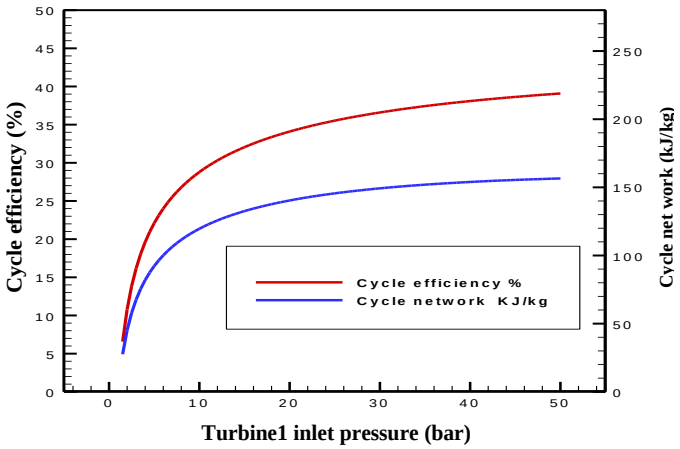

Figure 3-5 Effect of the turbine1 inlet pressure on OR cycle efficiency and net specific power, at environmental temperature 298K

Figure 3-6 presents the effect of waste heat source temperature on the cycle thermal efficiency and the net specific work output within a temperature range from 350K in renewable solar source to 420K in the renewable geothermal source as mentioned above. Increasing the turbine inlet temperature increases the cycle specific power output due to increasing the inlet power in the fluid which enhances the cycle performance and increases the cycle thermal efficiency. The performance for HOCR cycle from Figure 3-6B are: an efficiency of 24.9% and a power output of 140.3 kJ/kg at temperature 420K which is better than efficiency of 17.8% and power of 98.5 kJ/kg for the OR cycle shown in Figure 3-6A. However, the efficiency increasing rate for OR cycle is better than that of the HOCR cycle where the rate for OR cycle is 3.78% while for HOCR cycle is 2.6%. The power output increase rate is approximately equal for both cycles with 17 % for the OR cycle and 16.7% for the HOCR cycle.

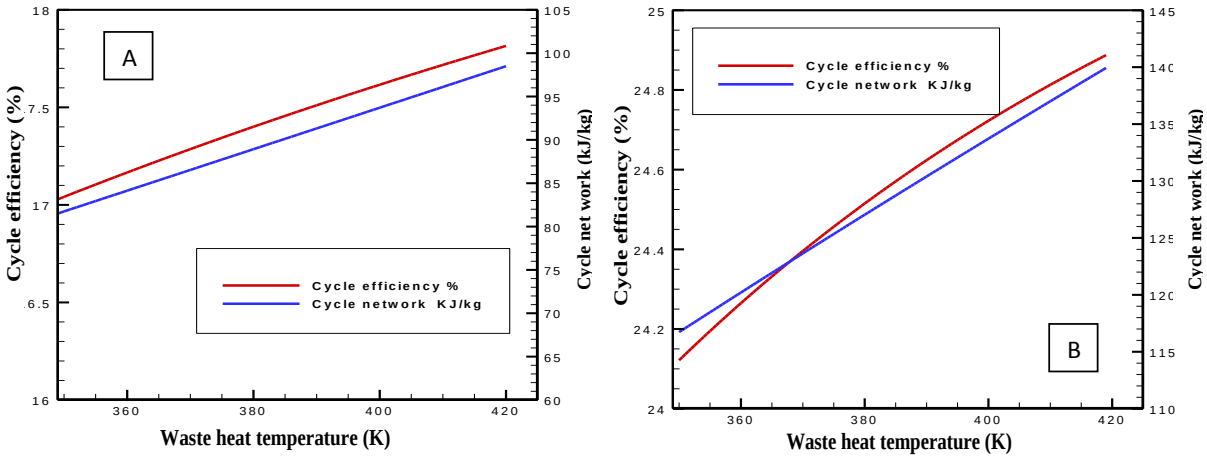

Figure 3-6 Effect of the waste heat temperature on cycle efficiency and cycle net specific power: (A) for the OR cycle, (B) for the HOCR cycle.

Figure 3-7 shows the effect of the nitrogen turbine efficiency ranging from 60% to 100% on the overall cycle thermal efficiency and the net specific work output. Increasing nitrogen isentropic efficiency will increase the extracted power from this turbine which in turn increases the cycle total net power and the cycle thermal efficiency. The linear relationship between nitrogen turbine efficiency, cycle thermal efficiency and cycle net total specific work in both OR cycle (Figure 3-7A) and HOCR cycle (Figure 3-7B) showing the significant impact of this parameter on the cycle performance. In the OR cycle when the nitrogen turbine efficiency changes from 60% to 100% the efficiency will change from 11.3% to 18.8% and specific work from 45.78 kJ/kg to 79.5 kJ/kg; in the HOCR cycle the efficiency changes from 20.11 % to 27.4 % and specific work from 108.78 kJ/kg to 148.67 kJ/kg. Figure 3-8 presents the effect of the nitrogen pump efficiency on the cycle thermal efficiency and the net specific work output. In both OR cycle (Figure 3-8 A) and HOCR cycle (Figure 3-8 B) the nitrogen pump efficiency does not have significant impact on the thermal cycle efficiency and the

specific power output from the cycle since the consumed power required for pumping liquid nitrogen is less than the power extracted from expanding the nitrogen gases by the turbine.

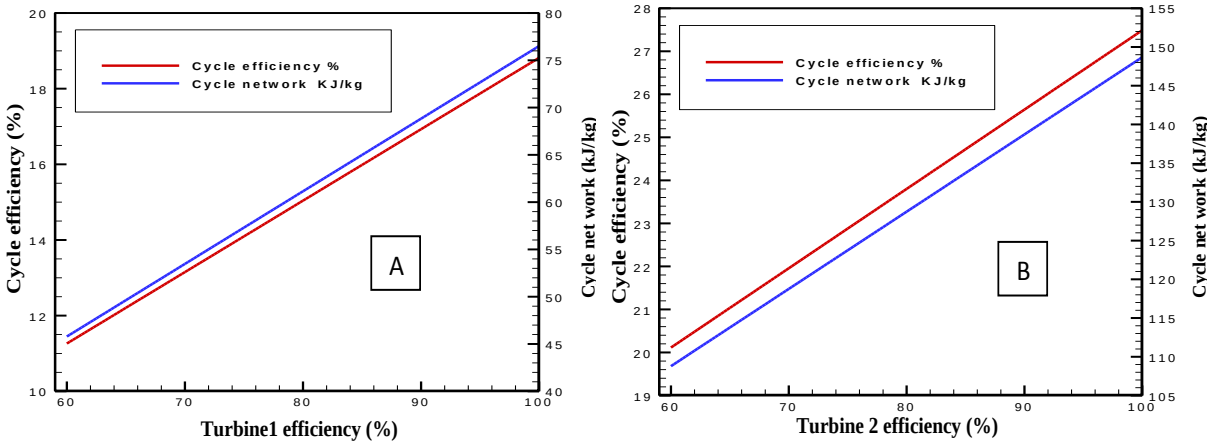

Figure 3-7 Nitrogen turbine efficiency effect on cycle thermal efficiency and cycle specific power: (A) for the OR cycle, (B) for the HOCR cycle.

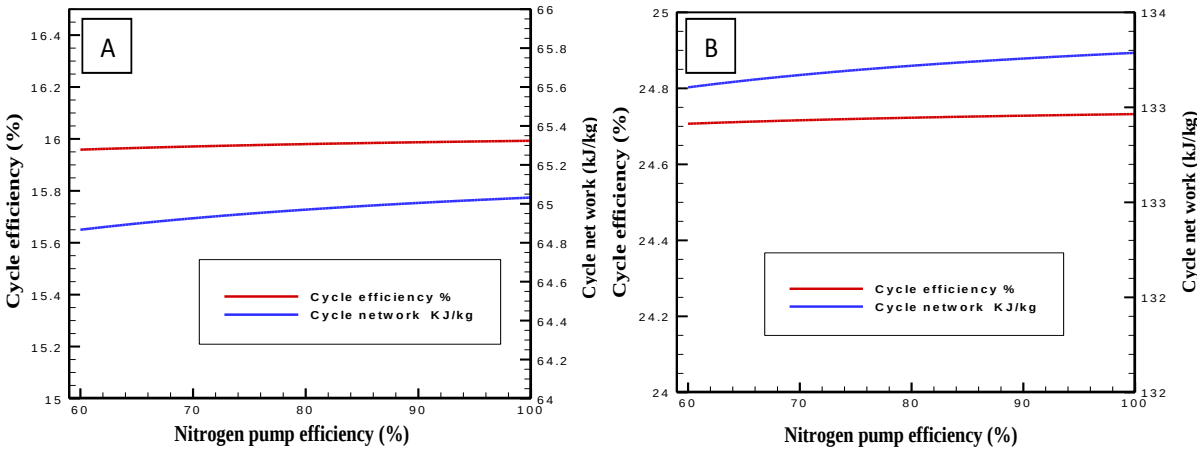

Figure 3-8 The nitrogen pump efficiency effect on cycle efficiency and cycle net specific power: (A) OR cycle, (B) HOCR cycle.

Figure 3-9 depicts the effect of nitrogen turbine inlet pressure on the cycle thermal specific cooling load capacity at ambient and waste heat temperature of 400K for the OR cycle. It is clear that increasing the inlet pressure will increase the cooling load for both ambient temperature and waste heat temperature of 400K, also while the cooling capacity stays

constant with high pressure after 50bar. In general, higher expansion ratios lead to higher power extraction and lower exhaust gases temperature at the turbine exit which will increase the cooling load extract from these outlet gases. The lower waste heat temperature like ambient temperature gives more cooling capacity than waste heat temperature of 400K. Figure 3-10 shows the effect of the nitrogen inlet pressure for the HOCR cycle at turbine2 on the specific work output of turbine2 and the cooling load capacity. The trend is the same for Figure 3-9 where increasing the inlet pressure increases the net specific work output and cooling load capacity for the same reason. The cooling energy extracted from the HOCR cycle at pressure of 50 bar and waste heat temperature of 400K is 139 kJ/kg which is higher than that of the OR cycle of 121 KJ/kg at the same operating conditions.

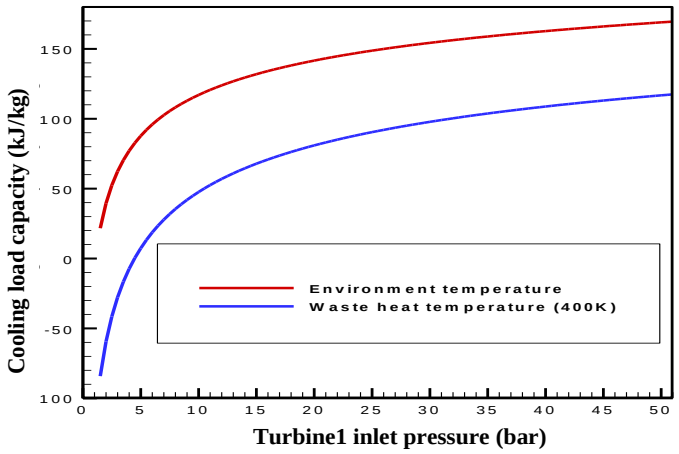

Figure 3-9 Effect of the turbine1 inlet pressure in OR cycle on cooling load capacity at an environmental temperature and waste heat temperature 400K

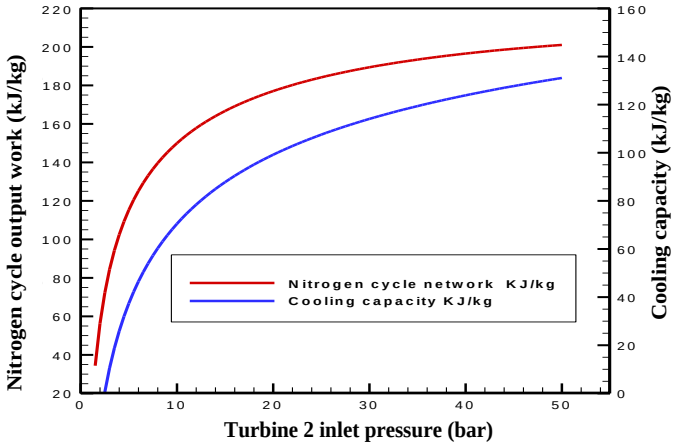

Figure 3-10 Effect of the turbine2 inlet pressure in HOCR cycle on cooling load capacity and nitrogen cycle output specific work

The Figure 3-11 shows the effect of the nitrogen turbine efficiency for the OR and HOCR cycles cooling load capacity at an expansion ratio of 50. Increasing the turbine efficiency means increasing work extract from the working fluid which in turn decreases the outlet gases temperatures thus increasing the cooling load capacity. The cooling energy extracted from the HOCR cycle is larger than that of the OR cycle for all nitrogen turbine efficiencies. Figure 3-12 shows the effect of waste heat temperature on cooling load capacity for the OR and HOCR cycles. In contrast to inlet pressure and turbine efficiency, increasing waste heat temperature decreases the cooling load due to increasing exhaust gases temperature. The HOCR cycle produces cooling more than the OR cycle where at waste heat temperature of 280 K the cooling capacity is 104.7 KJ/kg while in OR cycle it is 74.3 kJ/kg Furthermore, the OR cycle stops producing cooling after waste heat temperature of 371 K while the HOCR cycle stops producing cooling after waste heat temperature of 410 K.

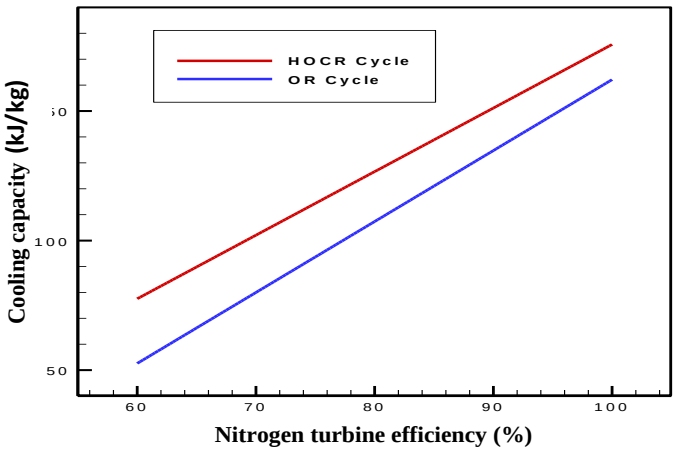

Figure 3-11 The nitrogen turbine efficiency effect on cooling load capacity for OR cycle and HOCR cycle at expansion ratio 50

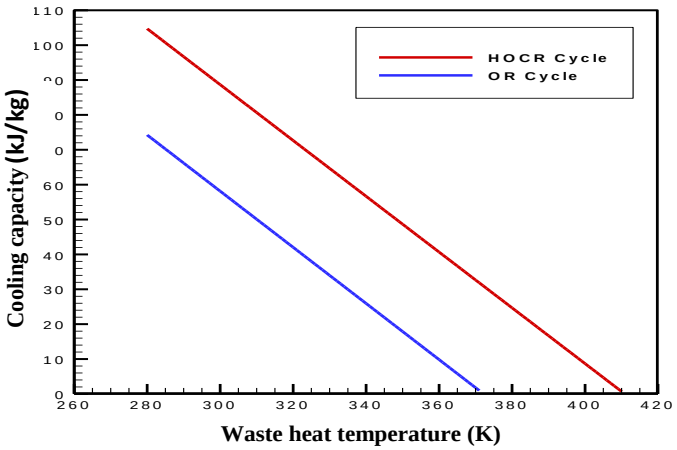

Figure 3-12 The waste heat temperature effect on cooling load capacity for OR cycle and HOCR cycle

In the closed Rankine cycle, many working fluids were tested (butane, propane, R143a, R142b, R134a, R125, R124, R123, R116, and R115). The best performance was obtained when using propane as the working fluid, as shown in Figure 3-13 [55].

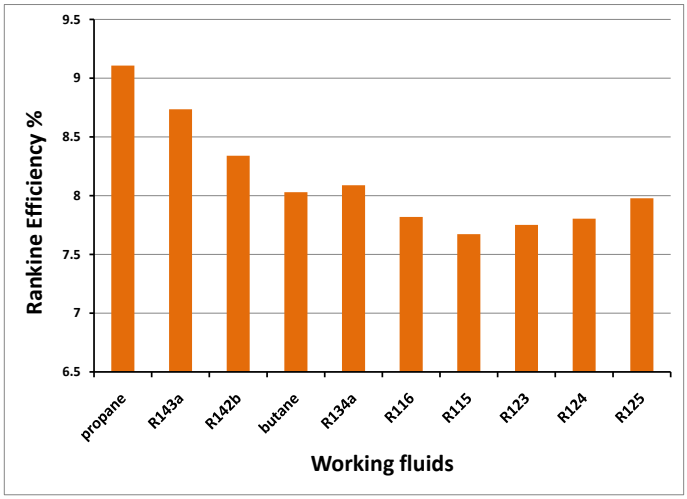

Figure 3-13 Comparison of different working fluids for closed Rankine cycle [55]

Figure 3-14 depicts the effects of inlet pressure on overall cycle efficiency for nitrogen and propane turbines, where the efficiency increases with increasing inlet pressure. It is noticeable that the effect of nitrogen inlet pressure is more significant than that of the propane pressure [55].

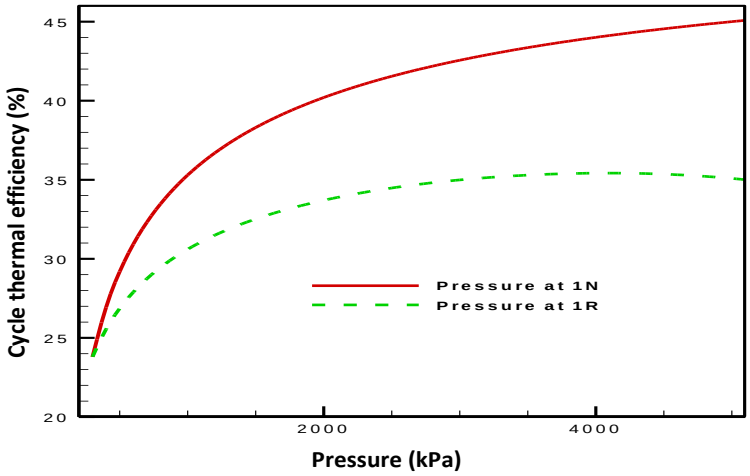

Figure 3-14 Effect of the expanders inlet pressures for nitrogen and propane on hybrid thermal efficiency cycle [55]

3.2.4 Integration of Liquefaction Cycle with Recovery Cycle in Storage Power Generation Plant:

The previous two cycles present the option of using environment heat or renewable heat sources for generating electricity from cryogen by direct expansion or cascading cycles. These cycles use the cryogen directly as a fuel, and also can handle low-pressure expansion ratios such as 1.5 and 3 and produce specific work output ranging from 38.1 to 133.7 kJ/kg. This indicates that such cycles can be considered as safe and more convenient for domestic applications. Using the cryogen as clean fuel directly in previous cycles raises the option of producing this cryogen using surplus (off peak) or cheap electricity coming from renewable sources then storing it to be used in the recovery cycle with integrating of heat storage between producing and recovery parts. A potential application of such systems is a microgrid for residential buildings, universities or hospitals [34] where the high demand for such applications can be addressed through bulky energy storage and the efficient recovery of the stored energy in the cryogen. In this study, two schemes for cryogenic energy storage power plant suitable for micro-grid system in a large residential building are proposed. The first scheme is based on upgrading the existing oxygen liquefaction plant by integrating it with a power recovery cycle which combines both open and closed Rankine cycles using the produced LN2. The current oxygen liquefaction plants produce surplus cryogenic fluids mainly LN2 as by-product without using it efficiently, which is about four times that of the main product (oxygen) [157]. The second scheme is based on storing the surplus energy at the off-peak times in the form of liquefied air which will be used to drive the recovery system, This scheme is considered as a standalone plant with no need for waste heat in the recovery part [34].

3.2.4.1 Scheme 1

The layout of this scheme in which an oxygen liquefaction cycle is integrated with combined cycle recovery system is presented in Figure 3-15 and Figure 3-16. In the liquefaction cycle, the ambient air is compressed to the required high pressure by two compressors (Comp1 and Comp2). The heat generated from the compression process is extracted by heat exchangers (HX1 and HX2) in order to store it in the hot storage system. The pressure is divided between the two compressors to minimize compressor input work and achieve maximum storage capacity. Then the compressed air is cooled further through a heat exchanger (HX3) using cold air from the separator unit, a cold storage system, and an external cooling system. The cold air passes through a cryo-turbine (Turb1) to decrease its temperature until it reaches to a two-phase liquid-vapor mixture at the same time while generating power. The liquefied air separates to its main components liquid oxygen and LN2 which will be stored at temperature 77K at atmospheric pressure to be used in the recovery system. All the above processes are running during the off-peak times to produce liquid oxygen and LN2 which is the main duty of the current oxygen liquefaction plants [34].

At the peak times, the stored LN2 is used to drive the recovery cycle when LN2 is pumped to a heat exchanger (HX4) to extract its coldness stored in cold storage system to be reused in liquefaction plant mode while LN2 evaporates and superheats. The nitrogen then flows through the heat exchanger (HX5) where it is further heated by the hot storage system. The nitrogen then expands through three turbines (Turb2, Turb3 and Turb4) with inter-heating heat exchangers (HX6, HX7) where heating is achieved by the hot storage system. The nitrogen gases emerging from the final turbine in the recovery cycle and the output from inter-heating exchangers are still at high temperature so they can be used to drive closed Rankine cycle via the heat exchanger (HX8) to recover waste heat until reaching the room temperature. In the closed Rankine cycle, many working fluids have been investigated such

as (R125, R13, R115, R116, R142b, R143a) where the working fluid R143a gives better performance due to its boiling temperature and other properties. The liquid R143a is pressurized by (pump2) and then flows into the heat exchanger (HX8) where it will evaporate and superheat by waste heat from nitrogen recovery open cycle. After heating, the R143a gasses generate work output through expanding in (Turb5) to flow through the condenser (HX9) [34].

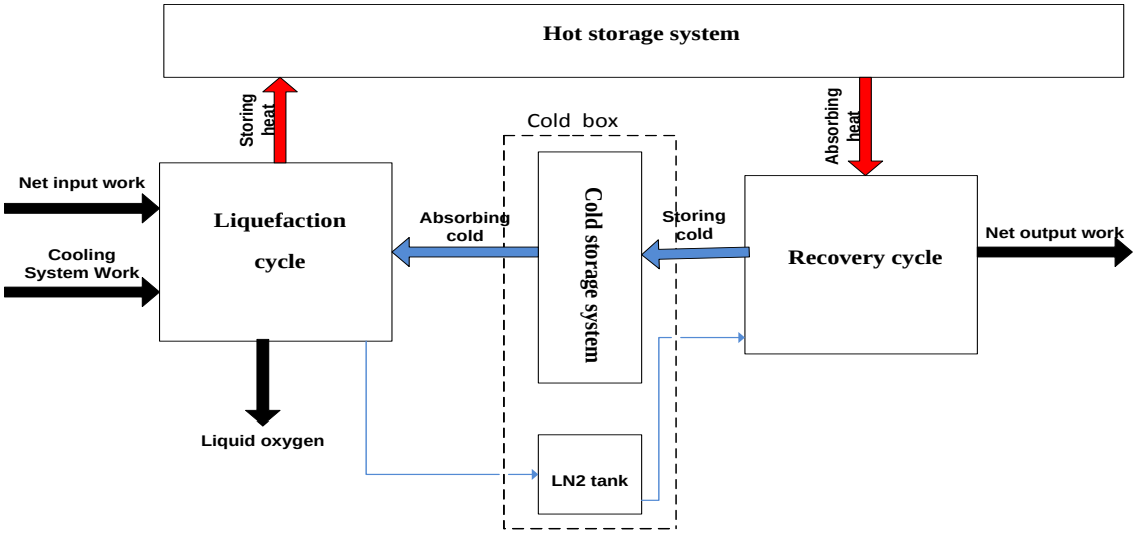

Figure 3-15 Scheme1 energy and workflow block diagram [34]

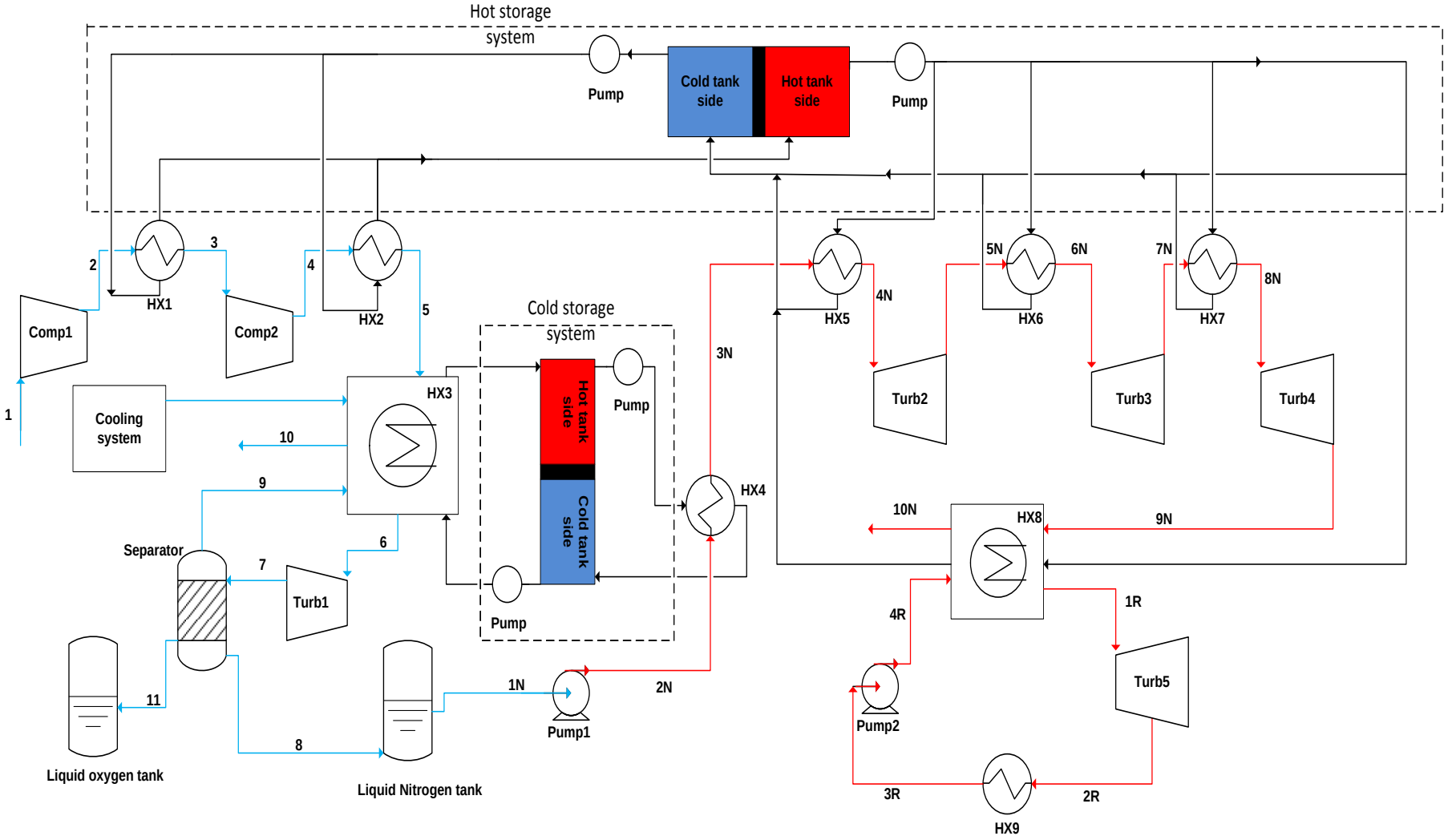

Figure 3-16 Scheme1 liquid nitrogen energy storage plant layout [34]

3.2.4.2 Scheme 2

The layout of this scheme, which integrates the air liquefaction cycle with a combined recovery cycle, is presented in Figure 3-17 and Figure 3-18. This liquefaction cycle is the same as in scheme1 where the air is compressed by two compressors (Comp1 and Comp2) with inter-cooling heat exchangers (HX1 and HX2). The compressed air is then cooled through the heat exchanger (HX3) by cold air from the separator and the cold storage system. It then flows into the cryo-turbine (Turb1) to expand to a two-phase liquid-vapor mixture which is then separated to liquid air, and cold air. So the difference in liquefaction part between scheme1 and scheme 2 is that there will be no need to use external cooling in heat exchanger (HX3) and also the liquid air will not separate into two parts (nitrogen and oxygen). The liquid air is stored in a tank at a temperature of 78 K and atmospheric pressure for use in the recovery cycle. In the recovery cycle, the liquid air is pumped from its tank to the required pressure and super-heated condition by the heat exchanger (HX4) to near room temperature [34]. The air then flows through the heat exchanger (HX5) where it is further heated to expand through three turbines (Turb2, Turb3, Turb4) with inter-heating heat exchangers (HX6, HX7), where heating is provided by the hot storage system. The air emerging from the final turbine in the recovery cycle and the inter-heating exchangers is still at a high temperature so it combines with Rankine cycle in heat exchanger (HX8) to recover the waste heat. In the closed Rankine cycle, the R143a liquid is pressurized by (pump2) and then flows into the heat exchanger (HX8) for heating and vaporization by waste heat from air recovery cycle. After heating, the R143a gas generates work output through expanding in expander (Turb5) and then flows through the condenser (HX9). The difference in the recovery part between scheme1 and scheme2 is that the air fraction flowing in the recovery cycle of scheme2 is higher than that of the nitrogen in scheme1 which will reflect on cycle generation performance. Scheme2 uses liquid air as energy storage media and generates

power from its recovery part without using any waste heat from an industrial plant or other sources, enabling this scheme to be considered as standalone storage power generation plant [34].

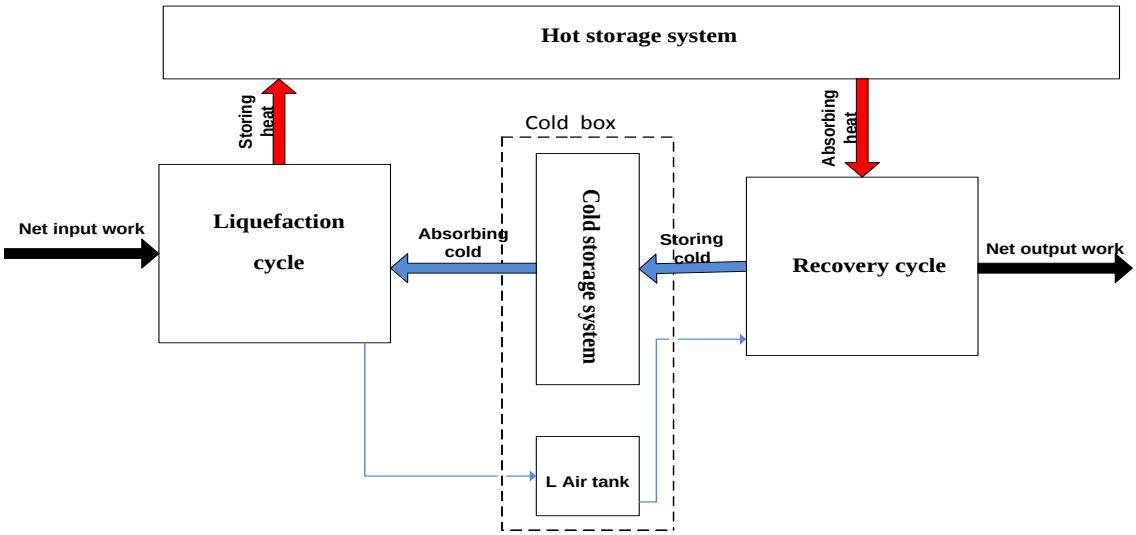

Figure 3-17 Block diagram for scheme 2 energy and workflow [34]

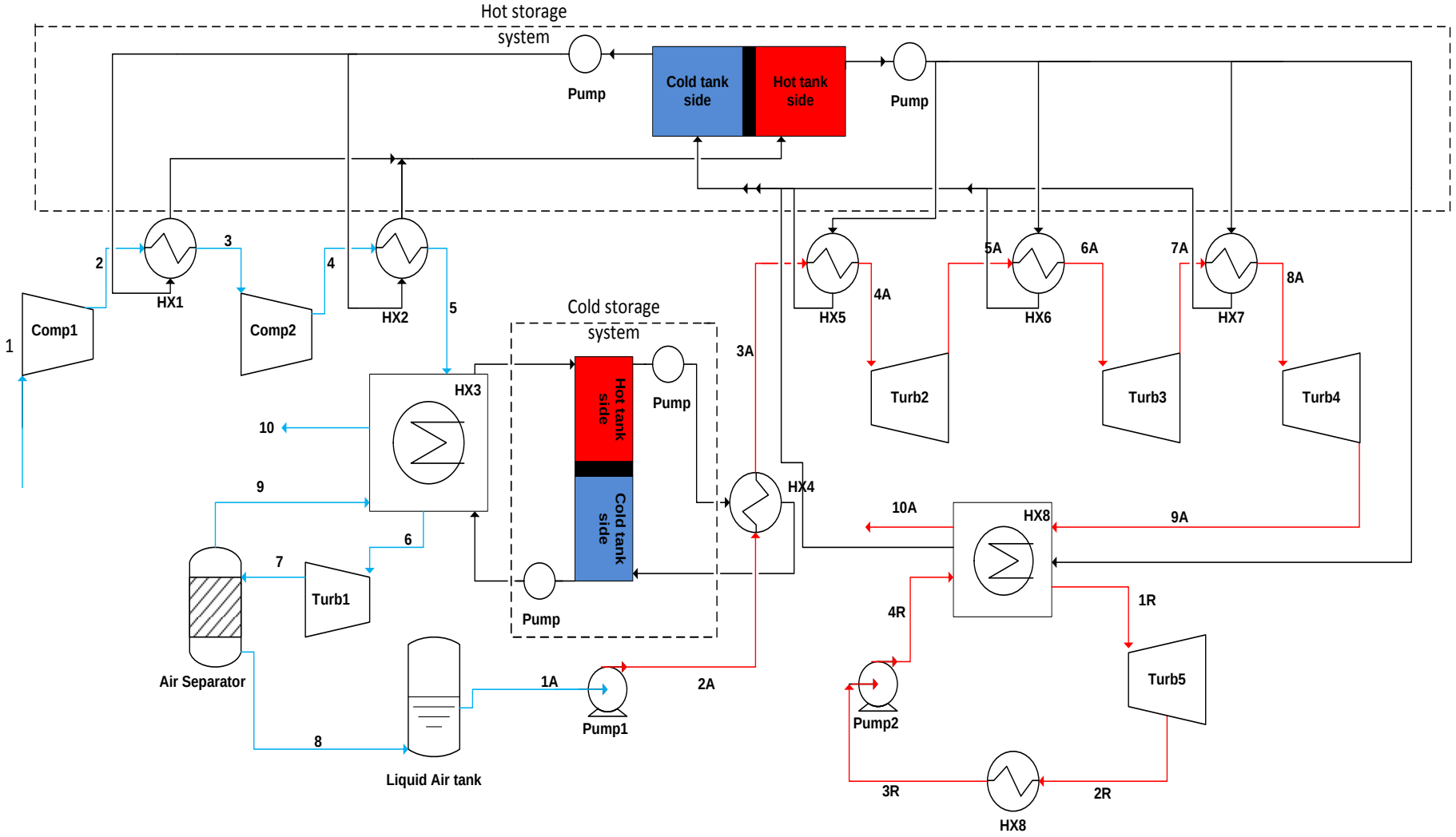

Figure 3-18 Scheme 2 liquid air energy storage plant layout [34].

3.2.4.3 Thermodynamic modeling of the storage power generation plants

To simplify the thermodynamic analysis of such cycles, general assumptions have been made as follows: (a) LAir and LN2 are stored at a saturated temperature and atmospheric pressure, (b) the ambient temperature for the system is 298 K and air and nitrogen leave the system at this temperature. (c) Pressure drops in the system pipes and heat exchangers are negligible, and heat loss to the surrounding is negligible. (d) The closed Rankine cycle condensation pressure is atmospheric pressure. The governing equations for the major components in the two proposed schemes are listed below [34]:

Compressor model:

$$h_{out} = h_{in} + \frac{h_{out,s} - h_{in}}{\eta_{s,comp}} \quad 3\text{-}17$$

Turbine model:

$$h_{out} = h_{in} + \eta_{s,turb}\left(h_{out,s} - h_{in}\right) \quad 3\text{-}18$$

Pump model:

$$h_{out} = h_{in} + \frac{h_{out,s} - h_{in}}{\eta_{s,pump}} \quad 3\text{-}19$$

Heat exchanger model:

$$\dot{m}_{hot}\left(h_{hot,in} - h_{hot,out}\right) = \dot{m}_{cold}\left(h_{cold,out} - h_{cold,in}\right) \quad 3\text{-}20$$

Separator model:

$$h_{in,gas} = Y * h_{out,liquid} + (1 - Y) * h_{out,gas} \quad 3\text{-}21$$

$$Y = \frac{\dot{m}_{out,liquid}}{\dot{m}_{in,gas}} \quad 3\text{-}22$$

The pressure ratio in the liquefaction process is:

$$\mathrm{Pr} = \frac{\mathrm{P4}}{\mathrm{P1}} \quad 3\text{-}23$$

The specific work input for the liquefaction cycle in scheme1 is:

$$w_{net,input} = w_{Comp1} + w_{Comp2} + w_{CS} - w_{Turb1} \quad 3\text{-}24$$

The specific work input for the liquefaction cycle in scheme2 is:

$$w_{net,input} = w_{Comp1} + w_{Comp2} - w_{Turb1} \quad 3\text{-}25$$

The specific work output for combined recovery cycle in scheme1 and scheme2 is:

$$w_{net,output} = w_{Turb2} + w_{Turb3} + w_{Turb4} + w_{Turb5} - w_{Pump1} - w_{Pump2} \quad 3\text{-}26$$

The round trip efficiency of the overall plant is [42]:

$$\eta_{round\ trip} = Y * \frac{w_{net,output}}{w_{net,input}} \quad 3\text{-}27$$

Where the (h_{in}) is inlet specific enthalpy, (h_{out}) is outlet specific actual enthalpy, ($h_{out,s}$) is outlet isentropic specific enthalpy after compressors, turbines, and pumps, ($\eta_{s,comp}$), ($\eta_{s,turb}$) and ($\eta_{s,pump}$) are isentropic compressors, turbines, and pumps efficiencies, ($h_{hot,in}$), ($h_{hot,out}$) are inlet and outlet specific enthalpies for the hot stream heat exchanger, ($h_{cold,in}$), ($h_{cold,out}$) are inlet and outlet specific enthalpies for the cold stream heat exchanger, ($\dot{m}_{hot}$), ($\dot{m}_{cold}$) are mass flow rates for hot and cold streams, ($h_{in,gas}$), is the inlet specific enthalpy to the cryo-turbine, ($h_{out,gas}$) is the outlet specific enthalpy for separator gas stream, ($h_{out,liquid}$) is the outlet liquid enthalpy from separate, ($\dot{m}_{in,gas}$) and ($\dot{m}_{out,liquid}$) are mass flow rates for gas and liquid in the separator component, (P1) and (P4) are the inlet and outlet pressures to compressors train, (w_{Comp1}) and (w_{Comp2}) are specific work input to the compressors, (w_{Pump1}) and (w_{Pump2}) are specific work input to the pumps, (w_{CS}) is

specific work input to the cooling system, (w_{Turb1}) to (w_{Turb5}) are specific work extract from the recovery cycle turbines, ($w_{net,output}$) is specific total net work extract from the cycle, ($\eta_{round\ trip}$) is the cycle round trip efficiency of the overall plant [34]. The system's performance is assessed in terms of their work output, work input, liquid yield, and round trip efficiency. In Equation 3-22) the liquid yield Y has been presented, which is the ratio of mass of (LAir or LN2) created by liquefaction to the mass of the air drawn by the two stage compressors; in the Equation 3-27) the liquid yield becomes part of round trip efficiency which means that this parameter becomes one of the key performance parameters in these plants. Equations 3-24) and 3-25) clarify the difference between the input works to liquefaction cycle in two schemes where in scheme1 the cooling system work will be added to the input work. Also, Equation 3-26) shows how the output work could decrease when pumps work increase [34].

3.2.4.4 Results for the storage power generation plants

The proposed plants aim is to use LN2 / LAir to generate power for residential buildings and to produce oxygen in scheme1, where the LN2 / LAir will be the main energy storage medium leading to zero environmental damage. This section presents the results from the two proposed schemes where a parametric study using the selected key performance parameters was carried out. The initial conditions and the ranges of these parameters are given in Table 3-2 and the results of these parametric studies are shown in Figure 3-19 to Figure 3-29 [34].

Liquefaction process depends mainly on two elements, compression and cooling; for the first process the compression ratio of the two-stage compressor with inter-cooling has a significant effect on system performance as shown in Figure 3-19. This figure shows the effect of varying liquefaction compression ratio on plant round trip efficiency and liquid yield (Y) for

the two schemes. In both schemes, the round trip efficiency decreases when the compression ratio increases while the liquid yield increases, which is due to the increase in the compressor work input being higher than the increase in liquid yield as reported by [158]. The minimum compression ratio gives the maximum round trip efficiency, which is 81% for scheme1 as shown in Figure 3-19A; and 61% for scheme2 as shown in Figure 3-19B [34].

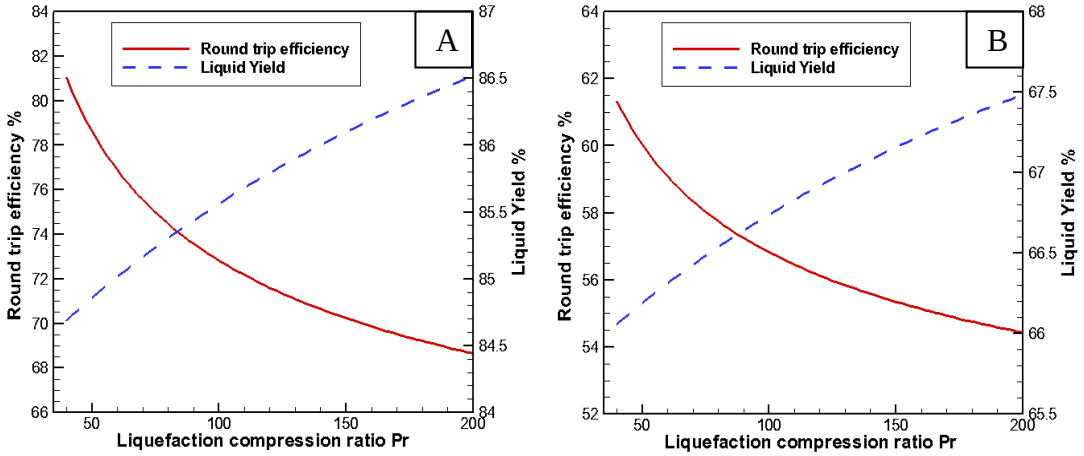

Figure 3-19 Effect of liquefaction compression ratio (Pr) on the round trip efficiency and liquid yield: A Scheme1, B Scheme2 [34]

Table 3-2 The investigated ranges and reference values of input parameters [34]

Parameters	Input range	Default Value	Units
Environment temperature	298	298	K
Environment pressure	100	100	kPa
Liquid air storage pressure	100	100	kPa
HX pinch-point	5	5	K
Liquefaction compression ratio (Pr)	40-200	40	-
Inlet cryo-turbine temperature (T6)	91-120	96	K
Recovery Turbine expansion ratio		4	-
efficiency of air compressors	70%-100%	85%	-
efficiency of cryo-turbine	60%-100%	75%	-
efficiency of cryogenic pump	75%	75%	-
efficiency of recovery turbines	70%-100%	85%	
Rankine inlet turbine pressure	200-2000	1000	kPa

The cooling process is the second step in the liquefaction process where part of cooling energy is stored in the hot storage system before the compressed air is cooled further in a cryogenic heat exchanger to the temperature T6. This temperature is the inlet temperature to the cryo-turbine, and it is considered as one of the key parameters in the proposed schemes because it has significant effects on liquid yield and overall efficiency as shown in Figure 3-20. From this Figure, it is clearly seen that in both schemes an increase in this temperature will decrease the round trip efficiency and liquid yield. The maximum round trip efficiency occurs at the minimum achievable temperature which indicates that enhancing this cryogenic heat exchanger will lead to better system performance. At the minimum temperature, the round trip efficiency reaches 63% and 84 % for scheme1 and scheme2 respectively as shown in Figure 3-20 (A, B) [34].

For both schemes, the inlet cryo-turbine temperature and the compression ratio have major effects on the net power output as shown in Figure 3-21 and Figure 3-22. Figure 3-21 shows that increasing the cryo-turbine inlet temperature decreases the net output work. The expansion process in the cryo-turbine is assumed to be adiabatic, thus increasing its inlet temperature (state 6) will increase the quality of the expanded air leading to reduction in the yield and the net-work output accordingly. Figure 3-22 shows that increasing the compression ratio will increase the work output, which is due to increasing the heat stored in the hot storage system when the pressure ratio increases. In the recovery cycle driven by the hot storage system, increasing the stored heat will increase the power output [34].

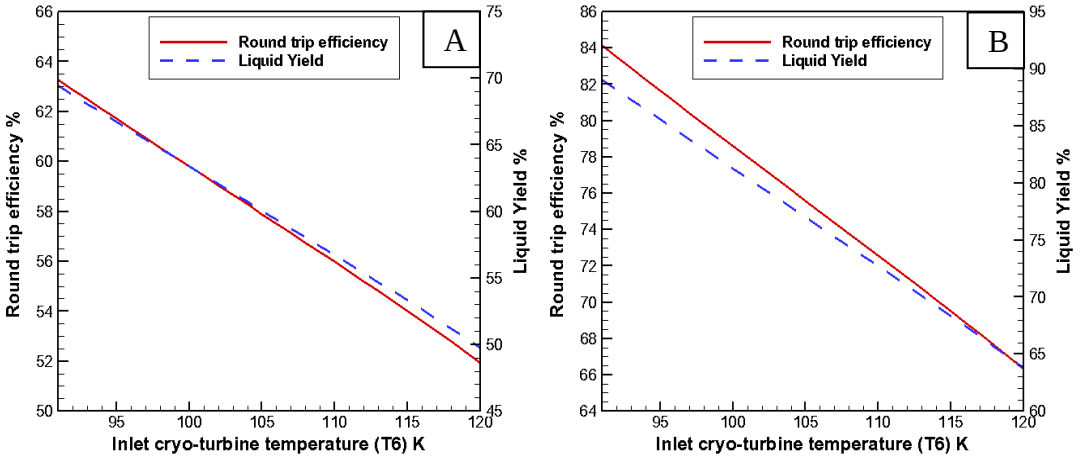

Figure 3-20 Effect of the Inlet cryo-turbine temperature (T6) on the round trip efficiency and liquid yield: (A) Scheme1, (B) Scheme2 [34]

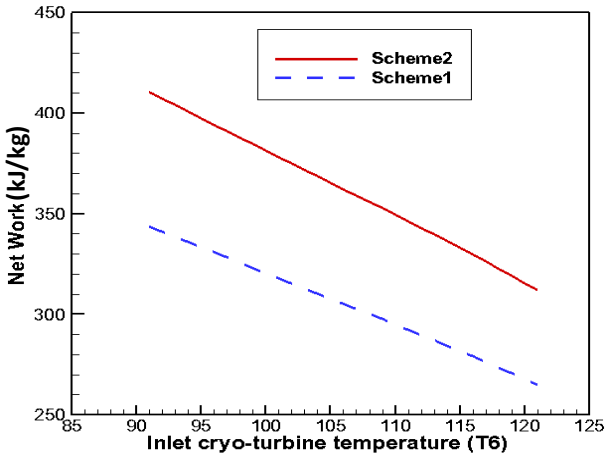

Figure 3-21 Effect of Inlet cryo-turbine temperature (T6) on network output for both schemes[34]

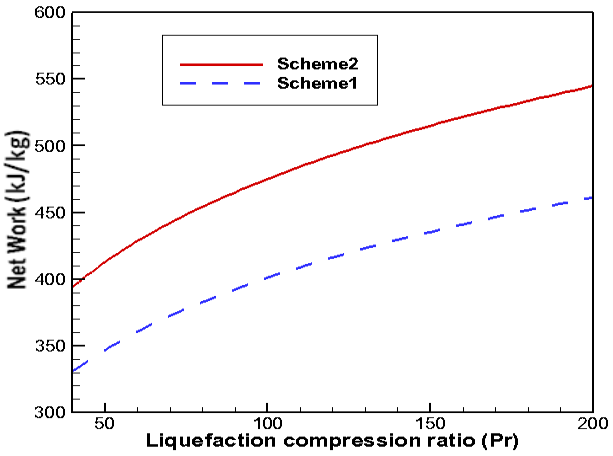

Figure 3-22 Effect of liquefaction compression ratio (Pr) on network output for both schemes [34]

Another parameter taken into consideration is the compressor isentropic efficiencies which affects the compressors' input power leading to significant impact on the round trip efficiency. The Figure 3-23 shows the effect of this parameter on the cycle's round trip efficiency and the net specific work output where increasing the compressors efficiency will increase the round trip efficiency. However, the net specific work output decreases due to decreasing the stored energy in the hot storage system. Each 10% increase in the compressor isentropic efficiency will enhance the round trip efficiency by 2.2% and 4.1% for scheme1 and scheme2 respectively [34].

The other critical component in the liquefaction cycle is the cryo-turbine (Turb1) which is commonly used in the liquefaction of natural gas with high isentropic efficiencies [159]; Figure 3-24 presents the effect of cryo-turbine efficiency on plant round trip efficiency and net specific work output for the two schemes. It is clearly seen that the effect of the cryo-turbine efficiency on the yield becomes significantly high at higher pressure ratio while it has lower effect on the round trip efficiency [34].

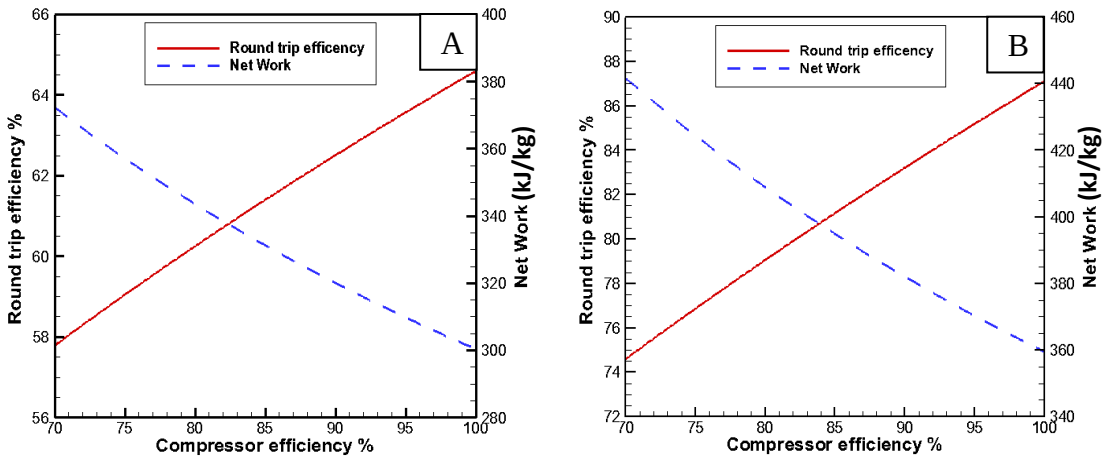

Figure 3-23 Effect of the compressor efficiency on the round trip efficiency and net output power: (A) Scheme1, (B) Scheme2 [34]

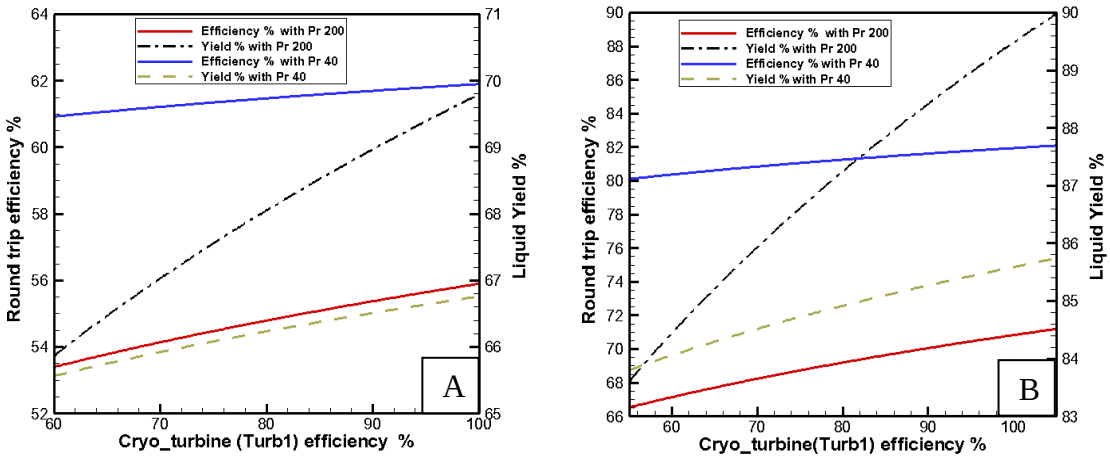

Figure 3-24 Effect of the cryo-turbine efficiency on the round trip efficiency and liquid yield: (A) Scheme1, (B) Scheme2 [34]

The second part of the cycle is the recovery system where the effect of the turbine expansion ratio, the turbine isentropic efficiency, and the Rankine inlet pressure are shown in Figure 3-25 to Figure 3-27. Figure 3-25 shows the effects of varying turbines expansion ratio on round trip efficiency and net specific work output for scheme1 and scheme2. Increasing the expansion ratio will increase the specific power output resulting in increasing the round trip efficiency; thus each 0.5 increase in expansion ratio will increase round trip efficiency by

4.3% for scheme1 and 6.7% for scheme2. Figure 3-26 shows the effect of turbine isentropic efficiency on the round trip efficiency and net work output where increasing the turbine isentropic efficiency will increase the specific net work output which in turn increases the round trip efficiency. For the closed Rankine cycle in both schemes, increasing the inlet turbine pressure (P1R) leads to the increase in power output of Turb5. This will in turn increase the Rankine cycle efficiency and round trip efficiency for the system as shown in Figure 3-27. However, this inlet pressure is limited by the working fluid boiling temperature and the inlet hot stream temperature for heat exchanger HX8 as explained above. At inlet pressure of 20 bar, the Rankine efficiency reaches 20.7% and round trip efficiencies of 62.5% and 81.9% for scheme1 and 2, respectively [34].

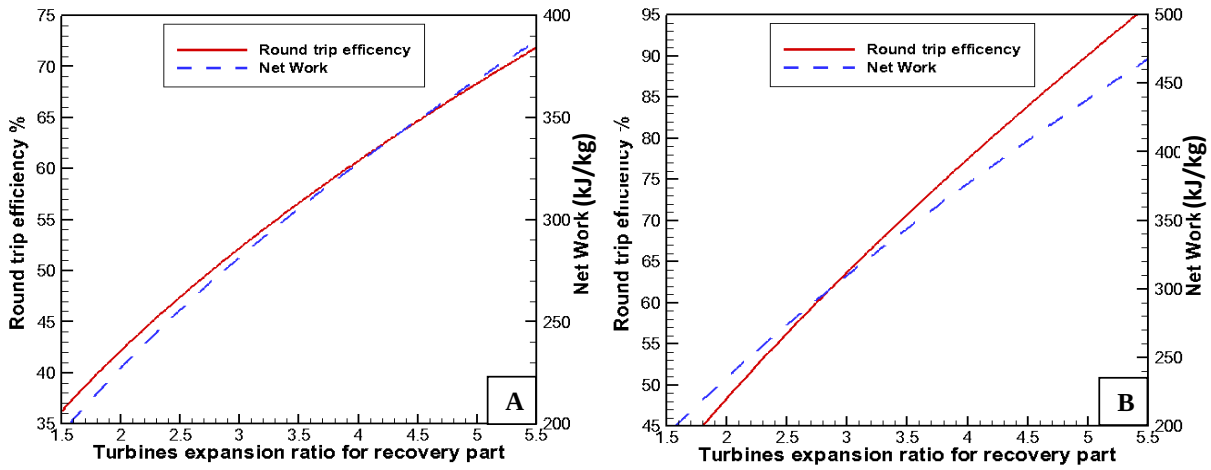

Figure 3-25 Effect recovery turbine expansion ratio on round trip efficiency and net work output: A Scheme1, B Scheme2 [34]

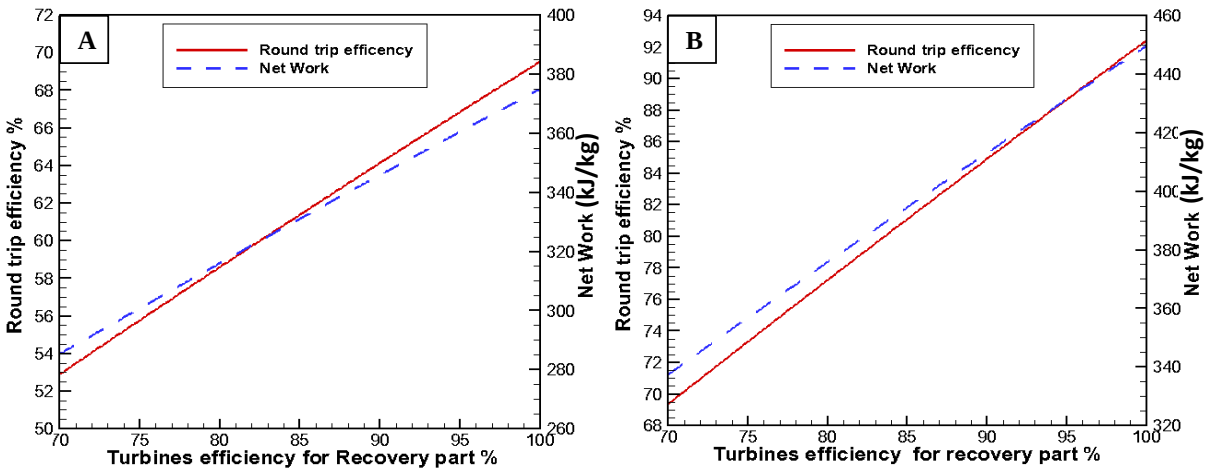

Figure 3-26 Effect recovery turbine efficiency on round trip efficiency and network output: A Scheme1, B Scheme2 [34]

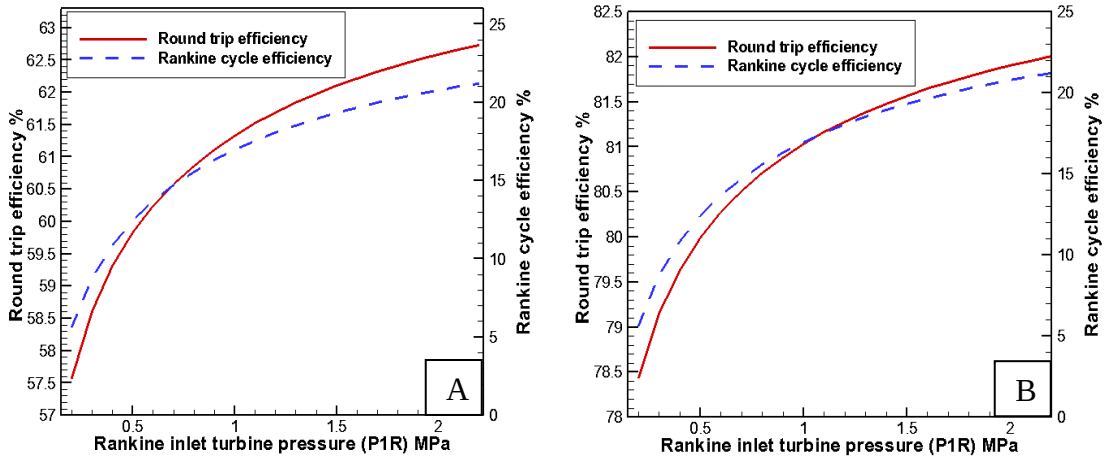

Figure 3-27 Effect Rankine inlet pressure (P1R) on round trip efficiency and Rankine cycle efficiency: A Scheme1, B Scheme2 [34]

The power consumption for a 50 units typical residential building is shown in Figure 3-28 [160]. This power requirement was used as a case study to determine the required air mass for the system to achieve the maximum specific work output. Figure 3-29A (scheme 1) shows the mass flow rate of air in the liquefaction stage, the nitrogen mass flow rate which drives the recovery part, and the oxygen production mass flow rate. Figure 3-29B (scheme 2) shows

the mass flow rate of air in the liquefaction stage and the air mass flow rate which drives the recovery part. The maximum mass flow rate values in recovery part are 0.11 kg/s of nitrogen for scheme1 and 0.093 kg/s of air for scheme2; such flow values indicate that these turbines can be classified as small-scale turbines [34].

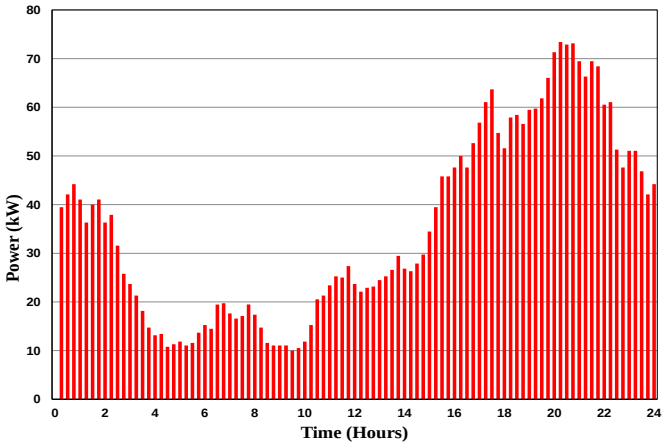

Figure 3-28 Load profile for the residential 50 units building on a winter day [34, 160]

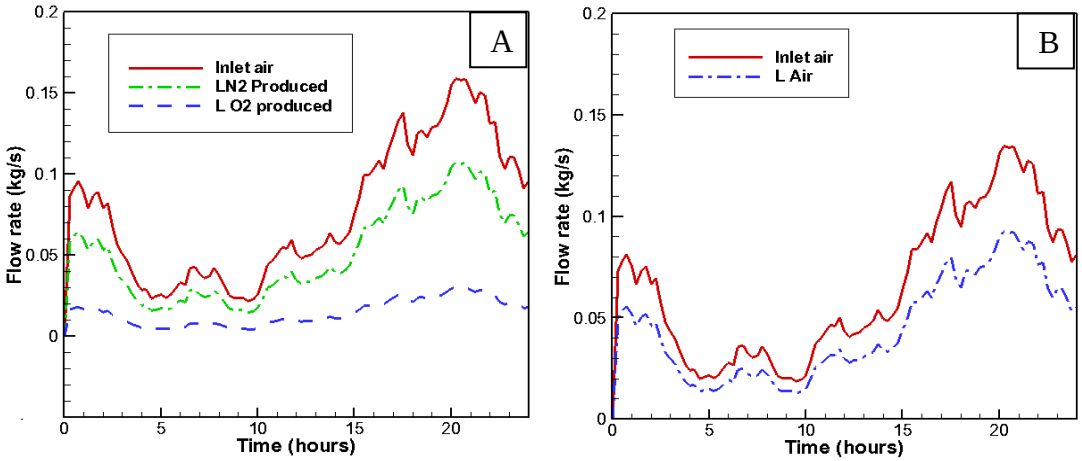

Figure 3-29 The system mass flow rates for the residential 50 apartments building on a winter day (A for scheme 1 and B for scheme 2) [34].

3.3 Selection of CES cycle and turbine operation conditions:

From the previous four proposed cycles that generate power by using cryogenic storage technology, this study chose the hybrid open-closed Rankine (HOCR) cycle as the case study for nitrogen turbine further analysis. The HOCR cycle considered as midway between simple OR cycle design and complex designs in the integrated liquefaction and recovery schemes. Moreover, this cycle can handle the low input pressure between (1.5-3bar) which is considered safe and convenient for small/medium buildings, rural and remote zone areas applications.

From the above study, it can be concluded that nitrogen gas turbine performance has significant effect on the cycle achievements because this component in the cycle converts the pressure and heat potential energy to kinetic energy and then to mechanical shaft power. This complex conversion process makes this expander a special component for each cycle type according to cycle thermodynamic properties. To design any turbine working in the thermodynamic cycle the operation conditions and design specifications for this turbine need to be defined by modeling this cycle thermodynamically. These operating conditions are turbine inlet pressure, turbine outlet pressure, turbine inlet temperature, turbine mass flow rate and turbine power output. With the obejctive of designing a small-scale nitrogen turbine with power output capacity ranged (1-10 kW) and mass flow rate 0.1kg/s [139] the HOCR cycle expansion ratios ranged from 1.5 to 3 gives the performance clarified in Table 3-3, where the pressure ratio range lay within the required power output. The heat source temperature 350 to 400 K have been chosen to cover a heat source temperature for solar thermal energy which is from 323 K to 473 K and geothermal which is from 373 K to 423 K that in turn will specify the inlet turbine temperature [55]. The above operating conditions for the turbine in the HOCR cycle are summarized in Table 3-4. The detailed design and optimization for such turbine will be presented in chapter 4.

Table 3-3 The performance values for HOCR cycle with expansion ratios 1.5 to 3

Expansion ratio [-]	Nitrogen turbine power [kW]	Thermal HOCR cycle efficiency [%]	HOCR cycle power [kW]
1.5	3.43	15.45	8.36
2	5.5	19.53	10.57
2.5	7.22	22.46	12.1
3	8.44	24.72	13.3

Table 3-4 Turbine design operation condition cycle parameters

Design parameter	Unit	Value
Target efficiency	-	85%
Target Power	kW	1-10
Turbine expansion ratio	-	1.5-3
Turbine inlet temperature	K	306-356
Inlet mass flowrate	kg/s	0.05-0.1

3.4 Summary

In this chapter, four new cryogenic power generation cycles ranging from the basic cycle to the complex combined one are developed to predict the performance of small-scale power generation system. The basic OR cycle has a simple design and a minimum number of components thus it is easier to manufacture and install with low cost, while the HOCR Cycle integrates the closed Rankine cycle and the open Rankine cycle to efficiently extract the stored energy in the cryogen. The comparison between these two cycles showed that the HOCR cycle performance is better than OR cycle where at pressure of 50 bar the efficiency is 47.4 % and specific power is 249 kJ/kg for HOCR cycle, while for OR cycle they are 43.5% and 227.5 kJ/kg respectively. Moreover, in terms of cooling load production the HOCR cycle produces more cooling than the OR cycle where at waste heat temperature of 280 K the cooling capacity is 104.7 kJ/kg for HOCR cycle while for the OR cycle it is 74.3 kJ/kg. Furthermore, the OR cycle stops producing cooling after waste heat temperature of 371 K while the HOCR cycle stops producing cooling after waste heat temperature of 410 K. In HOCR cycle many working fluids were tested and the best performance was obtained when using propane as working fluid also the effect of nitrogen inlet pressure is more significant than that of the propane[55].

Two schemes for power plant combined liquefaction and recovery cycles integrated with cryogenic energy storage and closed Rankine cycle suitable for micro-grid systems in a medium size residential building are developed. The first scheme is based on upgrading the existing oxygen liquefaction plant by integrating it with a power recovery cycle while the second scheme is based on storing the surplus energy at the off-peak times in the form of liquefied air which will be used later on to drive the recovery part and generate power output [34]. The comparative results between these two schemes showed that the scheme2 has better performance than that of scheme1 where at the temperature of 96 ^{o}C; the round trip efficiency

reached 63% and 84 % for scheme1 and scheme2 respectively. Also combined closed Rankine cycle with recovery part enhanced the system performance where at Rankine inlet pressure of 20 bar, the Rankine efficiency reached 20.7% and system round trip efficiencies of 62.5% and 81.9% for scheme1 and 2, respectively. Applying the power consumption trend for a 50 unit's typical residential building on the proposed two schemes produced maximum mass flow rate values in the recovery part which were 0.11 kg/s of nitrogen for scheme1 and 0.093 kg/s of air for scheme2 [34]. The hybrid open-closed Rankine (HOCR) cycle has been selected as the case study for nitrogen turbine further analysis. The HOCR cycle is considered as midway between simple OR cycle design and complex designs in the integrated liquefaction and recovery schemes. Moreover, this cycle can handle the low input pressure between (1.5-3bar) which is considered safe and convenient for small/medium size buildings, rural and remote zone areas applications.

CHAPTER 4

METHODOLOGY FOR DEVELOPING SMALL-SCALE AXIAL TURBINE

4.1 Introduction

This chapter presents the methodology for designing nitrogen driven small scale axial turbine which includes: (1) modeling one-dimensional preliminary design using the mean line theory, (2) modeling 3D CFD analysis, and (3) three dimensional CFD optimization with developed camber line control point parametrization technique. Moreover, the procedure for developing axial turbine advanced four blade configurations (lean, twist, sweep, and bow) is explained in detail. The advantage and disadvantage of turbine number of stages with design concept are clarified. The gear diagram shown in Figure 4-1 summarizes the steps for the design methodology where the first step is the one-dimensional preliminary design. The second step gives the initial data to the three dimensional CFD analysis, and the third step is the prototype manufacture for experimental testing and CFD validation purposes. Once the CFD modelling is validated then it can be used as a tool for further developments to enhance the turbine performance such as three-dimensional design optimization approach, advanced turbine blade configurations and dual stage turbine.

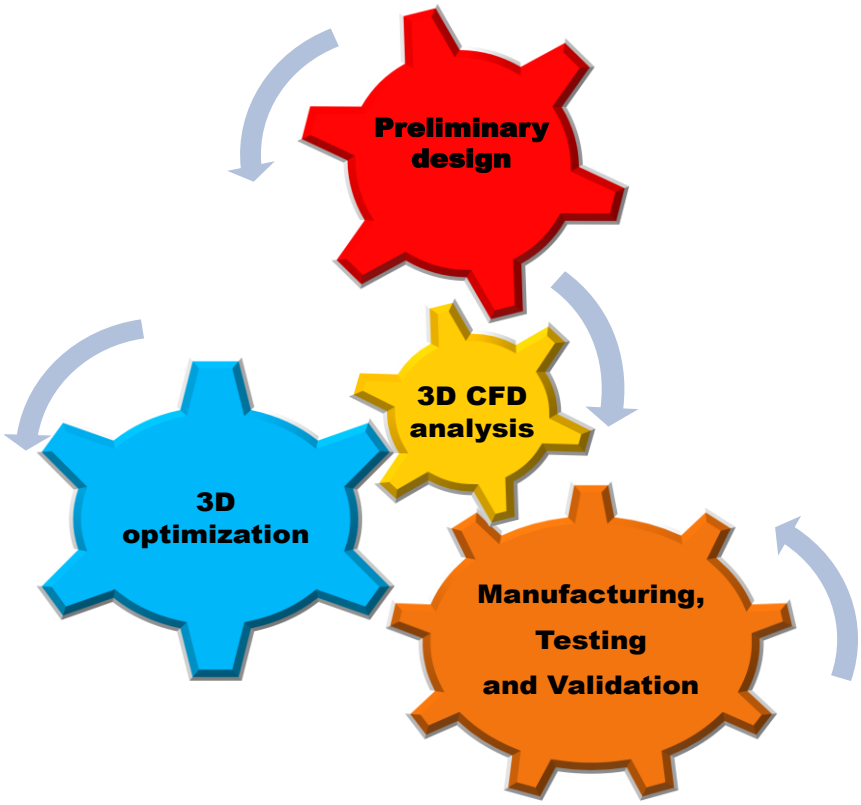

Figure 4-1 Turbine design methodology gear diagram

4.2 Turbine dimensionless parameters approach

There are a number of dimensional parameters that interact with each other and affect the turbine performance. Therefore, there is a need for non-dimensional parameters approach that provides effective and quick way to assess the turbine performance. Such parameters can be used for reducing huge experimental data taken from many types of turbomachinery and make it manageable for assessment, selection, and comparison. Moreover this approach can evaluate the performance of a range of machines with the same geometrical characteristic or scale the geometry of existing machine to another size [161]. This approach is presented in all basic turbomachinery textbooks [162, 163] based on Buckingham Pi theory [164]. In order to have an idea about all parameters that affect the turbine performance the reference [161] collected them in the equation below:

$$f\left(P_{t\ in}, T_{t_{in,}} D, \dot{m}, N, P_{t\ out}, T_{t_{out}}, \mu, R, \gamma\right) = 0 \quad 4\text{-}1$$

Where the Pt is total pressure, Tt is total temperature; D is the turbine diameter, ṁ is the turbine flow rate, N is rotational speed, μ is fluid viscosity, R is the universal gas constant and γ is the fluid specific heat capacity. Using Buckingham Pi theory reduces the dimensional parameters to a few number of non-dimensional parameters based on the turbine total efficiency as in the below equation [108]:

$$\eta_t = \boldsymbol{f}\left(Er_t, \frac{\dot{m}\sqrt{\gamma R\, T_t}}{P_t\, D^2}, \frac{ND}{\sqrt{\gamma R T_t}}, Re, \gamma\right) \quad 4\text{-}2$$

With assumptions of one compressible working fluid and negligible effects of Reynolds number this relationship can be simplified to:

$$\eta_t = \boldsymbol{f}(N_s, D_s, M_a) \quad 4\text{-}3$$

$$\eta_t = \boldsymbol{f}(\varphi, \psi, M_a) \quad 4\text{-}4$$

$$\eta_t = \boldsymbol{f}(\varphi, \nu, M_a) \quad 4\text{-}5$$

Where N_s is the specific velocity, D_s is a specific diameter, M_a is the Mach number, φ is the flow coefficient, ψ is the loading coefficient, and ν is the velocity ratio. These non-dimensional parameters can be expressed in dimensional form by:

$$N_s = \frac{\omega\sqrt{\frac{\dot{m}}{\rho_{out}}}}{(\Delta h_{is})^{0.75}} \quad 4\text{-}6$$

$$D_s = \frac{D(\Delta h_{is})^{0.25}}{\sqrt{\frac{\dot{m}}{\rho_{out}}}} \quad 4\text{-}7$$

$$\varphi = \frac{C_x}{U} \quad 4\text{-}8$$

$$\psi = \frac{\Delta h_{actual}}{U^2} \quad 4\text{-}9$$

$$\nu = \frac{U}{\sqrt{2\Delta h_{is}}} \quad 4\text{-}10$$

Using this approach for scaling down large-scale turbines to small-scale may not be possible due to lack of accuracy with scaling down some dimensions such as blade trailing edge thickness, tip clearance thickness, and blade thickness which could cause significant error in predicting turbine performance. Moreover, the Reynolds number could not be scaled down without controlling the fluid density at the inlet independently which is impossible with compressible flow [165]. However, these non-dimensional parameters are still a useful tool for small-scale turbines for evaluating, describing and choosing the suitable machine type according to the required operating conditions.

4.3 Turbine type selection

If specific turbines are tested for various operating conditions and the total efficiency is plotted against the non-dimensional parameter specific speed N_s, then a unique plot will be developed showing the specific speed that produces maximum turbine efficiency. An example of this are done by Balje [166] and Wood [167] as shown in Figure 4-2. According to cycle analysis and better efficiency the operating conditions with flow rate of 0.1kg/s, power output of 5kW, and rotational speed of 60000RPM have been chosen to produce specific speed of 0.48 according to Equation 4-6. It is clear from Figure 4-2 that maximum efficiencies between 80% and 100% can be achieved by both the axial and radial turbines, but the axial turbine has the advantage of wider off design specific speeds range that produces

higher efficiencies than that of the radial turbine, therefore the axial turbine has been selected in this work.

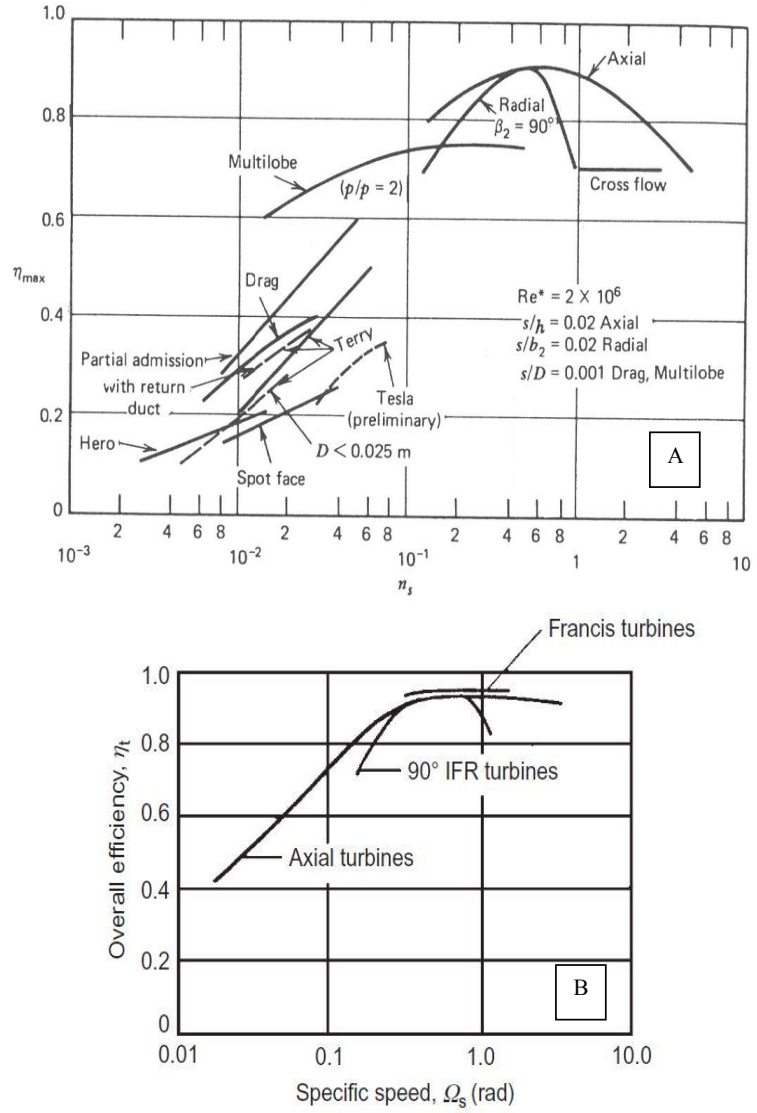

Figure 4-2 Overall efficiency against specific speed for various turbines types, (A) [166] and (B) [167]

4.4 Axial turbine preliminary design mean-line method

The preliminary design analysis for the turbine involves many repetitive calculations to evaluate the system performance and components initial geometries over the range of

operating conditions. Such screening analysis is an approximate and general procedure rather than a final design tool. It is used as the initial step for finding the overall geometries and performance characteristics at the required operating conditions and it is used where the flow properties are based on turbine mean diameter and neglecting any radial gradients.

4.4.1 Turbine blades velocity triangle

Figure 4-3 shows the single-stage stator and rotor passage arrangements with flow angles and velocity vectors. The flow enters the stator with a horizontal velocity, leaving the stationary blades with velocity (V2) at the absolute angle (α_2). The flow then enters the rotor blades at a relative angle (β_2) and relative velocity (w2); and leaves the rotor blade at a relative angle (β_3) and relative velocity (w3) [55].

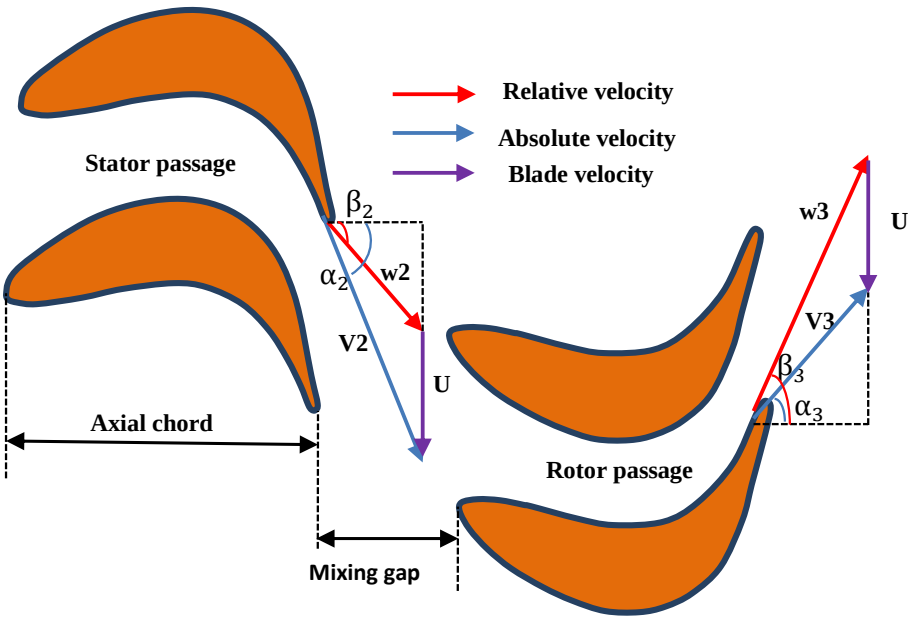

Figure 4-3 Axial turbine stage blades and velocity arrangement [55]

Figure 4-4, shows the velocity triangle diagram which clarifies the trigonometric relationships between blade velocities vectors and their angles.

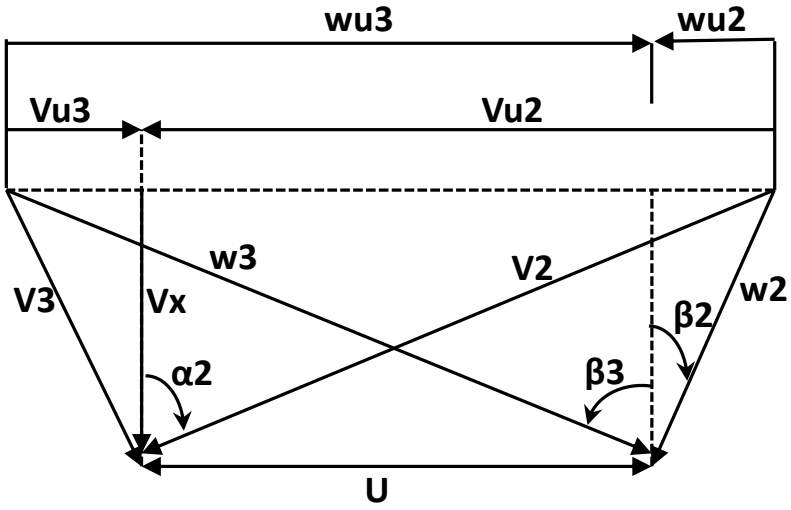

Figure 4-4 Velocity diagram for single-stage axial turbine [55]

4.4.2 Axial turbine thermodynamics and total efficiency

Turbines are designed to convert the fluid energy to the useful mechanical work delivered to the shaft coupling. Figure 4-5 shows a schematic for the meridional view of axial turbine single stage with main flow path dimensions and three recognizable stations. The specific work done on the rotor blades is equal to the stagnation enthalpy drop during expansion process through the turbine with the assumption of adiabatic flow that can be found in the general form of the Euler work equation:

$$\Delta W = h_{o1} - h_{o3} = U(V_{u2} - V_{u3}) \qquad 4\text{-}11$$

In this equation, the absolute flow tangential velocities (Vu) are included, as to adhere to the velocity sign of Figure 4-4. As the stator blades are stationary blades so the stagnation enthalpy drop across it is equal to zero.

$$h_{o1} = h_{o2} \tag{4-12}$$

In the axial turbine, the radial velocity components are small, thus [108]

$$h_o = h + \frac{1}{2}(V_x^2 + V_u^2) \tag{4-13}$$

By substituting equation 4-13 in equations 4-11 and 4-12 we obtain

$$h_{o1} - h_{o3} = (h_2 - h_3) + \frac{1}{2}(V_{u2}^2 - V_{u3}^2) = \mathrm{U}(V_{u2} - V_{u3}) \tag{4-14}$$

Hence

$$(h_2 - h_3) + \frac{1}{2}(V_{u2}^2 - V_{u3}^2)[(V_{u2} - U) - (V_{u3} + U)] = 0 \tag{4-15}$$

It is observed from velocity diagram in Figure 4-4 that:

$$V_{u2} - U = w_{u2} \tag{4-16}$$

$$V_{u3} + U = w_{u3} \tag{4-17}$$

$$V_{u2} + V_{u3} = w_{u2} + w_{u3} \tag{4-18}$$

Thus

$$(h_2 - h_3) + \frac{1}{2}(w_{u2}^2 - w_{u3}^2) = 0 \tag{4-19}$$

The thermodynamic expansion process through turbine stator and rotor at three stations clarifies in Figure 4-5 and are represented by reference [108] in Mollier diagram as shown in Figure 4-6.

The efficiency of expansion process through the turbine can be described by total efficiency which is considered an important performance parameter of interest to both designers and users. The isentropic total efficiency can be expressed as

$$\eta_t = \frac{\text{actual work}}{\text{ideal (isentropic) } work} \qquad 4\text{-}20$$

The actual work can be calculated by using equation 4-11 for the steady adiabatic process while the ideal work is slightly more complicated due to its dependence on ideal process definition. In isentropic expansion process, the turbine gives maximum work output; which process is clarified in Figure 4-6 by line (01-3SS).

$$\eta_t = \frac{h_{o1} - h_{o3}}{h_{o1} - h_{o3ss}} \qquad 4\text{-}21$$

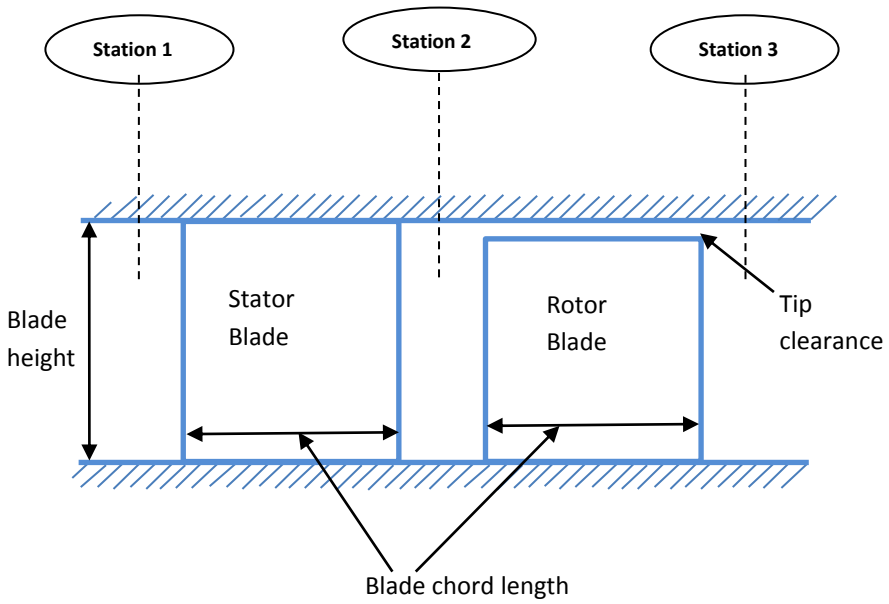

Figure 4-5 Schematic view for single-stage meridional view of an axial turbine

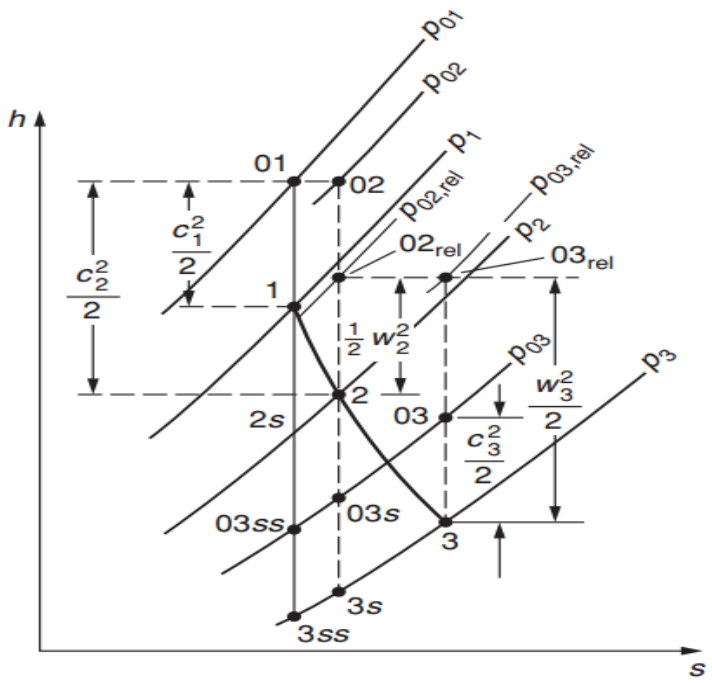

Figure 4-6 Mollier diagram for turbine stage [108]

4.4.3 Mean line mathematical model

To derive the mathematical equations of preliminary mean line method the approach which was used by Glassman and Stewart [168, 169] has been adopted here. This approach is able to generate preliminary geometry consistent with the operational conditions and is an appropriate starting point for CFD 3D analysis [55]. The blade velocity is calculated using mean diameter (D_m) and rotational speed (N) [55]:

$$U = \frac{\pi N D_m}{60} \qquad 4\text{-}22$$

The total turbine specific work is given by:

$$\Delta h_t = \frac{\text{Power}}{\dot{m}} \qquad 4\text{-}23$$

Expressing stage speed-work parameter as:

$$\lambda = \frac{U^2}{\Delta h_t} \qquad 4\text{-}24$$

The value of (λ) is the primary factor for determining turbine total and static efficiencies.

$$\eta_t = \frac{\lambda}{\lambda + \frac{A}{2}} \qquad 4\text{-}25$$

$$\eta_s = \frac{\lambda}{\lambda + \frac{1}{2}(A + B)} \qquad 4\text{-}26$$

The stage loss parameter A is expressed as

$$A = \frac{K * Re^{-0.2}}{\cot\alpha_2}(F_{st}C_{st} + F_{ro}C_{ro} + C_{ev}) \qquad 4\text{-}27$$

The constant of proportionality K is the turbine loss coefficient which is determined by empirical correlations [168]. The Reynolds number used in this study was calculated using [55]:

$$Re = \frac{2\dot{m}}{\mu D_m} \qquad 4\text{-}28$$

For the velocity diagram 50% reaction the inlet and exit swirl parameters are calculated as:

$$\frac{V_{u2}}{\Delta V_u} = \frac{\lambda + 1}{2} \qquad 4\text{-}29$$

$$\frac{V_{u3}}{\Delta V_u} = \frac{\lambda - 1}{2} \qquad 4\text{-}30$$

The rotor weighting factor F_{ro} is equal to 2 for all cases while the stator weighting factor F_{st} is equal to 1 for the first stage in case of velocity diagram 50% reaction according to[168]. The rotor loss parameters C_{ro} are calculated as [55]:

$$C_{ro} = 2 * \cot^2\alpha_2 \left(\frac{V_{u2}}{\Delta V_u}\right)^2 + \left(\frac{V_{u2}}{\Delta V_u} - \lambda\right)^2 + \left(\frac{V_{u3}}{\Delta V_u} - \lambda\right)^2 \qquad 4\text{-}31$$

And for first stage stator is:

$$C_{st} = (1 + 2\cot^2\alpha_2)\left(\frac{V_{u2}}{\Delta V_u}\right)^2 \qquad 4\text{-}32$$

For all stators other than the first stage, the stator loss parameter is:

$$C_{st} = (1 + 2\cot^2\alpha_2)\left(\frac{V_{u2}}{\Delta V_u}\right)^2 + \left(\frac{V_{u3}}{\Delta V_u}\right)^2 \qquad 4\text{-}33$$

At the last stage where exit vanes are not used, the exit vane loss parameter C_{ev} is equal to zero. The exit loss parameter B of Equation 4-26 is expressed as [55]

$$B = E * \cot\alpha_2{}^2 \left(\frac{V_{u2}}{\Delta V_u}\right)^2 + \left(\frac{V_{u3}}{\Delta V_u}\right)^2 \qquad 4\text{-}34$$

Where E is the ratio of the stage axial exit velocity to the stage average axial velocity, which is equal to 1 in the case of constant axial velocity through the stage. The turbine state conditions and exit velocities are calculated as follows[55]:

$$\Delta V_u = \frac{U}{\lambda} \quad 4\text{-}35$$

$$V_{u,2} = \frac{V_{u2}}{\Delta V_u} \Delta V_u \quad 4\text{-}36$$

$$V_{u,3} = \frac{V_{u3}}{\Delta V_u} \Delta V_u \quad 4\text{-}37$$

$$V_x = V_{u,2} \ \cot \alpha_2 \quad 4\text{-}38$$

$$p_{ex} = p_{in}^t \left(1 - \frac{\Delta h_t}{c_p T_{in}^t \, \eta_s}\right)^{\gamma/(\gamma-1)} \quad 4\text{-}39$$

$$T_{ex}^t = T_{in}^t - \frac{\Delta h_t}{c_p} \quad 4\text{-}40$$

$$T_{ex} = T_{ex}^t - \frac{V_{ex}^2}{2c_p} \quad 4\text{-}41$$

$$p_{ex}^t = p_{ex} \left(\frac{T_{ex}^t}{T_{ex}}\right)^{\gamma/(\gamma-1)} \quad 4\text{-}42$$

In order to check if total efficiencies are consistent with the computed velocities, the total efficiency is calculated as [55]:

$$\eta_t = \frac{\Delta h_t}{c_p T_{in}^t \left[1 - \left(\frac{p_{ex}^t}{p_{in}^t}\right)^{(\gamma-1)/\gamma}\right]} \quad 4\text{-}43$$

The annular areas (A_{an}), hub to tip ratio ($\frac{r_h}{r_t}$), and diameters for hub (D_h) and tip (D_t) are calculated as follows [55]:

$$\rho_{ex} = \frac{p_{ex}}{RT_{ex}} \quad (4\text{-}44)$$

$$A_{an,ex} = \frac{\dot{m}}{\rho_{ex} V_x} \quad (4\text{-}45)$$

$$\left(\frac{r_h}{r_t}\right)_{ex} = \frac{1 - \frac{A_{an,ex}}{\pi D_m^2}}{1 + \frac{A_{an,ex}}{\pi D_m^2}} \quad (4\text{-}46)$$

$$D_{t,ex} = \frac{2D_m}{1 + \left(\frac{r_h}{r_t}\right)_{ex}} \quad (4\text{-}47)$$

$$D_{h,ex} = D_{t,ex}\left(\frac{r_h}{r_t}\right)_{ex} \quad (4\text{-}48)$$

And for re-check, the input mean line diameter (D_m) by[55]:

$$D_m = \frac{\left(1 + \frac{r_h}{r_t}\right) D_h}{2\frac{r_h}{r_t}} \quad (4\text{-}49)$$

Absolute and relative flow angles are computed from

$$\alpha_2 = \tan^{-1}\frac{V_{u2}}{V_x} \quad (4\text{-}50)$$

$$\beta_2 = \tan^{-1}\frac{w_{u2}}{V_x} \quad (4\text{-}51)$$

$$\beta_3 = \tan^{-1}\frac{w_{u3}}{V_x} \quad 4\text{-}52$$

the stagger angle can be calculated from [108]

$$\tan\zeta = \frac{\cos\alpha_{in} - \cos\alpha_{out}}{\sin\alpha_{in} + \sin\alpha_{out}} \quad 4\text{-}53$$

The blade deflection angle can be obtained by [163]

$$\varepsilon = \alpha_{in} - \alpha_{out} \quad 4\text{-}54$$

4.4.3.1 The Zweifel ratio

The turbine blades have an optimum pitch to chord ratio which gives better performance [108]. If the pitch between blades is small that will give the fluid flow best guidance, however that will increase friction loss due to increased wet area. On the other hand, large pitch between blades makes the possibility of flow separation high due to poor flow guidance. These facts led to invent Zweifel optimum ratio of the blade by Zweifel [170] represented by an actual (Y) to an ideal tangential loading(Y_{id}) which is approximately constant for minimum losses.

$$Zw = \frac{Y}{Y_{id}} \quad 4\text{-}55$$

This can be simplified to describe blade pitch to chord ratio

$$S/bx = \frac{Zw}{2[\cos\alpha_{out}{}^2\,(\tan\alpha_{in} + \tan\alpha_{out})]} \quad 4\text{-}56$$

4.4.3.2 Number of blades

The number of the blade in each turbine row and the chord length of the stator and rotor can be calculated during the preliminary design stage. The aspect ratio of the blade can be calculated by:

$$\text{Aspect ratio} = \frac{H}{bx} \qquad 4\text{-}57$$

The optimum Zweifel ratio can be utilized to find the pitch to chord ratio as detailed in equation 4-56 and for a known axial chord the number of blades can be calculated from

$$\mathrm{Z} = \frac{2\pi r_m}{S} \qquad 4\text{-}58$$

4.4.3.3 Analysis of axial turbine losses

The flow losses process through the axial turbine passage is very complex one, but it can be identified by a number of processes which generates entropy or losses. Many schemes have been developed to describe the losses, where the AMDC+KO scheme (Ainley and Mathieson [171], Dunham and Came[172], Kaker and Okapuu [173]) are considered as the best several correlation based on a lot of comprehensive experimental data [165]. The total loss coefficient (K) according to AMDC+KO scheme can be express as

$$\mathrm{K}_{total} = \mathrm{XRe} * \mathrm{K_P} + \mathrm{K_{se}} + \mathrm{K_{Te}} + \mathrm{K_{Tc}} \qquad 4\text{-}59$$

4.4.3.3.1 Profile losses

By analyzing the fluid flow energy through the turbine passages with generated boundary layers effects, the profile losses expression can be driven based on energy dissipation in the boundary layers due to the viscosity effect. The XRe correction factor is calculated from the following equation [55]:

$$X\mathrm{Re} = \begin{cases} \left(\frac{\mathrm{Re}}{2*10^5}\right)^{-0.4} & \mathrm{Re} \le 2*10^5 \\ 1.0 & 2*10^5 < Re < 10^6 \\ \left(\frac{\mathrm{Re}}{10^6}\right)^{-0.2} & \mathrm{Re} > 10^6 \end{cases} \quad 4\text{-}60$$

The profile loss coefficient is calculated from:

$$\mathrm{K_P} = 0.914\left(\frac{2}{3}\mathrm{M_p X_{\theta i} K_{p(\theta i=0)}}\right) \quad 4\text{-}61$$

$$\mathrm{M_p} = 1 - 1.25(\mathrm{M_{out}} - 0.2)\left(\frac{\mathrm{M_{in}}}{\mathrm{M_{out}}}\right)^2 \qquad \text{for} \quad \mathrm{M_{out}} > 0.2 \quad 4\text{-}62$$

$$\mathrm{K_{p(\theta i=0)}} = \left\{\mathrm{K_{p(\alpha_{in}=0)}} + \left|\frac{\alpha_{in}}{\alpha_{out}}\right|\left(\frac{\alpha_{in}}{\alpha_{out}}\right)\left[\mathrm{K_{p(\alpha_{in}=\alpha_{out})}} - \mathrm{K_{p(\alpha_{in}=0)}}\right]\right\}\left(\frac{\mathrm{t_{max}/bx}}{0.2}\right)^{\frac{\alpha_{in}}{\alpha_{out}}} \quad 4\text{-}63$$

θi is blade incident angle, the $\mathrm{K_{p(\alpha_{in}=0)}}$, $\mathrm{K_{p(\alpha_{in}=\alpha_{out})}}$, and $\mathrm{X_{\theta i}}$ can be specified by Ainley-Mathieson and Dunham-Came charts [173]. Also the $(\mathrm{t_{max}/bx})$ is the ratio between trailing edge thickness and the chord[55].

4.4.3.3.2 Secondary flow loss

The secondary flow losses are generated by the flow vortices through the turbine passages. Since the flow velocity in the middle of the turbine blade passage is greater than that at the end wall boundary layers the flow will turn in the center of the passage to form what is called passage vortex. Moreover, the horseshoe vortex is generated by the end wall boundary layers at the blade leading edge point to spread around blade two sides as shown in Figure 4-7 which clarifies the passage vortex formation.

The secondary losses can be specified by the following equations [55]:

$$K_{se} = 0.04\left(\frac{b}{H}\right)\chi_{AR}\left[4(\tan\alpha_{in} - \tan\alpha_{out})^2\right]\left(\frac{\cos\alpha_{out}^{\,2}}{\cos\alpha_m}\right)\left(\frac{\cos\alpha_{out}}{\cos\alpha_{in}}\right)\left[1 - \left(\frac{b_x}{H}\right)^2(1 - K_p)\right] \quad 4\text{-}64$$

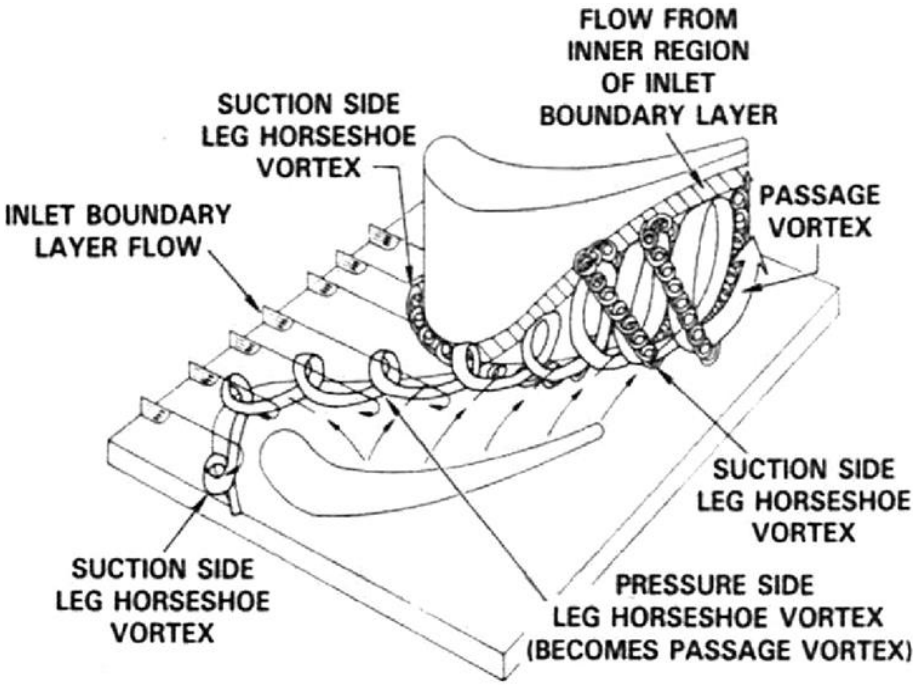

Figure 4-7 Schematic diagram of passage vortex generation

$$\alpha_m = \tan^{-1}[(\tan\alpha_{in} + \tan\alpha_{out})/2] \quad 4\text{-}65$$

$$\chi_{AR} = \begin{cases} 1 - 0.25\sqrt{2 - H/b} & \text{for } H/b \le 2 \\ 1 & \text{for } H/b > 2 \end{cases} \quad 4\text{-}66$$

H/b is the blade height to blade chord ratio and $(\frac{b_x}{H})$ is the axial chord to blade height ratio [55].

4.4.3.3.3 Trailing edge losses

At the end of any real blade there is a finite trailing edge thickness causing the flow on blade sides, the pressure side and the suction side, the flow of pressure side and the suction side separate at their ends by two points and the thickness between these points forms the base region at trailing edge. This base region has a pressure less than free stream flow, therefore with this low pressure and separation points the trailing shed vortex and single wake generate as shown in Figure 4-8. The trailing edge losses can be calculated by the following equations [55]:

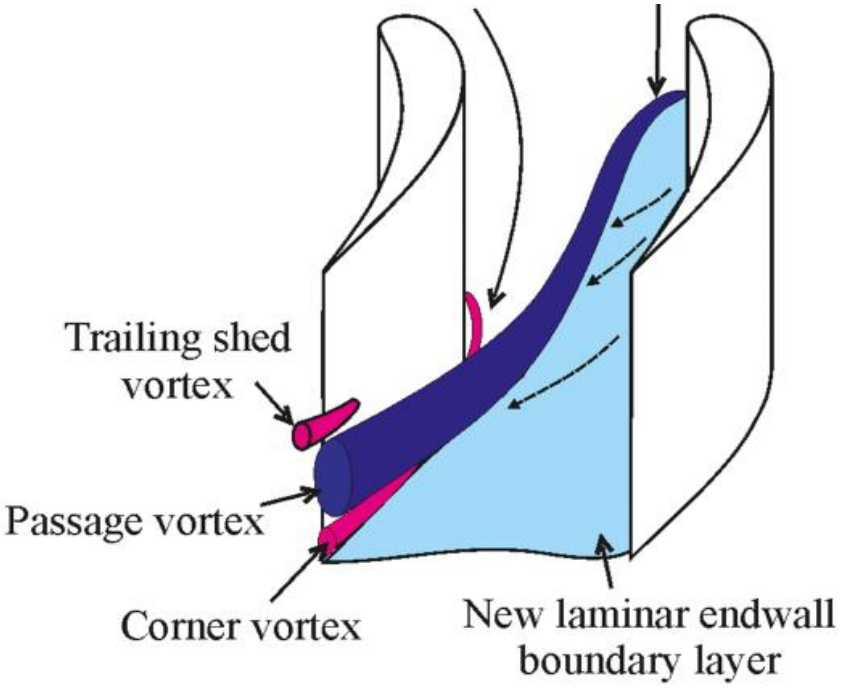

Figure 4-8 Schematic diagram of shed vortex generation

$$K_{Te} = \frac{\left[1 + \frac{\gamma - 1}{2} M_{out}^2 \left(\frac{1}{1 - \Delta E_{Te}} - 1\right)\right]^{-\gamma/(\gamma-1)} - 1}{1 - \left(1 + \frac{\gamma - 1}{2} M_{out}^2\right)^{-\gamma/(\gamma-1)}} \quad 4\text{-}67$$

The same procedure to specify $K_{p(i=0)}$ the energy loss coefficient ΔE_{Te} can be specified at the trailing edge by [55]:

$$\Delta E_{Te} = \Delta E_{Te(\alpha_{in}=0)} + \left|\frac{\alpha_{in}}{\alpha_{out}}\right| \left(\frac{\alpha_{in}}{\alpha_{out}}\right) \left[\Delta E_{Te(\alpha_{in}=\alpha_{out})} - \Delta E_{Te(\alpha_{in}=0)}\right] \quad 4\text{-}68$$

4.4.3.3.4 Tip clearance loss

In order to achieve free moving rotor, a rotor blade tip clearance between rotor tip and the outer casing must be left. This tip clearance will cause fluid leakage between blade pressure side and suction side due to the pressure difference. Such leakage will pass part of the flow rate without producing any useful work output and also generates vortex as shown in Figure 4-9 which in turn affects the turbine performance significantly.

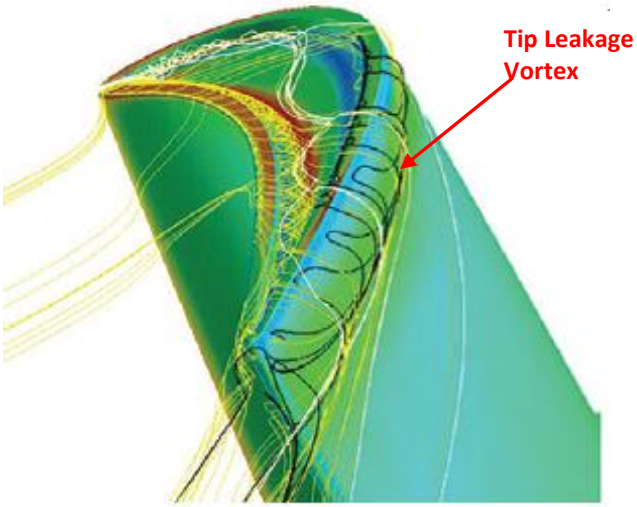

Figure 4-9 Tip leakage vortex formation through tip clearance

The designers usually aim to minimize this clearance distance but with the fact that this gap is affected by elongation due to thermal stress in the outer casing and centrifugal stress in the rotor blade as shown in Figure 4-10 [142], making this task quiet challenging.

The tip leakage loss can be calculated by the variation of the total stage efficiency η_t and tip clearance $\Delta\tau$ [55].

$$K_{Tc} = 0.93\left(\frac{r_h}{r_m}\right)\left(\frac{1}{H\cos\alpha_{out}}\right)\eta_t\Delta\tau \qquad 4\text{-}69$$

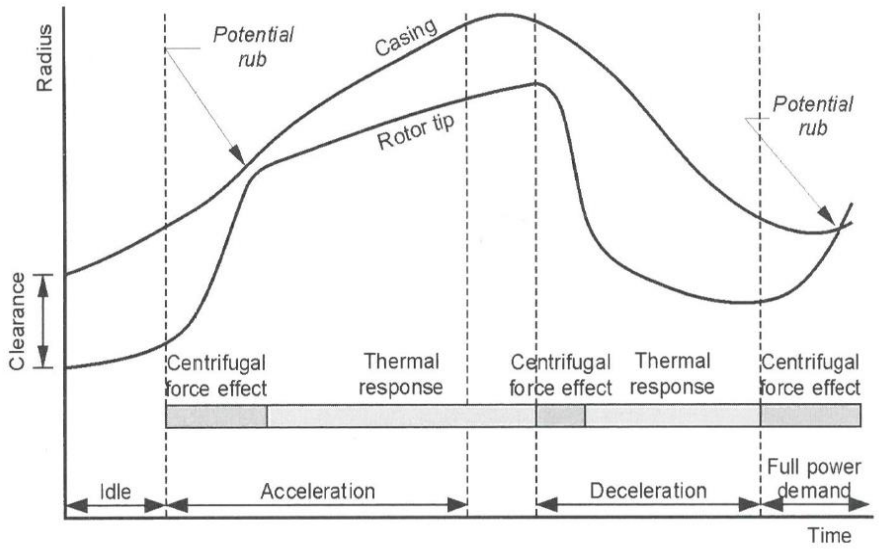

Figure 4-10 Tip clearance variation through typical turbine cycle [142]

4.4.3.4 Preliminary design modeling code

The mean line preliminary design approach was developed using MATLAB code [174] with input parameters such as inlet pressure, inlet temperature, power, mass flow rate, rotational speed, mean diameter, and stator exit angle [55]. To ensure stable and accurate solution the iterative process calculates and compares total efficiencies described by equation 4-25 with equation 4-43 and the mean line diameter equation 4-49 with the input value until reaching convergence. The calculations estimate the output parameters such as exit pressure and temperature, inlet and exit annular dimensions, total efficiencies, blade angles, and absolute and relative velocities. The preliminary design mean line modeling and procedure sequences are outlined in the flowcharts shown in Figure 4-11.

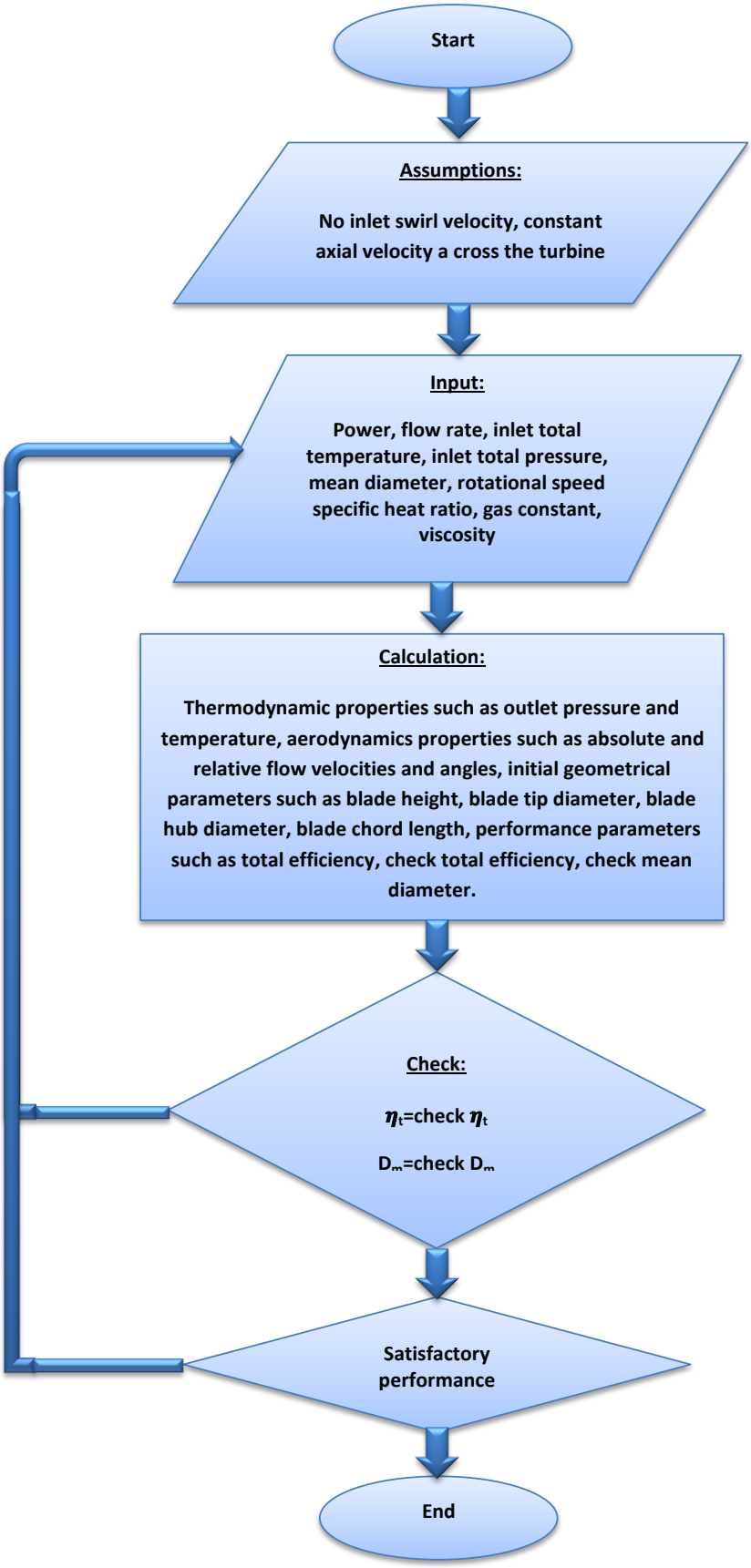

Figure 4-11 Preliminary design modeling code flowchart

4.5 Three dimensional CFD design analysis

The actual flow analysis for an axial turbine includes, compressible, turbulent, viscous and secondary flow characteristics; and therefore, a three-dimensional analyses is required to describe the flow accurately. More complexity can be added for tip clearance effects and interaction between stator and rotor blade rows. Although the one-dimensional preliminary design analysis is simple and fast for turbine performance analysis, it cannot provide the required flow details. The CFD three dimensional analyses integrated with preliminary design analysis can be used as an accurate tool for predicting the turbine performance. A lot of commercial CFD packages are available nowadays some of which are specifically used for turbomachines such as CFX solver, and others for general purpose such as Fluent solver [142]. Once the CFD analysis is validated, it can be used as a powerful design tool that will save a lot of time and cost associated with turbine prototype manufacturing and testing. The stairs diagram in Figure 4-12 shows the design steps of ANSYS-CFD that have been used in this study.

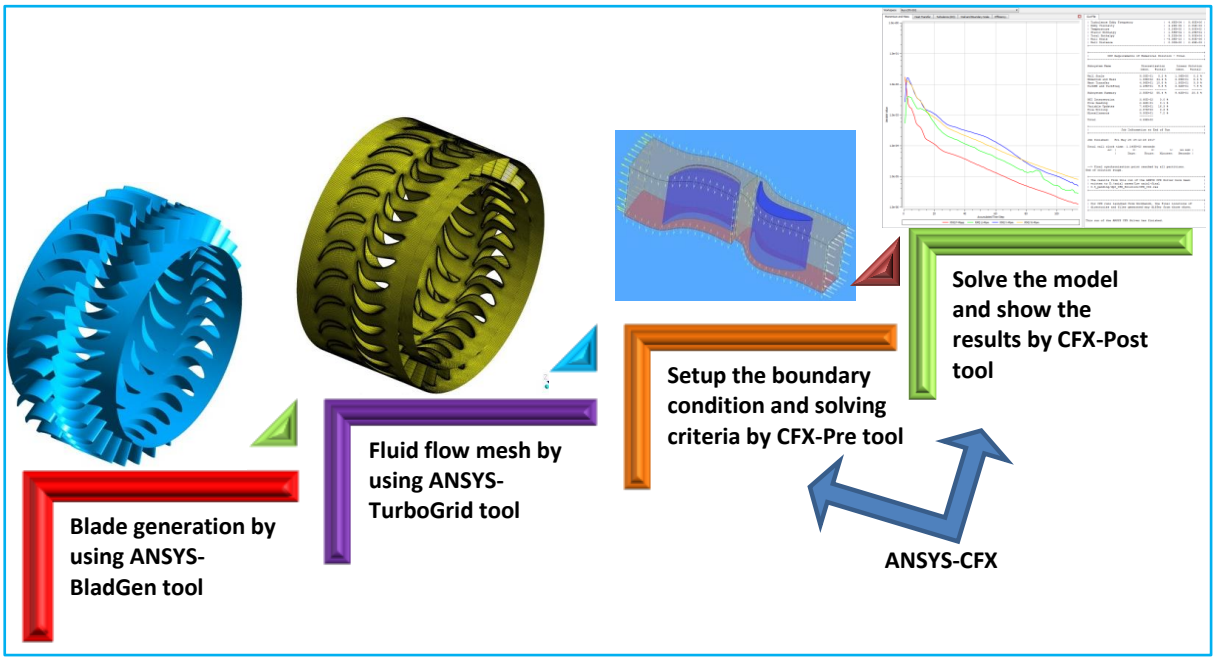

Figure 4-12 Stairs diagram of ANSYS- CFD design steps

4.5.1 Blade generation module

In the ANSYS-CFD software, the 3D blade developing was created by utilizing the BladeGen module which defines the both the stator and rotor blade geometry. Apart from the mean line preliminary design which defines the meridional flow path dimensions as shown in Figure 4-5, there is a need to set the blade angles and thicknesses in more details for the three-dimensional geometry. Figure 4-13 presents the main angles and thickness which control the blade profile in the ANSYS-CFD BladeGen module. It can be seen from this figure that the BladeGen module controls the stator and rotor geometry by stagger angle, inlet angle, outlet angle, leading edge thickness and trailing edge thickness at each blade section; while also ensuring that the number of the blades and gap between stator and rotor can be specified.

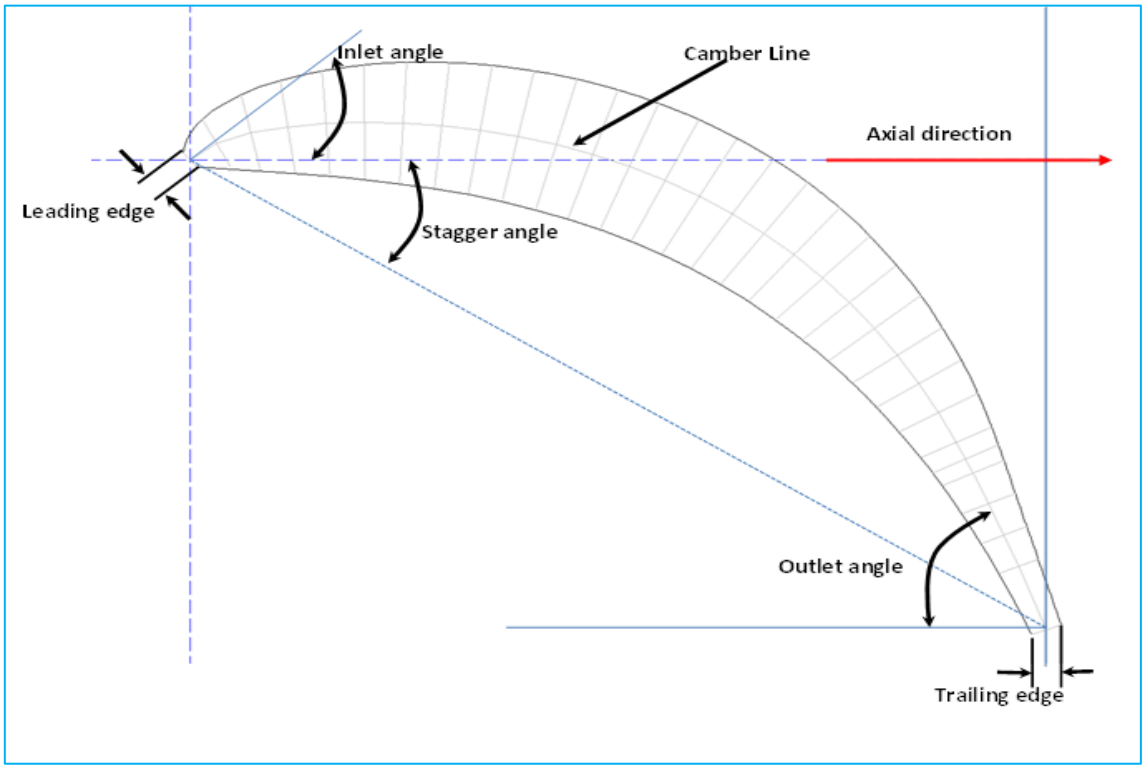

Figure 4-13 ANSYS-CFD BladeGen module blade profile main angles and thickness parameters

The completed three-dimensional geometries for stator and rotor rows connected with each other in one stage turbine are shown in Figure 4-14. To make the curvature of rotor blade reverse the stator blade by BladeGen module the coordinate system orientation for the stator is right-handed while for the rotor is left-handed.

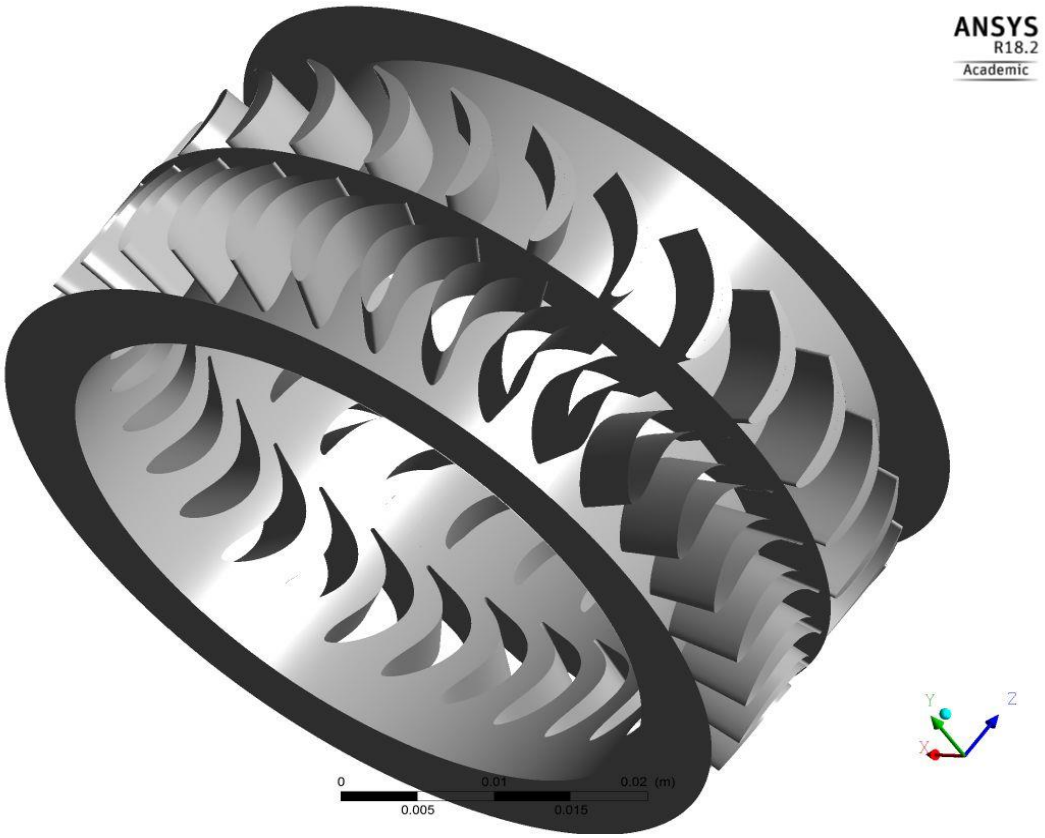

Figure 4-14 the three-dimensional geometry created by ANSYS-CFD BladeGen module

4.5.2 Mesh generation module

Once the 3D geometry is defined in the CFD modelling, the mesh generation task is started by importing this geometry into TurboGrid module. The ANSYS Workbench interfaces BladeGen module with TurboGrid module to make it easy to modify the geometry and flow domains during meshing process. The ANSYS TurboGrid module is the powerful tool which can create good quality hexahedral meshes while keeping the underlying geometry for turbomachinery. The setup of the TurboGrid needs to specify the following parameters: machine type (axial turbine), details of (hub, tip, and blade), tip clearance distance, inlet and outlet domains extension satiation (fully extend), and created the topology which guides the mesh. The automatic topology method ATM has been chosen in this work since it can create a high-quality mesh with minimal effort [175]. The flow is divided into three domains (inlet, passage, and outlet), Figure 4-15 shows the details for outlet domain topology where the green labels are used for topology edges; blue labels are used for topology nodes, and the red lines outline the blades. The topology surfaces are created at three locations along blade span (hub, mid-span, and shroud) to produce effective mesh element distribution.

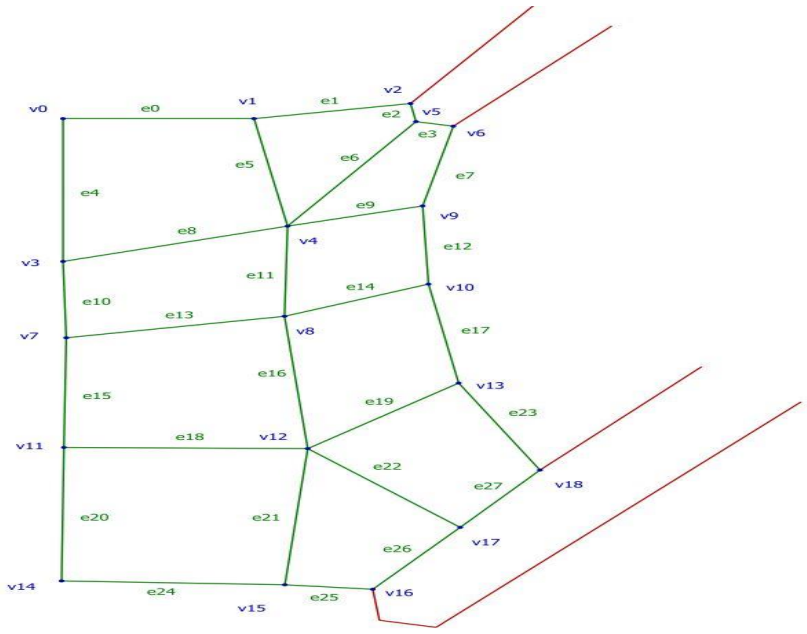

Figure 4-15 Topology mesh details for outlet domain

The topology mesh data can be controled by setting a group of parameters such as mesh size method, boundary layer refinement method, and near wall element size specification. The y^+ method is used with the near wall element size specification, where the non-dimensional parameter (y^+) can describe compatibility of the mesh size near to the wall with the turbulence model. To achieve adequate solution accuracy in minimum computational time, the grid size sensitivity was investigated with respect to turbine efficiency as shown in Figure 4-16 for baseline CFD model and Figure 4-17 for dual stage model [55]. The solution for isentropic turbine efficiency becomes stable after node count per passage reaches 500 000 in the baseline CFD model, while 400 000, 500 000, and 600 000 are required for the single-stage, two repeated stages, and two non-repeated stages, respectively [55]. Figure 4-18 and Figure 4-19 show the 3D mesh structure for baseline CFD model and dual stage model respectively. It can be seen from these figures that the mesh density near to the blade walls is higher than those at other flow regions; this mesh distribution saves time and provides higher solution accuracy.

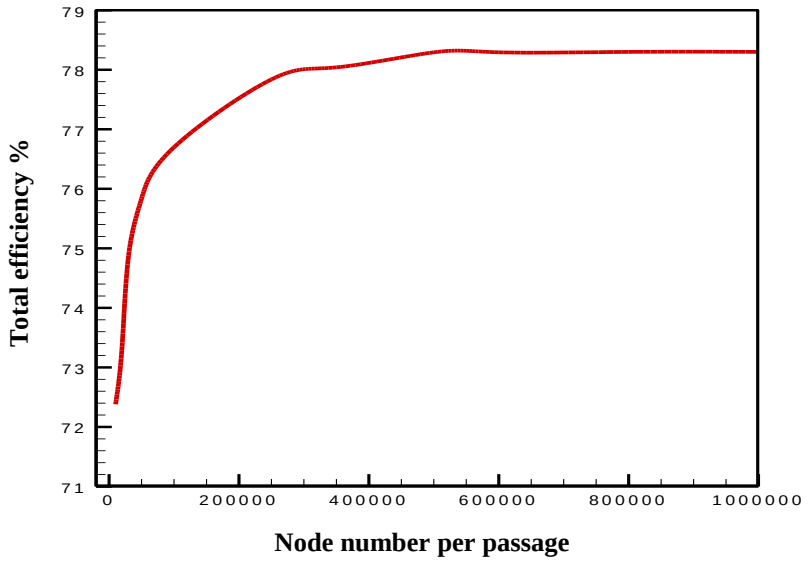

Figure 4-16 Mesh size sensitivity based on isentropic turbine total efficiency for CFD baseline model [55]

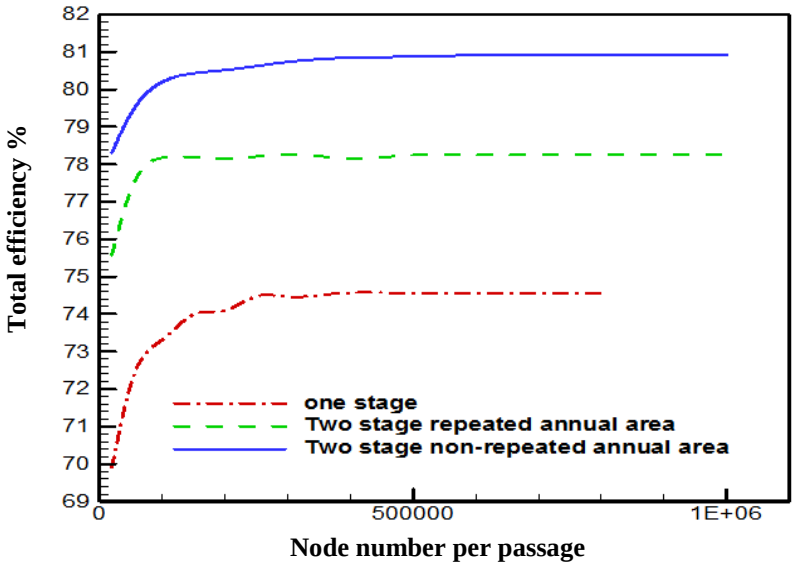

Figure 4-17 Mesh size sensitivity based on isentropic turbine total efficiency for dual stage turbines configurations with single stage [55]

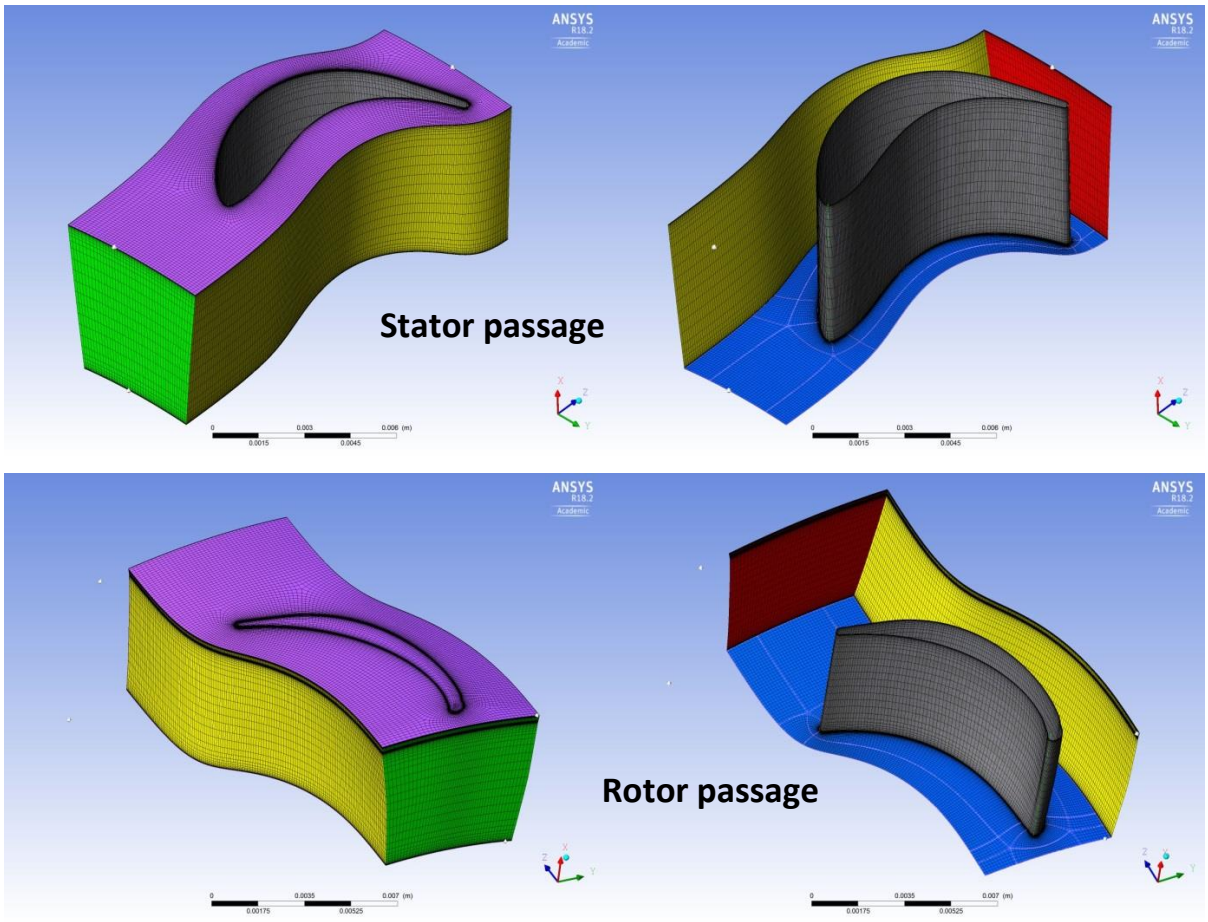

Figure 4-18 Stator and rotor passages 3D mesh structure for CFD baseline analysis

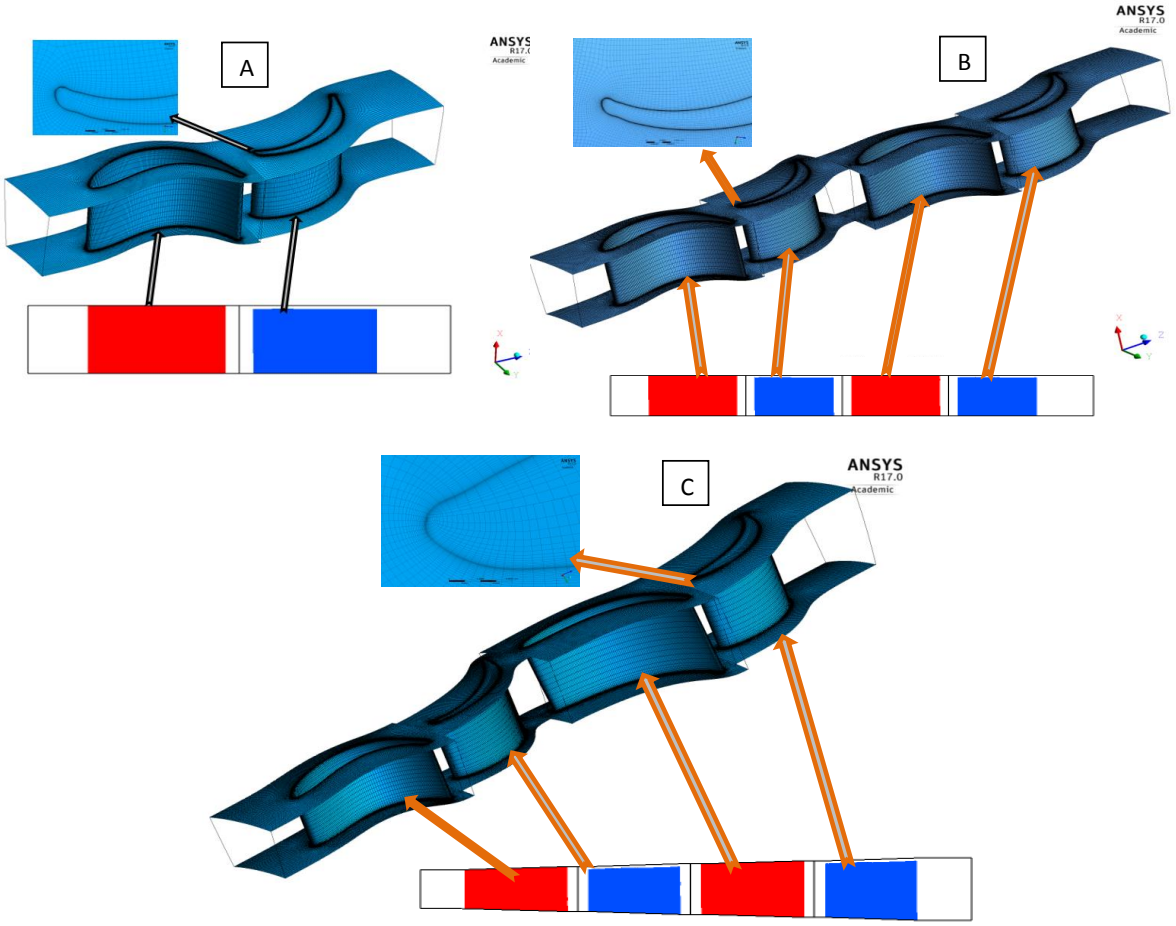

Figure 4-19 CFD mesh structure and meridional view (A) single stage axial turbine, (B) two repeated stages axial turbine, and (C) two non-repeated stages axial turbine [55]

4.5.3 ANSYS CFX-Solver module

The solver ANSYS CFX is recognized for its robustness, accuracy and high speed with turbomachinery complex geometry such as axial gas turbines. As clarified in Figure 4-12 the design process is a sequential process where, after finalizing the 3D geometry and mesh structure, the ANSYS Workbench interfaces between TurboGrid module and CFX-solver module to complete the CFX-solver three steps CFX-Pre, CFX-Solution, and CFX- post.

4.5.3.1 CFD governing equations

The governing equations solved by ANSYS CFX-Solver are Navier-Stokes equations in their instantaneous form, the equation of mass, momentum, and energy conservation can be written as following [176]:

- Continuity Equation

$$\frac{\partial \rho}{\partial t} + \nabla.(\rho U) = 0 \qquad 4\text{-}70$$

- Momentum Equation

$$\frac{\partial (\rho U)}{\partial t} + \nabla.(\rho U \otimes U) = -\nabla P + \nabla.\tau + S_M \qquad 4\text{-}71$$

the stress tensor τ, can be related to the strain rate

$$\tau = \mu \left[\nabla U + (\nabla U)^T - \frac{2}{3}\delta \nabla.U\right] \qquad 4\text{-}72$$

- Energy Equation

$$\frac{\partial (\rho h_t)}{\partial t} - \frac{\partial P}{\partial t} + \nabla.(\rho U h_t) = -\nabla.(\lambda \nabla T) + \nabla.(U.\tau) + U.S_M + S_E \qquad 4\text{-}73$$

Where the S_M and S_E are the source term of momentum and energy equations respectively. Reynolds average Navier-Stokes (RANS) equations can be derived by substituting the instantaneous velocity in terms of long-time average value $\overline{U_\iota}$ and a fluctuating value U_i' [177].

$$u_i = \overline{U_\iota} + U_i' \qquad 4\text{-}74$$

$$\bar{U}_i = \frac{1}{\Delta t}\int_t^{t+\Delta t} u_i dt \qquad 4\text{-}75$$

The turbulent flow occurs when the fluid inertia force becomes significantly higher than the fluid viscous force which will be inevitable with distortion and interaction processes caused by turbine geometry. The turbulent model which has been chosen in this study is the shear stress transport (k-ω SST) to evaluate the flow separation from the blade surface. This model uses the k-ε model in the free stream to avoid the too sensitive k-ω problem. The ANSYS CFX k-ω turbulence model transports the equations developed by [178] to calculate the specific dissipation rate (ω) and kinetic energy (k) which are [55]:

$$\frac{\partial}{\partial t}(\rho k) + \frac{\partial}{\partial x_i}(\rho k u_i) = \frac{\partial}{\partial x_j}\left(\Gamma_k \frac{\partial k}{\partial x_j}\right) + G_k - Y_k + S_k \qquad 4\text{-}76$$

$$\frac{\partial}{\partial t}(\rho \omega) + \frac{\partial}{\partial x_i}(\rho \omega u_i) = \frac{\partial}{\partial x_j}\left(\Gamma_\omega \frac{\partial \omega}{\partial x_j}\right) + G_\omega - Y_\omega + S_\omega \qquad 4\text{-}77$$

where Yk and Yω are the fluctuating dilations of compressible turbulence, Gk and Gω are the turbulent kinetic energies and dissipation generation terms, Γk and Γω are k-ω effective diffusivity terms, and Sk and Sω are k-ω turbulence model source terms [55].

4.5.3.2 CFX-Pre

In this part of CFX-Solver, the setup of the turbine boundary conditions which defines the turbine passage can be set. The boundary conditions such as the working fluid, inlet conditions, outlet conditions, and solving criteria such as the turbulence model and stator-rotor interaction model can be specified. The interfaces and periodic boundaries are defined by using the turbo mode tool. The turbine analysis steady state type gives accurate evaluation with lower time consumption over the transient type [176]. For steady-state problems, the CFX-Solver applies a false time step as a means of under-relaxing the equations as they iterate towards the final solution. Because the solver formulation is robust and fully implicit, a relatively large time scale can typically be selected, so that the convergence to steady-state is as fast as possible. A steady-state calculation will typically require between 50 and 100 outer loop iterations to achieve convergence. In this work, the steady state, turbulent, compressible, 3D viscous flow analysis has been adopted for axial turbine machine. In the wall configuration, the option rotor tip clearance at shroud is activated to include the tip leaked effect on the analysis results.

In the CFX-solver parameters, the high resolution advection scheme with auto conservative time scale convergence control is used to be compatible with the turbulence model k-ω SST. This model combines the k-ε and k-ω turbulent models to accurately solve a wide range of applications [179, 180] such as turbomachinery [75]. The automatic near wall function has been used because of its gradual transition between the wall functions and the sublayer according to grid density [7]. In order to ensure smooth solution for this turbulent model, the non-dimensional parameter (y^+) has to be near to unity as shown in Figure 4-20. Since there is no information about intensity of turbulence at the stator entry this value is kept at 5% as recommended by [176].

The flow field is not in thermal equilibrium because of temperature differences across the flow and boundaries; such heat transfer usually is defined by a heat transfer coefficient which is the heat amount across unit area per unit time and temperature difference. The heat transfer in CFX-Pre has a number of models to calculate heat transfer coefficient, the total energy model is suitable for single phase case to predict temperatures and enthalpies across the flow domains [176].

Figure 4-21 shows the boundary conditions faces and interfaces for one stage stator-rotor passage, where the periodic interfaces are chosen for connecting passage with other passages to ensure symmetric discretization of heat and mass flow through fluid domains. The Stage (Mixing-Plane) interface between rotor and stator fluid domains have been chosen because this model performs a circumferential averaging of the fluxes through bands on the interface instead of assuming a fixed relative position of the components [55]. The tip clearance interface set at GGI (Generalized Grid Interface) to ensure that each connection side is working with non-overlap regions in case that they have different sizes. The inlet stator boundary condition is total pressure while rotor outlet is static pressure; while all passage faces are assumed to be non-slip, smooth and adiabatic [55]. Table 4-1 summarizes the main CFX-Solver setup selected options.

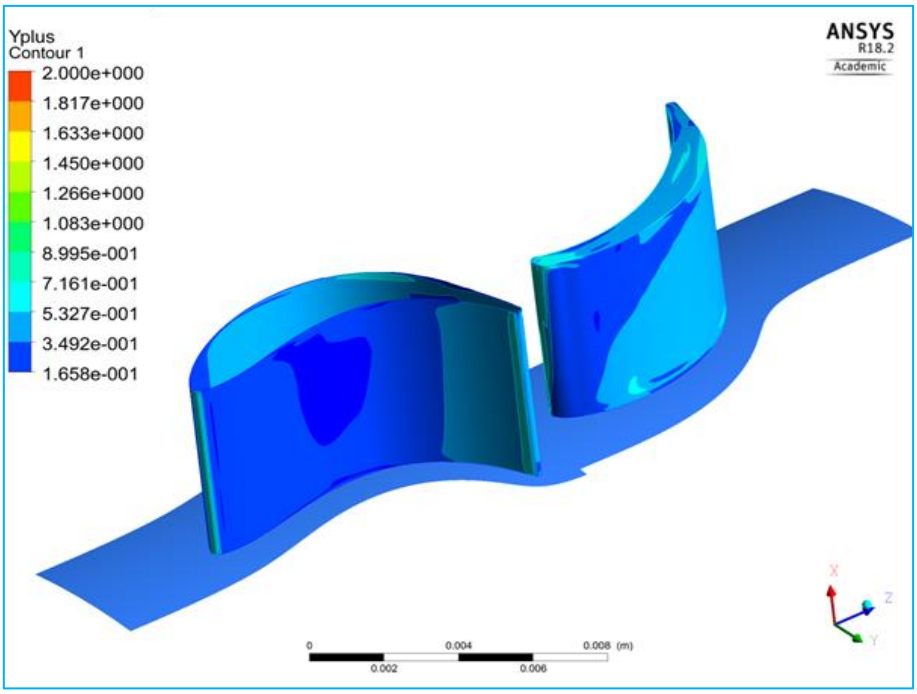

Figure 4-20 Yplus contour distribution cross the stator and rotor blade

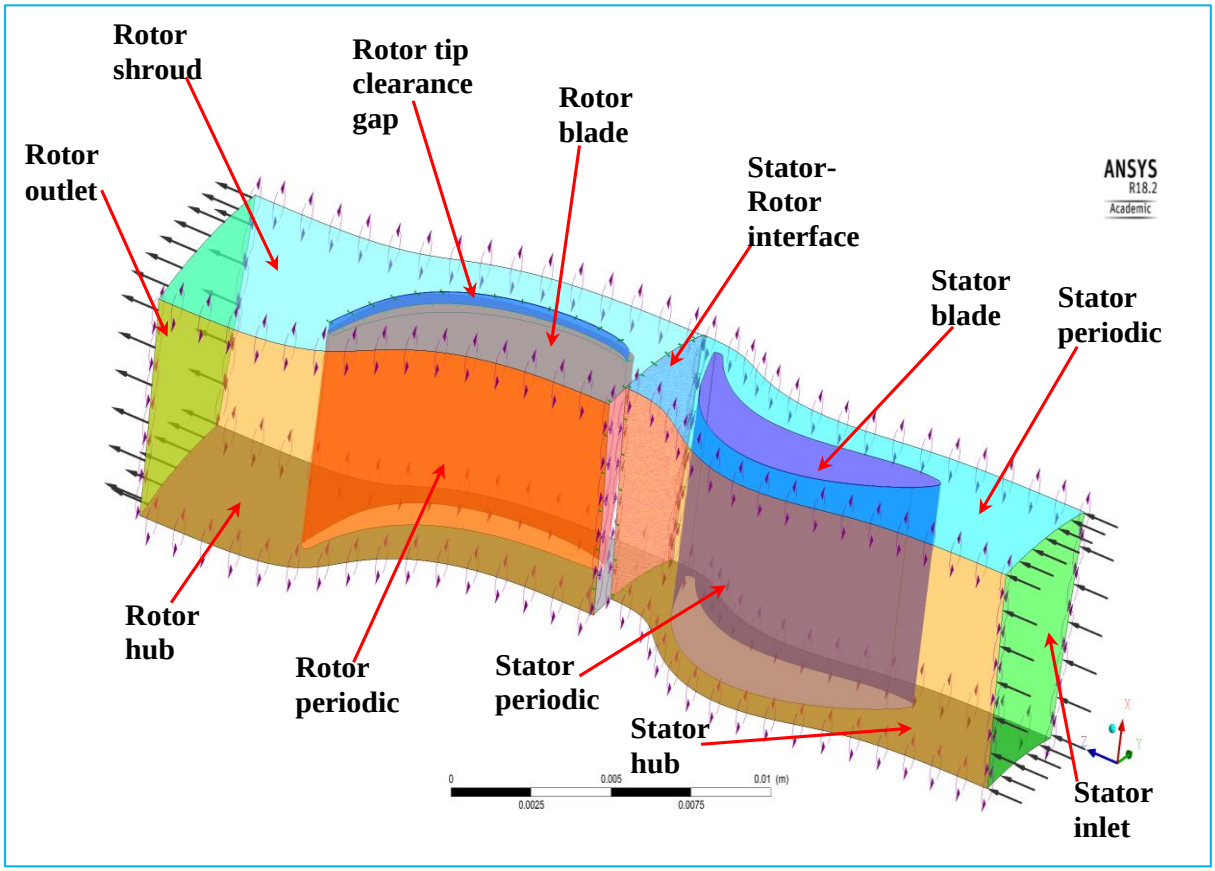

Figure 4-21 Boundary conditions and interfaces for the one stage stator-rotor passage

Table 4-1 Main setup setting details in CFX-Solver

Setting description	Options selected
Basic setting	
Machine type	Axial turbine
Analysis type	Steady state
Component definition	
Tip clearance at the shroud	Yes
Tip clearance at the hub	NO
Physics definition	
Reference pressure	0 bar
Heat transfer	Total Energy
Turbulence model	Shear Stress Transport
Interface default type	Stage (Mixing-Plane)

4.5.3.3 CFX-Solution

Once the CFX-Pre setup finishes the CFX-Solution can be started. In this step the solver control is set at a high resolution of turbulence numeric and the convergence control number of iterations from 1 to 500. Also, the convergence criteria residual type is set at RMS with target $1.e^{-5}$ as shown in Figure 4-22, which is shown on the convergence parameters monitor screen. By this monitor screen, the convergence can be checked for example if the convergence stalls directly or becomes very slow so that the conservation and imbalances need to be checked at the end of the output file.

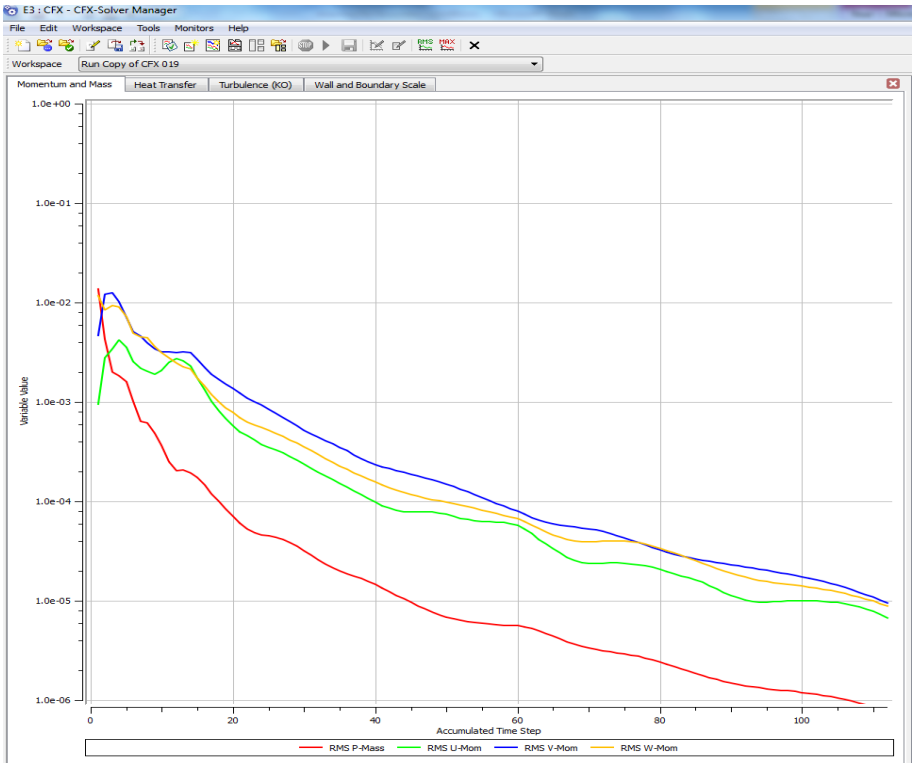

Figure 4-22 The CFX-solution convergence parameters monitor screen

4.5.3.4 CFX-Post

The solution data is exported to CFX-Post which in turn manages the visualization and quantitative analysis of results. The results show the data on domains and boundaries by changing their color setting. The results can be also written in the special file (rst or rth) type which can be mobilized and present the solution results in any other computer. Furthermore, the data can be exported to Excel file. CFX-Post supports various types of graphs and drawings with the geometric object to enable post-processing from visualizing the mesh and specify the location and quantity of the required calculation.

4.6 Mechanical structural CFD analysis

After 3D CFD aerodynamics analysis is completed, the mechanical structural analysis needs to be performed to check the design durability before manufacturing. After defining the

structural material specifications, the design checks the effect of aerodynamic loads produced by the pressure distribution and centrifugal load generated by rotational speed on the mechanical structure of the turbine. The main objective of this analysis is to check whether the stress in the turbine structure is lower than the maximum allowable material tensile strength, or if the deformation in the rotor blades is not larger than the tip clearance distance. The ANSYS workbench has the ability to integrate the aerodynamic analysis and structural analysis by interfacing the CFX-Solution with structural analysis setup as shown in Figure 4-23. Such integration imports the solution generated data in CFX-Solution like pressure distribution as shown in Figure 4-24 and rotor rotational speed as shown in Figure 4-25 to be boundary conditions for the structural analysis. If the duct casing wall thickness does not tolerate the pressure distribution, the wall thickness can be changed without rechecking the aerodynamic calculations because it is out of the fluid domain.

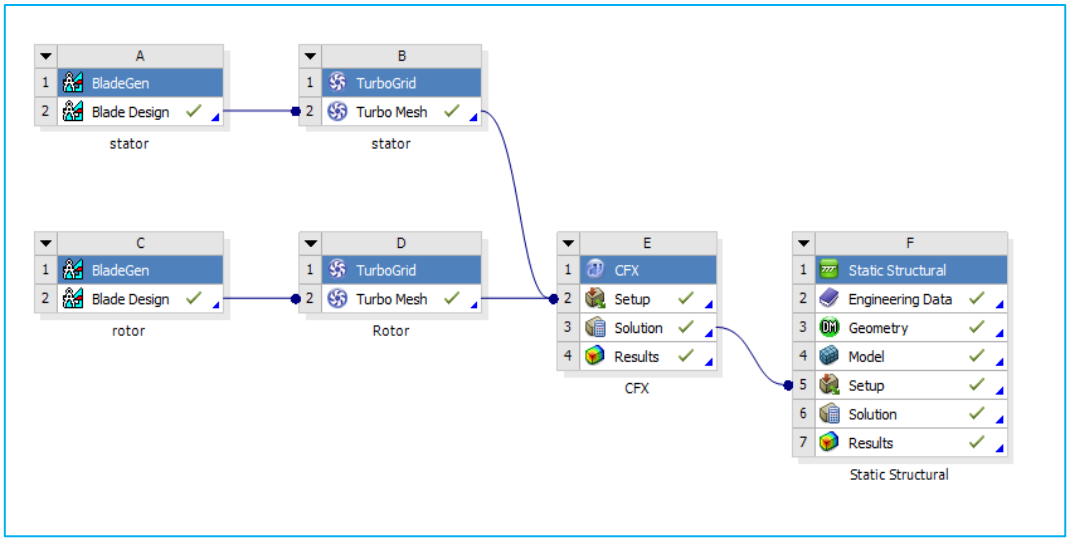

Figure 4-23 integration between aerodynamic analysis and structural analysis in one design project

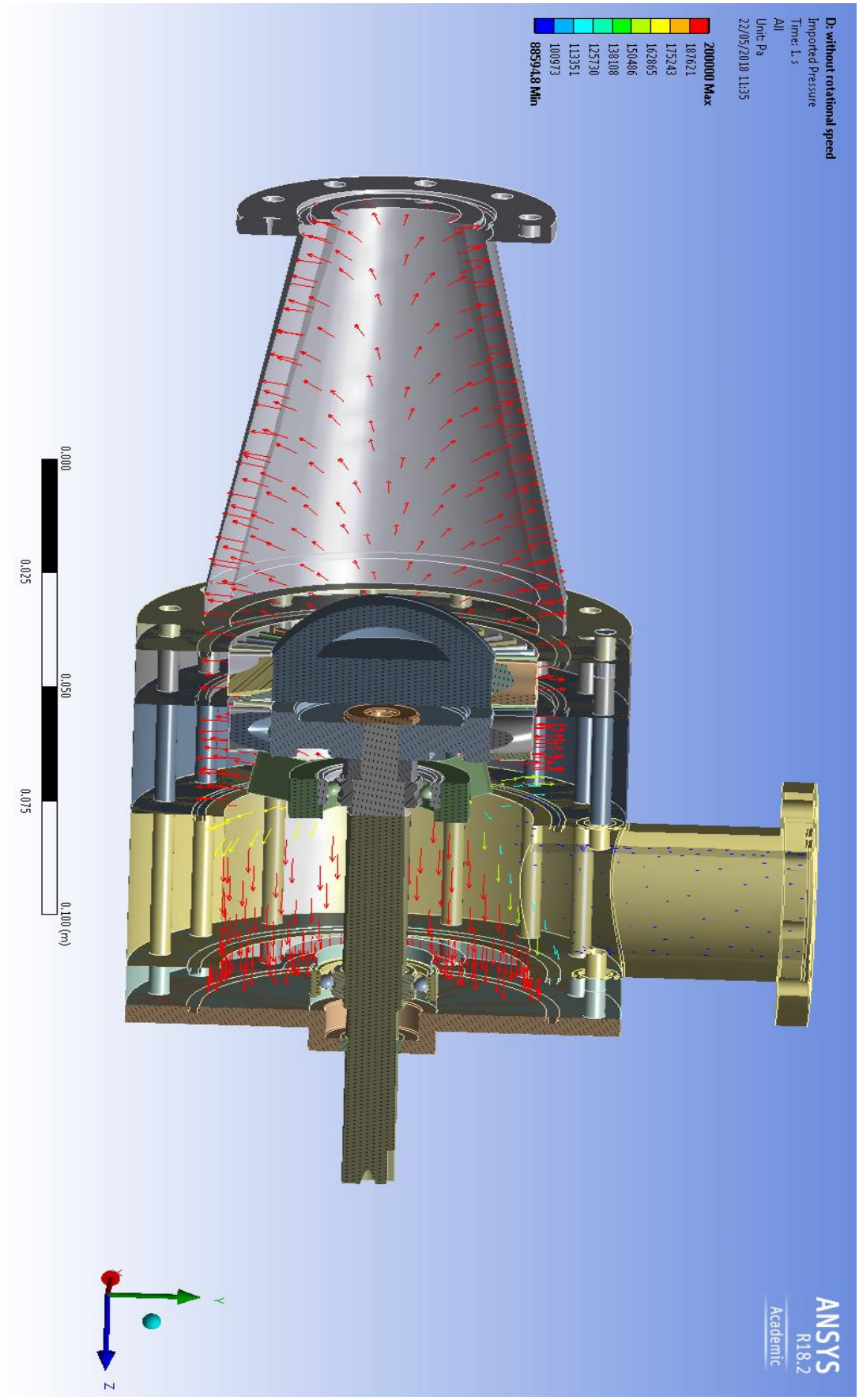

Figure 4-24 imported pressure distribution along turbine passage

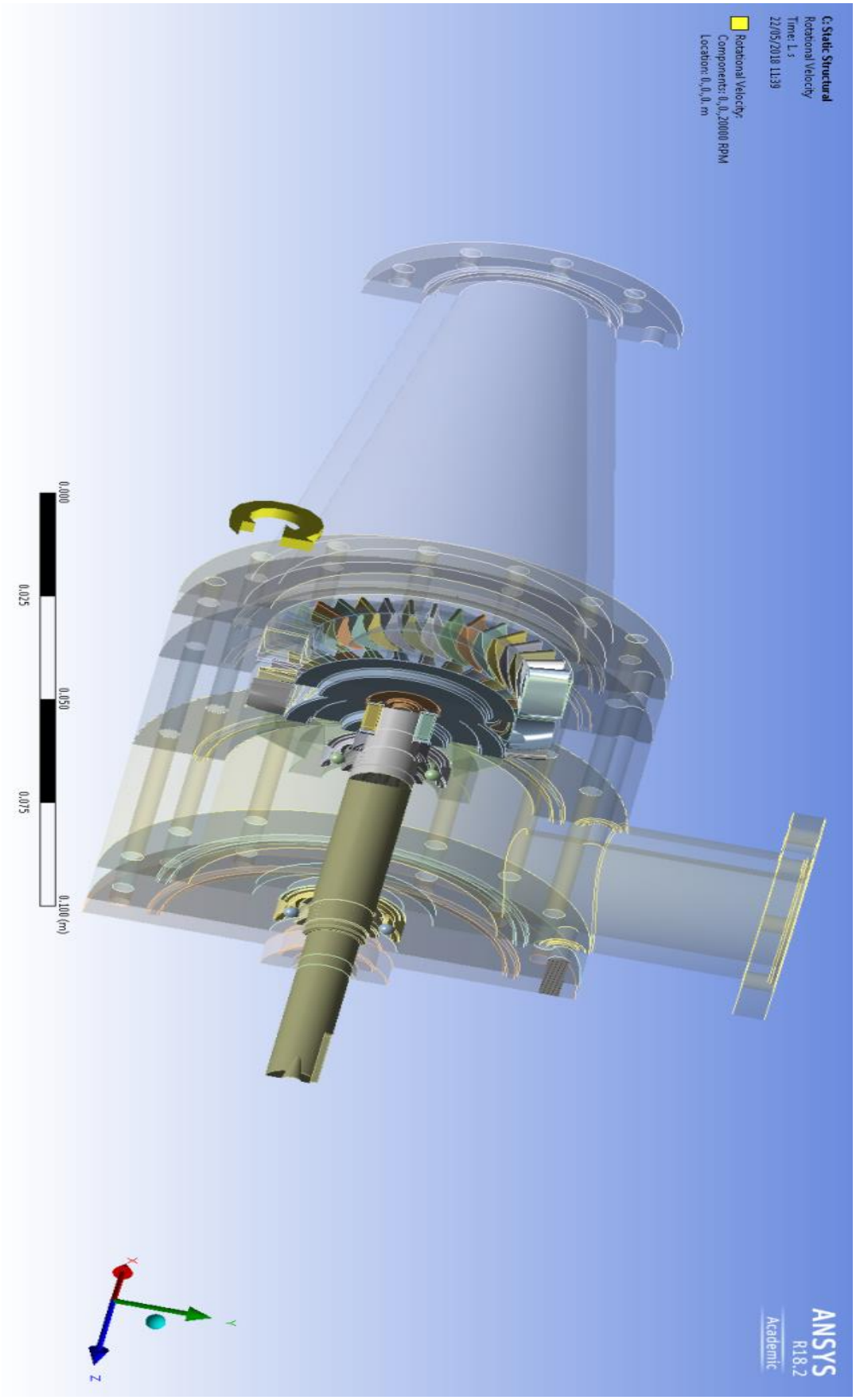

Figure 4-25 Rotational speed as a boundary condition in the structural analysis

4.7 Small-scale axial turbine 3D optimization

The turbine good design often results in a trade-off between various objectives and constraints for many significant design parameters. The ANSYS workbench presents DEO (Design Exploration Optimization) as a tool to perform this complex task for any complex process like turbine design optimization. In order to complete this task, design exploration needs to gather enough information about the turbine design to finalize the optimization in an efficient way.

The DEO describes the relationship between input parameters such as geometry and output parameters such as performance parameters by using sequential tools. These tools are Design of Experiments (DOE), Response Surfaces meta-model (RSM) and finally optimization as shown in the flowchart Figure 4-26. This flowchart clarifies the whole optimization design process where the first step is complete preliminary design to get a starting point for the CFD model. Following that, the CFD initial simulation model is built by BladeGen module to create geometry for the blade and flow path. Following which the TurboMesh module creates the mesh size suitable for geometry, and finally the CFX-Solver sets up and solves the model to get results. This integrated1-D and 3D design process was explained in details in previous sections. In order to start design exploration, the blade geometries created by BladeGen module need to be exported to the Design Modeler DM module, which has the ability of creating geometric parameters compatible with DEO. After that, the same procedure in the CFD design has to be followed then specifies the required output parameters in the DM CFD model by CFX-solver.

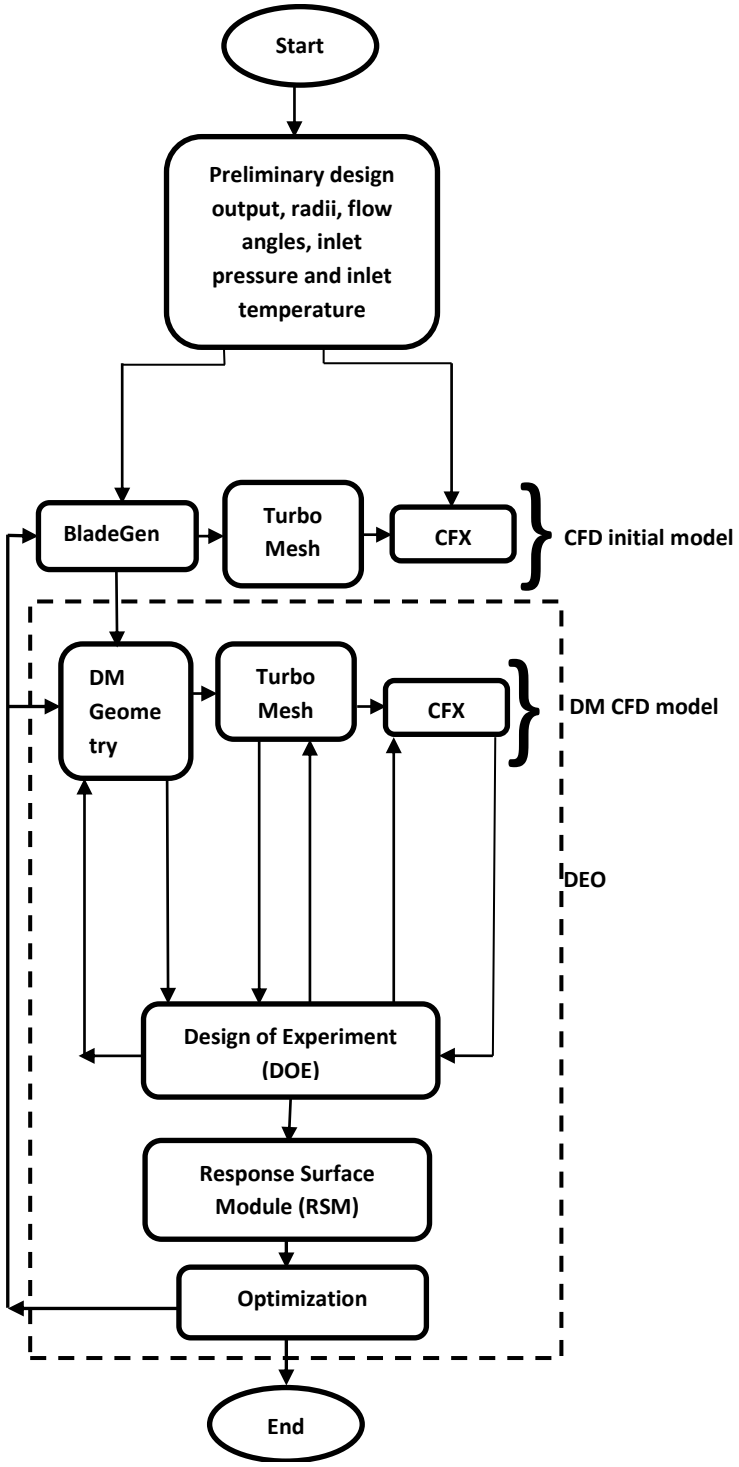

Figure 4-26 Design Exploration optimization flow chart

4.7.1 Camber line control point's parameterization technique

As outlined in the above sections, geometry is imported to Design Modeler DM module in order to create the geometrical parameters. These geometrical parameters have to describe the blade geometry and profile in an easy and efficient way. These parameters change within ranges during the optimization to change the blade geometry and profile for realistic shapes. A high number of design parameters mean complex optimization process and a time-consuming simulation process that is known as (the curse of dimensionality) in advanced optimization process. Therefore, choosing these parameters needs an expert designer with good engineering sense. Moreover, the quality of response surface is depending on the relationships between design parameters; so the fewer parameters the more accurate the response surface [181].

The camber line control point's parameterization technique is developed in this work to describe the blade passage geometry by only six geometrical parameters. The geometrical parameters that control the stator blade profile are stator first angle (SA1), stator second angle (SA2), stator blade peak location (SX), and stator blade thickness (ST) as shown in Figure 4-27. Similarly, the geometrical parameters that control the rotor blade profile are the rotor first angle (RA1), rotor second angle (RA2), rotor blade peak location (RX), and rotor blade thickness (RT), as shown in Figure 4-28. In addition, the stator chord length (SC) and the rotor chord length (RC) are chosen as flow path geometrical parameters as shown in Figure 4-29. The effect of the number of the blades on the passage areas makes it an important parameter in any design process; therefore, it is included in this technique as the stator number of blades (SN) and the rotor number of blades (RN). In this geometry definition approach, both pressure and suction sides of the turbine blade are defined with respect to the camber line, which is identified as shown in Figure 4-13. The blade first angle and second angle parameters specify the blade deflection while the peak location parameter

for the blade represents the point where the deflection starts to change from upstream to downstream or vice versa, so as a unique parameterization technique these, only three parameters, control the blade curvature.

To control the blade normal thickness on both sides of camber line suction side and pressure side the only one parameter utilized to control the maximum blade thickness is the ST for stator blade or RT for the rotor blade as shown in Figure 4-27B and Figure 4-28B. While the minimum thickness at the leading edge and trailing edge, which are clarified by red points in the same previous figures are kept constant. Using blade chord as a geometrical parameter is another novel aspect that makes this parameterization technique more robust and reliable. In the process of selecting these design parameters, the control points at the hub section will update the other blade sections along the blade span automatically; this will decrease the number of design parameters along the blade span [75].

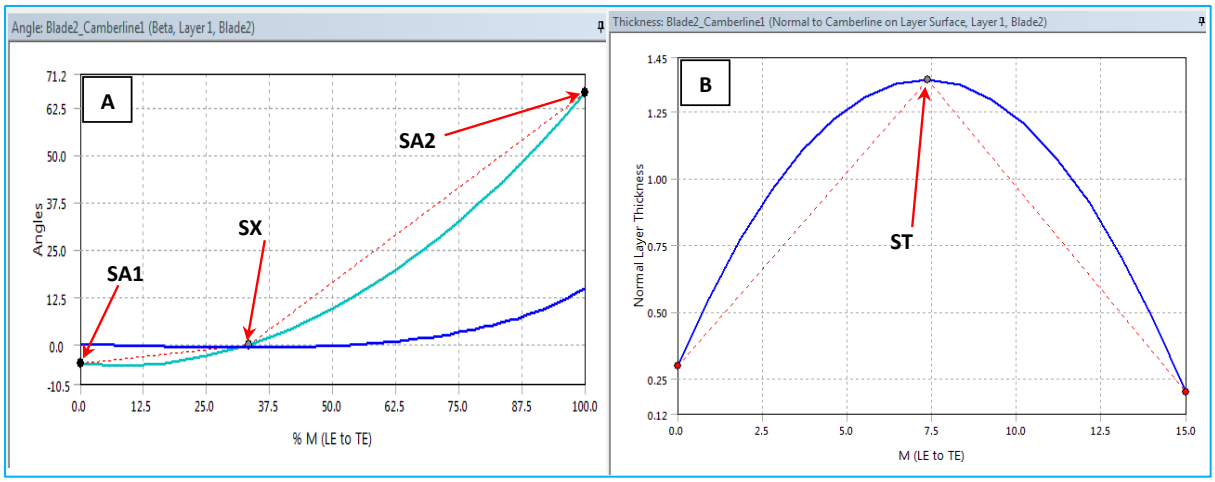

Figure 4-27 Stator blade camber line parameters, (A) Angles and (B) Normal thickness

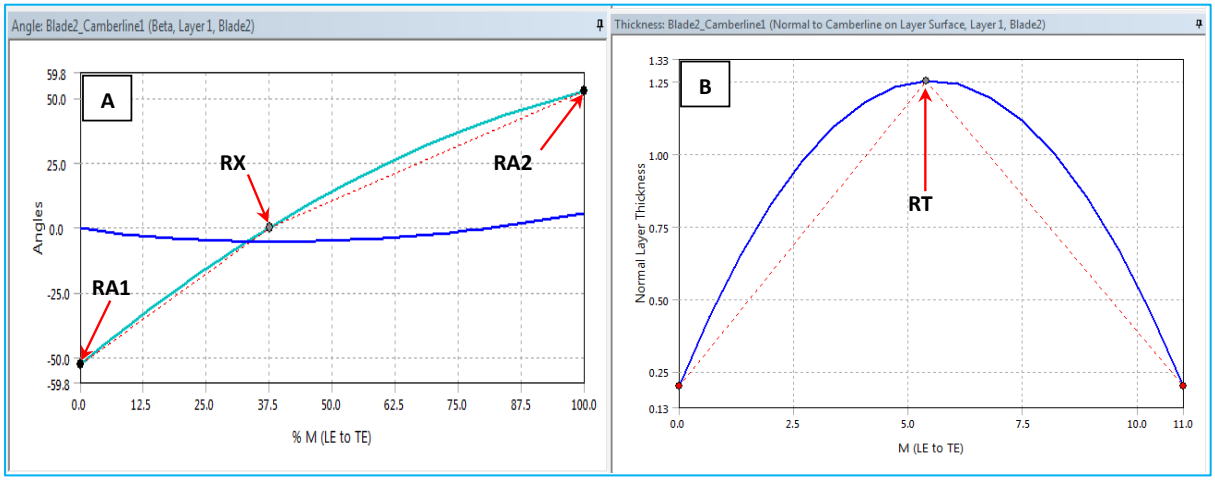

Figure 4-28 Rotor blade camber line parameters, (A) Angles and (B) Normal thickness

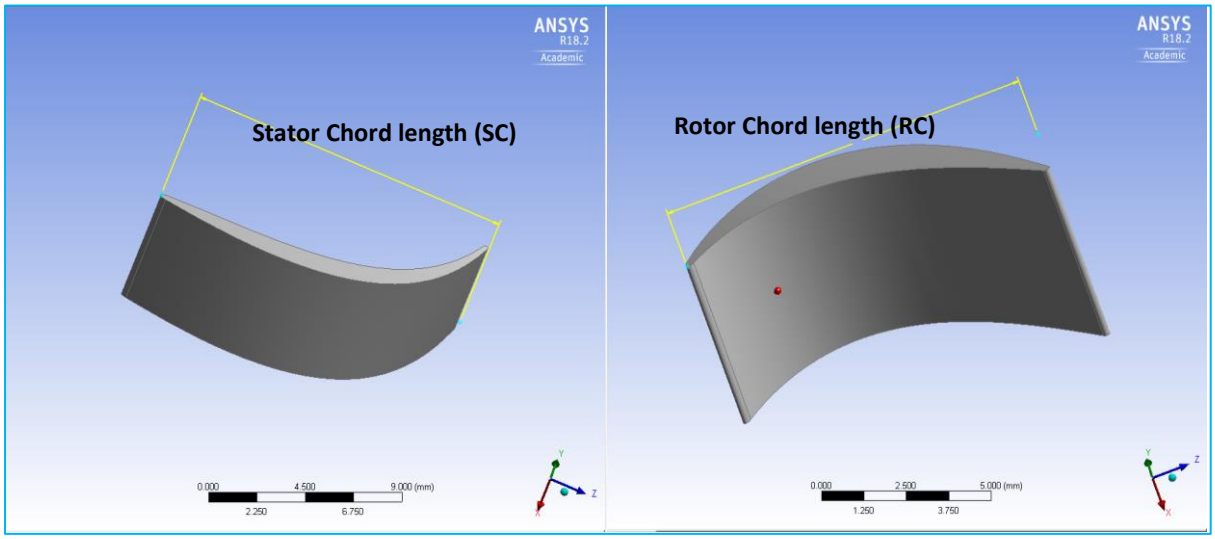

Figure 4-29 Stator chord length parameter (SC) and rotor chord length parameter (RC)

4.7.2 Design of Experiments (DOE)

Design of Experiments (DoE) module will divide the selected geometrical parameters into a number of divisions or steps through the specified range or domain limits. Then it will use a combination of all steps of the geometrical parameters to generate a matrix of design configurations which will then be simulated using the DM-CFD model as shown in Figure 4-26 [75]. The DOE objective is making better vision through the design domain with minimum number of design points. To have an example of this division and connection process between geometrical parameters Figure 4-30 shows the procedure of two geometrical parameters; namely stator blade thickness ST and rotor blade thickness RT. The geometrical parameters as a source of generating design points should be adequately defined within the ranges or domain limits, which give a better representation of geometrical limits which need to be investigated. After this design point creation process these points are sent to DM-CFD model to complete the solution process for these design points, and then all the data (input and output) are sent to Response Surfaces meta-model (RSM).

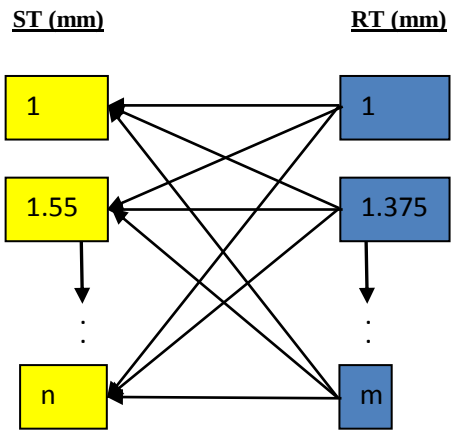

Figure 4-30 DOE division and connection procedure for two geometrical parameters ST and RT

The type of DOE used in this study is Central Composite Design (CCD) which is the most common type compatible with quadratic response surface. This type is usually used when the expected response surfaces are sequential, in that case the generated matrix of design point configurations needs to include correctly planned design points [181]. In order to explain the relation between the DOE and the RSM in a simple way: if the problem has just one parameter and the range of this parameter has two points maximum and minimum, then the DOE specifies these two points as design points and solves it by DM-CFD model before sending the design points input and outputs to the RSM. The relationship created by RSM between design points input and outputs will create a linear relationship to describe outputs at any input within the optimization range. Therefore to have a quadratic relationship there is a need for other design points between the two limiting points, maximum and minimum.

Figure 4-31 explains design points distribution for CCD DOE type with three parameters (x, y, and z) with each parameter having a range limit (1, -1): the black points called factorial points at ± 1 domain limits, the blue points called fractional factorial at $|\alpha_c|> 1$ domain limits and the red point is the center point at 0. The exact value of α_c depends on the number of parameters involved in the DOE. In the CCD type, the fractional factorial always has a number of points twice as many as there are parameters in the domain and these points represent the new extreme limits of maximum and minimum for each parameter in the domain.

The value of α_c depends on the number of factorial points of the central composite domain:

$$\alpha_c = [\text{number of factorials}]^{1/4} \quad \text{4-78}$$

$$\alpha_c = [2^k]^{1/4} \quad \text{4-79}$$

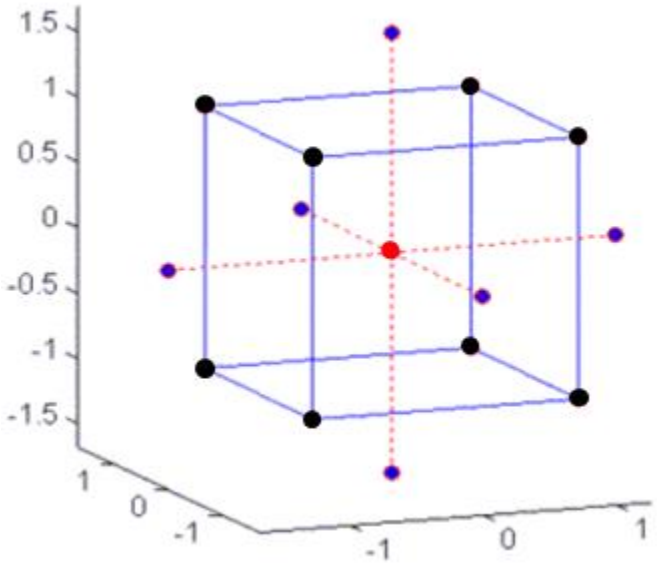

Figure 4-31 DOE CCD type design points distribution [181]

The maximum number of parameters can be handled by the CCD type is 20 and the parameters are two types: discrete and continuous. The discrete parameters represent the state of geometry or configuration, for example, the rotor or stator number of blades, which need to be an integer number, and these numbers are defined by levels, where each level contains the value to be used in the analysis. Using this kind of parameter doubles the number of design points according to the number of levels. A continuous parameter is one that can vary continuously within a specified range; this range needs to be defined by two values upper and lower. The number of design points generated from this kind of parameters depends on the type of DOE. In this work, 12 parameters were used to define the stator and rotor geometry; two of them are discrete parameters - the stator number of blades and the rotor number of the blades. While the rest are continuous parameters the design points generated by continues parameters are increased 9 times, since each discrete parameter has 3 levels to be at the end of 1341 design points.

4.7.3 Response Surfaces meta-model (RSM)

The Response surface meta-model (RSM) is a group of approximated algorithms whose creation is based on mathematical techniques [182]. The main target for this algorithm is to find the best functions or relationships between the input geometrical parameters and output performance parameters. The RSM is used to predict the performance of an objective function at any geometrical design point within the DOE domain range based on the design point's outputs delivered by DOE. As a result, the DEO considers RMS as a tool that can replace the CFX-Solver with lower time consumption and accuracy. The linear regression creates the function between two parameters to fit a linear equation between design points as:

$$Y = a + bX + e \qquad 4\text{-}80$$

Where Y is the output parameter and X is the input parameter, a and b are the regression equation constants and e is the random error constant. Figure 4-32 shows the linear regression function between two parameters Y and X which fit the blue sampling points.

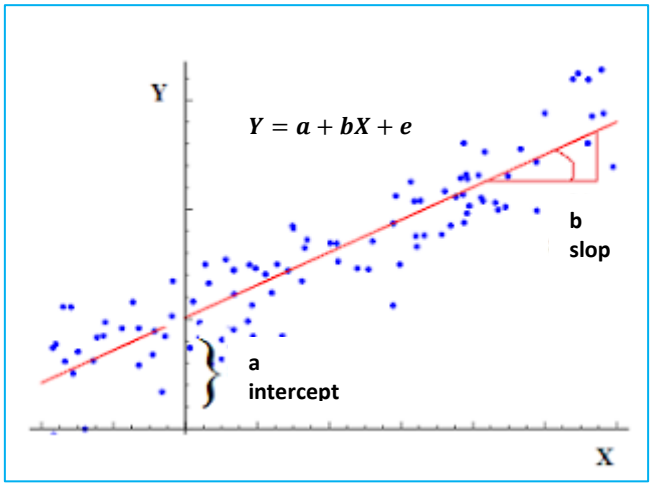

Figure 4-32 linear regression function between two parameters

With more than two parameters finding regression function will be a difficult task; however, there are other types of response surface that could handle this task. In this study the full 2nd-order polynomial algorithm has been used due to its ability to give an approximation of the true input-to-output relationship, this regression meta-model is typically described by Shyy [183] in equation 4-81 [75]:

$$Y = \beta_o + \sum_{i=1}^{k} \beta_i x_i + \sum_{i=1}^{k} \beta_{ii} x_i^2 + \sum_{i=1}^{k-1} \sum_{j=2}^{k} \beta_{ij} x_i x_j \ + \Psi \qquad 4\text{-}81$$

Where x is the independent variable, β is the regression coefficient and Ψ is the random error. These relationships will then be used to describe the turbine performance by the geometric parameters at certain boundary conditions as shown in the Figure 4-33 [75].

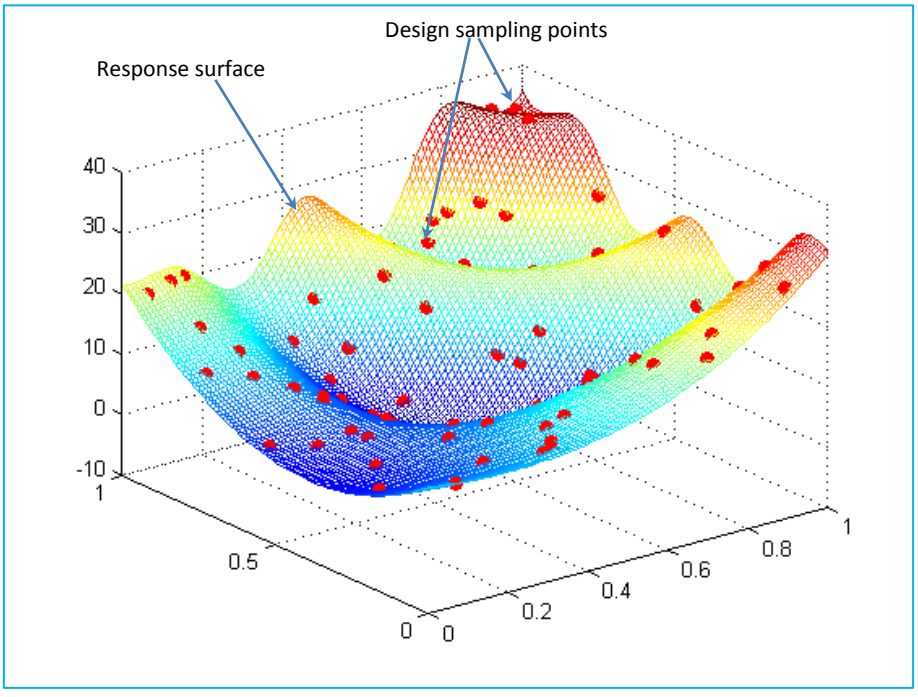

Figure 4-33 Response surface fit for the design sampling points created by DOE

The goodness of fit can be displayed for each output parameter of response surface for the purpose of checking the quality of the response surface. The goodness of fit can be specified by the coefficient of determination (R^2), which is mathematically represented as [181]:

$$R^2 = 1 - \frac{\sum_{i=1}^{N}(y_i - \hat{y}_i)^2}{\sum_{i=1}^{N}(y_i - \overline{y}_i)^2} \quad 4\text{-}82$$

Where y_i is the output parameter from DOE design point, $\hat{y}_i$ is the output parameter from the response surface, and $\overline{y}_i$ is the arithmetic mean value of the output parameter from the DOE design point.

Another evaluation tool for the response surface is local sensitivity which is one of the powerful tools, since it can show at a glance the impact of all input parameters on output parameters by using response surface functions. If Y is a function of X, then to find the local sensitivity of the parameter X on the parameter Y, the local sensitivity will be defined as [181]:

$$\text{local sensitivity} = \frac{(Max(Y) - Min(Y))}{Avg(Y)} \quad 4\text{-}83$$

4.7.4 Optimization

Optimization is the final step in ANSYS Design Exploration as shown in Figure 4-26. There are mainly two types of ANSYS Design Exploration optimization: direct optimization and response surface optimization.

4.7.4.1 Direct optimization

This type of optimization process performs the optimization task by using a matrix of design point configurations which are created by DOE directly. The direct optimization system does not need the response surface to draw its information but it accepts any data from any other source in the form of design points. That will give some advantage in terms of reusing existing data with any specific limit to do the optimization on them. The disadvantage of this optimization type is that with accurate optimization there is a need for a huge number of design points which is very demanding in computational time.

4.7.4.2 Response surface optimization

This type of optimization system draws its information from its own response surface components, and so it depends on the quality of this response surface. The available optimization methods in ANSYS design exploration are (Screening, MOGA, NLPQL, and MISQP) which utilize the response surface evaluations rather than the real solution data points. This type of optimization process has been chosen in this study as shown in Figure 4-34, which clarifies the integration between response surface optimization process and the design modeler DM model.

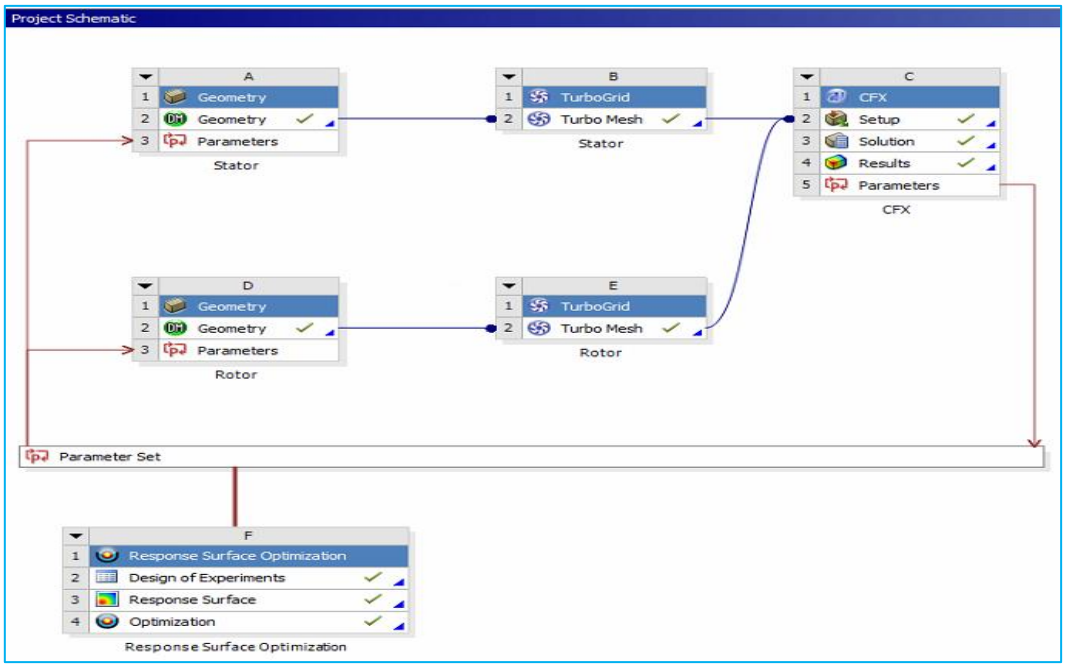

Figure 4-34 Response surface optimization integrated with DM CFD model

4.7.4.2.1 Screening optimization method

The screening optimization method is a continuous approach without iteration that makes it possible to use any type of parameters. Using sampling data in a random way may lead to noisy results, while the regular way gives aliasing results. Thus the screening optimization method depends on Shifted-Hammersley approach which is between these two basic sampling approaches. The screening method can be utilized for optimizing the preliminary data to give quick results or combined with another optimization method such as NLPQL for more refined results [181].

The optimized problem with this method can have continuous and discrete parameters but the problem needs to be multi-objective rather than a single objective. Typically the screening method is recommended for preliminary problems because of its quick response and low accuracy which make it suitable for locating approximate solutions for a huge study in a short time. Since the screening method does not depend mainly on one objective parameter, this

parameter can be changed after performing the analysis to see if the problem can meet different objectives [181].

4.7.4.2.2 MISQP and NLPQL optimization methods

The Mixed Integer Sequential Quadratic Programming (MISQP) method is a gradient based approach, and is a single objective optimizer which can solve the nonlinear programming problems by Sequential Quadratic Programming (SQP) method. The Nonlinear Programming by Quadratic Lagrangian (NLPQL) method is a gradient based, single objective optimizer, which is based on quasi-Newton approach. These two methods are recommended for continuous parameter problems only, and single objective function. Moreover, the problem may or may not be constrained but without exhibited sudden jumps in the objective and constraint function. These methods are local optimization designed for accurate forward and central difference techniques, which are used for predicting the gradient of an objective function.

The convergence rate for the MISQP and NLPQL methods is ($1.e^{-06}$) where this convergence is based on normalized Karush-Kuhn-Tucker (KKT) condition. The advantage of this convergence setting is that for large problems it is possible to get near optimum solution without being trapped into a series of small solution iterations. However, for problems that need higher numerical accuracy and may involve those small solutions the convergence rate needs to be set at ($1.e^{-12}$)[181].

4.7.4.2.3 MOGA optimization method

Multi-objective genetic algorithm (MOGA) applies the genetic algorithms to solve the multi-objective problem. The problem parameters could be continuous and discrete, which allows generating different kinds of sampling. When the design point fails, the MOGA does not include it in results or try to solve another design point in its place. The convergence criterion

in this method is (Stability Percentage) which looks for the stability of population based on standard deviation output parameters. If the population compared with a previous one is stable then the optimization is converged. The dominance solution is an important concept in a multi-objective optimization especially when there is a conflict between the objectives and the constraints. In such case, there is no dominance solution but a group of solutions and selecting any one of them will sacrifice at least one of the objectives or constraint quality. Therefore the MOGA is an evolutionary method that can handle the non-linear complex problems with non-continuous nature and multi objective or multi constraints. The objective functions in this study are total efficiency and power output, also the constraint function is the turbine flow rate. The optimization process can be done by natural and genetic selection of solutions evolving through a lot of population of solution generations under the effect of random selection, crossover reproduction and mutation as shown in Figure 4-35 [184].

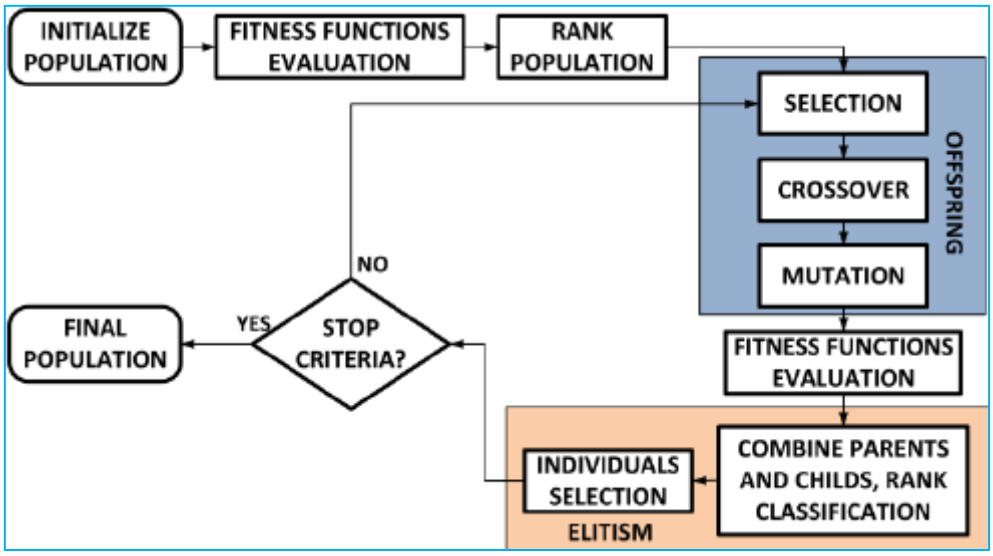

Figure 4-35 diagram represent MOGA procedure [184]

In this study, the MOGA method has been chosen over MISQP and NLPQL methods because it is a multi-objective method with global accurate search for discrete inputs. Moreover, the MOGA has been chosen over Screening because of its iterative and more accurate nature than the Screening method.

4.8 Axial turbine blade configurations

The use of the advanced three-dimensional blade configuration is another way for enhancing the turbine aerodynamic performance. When the blade sections have been laid out in the required direction the stacked sections will create new three-dimensional blade shapes or configurations as shown in Figure 4-36. This change in stacking was made to improve the three-dimensional aerodynamic performances of the blade by altering the spanwise distribution for the pressure and flow rate [142]. This complex geometry brings complications to the flow, which needs to be fully investigated by using three-dimensional modelling [7].

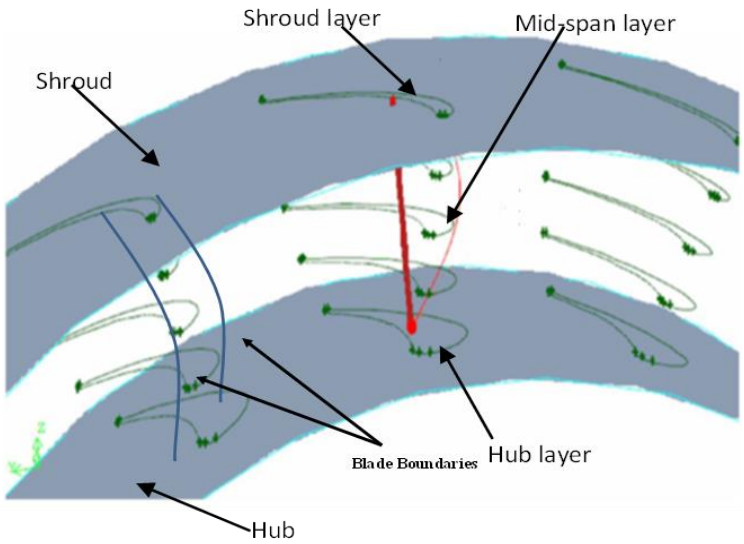

Figure 4-36 Blade layers arrangement in the axial turbine

As mentioned in previous sections the flow is affected by secondary flow vortices such as horseshoe, upper passage and lower passage vortices, which cause three-dimensional separations and dissipate the flow energy. Using blade lean configurations an efficient way of reducing these secondary losses [185] because the flow between the blade pressure side and hub end wall are improved [186]. The blade can be leaned in two directions negative or positive as shown in Figure 4-37 [7]. In the straight blade configuration, the lean angle between shroud and hub sections is zero; this angle changes when the blade shroud section moves in a circumferential direction to make a slope with respect to the hub section. Other blade sections follow this slope from hub to shroud to make a three-dimensional lean configuration.

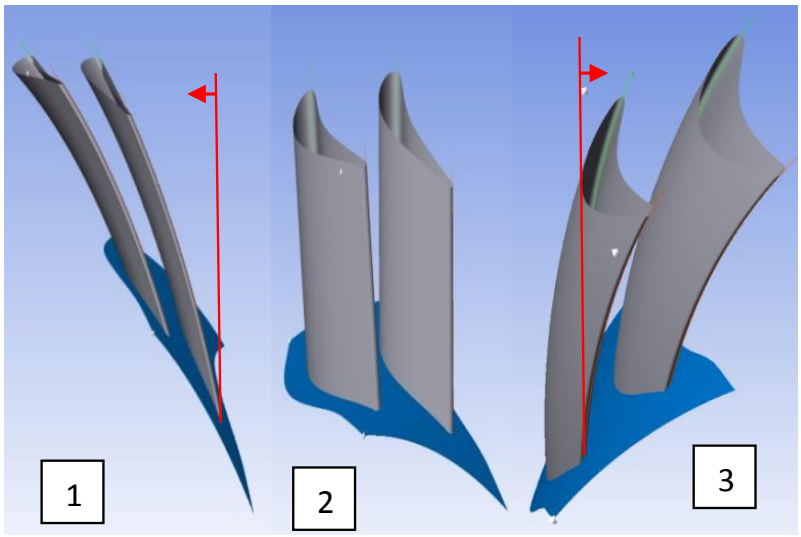

Figure 4-37 Lean blade configuration: 1 negative lean, 2 straight, and 3 positive lean [7]

If the blade shroud section is twisted with respect to the hub section and all blade sections follow this twisting, the twist blade configuration will be generated as shown in Figure 4-38. Such twist will change the blade deflection at every point along the blade span from hub to the shroud section and with blade section low deflections the section will look flatter. So, at this section, the flow will accelerate more than other sections while at the section with high

deflection the torque will be higher than at other sections. This balance between the loaded suction at high deflection section and the unloaded section with high acceleration can be used to enhance the blade aerodynamic characteristics [7].

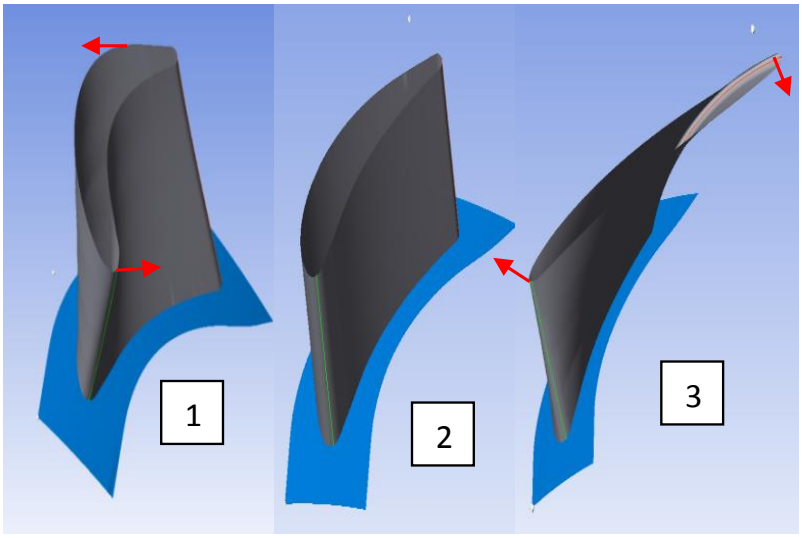

Figure 4-38 Blade twist configuration: 1 negative twist, 2 straight and 3 positive twist [7]

When the leading edge and trailing edge lines are not perpendicular to the flow direction, the blade is considered as a sweep [7]. When the chord length for the blade shroud section is minimum and the blade hub section chord length is maximum, then the configuration can be considered as a negative or backward sweep. When the shroud section is maximum and the blade hub section is minimum, the configuration is considered as positive or forward sweep as shown in Figure 4-39. Such arrangement can balance the flow acceleration along the blade span, where at the long chord blade section the acceleration will be higher than the short chord section which in turn can enhance the blade performance when used in the right way[7]. The blade bow configuration is the same as in lean configuration but the shroud and hub sections stay constant while the mid-span section moves in the circumferential direction to curve the blade as shown in Figure 4-40.

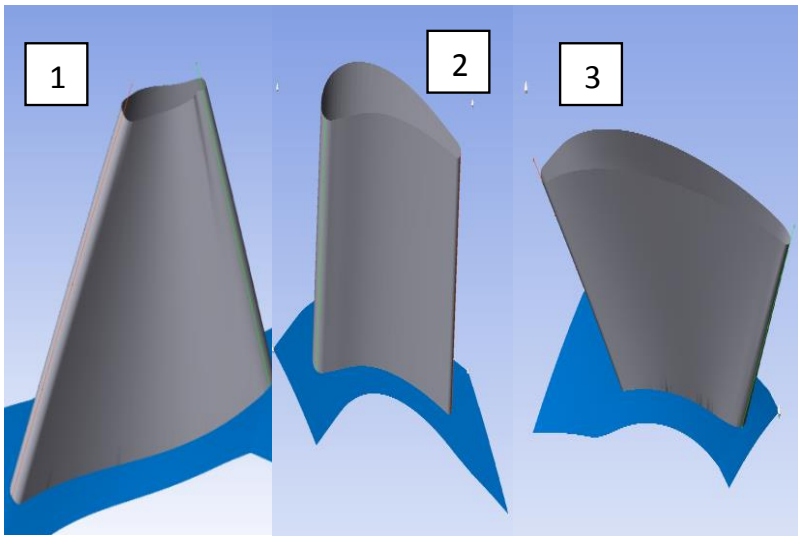

Figure 4-39 Blade sweep configuration: 1 negative backward sweep, 2 straight and 3 positive forward sweep [7]

With this configuration, the mid-span section will be loaded while the shroud and hub sections are unloaded which will decrease the secondary losses at the end walls [7]. However, the mid-span losses will rise with this configuration, which requires a compromise between the two loss locations [187].

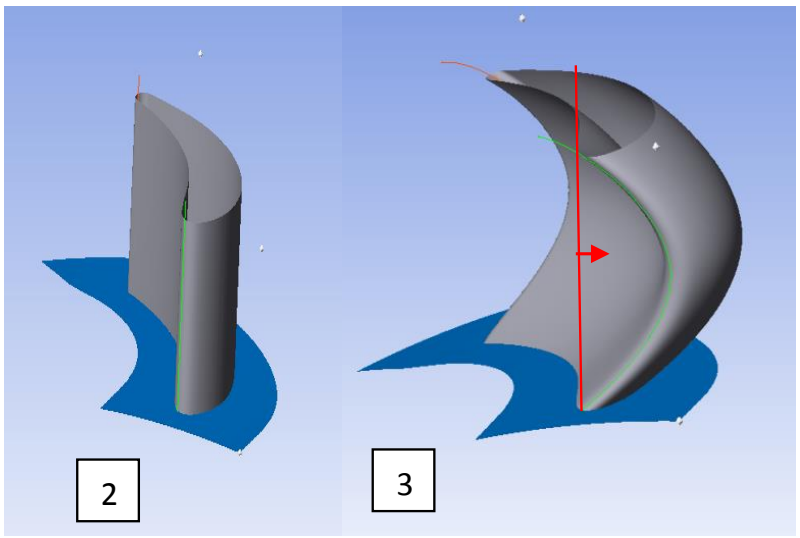

Figure 4-40 Blade bow configuration: 2 straight and 3 bow [7]

4.9 Multi-stage axial turbine

To improve the small-scale cryogenic cycle performance, the design of the small-scale turbine needs to be developed for higher expansion ratios. Increasing expansion ratio for the single stage has limitation such as increasing the possibility of supersonic flow which causes shockwave losses through turbine passages; and so also the turbine flow rate can increase with inefficient power extraction [55]. Therefore, the development of a multi-stage turbine can overcome these limitations. In the multi-stage turbine, the flow expands with an accompanying density reduction; and so to avoid unnecessary flow acceleration within the next forward stage the annular area needs to be increased [188]. Increasing the annular area leads to the radial offset between rotor stages, which in turn reduces the stage loading coefficient (ψ), and in addition, diffusing the flow will decrease the flow coefficient (φ). Reducing these two coefficients will enhance the turbine performance according to the Smith turbine diagram [189]. Giving the turbine duct a conical shape can achieve an expansion of the annular area in the stream-wise direction. Selection of the slope angle from the inlet to outlet is important for good turbine design since increasing this angle can increase the turbine reaction; but on the other hand will decrease the Mach number [190]. Figure 4-41 depicts the axial turbine dual stage non-repeated annular area [55]. From the turbine specification the work output ΔW, work coefficient ψ and blade speed U can be specified; therefore the number of stages can be calculated by [108]:

$$N_{stage} \geq \frac{\Delta W}{U^2 \psi} \qquad 4\text{-}84$$

Assuming equal expansion ratios through the turbine stages, the stage expansion ratio can be calculated by [191]:

$$Er_{stage} = Er_{overall}^{\left(\frac{1}{N_{stage}}\right)} \qquad 4\text{-}85$$

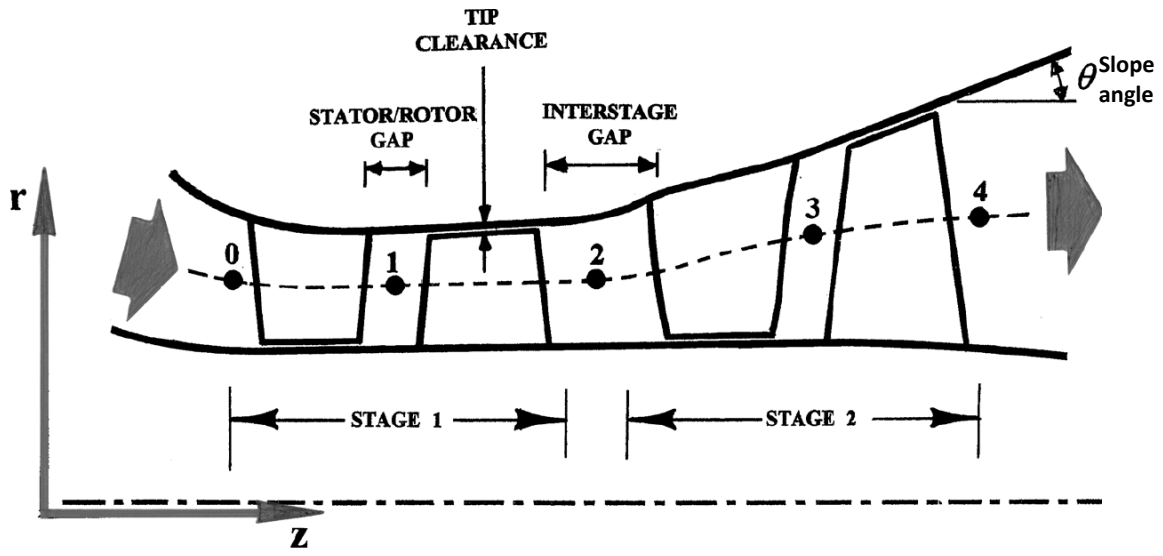

Figure 4-41 Dual stage non repeated annular area axial turbine [192]

As the number of stages increases, the turbine performance improves because the losses of each stage consequently decrease. However, the increase in the turbine number of stages affects the turbine size, weight, and cost and therefor a balance should be made to have an optimum number of stages. Another disadvantage for increasing the number of stage especially with axial cantilever rotor shaft is increasing the torsional and flexing frequencies of the shaft with the danger of resonance and mechanical failure [147]. Figure 4-42 shows the expansion process for a 5 stages axial turbine which works between two pressures limits P1 and P6. The total isentropic specific work which can be harvested from this turbine is:

$$\dot{W}_s = \sum_2^n h_{(n-1)s} - h_{ns} \qquad 4\text{-}86$$

Where n is the number of stages. Similarly the actual specific work can be calculated by

$$\dot{W} = \sum_2^n h_{(n-1)} - h_n \qquad 4\text{-}87$$

For one stage turbine, the isentropic and actual specific work can be calculated by

$$\dot{W}_s = h_1 - h_{6ss} \quad 4\text{-}88$$

$$\dot{W} = h_1 - h_6 \quad 4\text{-}89$$

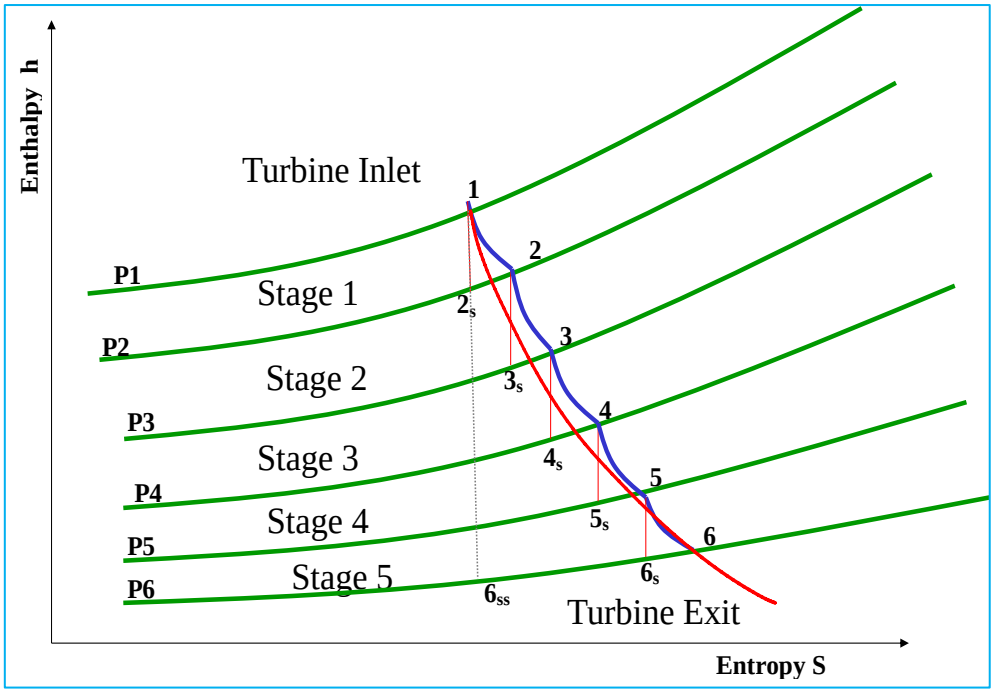

Figure 4-42 Enthalpy-Entropy diagram for 5 stages turbine expansion process

4.10 Summary

In this chapter, the non-dimensional approach is explained and the turbine type selection criterion is clarified for the axial turbine. The one-dimensional preliminary design which uses mean-line method and Glassman approach is explained by clarifying the mathematical model equations in sequence. The losses model and analysis are presented for four types of losses:

profile, secondary, trailing edge, and tip clearance. The mean line preliminary design approach was developed using MATLAB code and this coding procedure was explained in detail and the solution steps were clarified in the flowchart. The preliminary design data was exported to the 3D CFD analysis tool for more detail and accurate evaluation which can be done by ANSYS-CFD commercial packages. The components of ANSYS-CFD for design of an axial turbine i.e. BladeGen, TurboGrid, and CFX-Solver were outlined in detail, also the components of CFX-Solver setup, solution, and results with governing equations were clarified. After 3D CFD aerodynamics analysis was completed, the mechanical structural analysis need was performed to check the design durability before manufacturing. The integration between CFX-Solver and CFD structural analysis in ANSYS workbench project was presented and explained. The turbine good design often results in a trade-off between various objectives and constraints for many significant design parameters. ANSYS workbench DEO was utilized to carry out the 3D optimization task, with the work procedure and steps explained in the flowchart. The novel camber line control point's parameterization method developed in this work and implemented with just six parameters for optimizing the blade geometry was presented. The components of DEO: DOE, RSM, and optimization were shown with their compatibility with the small axial turbine case. The developed axial turbine advanced blade configurations (sweep, twist, lean, and bow) were explained in detail. To enhance the small scale cryogenic cycle output, the small turbine design needs to be improved through working with higher expansion ratios which needed a multi-stage turbine to handle this operating condition. The multi-stage advantages and disadvantages with design specification were presented in detail.

CHAPTER 5

TEST RIG FACILITY FOR AXIAL TURBINES

5.1 Introduction

This chapter outlines the CAD modelling, manufacturing method and test rig facilities for three axial turbines with different blade heights (4mm, 6mm, and 8mm) and describes, in some detail, the components and instruments used. This laboratory work aims to show an experimental parametric study map for different blade heights on small-scale turbine performance. Also, the blade height (4mm) is used for the first time in a small-scale experimental work to contribute and to fill the lack of knowledge of the minimum blade height that could be manufactured and used. The importance of blade height design parameter can be highlighted by affecting passage annular area which in turn affects turbine flowrate and expansion ratio. The other objective of this experimental work is to measure, evaluate and compare the performance of these axial turbines where the generated results used to validate the turbine design methodology are as outlined in the previous chapters.

5.2 Solid Works modeling and 3D printing manufacturing

The axial turbine rotors and stators were developed through extensive CFD modelling using ANSYS BladeGen module and then exported to SolidWorks CAD package as parasolid files. The complementary parts such as turbine duct or casing, shafts and bearing supports were

designed using SoildsWorks software to be consistent with the rotor and stator configurations. Figure 5-1 shows the SoildsWorks Isometric 3D view for the complete axial turbine assembly and Figure 5-2 shows its cross-sectional view. The outer casing was designed in many pieces to facilitate the manufacturing task and assembly process as shown in the exploded assembly drawing of Figure 5-3, (for more details see Appendix B). The ball bearings SKF brand, 61901ZZ model, deep groove with two steel shields were selected because they are suitable for high rotational speeds (40000 RPM) and can accommodate axial and radial loads in both directions. These kinds of bearings need little maintenance. Every two flanges within the casing were made with grooves to accommodate the Nitril O-rings for appropriate sealing purpose according to Polymax manufacturer dimensions standard. The (ISO 286-2) ISO tolerances standard for shafts and holes has been adopted in this design.

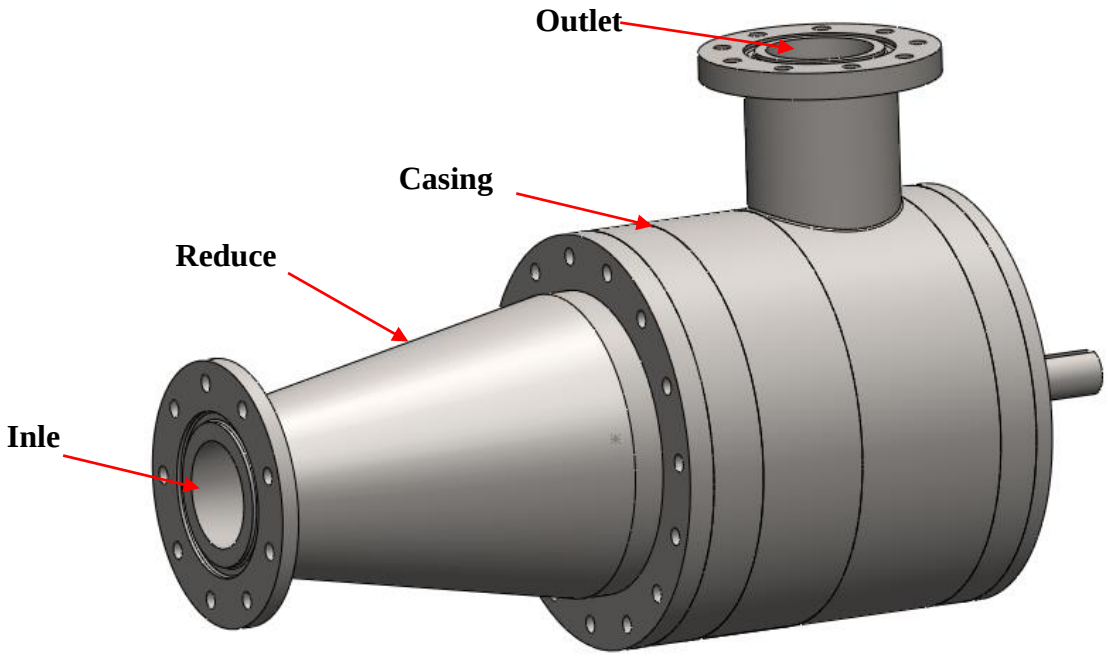

Figure 5-1 Isometric 3D view for a complete axial turbine assembly

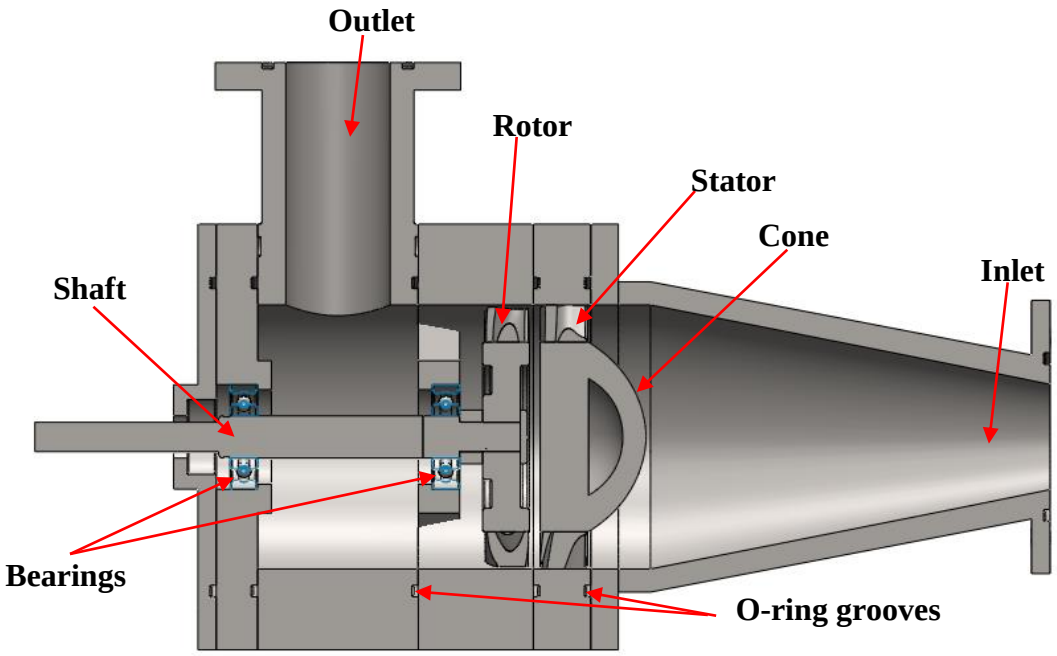

Figure 5-2 Sectional view for a complete axial turbine assembly

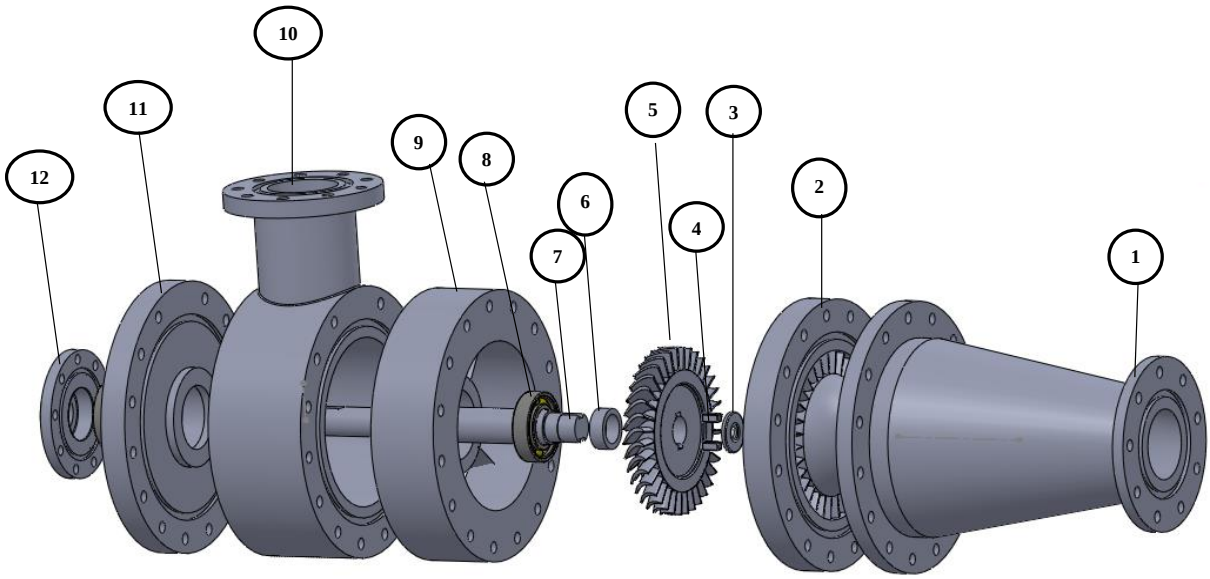

Figure 5-3 Assembly exploded schematic: 1- Reducer 2- Stator 3Disc 4- shaft key 5- Rotor 6- Spacer 7- Shaft 8- Bearings 9- Rotor case 10- Outlet ring 11- closing end 12- shaft sealing house.

The 3D printing process is a method for making 3D parts using the 3D solid surface drawing, also known as additive layer manufacturing technology, it has been used to manufacture the turbine parts in this work. In this additive printing process controlled by computer software, where the object is created layer by layer, the data for each layer is produced by computer software's slicing algorithm. A two-dimensional layer is made by adding a layer of powder, which follows by ink-jet printing of a binder liquid material to join the new powder layer with the old one. The layering and binding process repeated until the 3D geometry is completely created. Following that is the heat treatment and removing unbound powder from the fabricated parts. This process can produce complex geometries by using less material compared to traditional manufacturing methods such as subtractive methods which cut out most of the material during machining. So this geometrical independence opens the way to both small and complex shapes in some applications such as energy or biomedical. However, this freedom in manufacturing is still restricted by the need to remove support material which is underneath the parts and inside internal cavities. Using the proper material in 3D printing is vital where it needs a compromise between required mechanical properties and the printing process properties. All the axial turbine stage components except the shaft were manufactured using the Object30 Prime 3D printer and RGD525 material at the mechanical workshop, school of physics, University of Birmingham, as shown in Figure 5-4 to Figure 5-9. The central shaft was manufactured from stainless steel to handle the high temperature and stress developed in the contact area between the bearing and the shaft due to rotating balls. Moreover, this will facilitate the connection with torque meter shaft made of stainless steel and handle vibration or torsion that may occur due to high speed or high pressure. This stainless steel shaft is connected to the rotor disc through two rectangular shaft keys to transfer the load. To prevent the shaft from slipping spacer, Washer, and screw are fixed between the shaft and rotor. The test rig piping fitting designed in SolidWorks CAD

package and manufactured by 3D printing from the Vero Blue material as shown in Figure 5-9.

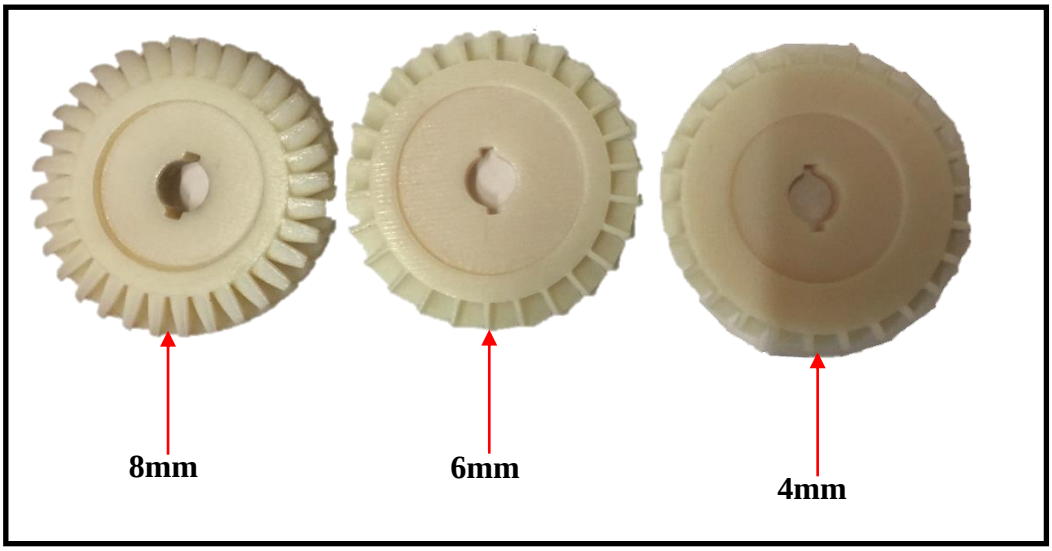

Figure 5-4 Pictures for manufactured rotors with blades heights (4mm, 6mm, and 8mm).

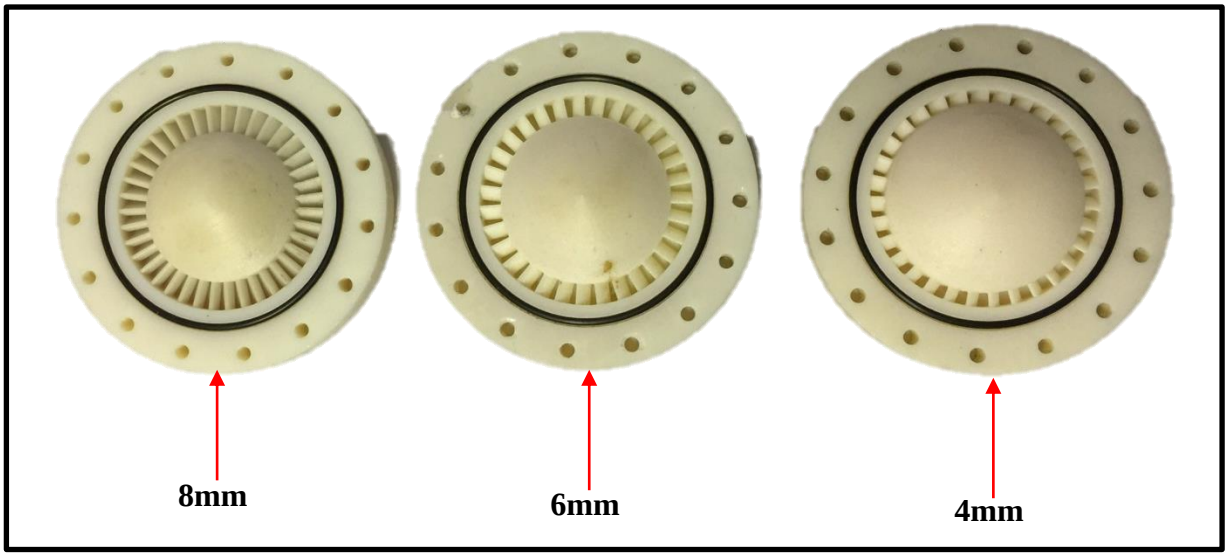

Figure 5-5 Pictures of manufactured stators with blades heights (4mm, 6mm, and 8mm)

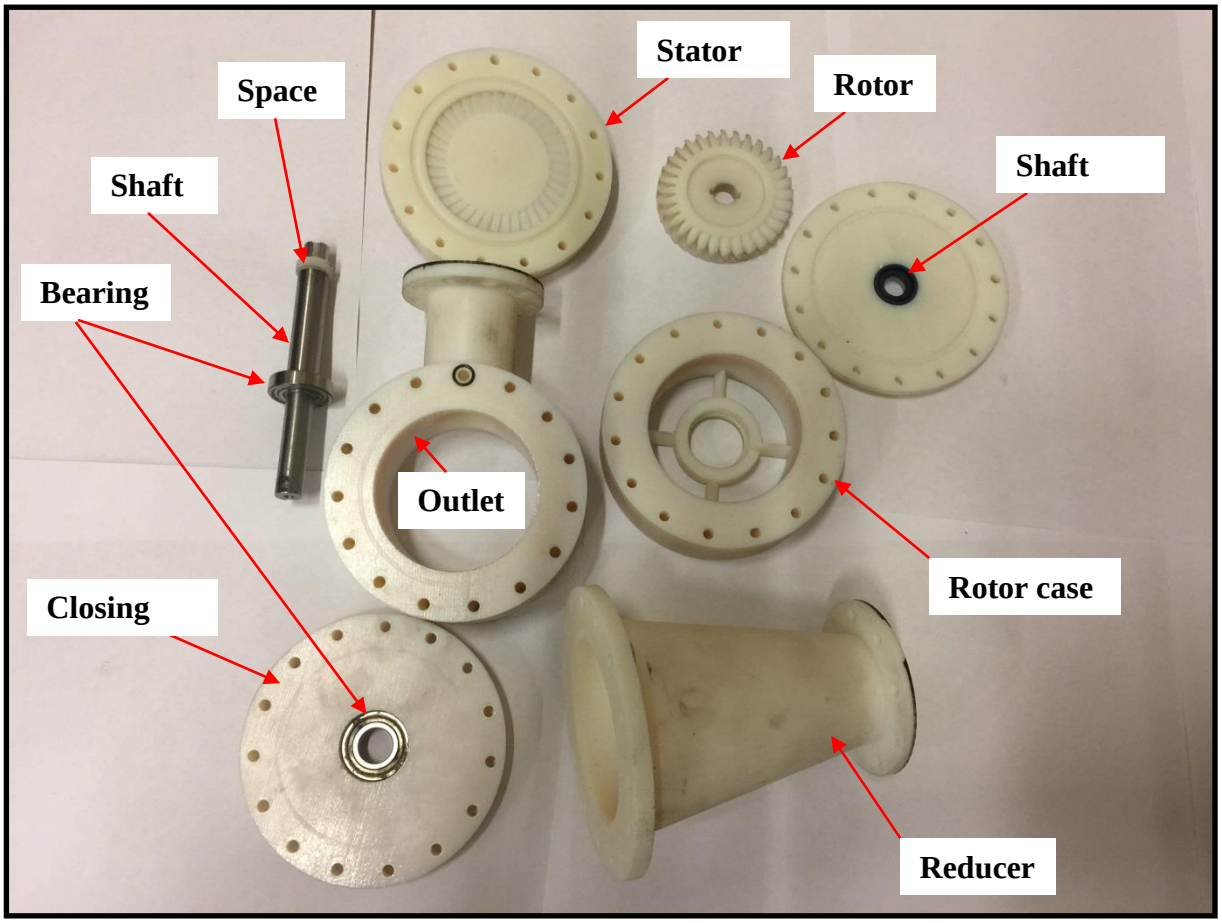

Figure 5-6 Pictures of manufactured all turbine parts

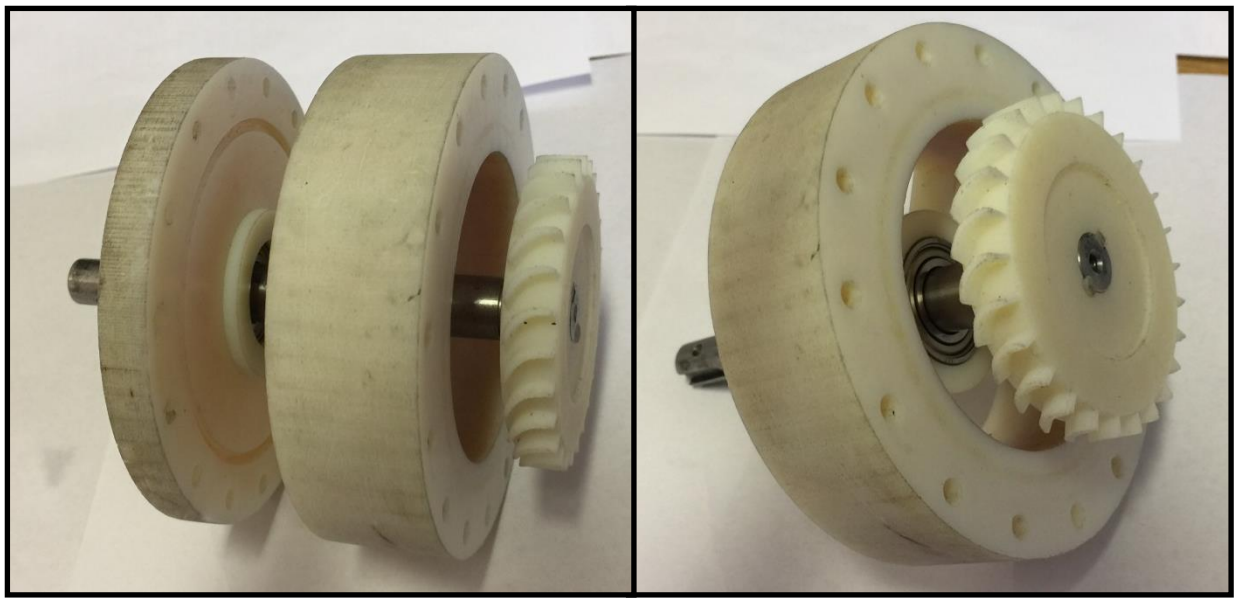

Figure 5-7 Pictures of manufactured rotors assembly with the shaft, bearing, rotor case and a closing end.

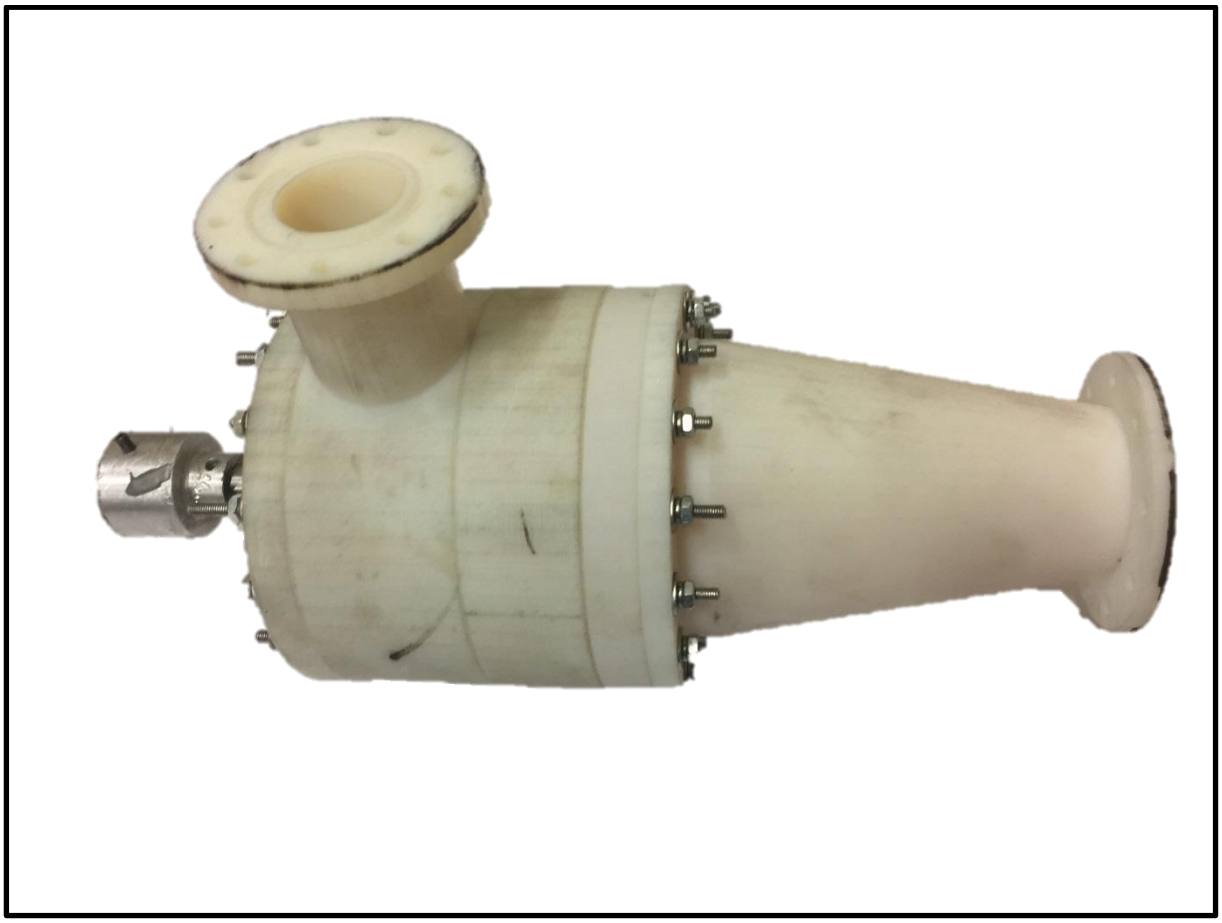

Figure 5-8 Pictures of the manufactured assembled small-scale turbine.

Figure 5-9 Pictures of the manufactured test rig pipe fitting.

The printing material RGD 525 PolyJet was selected due to its high dimensional stability, good temperature limits, stress durability, and cost effectiveness. Table 5-1 summarizes the mechanical properties for this material.

Table 5-1 RGD 525 PolyJet mechanical properties

Mechanical properties	Unit	Value or range
Tensile strength	MPa	70-80
Elongation at break	%	10-25
Modulus of elasticity	MPa	3200-3500
Flexural Strength	MPa	110-130
Heat Deflection Temperature , at pressure 0.45MPa	°C	63-67
Heat Deflection Temperature , at pressure 0.45MPa after thermal treatment	°C	75-80
Polymerized density	g/cm3	1.17-1.18

In order to ensure suitable functionality of this material before starting production, tensile strain tests were carried on a RGD525 specimen using a tensile test machine as shown in Figure 5-10. The dumbbell RGD525 specimen was designed according to ASTM D638 standard as shown in Figure 5-11. The test procedure was carried out according to the same standard where the specimen was extended by applying displacement rate ranging from 0.05-20 inch per min and axial load of 5 KN. Figure 5-12 shows the results from this tensile strain test with maximum tensile stress of 58.63 MPa.

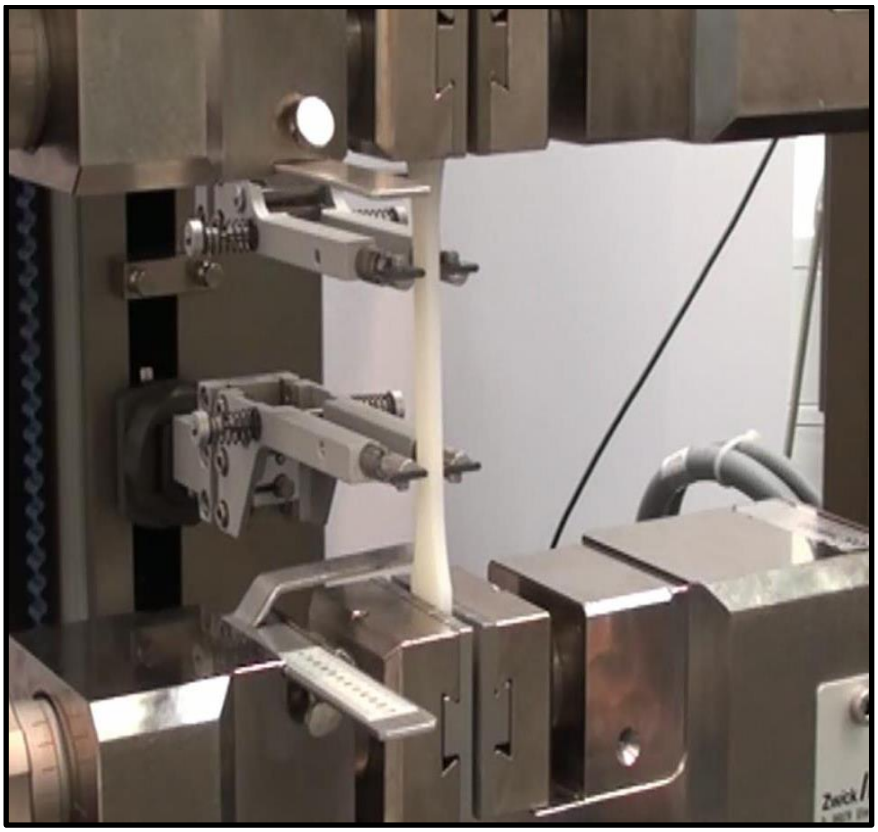

Figure 5-10 Tensile test machine

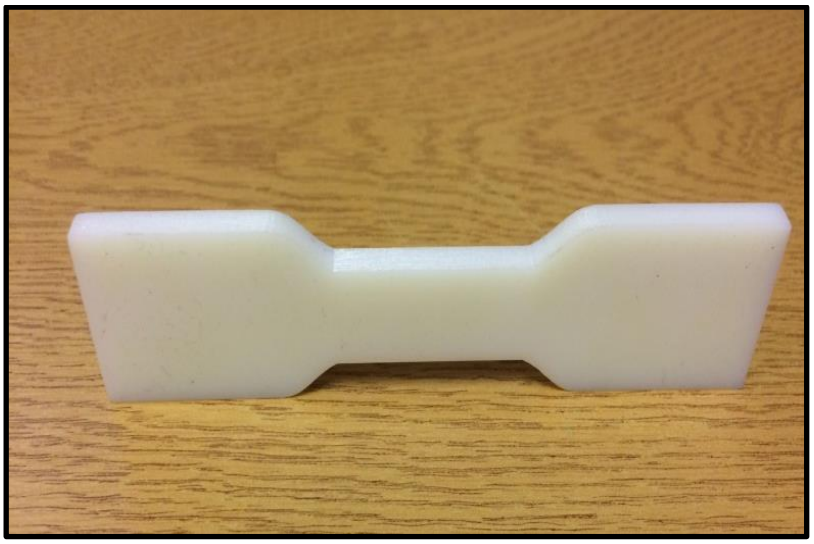

Figure 5-11 Dumbbell RGD525 specimen picture

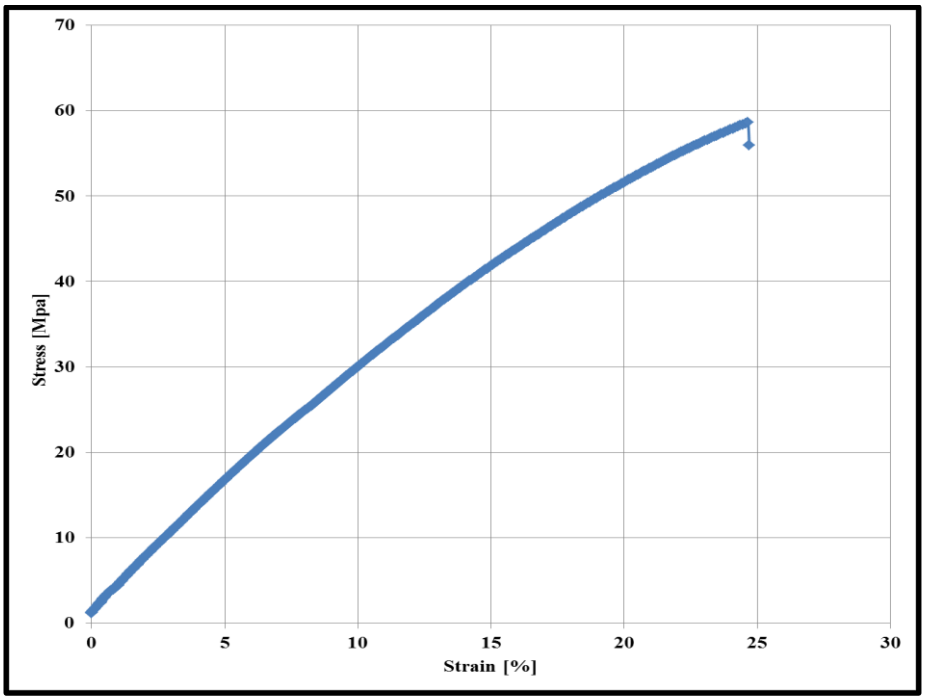

Figure 5-12 Printing material (RGD 525 PolyJet) experimental tensile strain curve

5.3 Description of experimental facility

Figure 5-13 illustrates a schematic diagram for the experimental facility which consists of an air compressor, a storage air tank, pressure gauges, a filter, a pressure regulator, control valves, a flow meter, pressure transducers, thermocouples, an axial turbine, a torque meter and data acquisition instruments. The air compressor produces pressure inside the storage air tank at 7.2 bar while the storage air tank assists the air compressor for not building up the pressure from environmental pressure next time. The pressurized air is passed to the pressure regulator and filters to adjust the required inlet pressure and clean the air from dust and condensate water drops. The pressure gauge is fitted after to measure the inlet pressure. The air is then passed by a control valve to regulate the flow rate which is measured using a flow meter. To increase inlet air temperature part of the piping system after the flow meter the pipe is wrapped with two heater tapes of 500W rating. These heaters are connected with a control box to control the tempreature which is measured by thermocouple connected after the

heaters. The air static pressure, the total temperature and pressure are all measured in the turbine inlet duct by using thermocouple and pitot-static tube which is connected to two pressure transducers. The air accelerates through the stator vanes to drive the rotor and shaft and exits by an outlet duct where the thermocouple and pressure transducer are positioned for temperature and static pressure measurements. To record the data the computer is connected to data loggers which are connected with the pressure transducers and thermocouples. The rotor shaft is connected by coupling with the torque meter shaft to measure torque, speed and power output from the turbine while the other shaft end of the torque-meter is linked by coupling to DC generator brushless motor shaft, for applying the load on the turbine shaft. In order to record the data out from torque meter, the computer is connected with it by datum universal interface unit. The turbine load is varied by a variable resistance which is connected electrically with the DC generator. Figure 5-14 shows the constructed small-scale axial turbine test rig facility with all components and instrumentations.

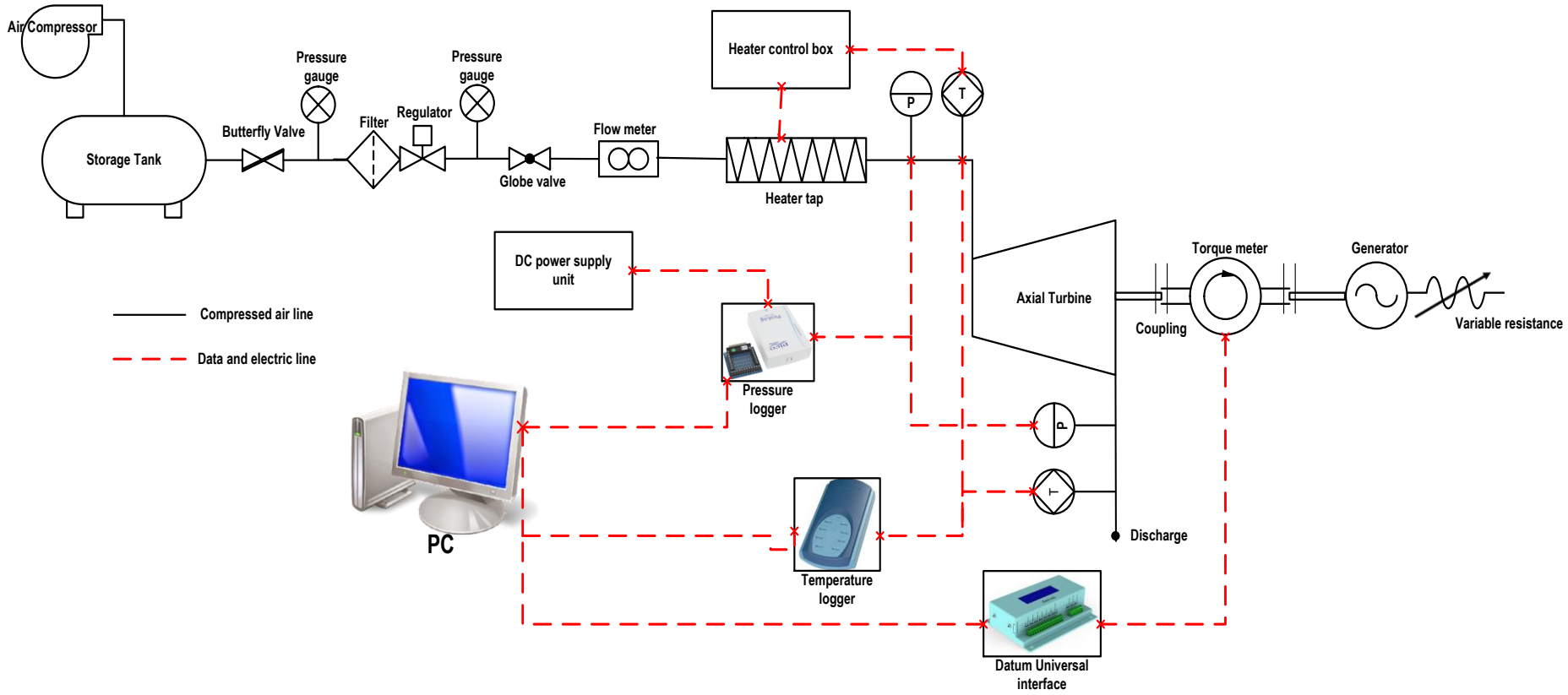

Figure 5-13 schematic diagram of compressed air open cycle test rig with axial turbine

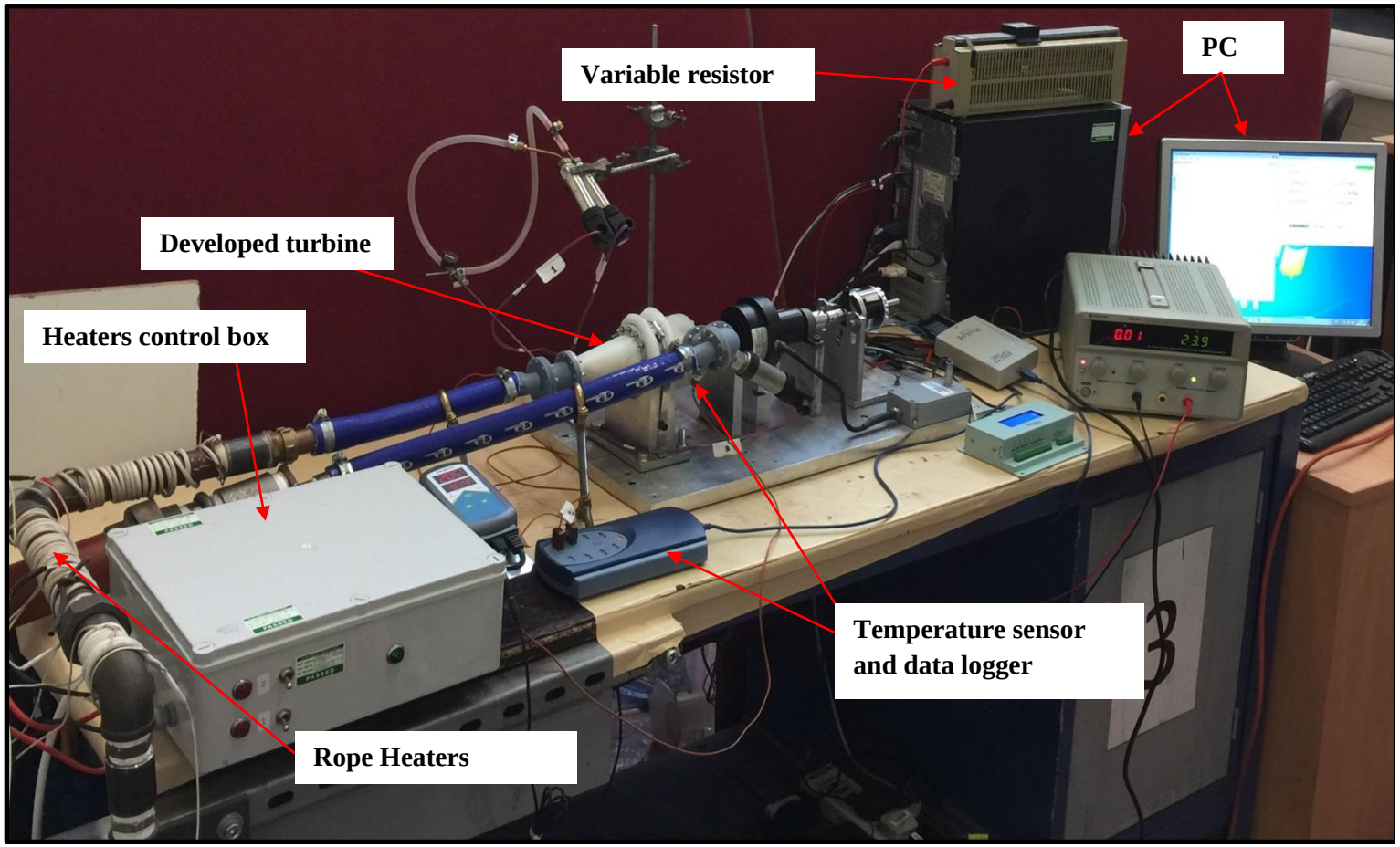

Figure 5-14 pictures of test rig and equipment's

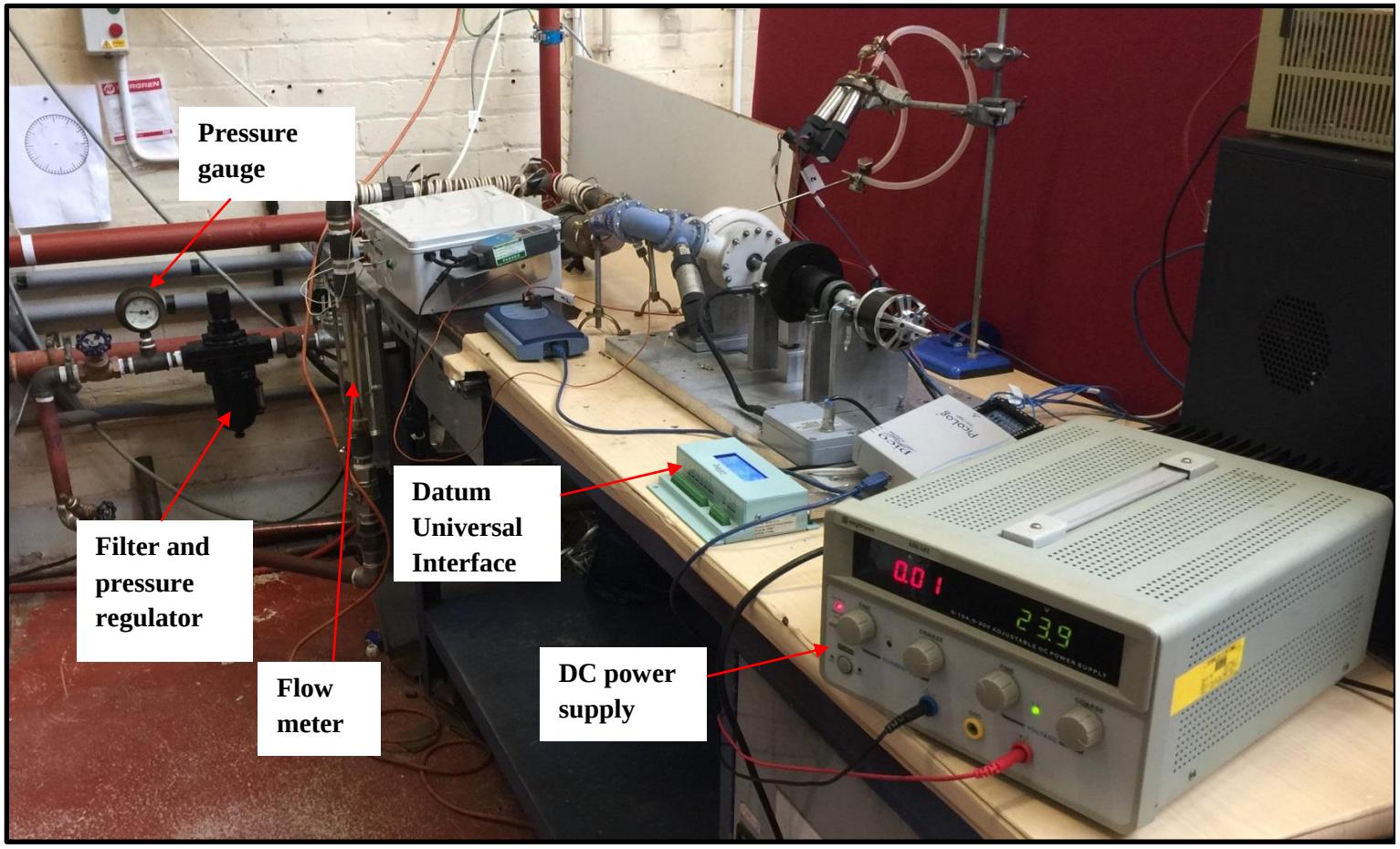
Pressure gauge
Filter and pressure regulator
Flow meter
Datum Universal Interface
DC power supply

(continue)

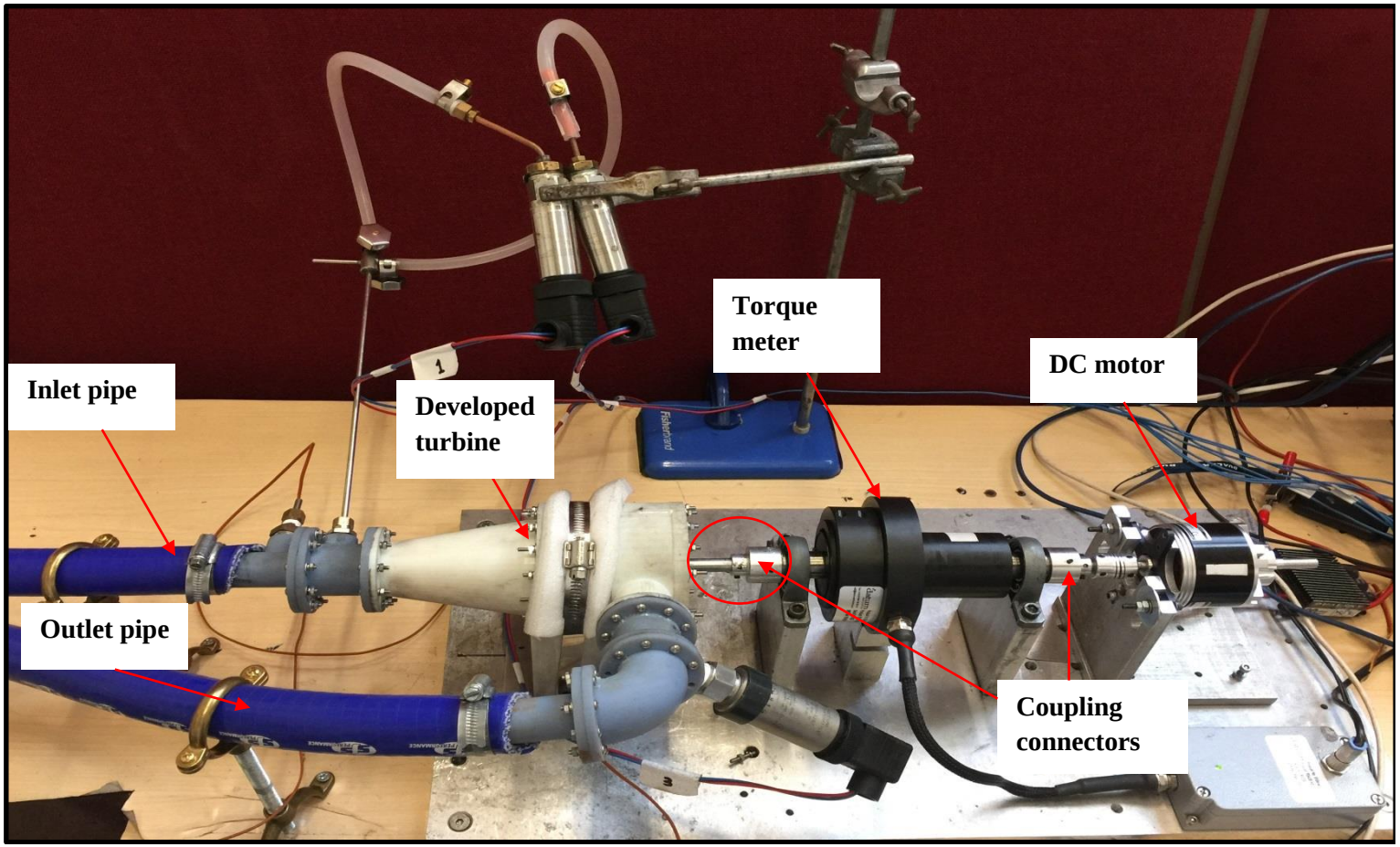
Inlet pipe
Developed turbine
Torque meter
DC motor
Outlet pipe
Coupling connectors

(continue)

5.4 Measuring Instruments

To evaluate turbine performance under various operating conditions different types of measuring instruments are used such as thermocouples, pressure transducers, a flow meter and a torque meter.

5.4.1 Thermocouples

The thermocouples are utilized to measure the air temperatures at the turbine entry and outlet to evaluate the turbine efficiency performance. All thermocouples used in the test rig are Omega T-type TJC100-CPSS-M050G-150 probe tip type. The probe tip is grounded and the sheath material is stainless steel with diameter 0.5mm, length of 150mm, while the temperature range according to manufacturer is (-200°C to 350°C) and standard limits of error 0.75%. Figure 5-15 shows the connection of the thermocouples with the test rig and data logger.

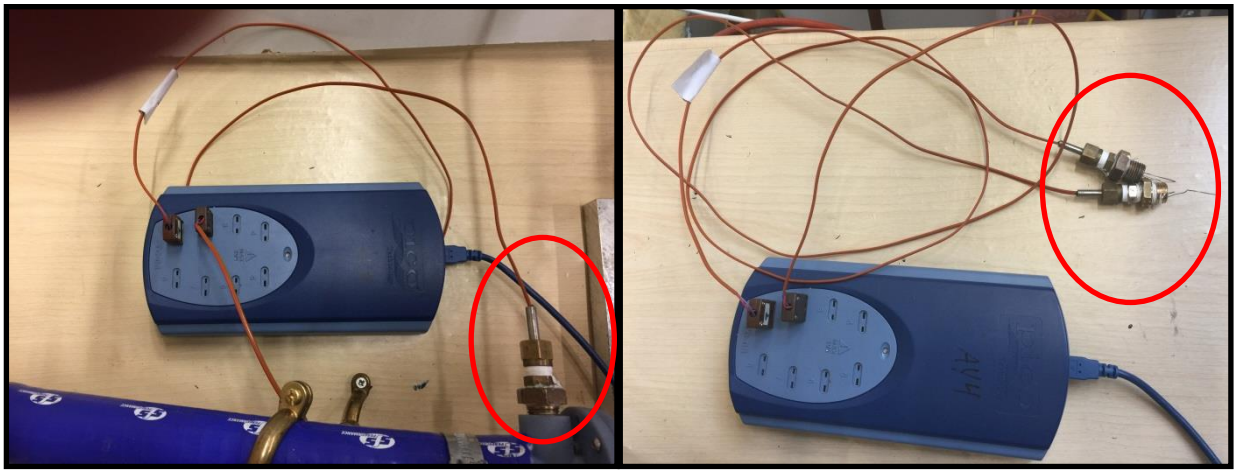

Figure 5-15 thermocouples connected with test rig and data logger

5.4.2 Pitot tube and pressure transducers

The turbine duct was instrumented by Pitot tube type-L ellipsoidal head which has two outlets to measure the total pressure of the moving fluid in the duct, with dynamic pressure deducted to measure the static pressure. Each outlet port is connected with Druck ATEX Gauge Pressure Sensor, 10bar Max Pressure Reading, 7 to 28 Volts to measure the total and static pressure at the turbine entry. The turbine outlet duct is instrumented with the same pressure transducer type to measure the static pressure at the outlet. The pressure sensors use silicon technology and low current output range 4-20 mA with an error range of ±0.04% according to the manufacturer's specifications. All transducers were connected with DC power supply and multi-channel voltage data loggers, as shown in Figure 5-16. The pressure transducers electrical circuit is fed with a voltage of 24V and DC current of 0.005A from a DC power supply unit. Figure 5-17 shows the Pitot tube before and after being connected with test rig and the pressure transducers connected with Pitot tube.

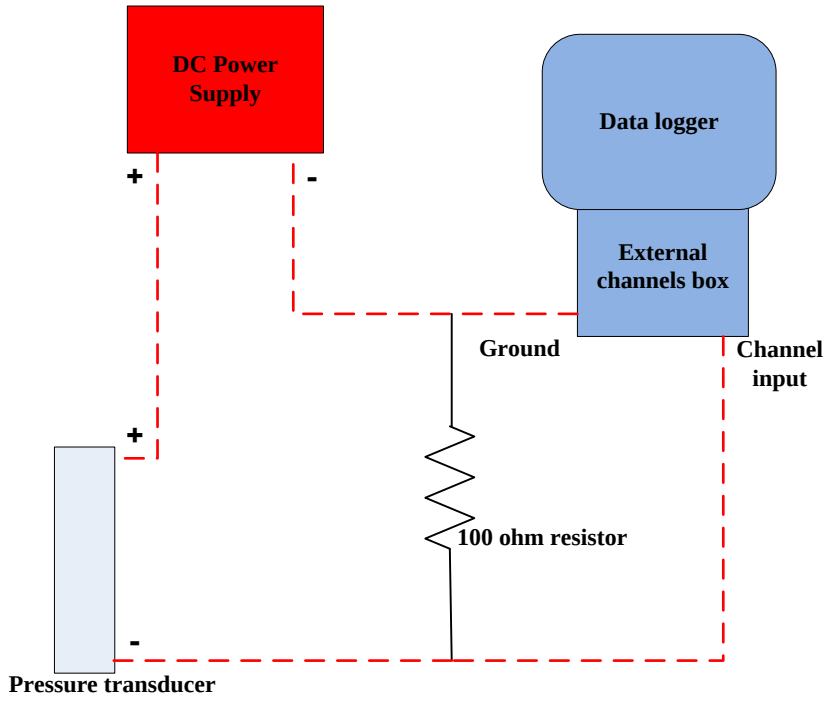

Figure 5-16 pressure transducer electric circuit connection diagram

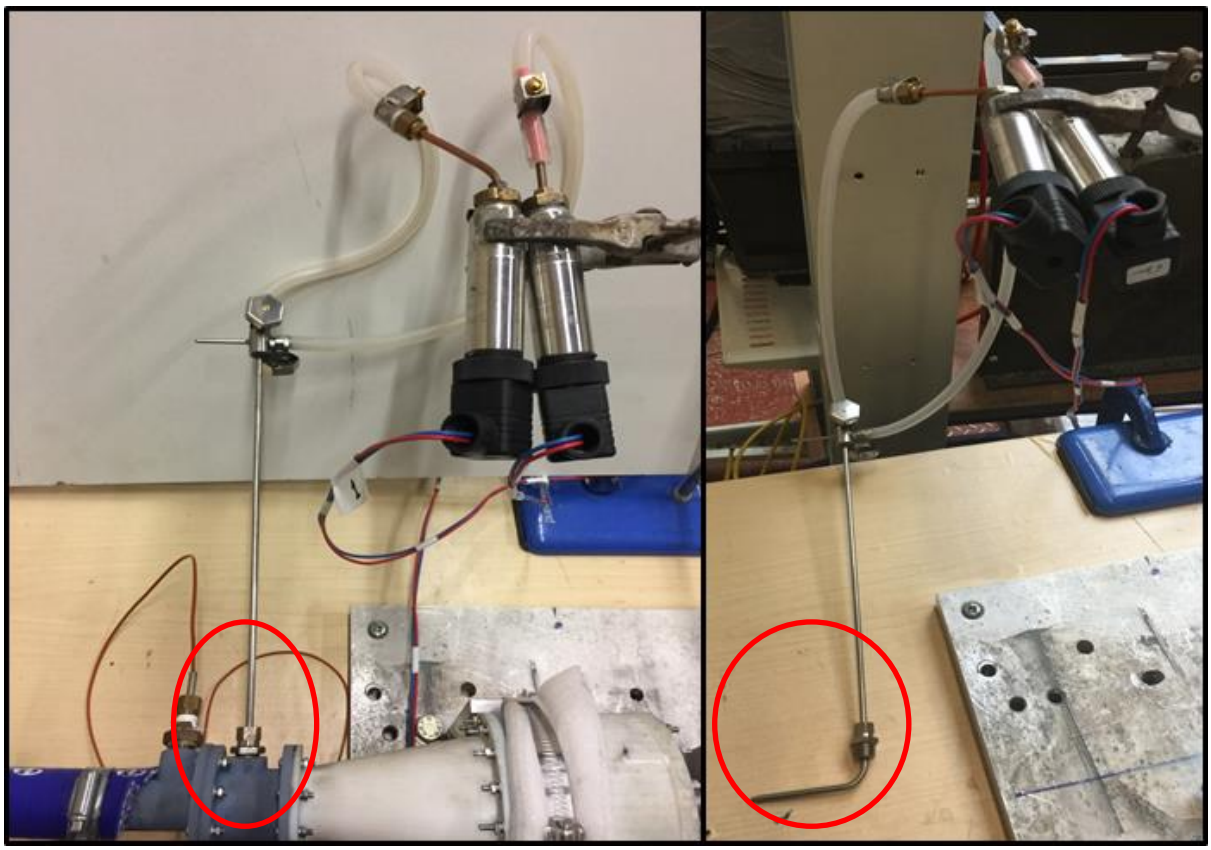

Figure 5-17 Pitot tube connected with pressure tranducers and test rig

5.4.3 In-line flow meter

A standard precision-machined acrylic flow meter with a variable area rotameter, shown in Figure 5-18 and Figure 5-19, was utilized to measure the volumetric flow rate of the air at turbine inlet. The flow meter is series FR5000-I, manufactured by KI key instrument with an operation range from 400 to 4000 litre per minutes and full scale error percentage of ±2% according to the manufacturer's specification.

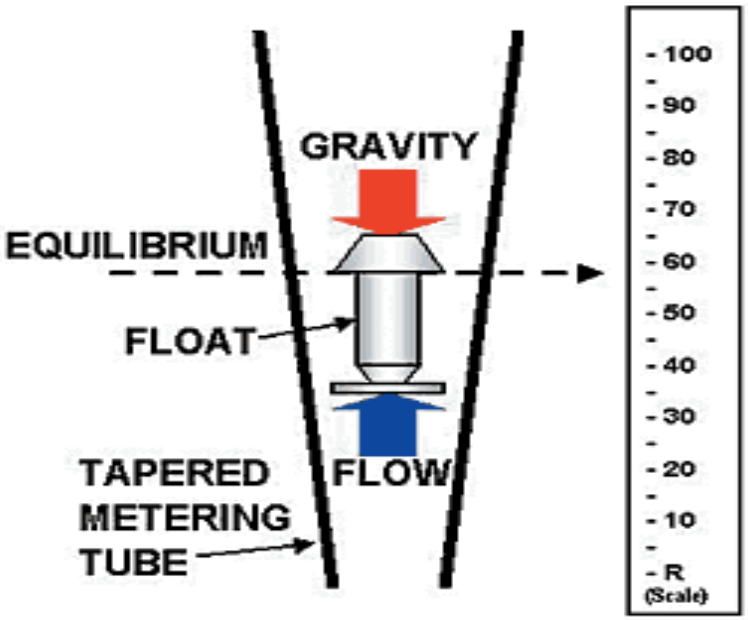

Figure 5-18 Flow meter operating principle

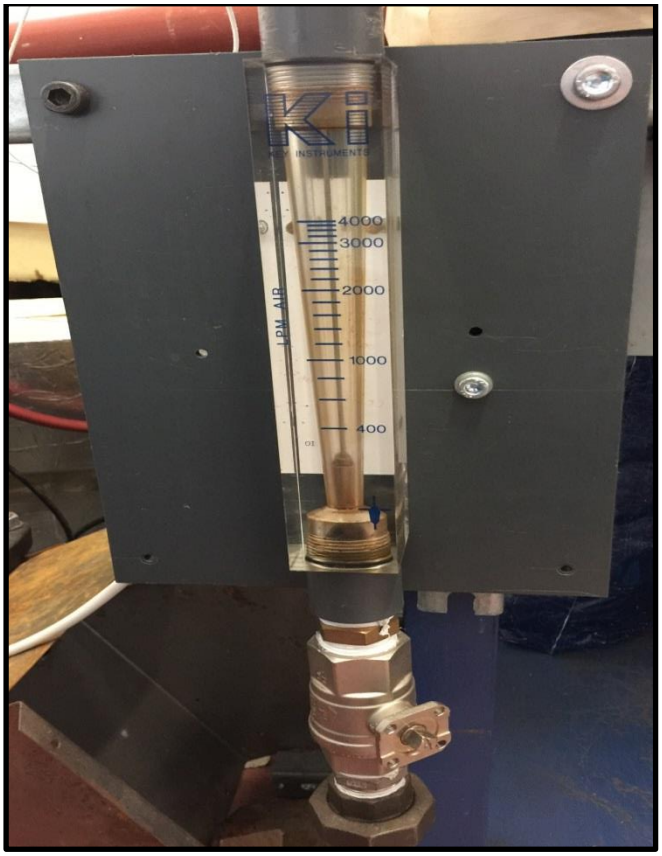

Figure 5-19 picture of flow meter connected with the supply air line

5.4.4 Rotating Torque meter

The in-line rotating torque meter series RS425-S1-HS, manufactured by Datum electronics with operation ranges, rotational speed (0-16000 RPM) and torque range (0-10Nm), was used in this work as shown in Figure 5-20 and Figure 5-21. The torque transducer shaft was made to fit in line with the turbine shaft by using standard keyway shaft and couplings fitting to measure the power output, torque and rotational speed. The torque transducer utilizes the strain gauge shaft and a set of rotating on-shaft conditioning electronics for reliable and accurate measurement. The data is then sent to the non-rotating part of the system or an electronic module to provide highly accurate measurement solution. This module was connected with the Datum Universal Interface (DUI), which was connected with the PC to record the measurement using datum data logging PC software. The torque meter system is designed with sampling rate of 100 samples per second and full scale accuracy percentage of ±0.1%. In addition its non-contact data transmission configuration gives a non-restricted movement and has no transducer tear or wear. The torque meter calibration according to manufacturer are 1.2597 mV/V for 10Nm clockwise and -1.2602 mV/V for -10Nm counter clockwise.

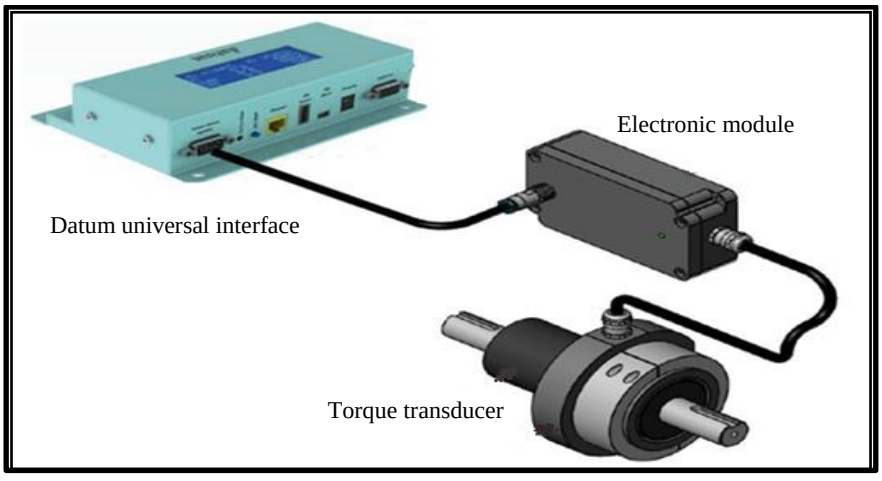

Figure 5-20 Torque meter assembly diagram

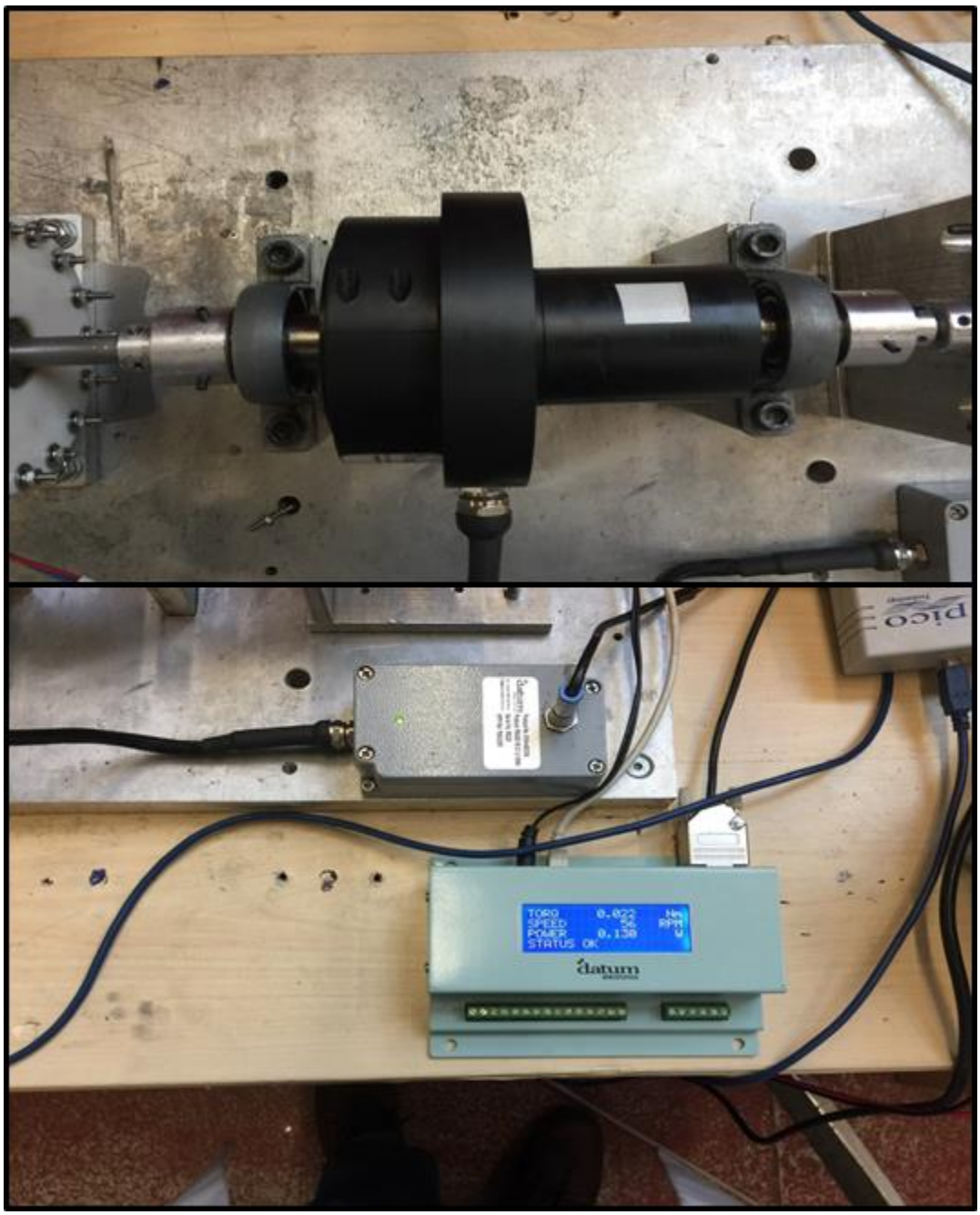

Figure 5-21 picture of torque meter connected with turbine and other facilities

5.4.5 Data acquiring devices

The measuring sensors are paired to the data logger devices which are linked to the PC for display and record acquiring data through logger PC software. The thermocouples are connected with data logger Pico TC-8, which is connected to the laptop or desktop PC without the need for a power supply. This data logger handles 8 thermocouple input channels simultaneously. The pressure sensors are connected with the voltage input general purpose data logger Pico 1012, which has an external terminal board, to screw wire terminals without soldering and fit the resistors to extend and offset the logger data ranges. The temperature and pressure data logger devices are clarified in Figure 5-22. Datum universal interface is connected to the torque-meter to record torque, speed and power produced by the turbine. This device provides all kinds of analogue interfaces and is fully compatible with most transducers type.

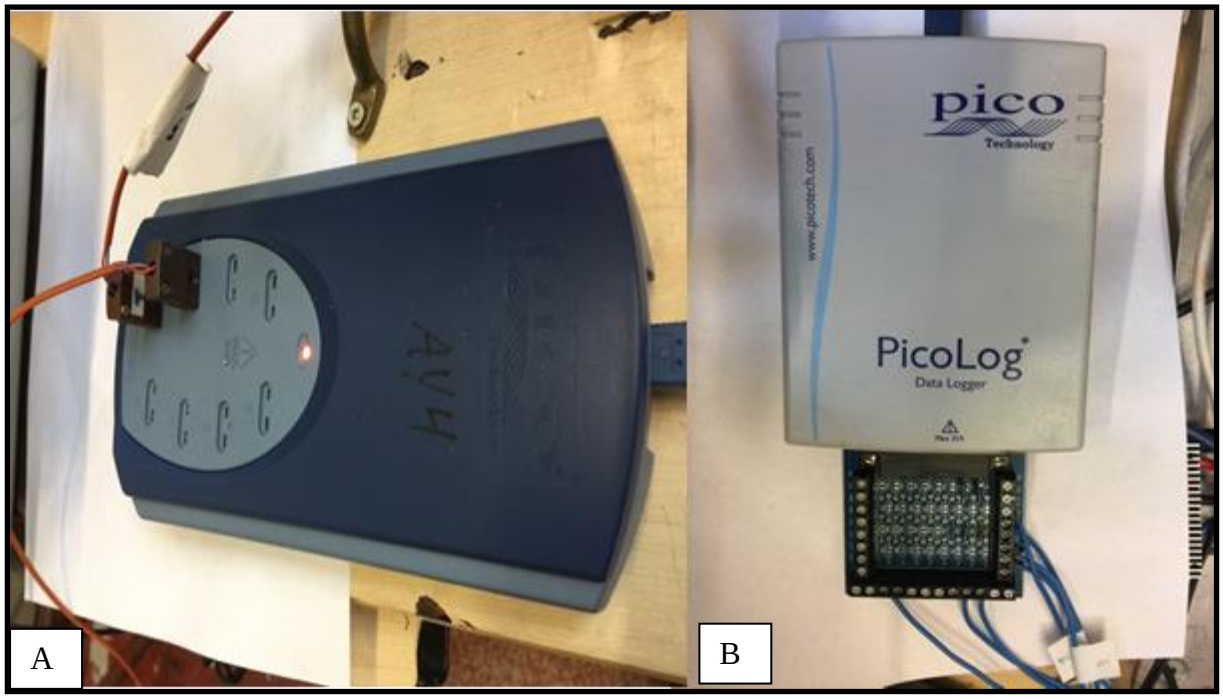

Figure 5-22 picture of (A) Pico TC-8 and (B) Pico 1012 data logger

5.5 Calibration of measuring instruments

The test rig instruments used for pressures and temperature measurements were calibrated before testing to ensure their accuracy and stability during test operation. The calibration was completed by comparing the instrument data against standard instrument data under various operating conditions. The calibration results created relationships between measured values and standard instrument values which make the measured values more accurate.

5.5.1 Pressure sensors calibration

The hydraulic pressure comparator is used in the calibration of the pressure transducer against a certified standard pressure gauge. The pressure in the pressure comparator was increased to the required value by using a rotating screwed shaft while pressure transducer and standard pressure gauge are connected on both sides as shown in Figure 5-23 with each standard pressure gauge value recorded against voltage reading from the pressure transducer. Figure 5-24 illustrates the calibration curve of one of the pressure sensors and the relationship between the standard pressure gauge values and the pressure transducer values.

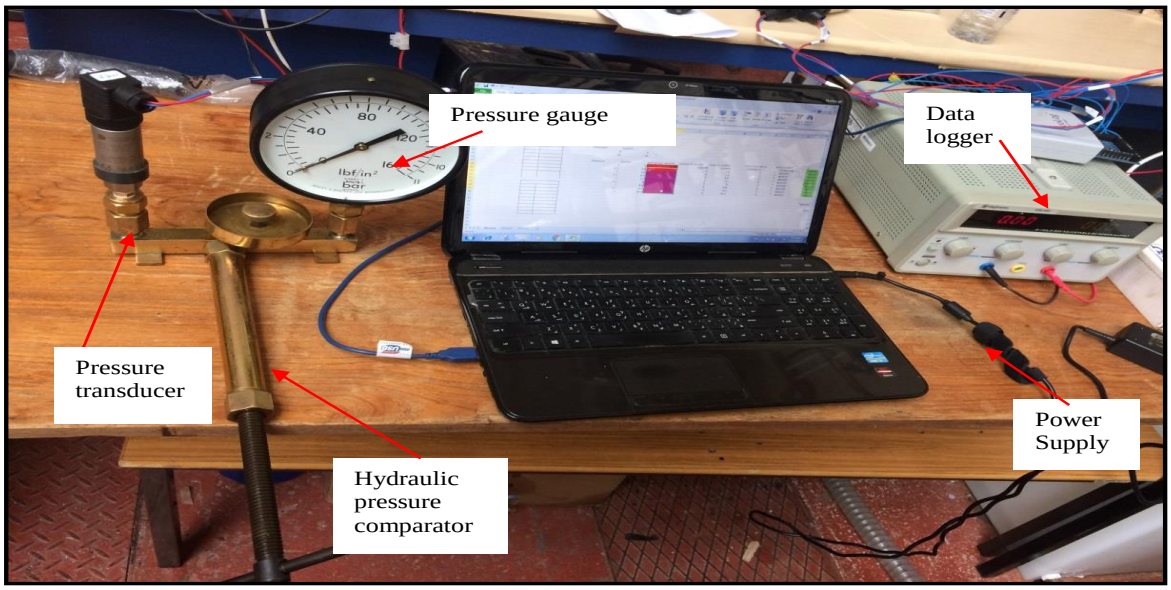

Figure 5-23 instruments for pressure sensor calibration

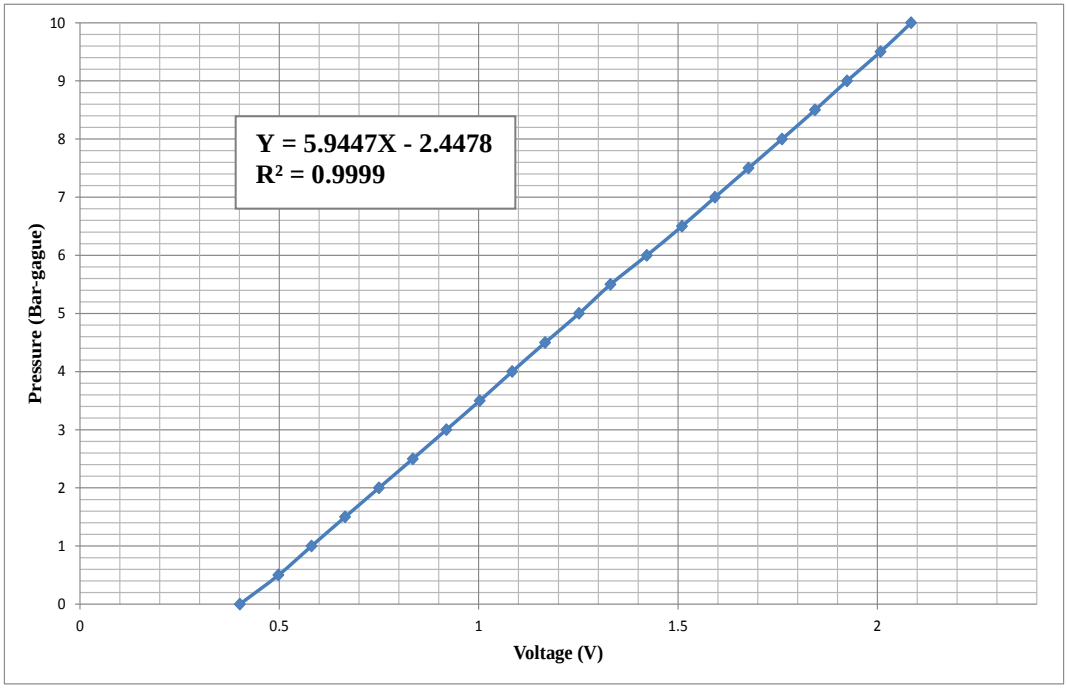

Figure 5-24 Pressure Sensor (GE-PTX5072) calibration curve

5.5.2 Temperature sensors (Thermocouples) calibration

The thermocouple probes TMQSS-IM050-150, T- Type were used to measure the inlet and outlet air temperatures; they have fine sheath diameter 0.5 mm, 150 mm length, stainless steel material 316SS and 310SS, and the sheath can be formed or bent as required. The thermocouples are calibrated against standard laboratory thermometer Fisher brand using electro-mantle and heat resistant glass flask as shown in the Figure 5-25. The glass flask was filled with water, the thermocouples and thermometer immersed in the water at the same level. The water temperature was controlled by the electro-mantle thermostat which controlled the heater. The thermocouples calibration method starts with adjusting the water temperature at a specific temperature. The thermocouples were connected to the Pico TC-08 data logger to collect and record the readings by the PC, the readings were recorded after about 5 minutes in order to reach steady state condition. The water temperature is increased

to a new value by the thermostat then the procedure is repeated. The calibration curve of one of the T-Type thermocouples is presented in the Figure 5-26.

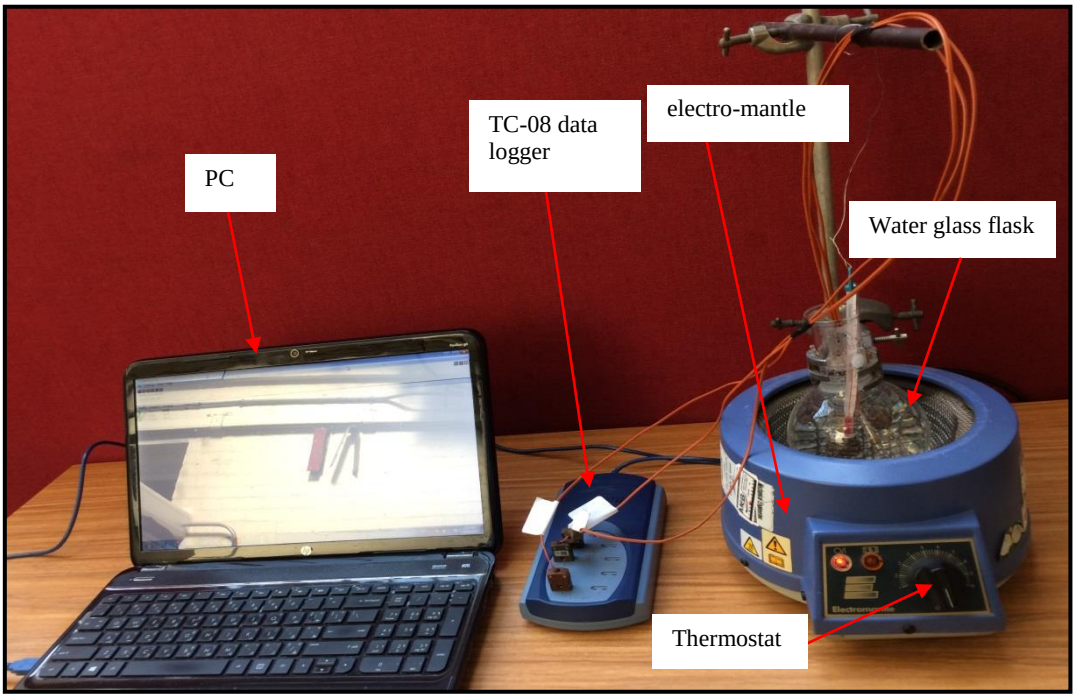

Figure 5-25 Apparatus of the thermocouples calibration process

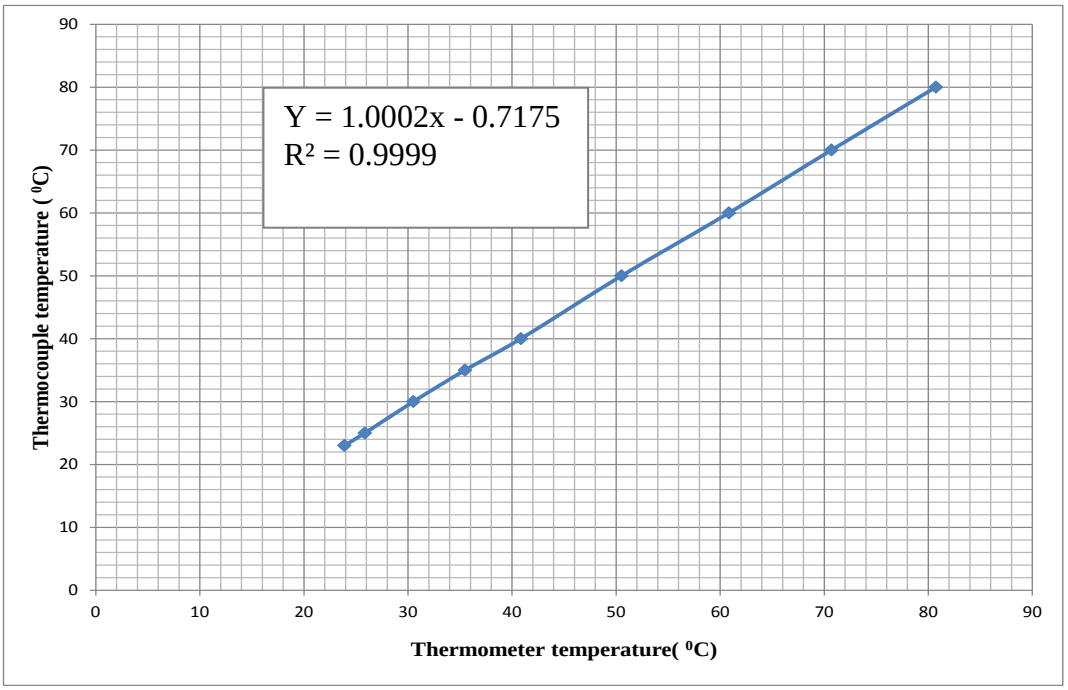

Figure 5-26 Thermocouple-1calibration curve

5.6 Uncertainty and accuracy of measurements

The uncertainty analysis determines the accuracy which should be expected with experimental results. The experiment is directed to study the results, R, as a function of controlled variables, Xi, with the objective that the results stay stable.

$$R = R(X_1 + X_2 + X_3, \dots \dots . + X_n) \quad 5\text{-}1$$

The results' accuracy depends on the system individual parameters accuracy which usually has two types of error. The first type of error called standard error (bias) and the second type is random error or (precision). The sources of errors are non-professional calibration, wrong equipment installation and personal user faults. The standard error could be evaluated by the manufacturer's recommendations or re-calibrate the equipment in the right way [192]. The random errors can be described as fluctuation of results around the true value, this kind of error can be specified statistically by using curve fit uncertainty analysis with 95% confidence level [193]. In the experimental work it is not easy to specify the true measured value and there is a need to define the uncertainty interval (±U). The uncertainty analysis combines both standard uncertainty and random uncertainty by using mean square approach as shown in Figure 5-27 [192].

The standard mean square equation in terms of these two errors can be written in below form

$$U_{total} = \pm\sqrt{(U_{st})^2 + (U_{curve\_fit})^2} \quad 5\text{-}2$$

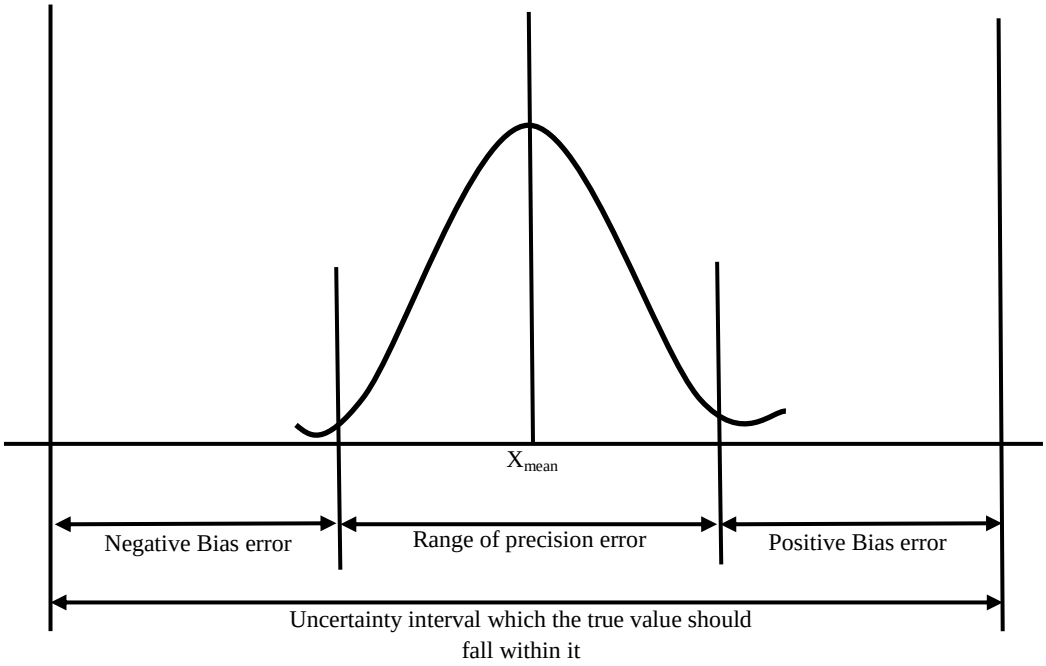

Figure 5-27 The uncertainty for combined bias and precision errors

Where(U_{total}), (U_{st}) and (U_{curve_fit}) are the uncertainties of the total, standard and curve fit, respectively. The curve fit uncertainties can be calculated by:

$$U_{curve\ fit} = t_{n-1,95\%} * \sigma_x \qquad 5\text{-}3$$

Where $t_{n-1,95\%}$ is student distribution coefficient with 95% confidence percentage, n is the number of sampled data, n-1 is the degree of freedom and σ_x is the mean line deviation which is calculated by:

$$\sigma_x = \frac{1}{\sqrt{n}} \sqrt{\frac{\sum_{i=1}^{n}(X_i - \overline{X})^2}{n-1}} \qquad 5\text{-}4$$

5.6.1 Uncertainty Propagation

The errors in the experimental individual variable X_i propagate through equation 5-5 to affect the experimental results R accuracy. As shown in Figure 5-28 the small deviation in the experimental variable δX_i causes deviation in the results δR . Thus, the error in the results can be specified by approximated product of factor $\frac{dR}{dX}$ by the error value δX_i [194]. To calculate the overall experimental results uncertainty generated from individual experimental variable uncertainty the method [194] used is:

$$U_{overall} = \sqrt{\left(\left[\frac{dR}{dX1}\right]U_{X1}\right)^2 + \left(\left[\frac{dR}{dX2}\right]U_{X2}\right)^2 + \cdots + \left(\left[\frac{dR}{dXn}\right]U_{Xn}\right)^2} \qquad 5\text{-}5$$

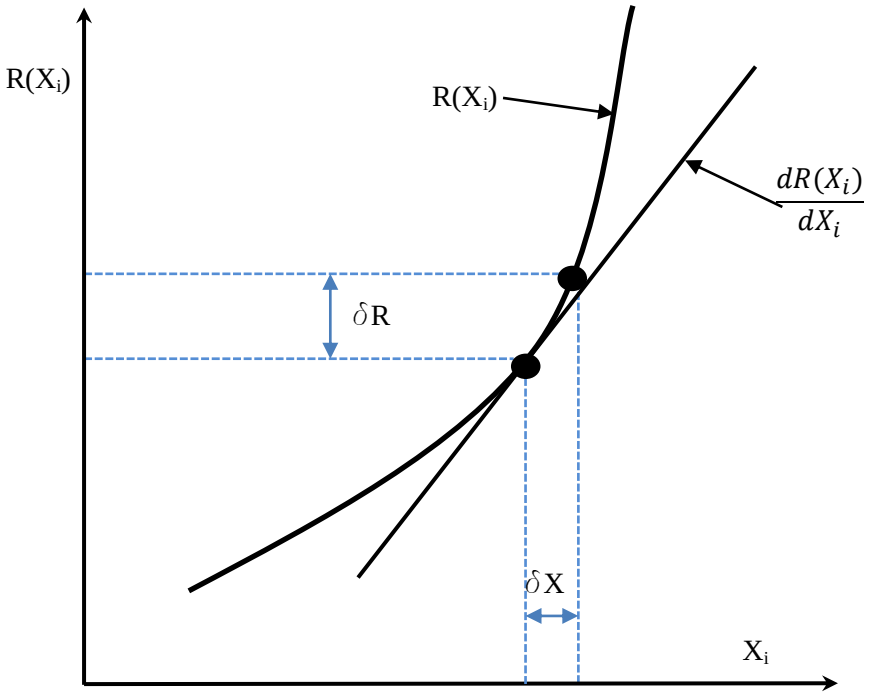

Figure 5-28 experimental variable error propagation into the result

5.6.1.1 Propagation of Uncertainty in thermocouples

The thermocouples used in measuring the turbine inlet and outlet regions air temperatures were T-type and as stated above these thermocouples were calibrated and compared with standard thermometer which has accuracy of ±0.04C. The curves of calibration fit for the thermocouples are showed in Table 5-2. The procedure for uncertainty is clarified in Appendix A.

Table 5-2 Thermocouples uncertainties and curve fit equations

Thermocouple name	Thermocouple region	Thermocouple curve fit formula	Thermocouple uncertainty (˚C)
Thermocouple-1	Stator Inlet	1.0002*T - 0.7175	±0.12
Thermocouple-2	Rotor outlet	1.0029*T - 0.688	±0.18

5.6.1.2 Propagation of Uncertainty in Pressure sensors:

The pitot static tube was instrumented at the stator entry to measure the total and static inlet pressures using two pressure transducers (10 bar) to measure these pressures. At the rotor case outlet another pressure transducer (10 bar) was installed to measure the exit static pressure. The calibration fit curves and uncertainties for the pressure sensors are summarized in Table 5-3 . The procedure for uncertainty is clarified in Appendix A.

Table 5-3 Transducers uncertainties and curve fit equations

Transducer name	Transducer location	Transducer curve fit formula	Transducer uncertainty (bar)
GE-PTX5072-1	Stator Inlet-pitot total port	5.9447*Voltage - 2.4478	±0.0428
GE-PTX5072-2	Stator Inlet-pitot static port	6.5344*Voltage - 2.4694	±0.0441
GE-PTX5072-3	Rotor outlet	6.0157*Voltage - 3.4368	±0.0440

CHAPTER 6

RESULTS OF TURBINE DESIGNS AND DISCUSSION

6.1 Introduction:

This chapter presents detailed results for the developed small-scale axial turbine design utilizing nitrogen as working fluid. These results include comprehensive parametric studies for one dimensional preliminary design, three dimensions CFD design, and the developed three dimensions CFD optimization method with novel parametrisation technique. Moreover, they show the impacts of four axial turbine blade configurations (sweep, twist, lean, and bow) on the turbine performance in terms of efficiency and power output. For high expansion ratio of 3, results from parametric comparison between three turbine configurations: one stage, double stage constant annular area, and double stage non-constant annular area show the importance of double stage non-constant annular area. Finally, the experimental parametric study results from the three small-scale axial turbines with different blade heights (4mm, 6mm, and 8mm) were compared with CFD results for validations and showed that the 8mm blade height configuration produced the highest turbine performance.

6.2 Preliminary Design 1D Mean Line Method Analysis Results:

In this section, the results from one-dimensional mean line method analysis are presented, which method has been explained in chapter 4. These results are the outcome of a parametric study aimed at identifying the best initial turbine geometry for the required operating conditions. Results are generated using MATLAB programming code, which predicts the

turbine performance and the initial geometry according to the input operating conditions shown in Table 6-1. The operating conditions include mass flow rate, inlet total pressure, inlet total temperature, rotational velocity, required power, and turbine mean-diameter. Such parametric study discloses the effect of operating conditions on the turbine geometry design and performance. This parametric study is based on fixing the values of input parameters at default values (Table 6-1) except one. The parameter is then changed and its effects on turbine performance are recorded. The total turbine efficiency has been used as the evaluation parameter for determining the best turbine geometry suitable to the target operating conditions. Figure 6-1 depicts the relationship between the turbine total efficiency and the rotational speed at various power output. It can be noticed from this figure that for each power output there is a rotational speed value that produces maximum total efficiency. The turbine with power output of 5 kW needs rotational speed of 60000 RPM to achieve maximum total efficiency of 87.43%.

Table 6-1 The investigated input parameters ranges and reference values

Input Parameters	**Unit**	**Default Value**	**Input Range Values**
Output power	kW	5	1-5
Flow rate	kg/s	0.1	0.05-0.3
Inlet total temperature	K	356	356
Rotational velocity	RPM	60000	20000-60000
Mean diameter	mm	50	40-100
Inlet total pressure	bar	2	2
Stator outlet angle	degree	70	40-80
Working fluid	-	Nitrogen	Nitrogen

The other operational parameter that affects the turbine performance is the flow rate as clarified in Figure 6-2. This figure presents the effect of turbine flow rate on the turbine total efficiency for various output power ranges from 1 kW to 5 kW. It is evident from this figure that total efficiency is decreasing as the mass flow rate increases. This is due to decreasing the work output for the same power rate and increasing the flow velocities.

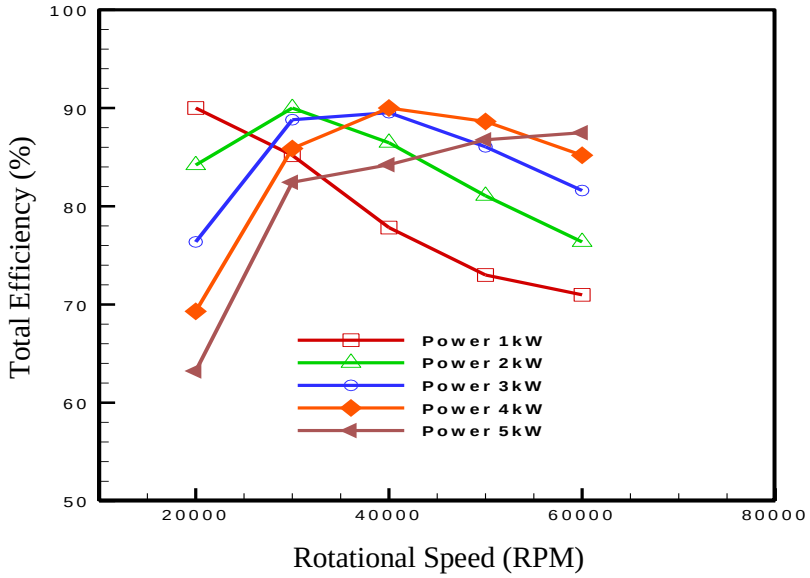

Figure 6-1 The effect of rotational speed on total efficiency for different output powers

The main geometric parameter in the mean line method is the turbine mean diameter, since it specifies the turbine geometrical size. Figure 6-3 presents the effects of this parameter on expander total efficiency for various power outputs, where increasing the turbine mean diameter decreases the turbine total efficiency for all power output ranging from 1kW to 5kW. This can be explained by equation 4-22, where increasing the turbine mean diameter increases blade velocity the higher velocity in turn adds more losses on the turbine flow stream.

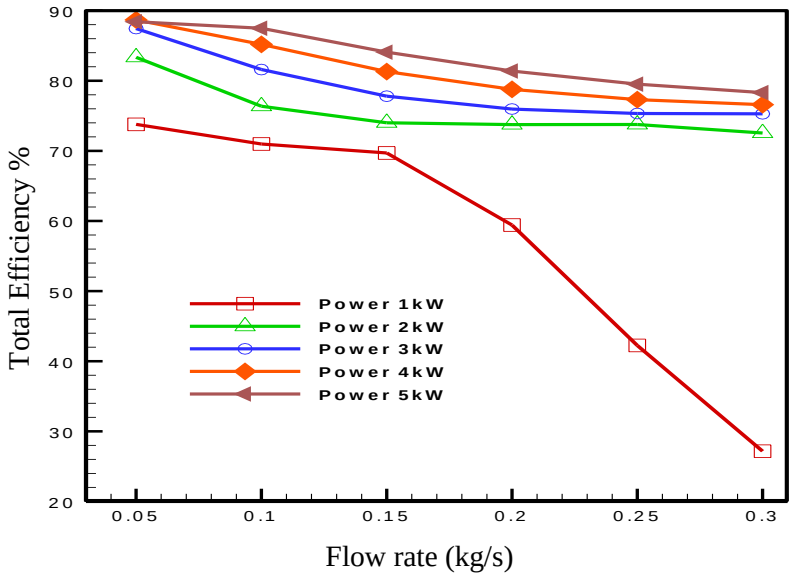

Figure 6-2 The effect of flow rate on total efficiency for different output powers

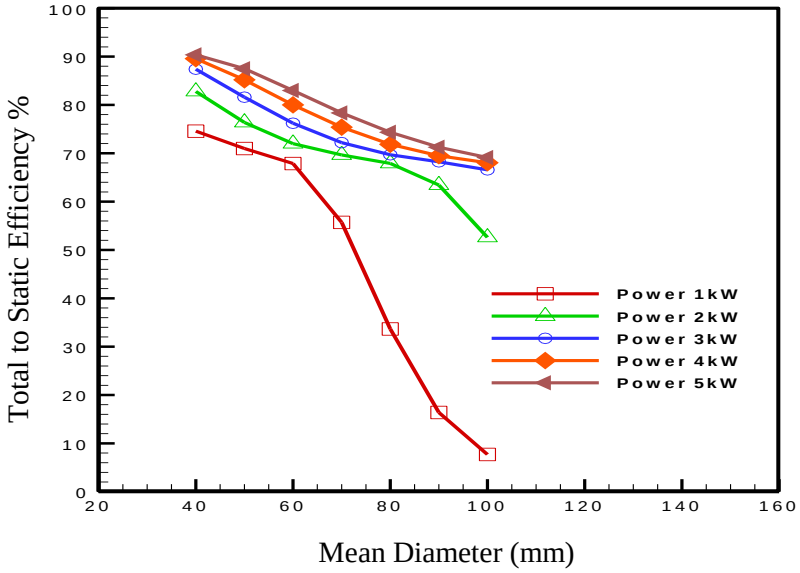

Figure 6-3 The effect of mean diameter on total efficiency for different output powers

Figure 6-4 shows the impact of turbine mean diameter on the rotational speed at various power output ranging from 1kW to 5kW, where increasing the turbine mean diameter will

decrease the rotational speed. Higher diameters produce higher torques which decreases the rotational speed for constant power rate. By the same concept increasing the power will increase the rotational speed at constant turbine mean diameter.

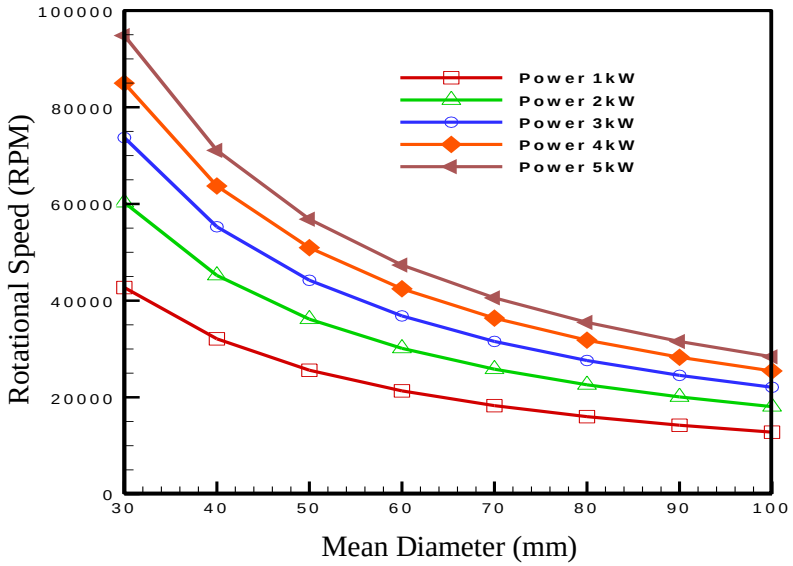

Figure 6-4 The effect of mean line diameter on rotational speed for different output power

The turbine blade height is one of the important flow path parameters since it has direct effect on the turbine mass flow rate. Figure 6-5 clarifies the effect of the turbine mean diameter on the blade height for various flow rates ranges from 0.05 kg/s to 0.3 kg/s. It is clear from this figure that increasing the turbine mean diameter decreases the blade height for constant flow rate value while increasing flow rate for constant turbine mean line diameter increases the blade height. Such behavior could be explained by the impact of the flow annular area on the turbine flow rate, where increasing the turbine mean diameter will increase the annular area, thus blade height needs to decrease in order to keep the flow rate constant. The turbine mean line diameter of 50 mm for flow rate of 0.1 kg/s produces blade height of 6 mm. Figure 6-6 presents the effect of power output on the expansion ratio for different flow rates ranging

from 0.05kg/s to 0.3 kg/s. It is evident from this figure that expansion ratio increases as the power output rate increases at constant flow rate, while at constant power rate the expansion ratio increases as the mass flow rate decreases. Such relationship confirms the fact that more flow rate means more power output so a decrease in flow rate needs compensation by increasing the expansion ratio to keep the power output at the same rate. For a flow rate of 0.1kg/s the expansion ratio is 2 and power output is 5 kW.

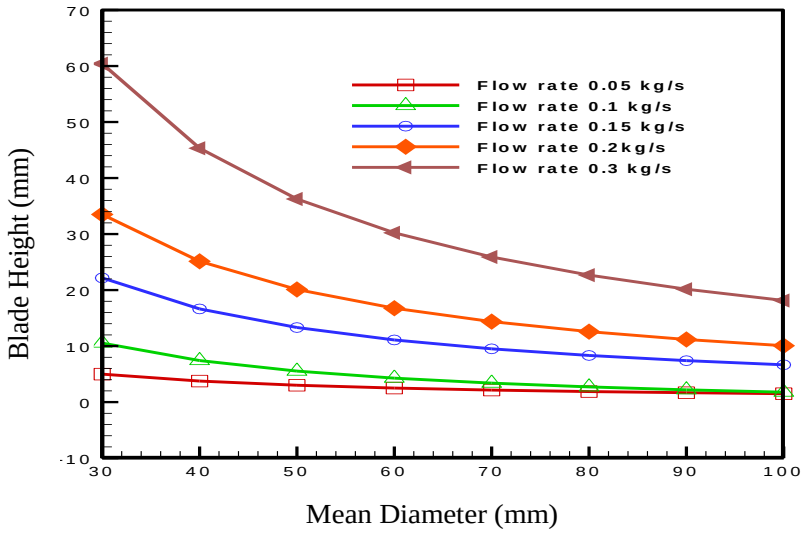

Figure 6-5 The effect of mean diameter on blade height for different flow rate

It is not just the pressure potential energy that affects the power extraction through the turbine expansion process but the heat potential energy also. Figure 6-7 depicts the effect of power output on the total temperature difference for different flow rates which ranges from 0.05kg/s to 0.3 kg/s. Increasing the output power increases the total temperature difference due to more potential energy extracting; also decreasing the flow rate increases total temperature difference due to less potential energy with less flow rate.

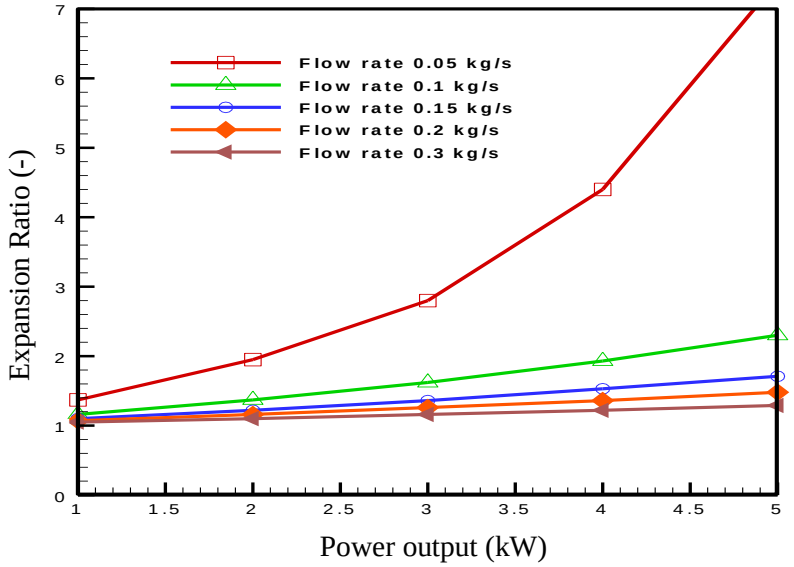

Figure 6-6 The effect of power output on expansion ratio for different flow rate

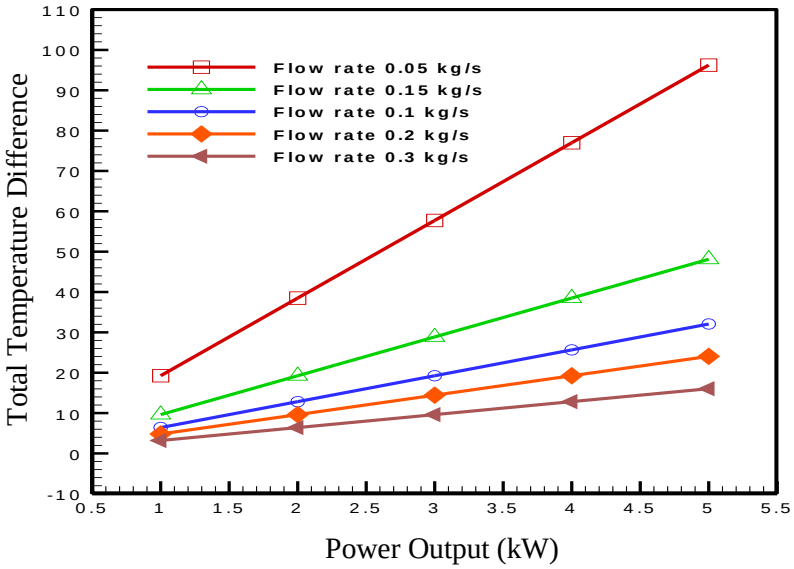

Figure 6-7 The effect of power output on total temperature difference for different flow rate

Hub and tip diameters are other design parameters that effect turbine performance, Figure 6-8 demonstrates the relationship between hub and tip diameters and the turbine flow rate. It can be noticed from this figure that tip diameter increases as the flow rate increases

while hub diameter decreases. This is due to the fact that the larger the difference between these two diameters the higher annular area which in turn means higher flow rate. The chord length is connected with the number of blades by the Zweifel ratio which is proportional with the ratio between blade space and chord axial length as illustrated by equation 4-56.

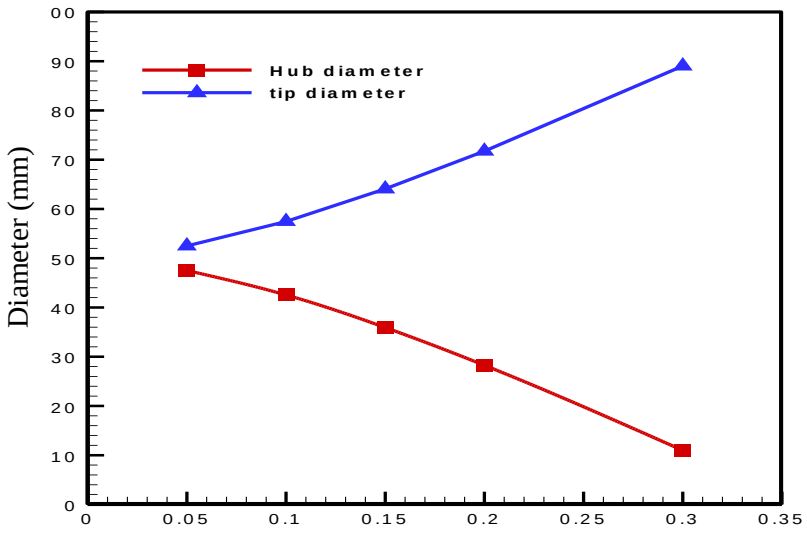

Fig.1. Flow rate (kg/s)

Figure 6-8 The effect of turbine flow rate on the tip and hub diameters

Figure 6-9 presents the effects of the number of blades on the chord length for different Zweifel ratios ranging from 0.45 to 0.85. Increasing the number of blades decreases the chord length for constant Zweifel ratio while the chord length decreases with increasing the Zweifel ratio at a constant number of blades. According to equation 4-58, increasing the number of blade decreases the blade pitch which in turn decreases the chord length for constant Zweifel ratio according to equation 4-57. Figure 6-10 depicts the effects of rotational velocity on the turbine work coefficient at various power output rates ranging from 1 kW to 5 kW. Increasing the rotational speed increases the work coefficient value for constant power rate while increasing the power rate decreases the work coefficient at the same rotational speed value.

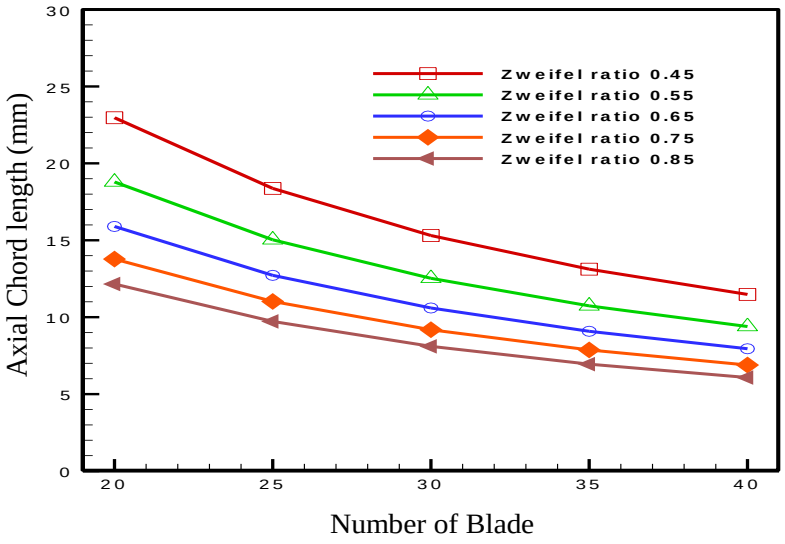

Figure 6-9 The number of blades effect on the blade axial chord length for the different flow rates

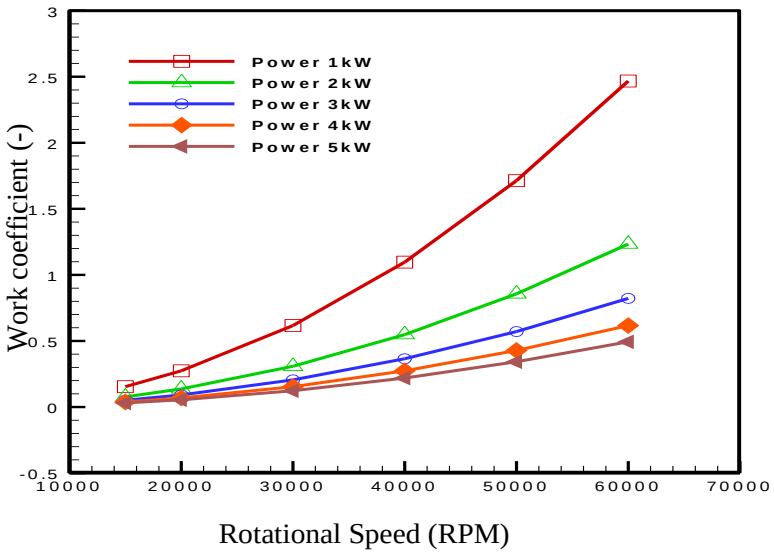

Figure 6-10 Effect of rotational velocity on the turbine work coefficient at different output power

Table 6-2 summarizes the results from a preliminary design based on the required cycle operating conditions explained in chapter 3 such as turbine power and flowrate. The

preliminary analysis parametric study can be an effective method for finding a preliminary design for the axial turbine. However, this design still needs more work to be developed into a 3D form, which means more details need to be added to this initial design to promote it to a 3D fluid flow level.

Table 6-2 axial turbine preliminary design results

input parameters	Unit	Value
Tip diameter	mm	56
Hub diameter	mm	44
Blade height	mm	6
Expansion ratio	-	2
Stator number of blades	-	23
Rotor number of blades	-	28
Work coefficient	-	0.5
Stator chord	mm	9
Rotor chord	mm	8
Stator Solidity	-	1.77
Rotor Solidity	-	1.42
Stator inlet angle	degree	0
Stator outlet angle	degree	70
Stator stagger angle	degree	32
Rotor inlet angle	degree	0
Rotor outlet angle	degree	70
Rotor stagger angle	degree	32
Turbine isentropic efficiency	%	87.49
Power output	kW	5

6.3 Axial turbine CFD 3D Analysis Results:

Part of the work presented in this section has already been published by the author [55].

The results produced using 1D preliminary design presented in Table 6-2 are used as input data to the ANSYS-CFX software to develop the 3D CFD model for the new 3D design. The blade profile for the stator and rotor were generated using BladeGen module which uses some of the geometrical parameters to control the blade profile as clarified in chapter 4, Figure 4-13. These blade profile parameters are investigated in terms of total efficiency and power output to show their effect on the turbine performance which leads to choosing better design parameters. Figure 6-11 depicts the effect of the blades number for the rotor and stator on turbine performance. It can be noticed that there is an optimum value of the number of the blades for both stator and rotor to produce maximum power output and turbine efficiency. Decreasing the number of blades can cause miss guide of the flow which in turn causes flow separation while increasing the number of blades will increase the wet area for the flow which in turn increases the losses. The other issue that can be noticed from this figure is that the stator number of blades has greater impact on the turbine performance than the rotor number of blades and that could be justified as the stator is the starting point of the flow so all its effects are propagated on the downstream domains.

Changing the number of blades for the stator or the rotor will change the area of its passage which in turn affects the flow rate through the turbine as clarified in Figure 6-12. Increasing the blade number for both stator and rotor decreases the flow rate at constant expansion ratio 2 and the stator number of blades is affects it more than the rotor number of blades as shown in Figure 6-12.

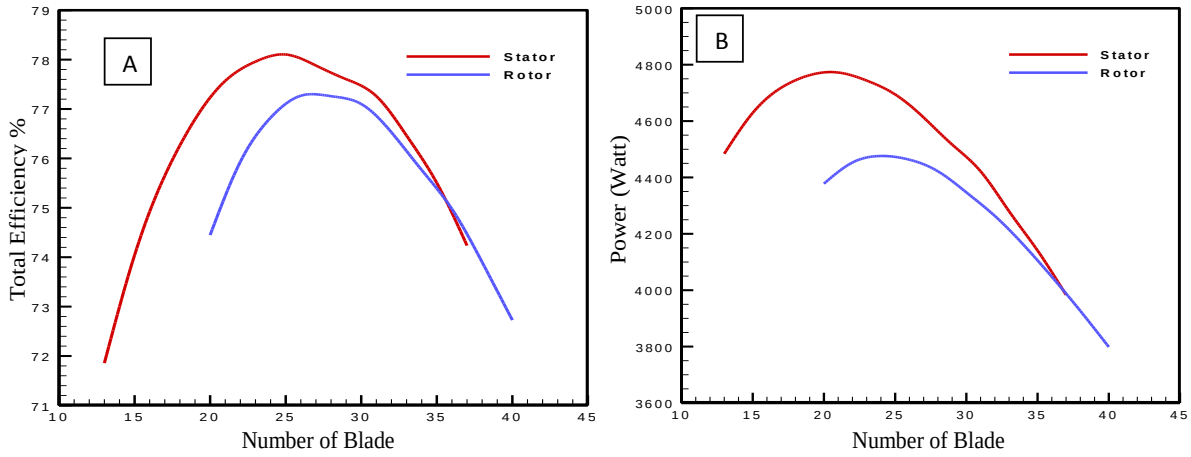

Figure 6-11 The impact of the rotor and stator number of the blade on the turbine (A) total efficiency and (B) output power

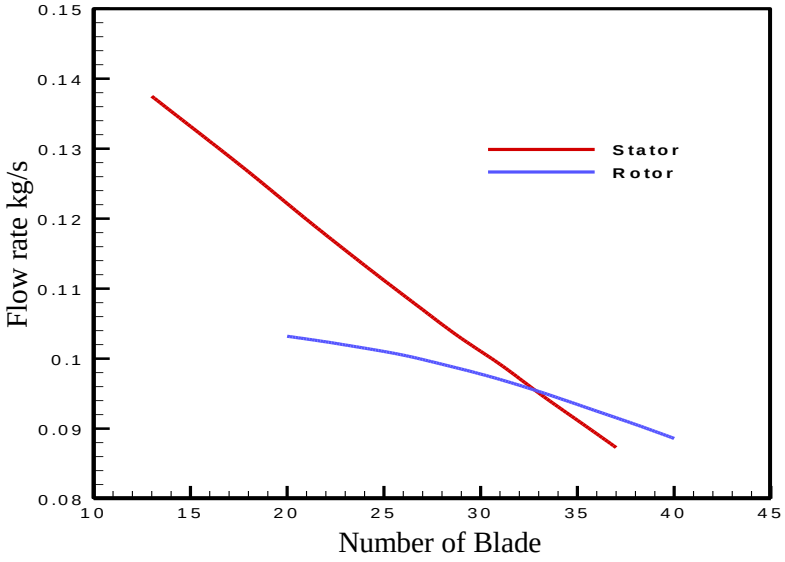

Figure 6-12 The effect of the stator and rotor number of the blades on the turbine flow rate at pressure ratio 2

Figure 6-13 presents the effects of the number of blades for the rotor and stator on the maximum Mach number through the stator passage and rotor passage respectively. From Figure 6-13A, increasing the stator number of blades from 10 to 40 increases the stator

passage maximum Mach number from 0.7 to 0.97 while decreasing it in the rotor passage from 1.4 to 0.74. Also adding more blades in the rotor increases the rotor passage maximum Mach number from 0.86 to 0.94 while decreasing it in the stator passage from 1.26 to 0.65 as clarified in Figure 6-13B. Increasing blades number will decrease the flow area which in turn increases the velocity of the flow and decreases the flow rate. In each graph one passage (rotor or stator) number of blade change while on the other passage its number of blades stays constant, so the flow area stays constant which means with low flow rate the flow velocity decrease in this passage. However, the throat area which is the minimum flow area through the turbine passage is preferred to be at the stator passage.

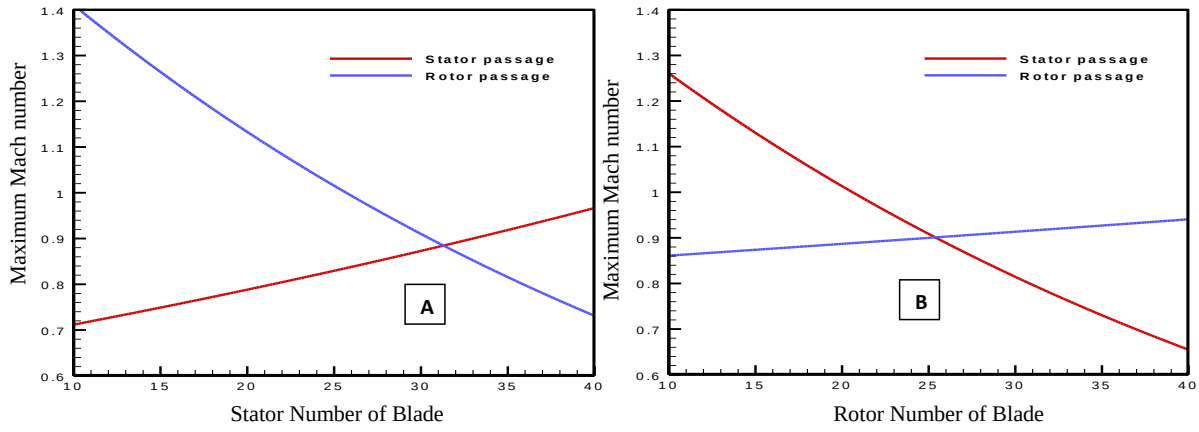

Figure 6-13 The effect of number of blade (A) stator (B) rotor on the maximum mach number in stator passage and rotor passage

Figure 6-14 presents the impact of rotor and stator stagger angle on the turbine efficiency and output power. In both, Figure 6-14A and Figure 6-14B there is an optimum stagger angle for each blade that produces maximum total efficiency and output power. Moreover, the stagger angle of the rotor is more effective on turbine performance than stator stagger angle. Increasing the stagger angle makes the blade profile longer and more straight which

accelerates the flow but increases the wet area. The optimum stagger angle for the stator blade is 15 degrees and for rotor blades is 32 degrees.

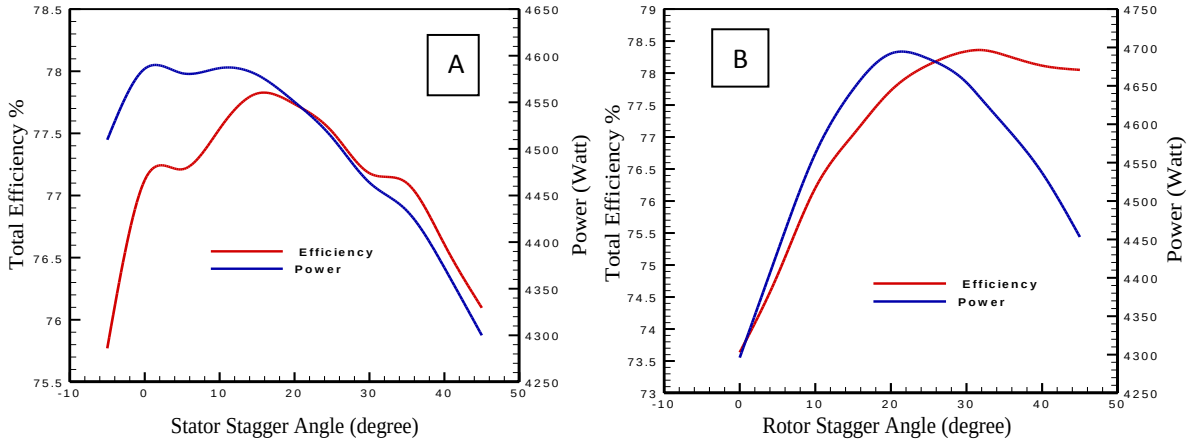

Figure 6-14 The effect of (A) stator stagger angle and (B) rotor stagger angle on the turbine efficiency and output power

Figure 6-15 shows the relationship between rotor and stator leading edge thicknesses with turbine total efficiency and output power. Increasing leading edge thickness for both rotor and stator does not have a significant effect on the turbine total efficiency and power output, since this thickness is located at the starting point of stator blades where there is minimum flow velocity. In contrast to leading edge thickness, the trailing edge thickness has a high impact on the turbine performance as depicted in Figure 6-16. This figure clarifies the effect of changing rotor and stator blade trailing edge thicknesses on the turbine total efficiency and output power. Increasing the thickness of the trailing edge in both rotor and stator blades from 0.1 to 0.8 mm decreases both the overall efficiency and output power for the stator from 80.47 %, 4437.19 W to 69.34 %, 3045.68 W respectively, and for the rotor from 80.06%, 4312 W to 76.39%, 3892.34 W respectively. Again the stator trailing edge thickness has more impact than the rotor trailing edge thickness. The thickness of trailing edge is the area where the blade suction side boundary layer and the blade pressure side boundary layer meet;

therefore less area will make more smooth interaction and fewer losses. The wake generated by the stator trailing edge is propagated downstream to the rotor, which makes the stator trailing edge thickness more effective compared to that of the rotor.

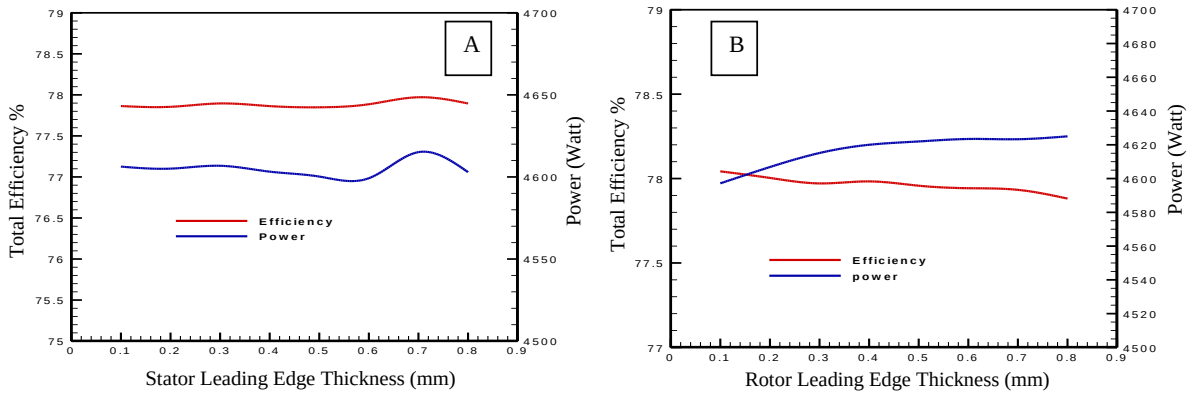

Figure 6-15 The effect of leading-edge thickness for (A) stator and (B) rotor on the turbine efficiency and output power

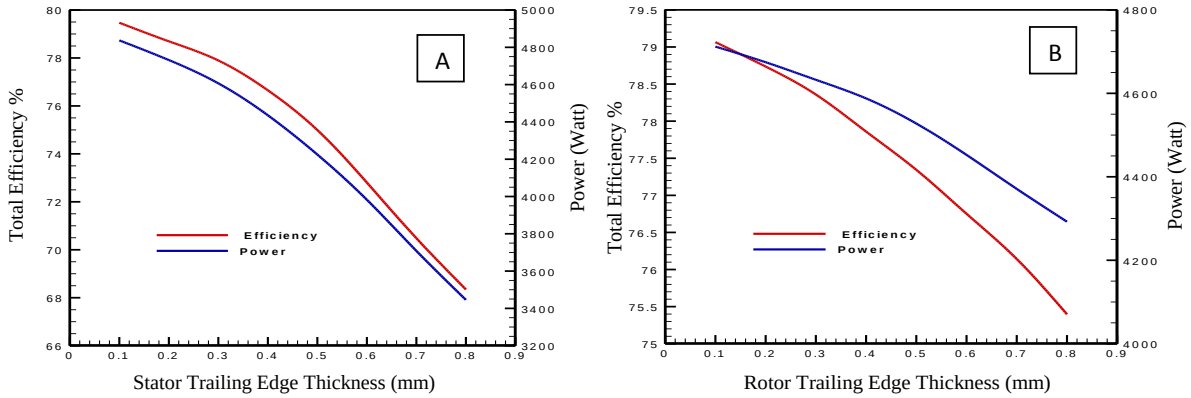

Figure 6-16 The effect of trailing-edge thickness for (A) stator and (B) rotor on the turbine efficiency and output power

Figure 6-17 depicts the effect of changing the stator and rotor blade outlet angles on the turbine total efficiency and output power. Increasing the blade outlet angle in the rotor and

stator increases the efficiency and output power to maximum values; following which the performance decreases. The optimum outlet blade angle for both stator and rotor is 70 degrees which is in accordance with [195] recommendation for axial stator outlet angle to be less than 75 degrees. Increasing the outlet angle increases the blade deflection which improves work extraction but increases the possibility of early separation.

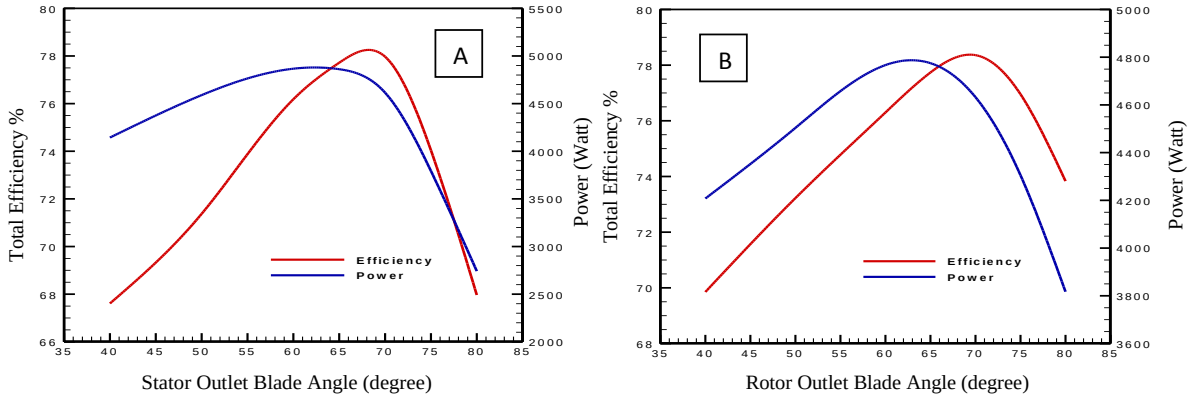

Figure 6-17 The effect of outlet blade angle for (A) stator and (B) rotor on the turbine efficiency and output power

The tip clearance thickness between the rotor tip and turbine casing is another design parameter that affects fluid flow and turbine performance. Figure 6-18 clarifies the effect of tip clearance on turbine total efficiency and output power, with tip clearance ranging from 0.1 mm to 0.6 mm. Increasing tip clearance distance decreases turbine overall efficiency and output power where the efficiency decreases from 82.24% at clearance 0.1 mm to 72.82 % at clearance 0.6 mm and power output from 4847.58 W to 4198.01 W. The difference in pressure between the rotor blade pressure side and suction side causes fluid leakage from the blade pressure side to the blade suction side through the open area of tip clearance which in

turn causes work loss that could be extracted from this leaked fluid. Therefore increasing the tip clearance distance will increase this leakage and decreases turbine performance.

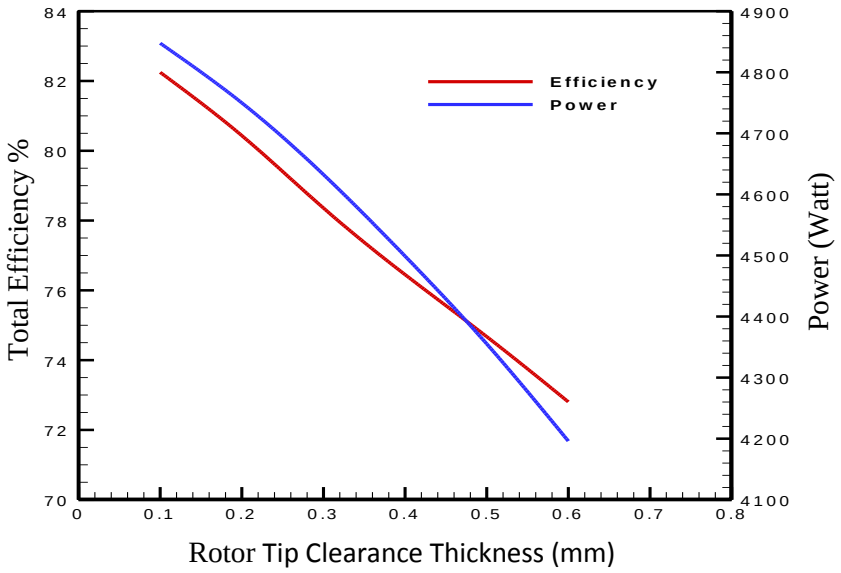

Figure 6-18 Rotor tip clearance thickness effects on the turbine total efficiency and output power

The other clearance or mixing gap between the stator and the rotor that affects the performance of the turbine is clarified in Figure 6-19. This figure depicts the effect of various gap distances as a percentage of the rotor chord length on the turbine overall efficiency and output power. Increasing mixing gap between stator and rotor will increase overall efficiency and output power up to a maximum value of between 22 & 24%, after which the performance will decrease. Increasing the mixing gap between rotor and stator improves mixing process but increases flow viscous losses. On the other hand, decreasing this gap will decrease the viscous losses but transfer the wakes generated by stator to the rotor without good mixing.

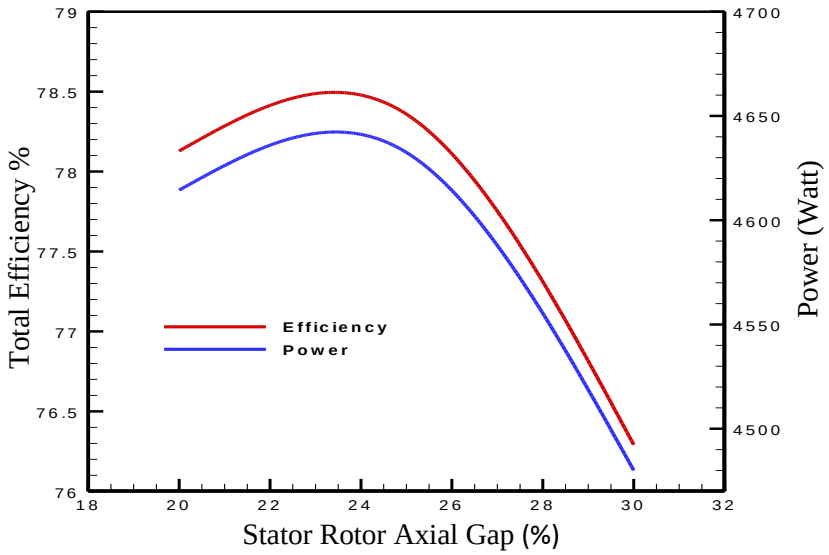

Figure 6-19 The effect of stator-rotor axial mixing gap on turbine total efficiency and output power

Current 3D CFD simulation results are compared against mean-line preliminary design results at various expansion ratios ranging from 1.2 to 2 to assess the quality of the preliminary design model and at the same time, to provide an overall check for the 3D CFD model. Figure 6-20 to Figure 6-22 show the comparison in terms of thermodynamic and aerodynamic parameters; total efficiency, power output and flow parameter such as relative outlet rotor velocity [55].

The maximum difference in terms of efficiency is 9.5 % as shown in Figure 6-20, the maximum differences in terms of power output and rotor outlet relative velocity are 7.9 % and 10.56 % as shown in Figure 6-21 and Figure 6-22 respectively. In general, the calculated parameters show good agreement between the two models. It is interesting to examine the relative outlet rotor velocity which showed the lowest agreement between the 3D CFD and mean line approach. The differences between 1D mean-line analysis and 3D CFD analysis is due to the first not being able to fully describe the flow field behavior [55]. Based on the

above 3D CFD parametric study for blade parameters the best values for all of the investigated blade parameters are summarized in Table 6-3. In this table the flow path dimensions such as tip and hub diameters stay constant from the preliminary stage. There are also some parameters after manual optimization that keep their preliminary design value after 3D CFD parametric studies such as stator and rotor outlet blade angles while the other 3D blade profile parameters were changed.

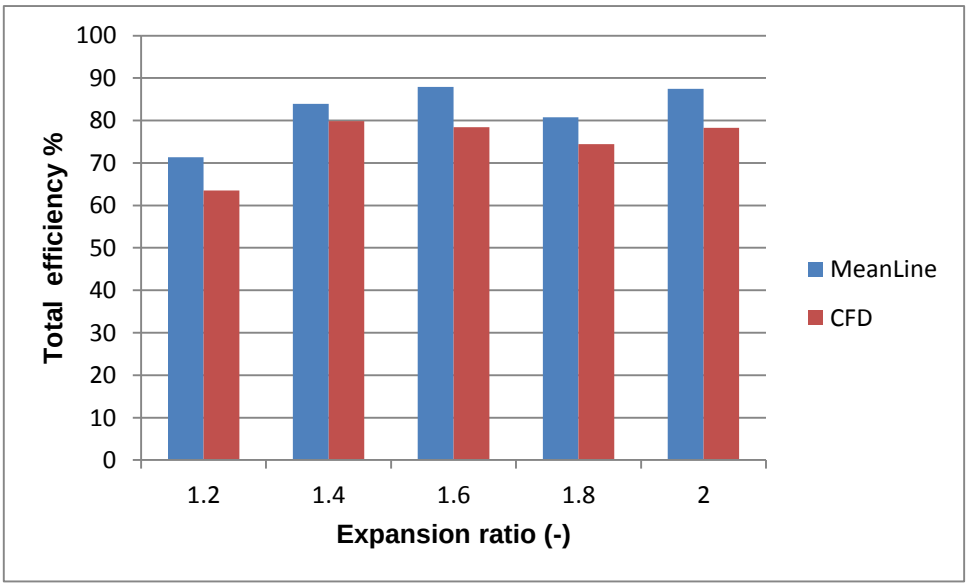

Figure 6-20 Comparison between mean line 1-D analysis and 3D CFD analysis based on total turbine efficiency [55]

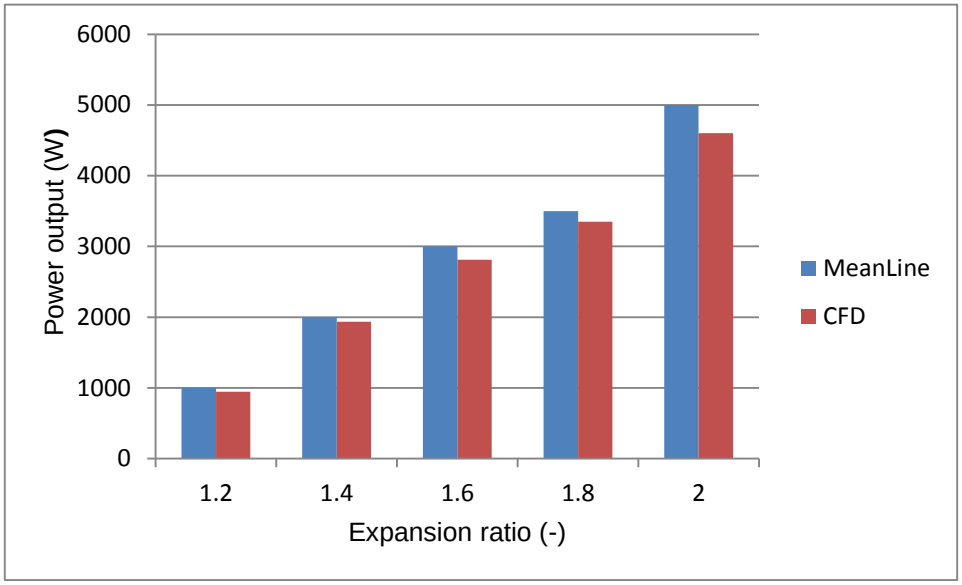

Figure 6-21 Comparison between mean line 1D analysis and 3D CFD analysis based on turbine output power [55]

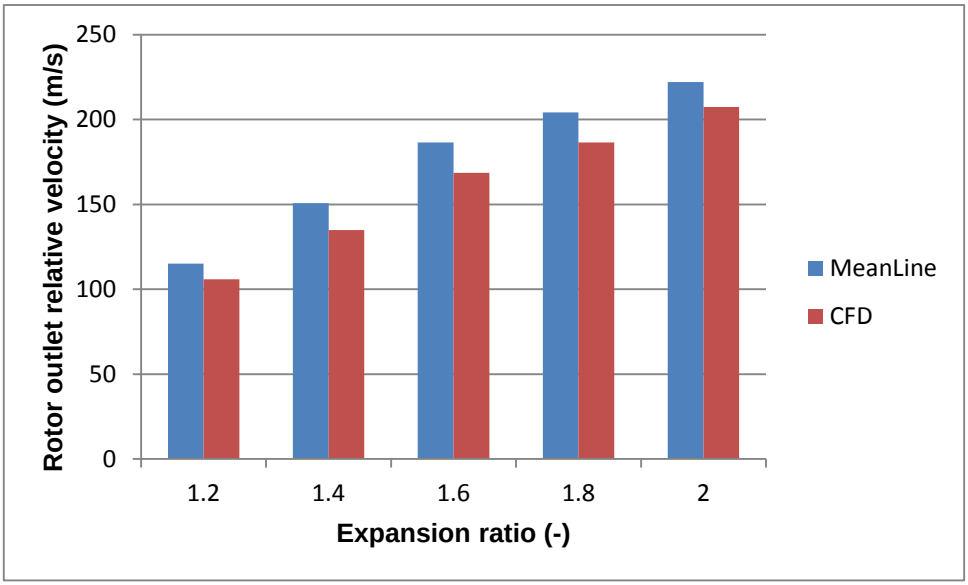

Figure 6-22 Comparison between mean line 1D analysis and 3D CFD analysis based on relative rotor outlet velocity [55]

Table 6-3 axial turbine 3D CFD parametric study results

input parameters	Unit	Value
Stator number of blades	-	31
Rotor number of blades	-	26
Stator inlet angle	degree	-30
Stator outlet angle	degree	70
Stator stagger angle	degree	15
Stator leading edge thickness	mm	0.2
Stator triling edge thickness	mm	0.3
Rotor inlet angle	degree	-40
Rotor outlet angle	degree	70
Rotor stagger angle	degree	32
Rotor leading edge thickness	mm	0.2
Rotor triling edge thickness	mm	0.3
Rotor tip clearance	mm	0.3
Rotor- stator gap	%	25
Mass flow rate	kg/s	0.11
Turbine isentropic efficiency	%	78.3
Power output	kW	4.6

6.4 Small-Scale Axial Turbine 3D Optimization Analysis Results:

Part of the work presented in this section has been published by the author [75].

The previous section dealt with manual parametric study to improve the turbine performance by fixing all geometrical parameters and changing just one of them at a time. Changing all geometrical parameters simultaneously to maximize or minimize certain performance indices will produce more accurate and optimised results. ANSYS Design exploration module can achieve this optimization if the user is successful in describing the geometry in simple parameterisation technique. As explained in chapter 4 the camber line control point's novel parametrization technique was developed in this study for small scale axial turbine optimization. The turbine rotor and stator blade geometries were controlled by 12 parameters: stator blades number (SN), rotor blades number (RN), stator chord length (SC), rotor chord length (RC), stator first angle (SA1), rotor first angle (RA1), stator second angle (SA2), rotor second angle (RA2), stator blade thickness (ST), rotor blade thickness (RT), stator blade peak location (SX) , rotor blade peak location (RX). The performance was optimized based on maximising the total efficiency and output power while keeping the flow rate within the limit of 0.1 kg/s.

6.4.1 Response Surface Results:

As mentioned in chapter 4 the main task of the response surface module is creating best fit functions or relationships between the input geometrical parameters and output performance parameters by using design of experiment module data. As clarified in equation 4-82 the quality of the response surface can be checked by the goodness of fit parameter. This quality can be checked by comparison between outputs predicted by response surface relationships and the one calculated by design of experiment module as shown in Figure 6-23. It can be noticed from this figure there is very good fitting between actual solver output data and

predicted data by standard response surface-full 2nd order polynomials of output parameters turbine normalized total efficiency, power output, and flow rate. Local sensitivity as defined by equation 4-83 is one of the powerful tools of response surface module, since it shows at a glance the impact of all the input parameters on output parameters as shown in Figure 6-24. It is evident from this figure that the parameter rotor second angle (RA2) has the largest impact on both total efficiency and output power which are -17.2%, and -14.54% respectively, while parameter stator second angle (SA2) is the second largest influential parameter. Moreover, the rotor blade thickness (RT) has significant impact on the turbine efficiency and output power while the stator thickness (ST) does not have that.

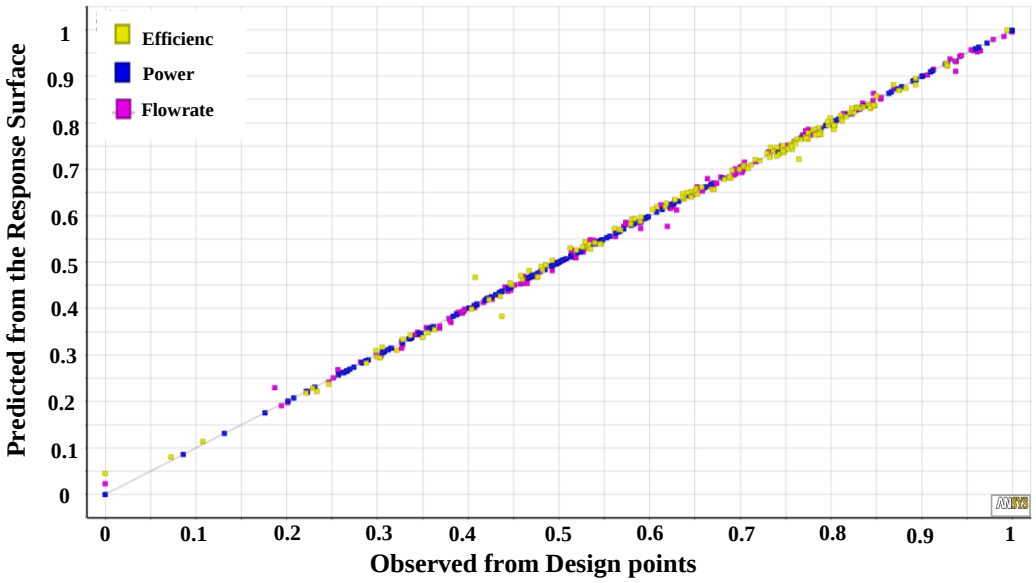

Figure 6-23 Goodness of fit for turbine performance parameters

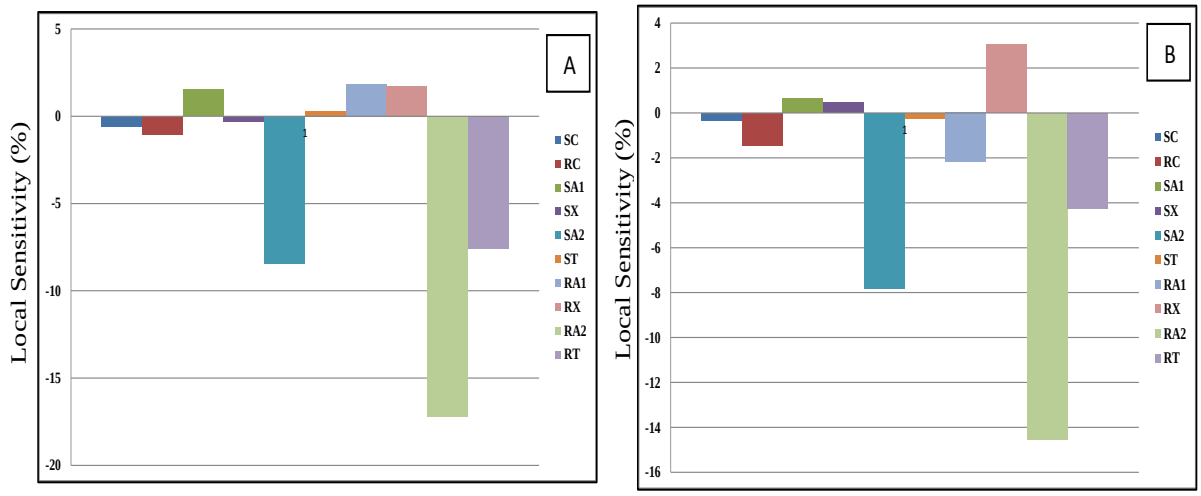

Figure 6-24 Local sensitivity of input design parameters on the (A) output power and (B) turbine efficiency

To have more details about the response surface module relationships which are between input parameters and output parameters, the 3D response surfaces between two input parameters and turbine performance parameters is shown from Figure 6-25 to Figure 6-34. Figure 6-25 and Figure 6-26 clarify the relationships between the stator chord length SC and the rotor chord length RC with total efficiency and power output. It can be seen that increasing the stator chord length from 15 to 20 mm and the rotor's one from 8 to 13 mm will decrease the efficiency from 78.81% to 77.86% and power output from 4.5kW to 4.2 kW. Increasing the blade chord length will increase the wet area which considerably raises the friction loss.

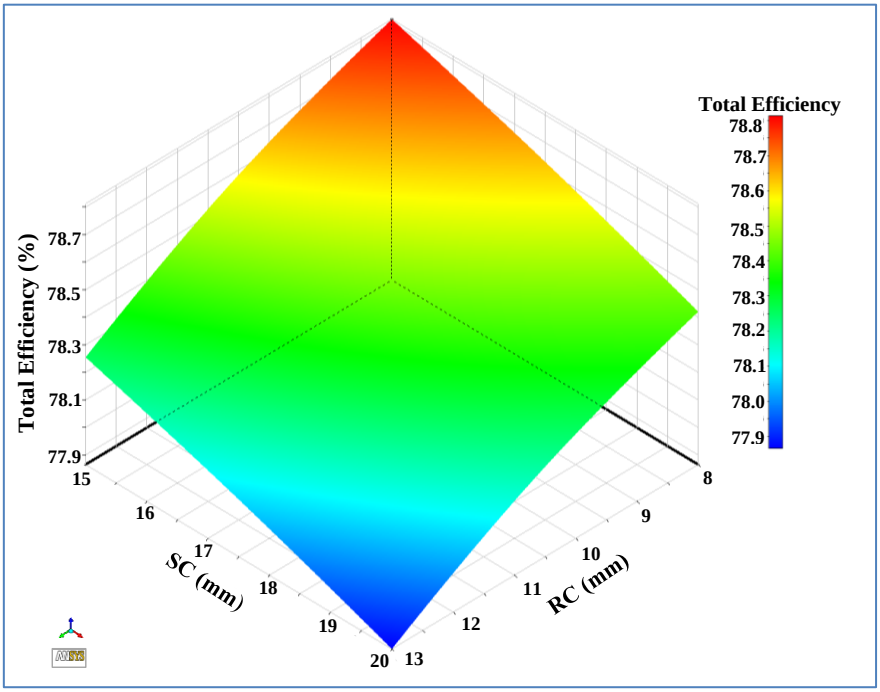

Figure 6-25 Effect of stator chord SC and rotor chord RC on total efficiency

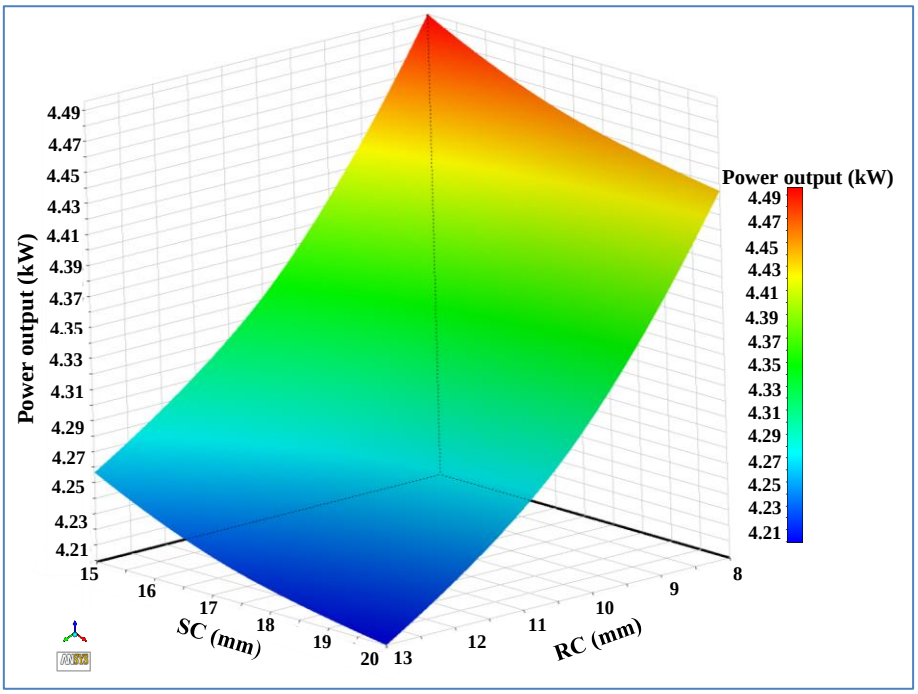

Figure 6-26 Effect of stator chord SC and rotor chord RC on power output

As shown in sensitivity analysis Figure 6-24 the outlet blade angle for the rotor (RA2) and stator (SA2) have a large impact on the turbine performance, Figure 6-27 and Figure 6-28 are utilized to show this impact in more details on the turbine efficiency and output power. It is evident from Figure 6-27 that there exists an optimum condition that yields highest total efficiency at the second stator blade angle (SA2) and second rotor blade angle (RA2) of about 65.62 degrees and 60.41 degrees respectively. While decreasing these angles from 75 degrees to 50 degrees increases the power output from 2.4kW to 5.1kW as depicted in Figure 6-28. This is due to the fact that increasing this angle increases turbine mass flow rate hence increases the power output.

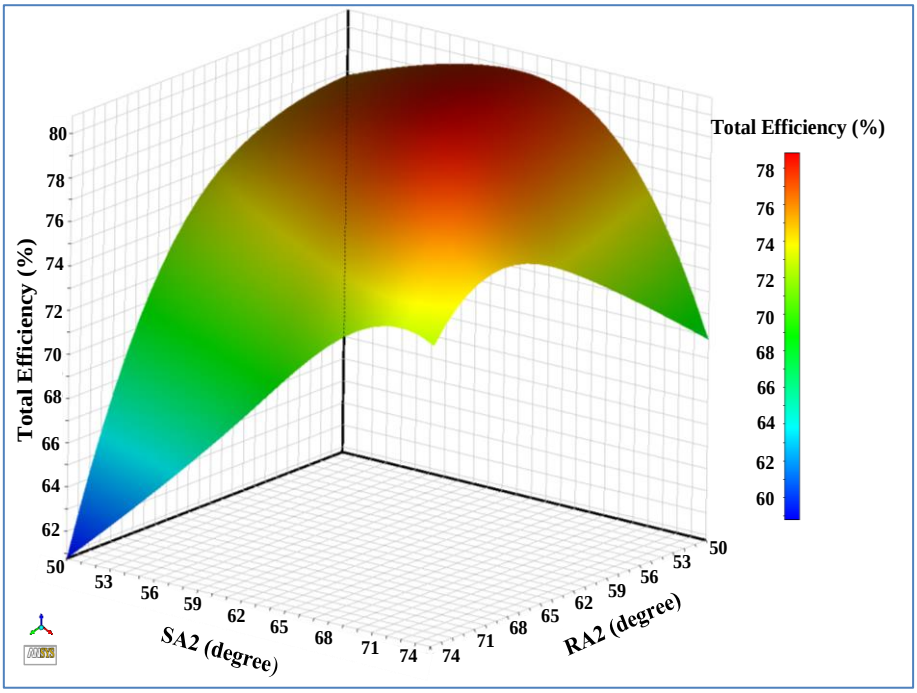

Figure 6-27 Effect of stator second angle (SA2) and rotor second angle (RA2) on total efficiency

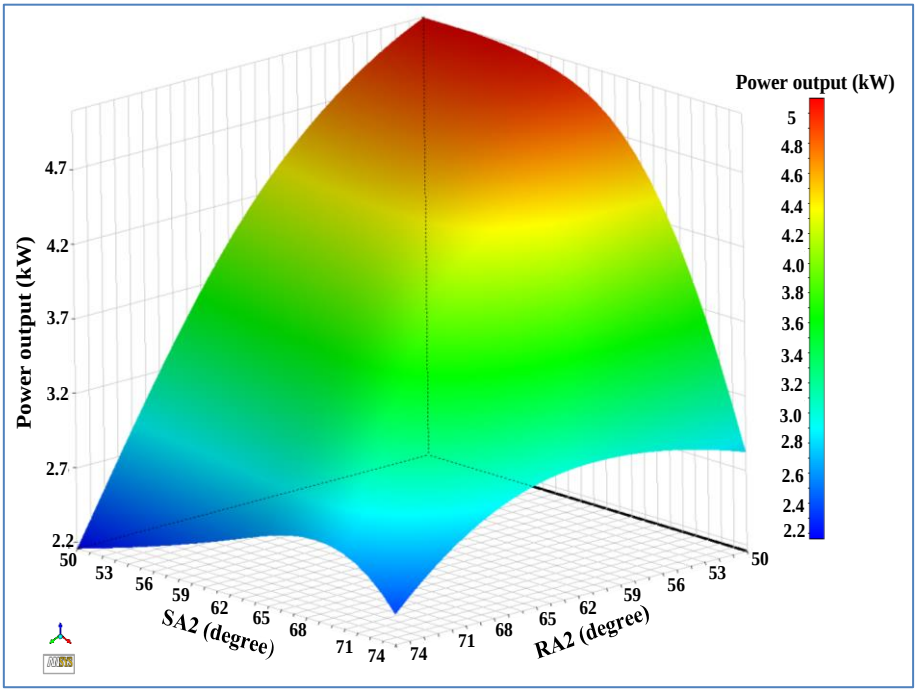

Figure 6-28 Effect of stator second angle (SA2) and rotor second angle (RA2) on power output

Figure 6-29 and Figure 6-30 show the effects of varying the stator blade thickness (ST) and the rotor blade thickness (RT) on the turbine total efficiency and power output. It can be seen from these figures that increasing the rotor blade thickness from 1mm to 2mm will decrease the total efficiency from 82.3% to 77.4% and power output from 4.6 kW to 3.9 kW; while the stator blade thickness does not have a significant effects on the turbine performance. Such behavior can be attributed to the fact that the blade thickness affects the lifting characteristics of the blade [196] where the entire turbine lift comes from the rotor blade.

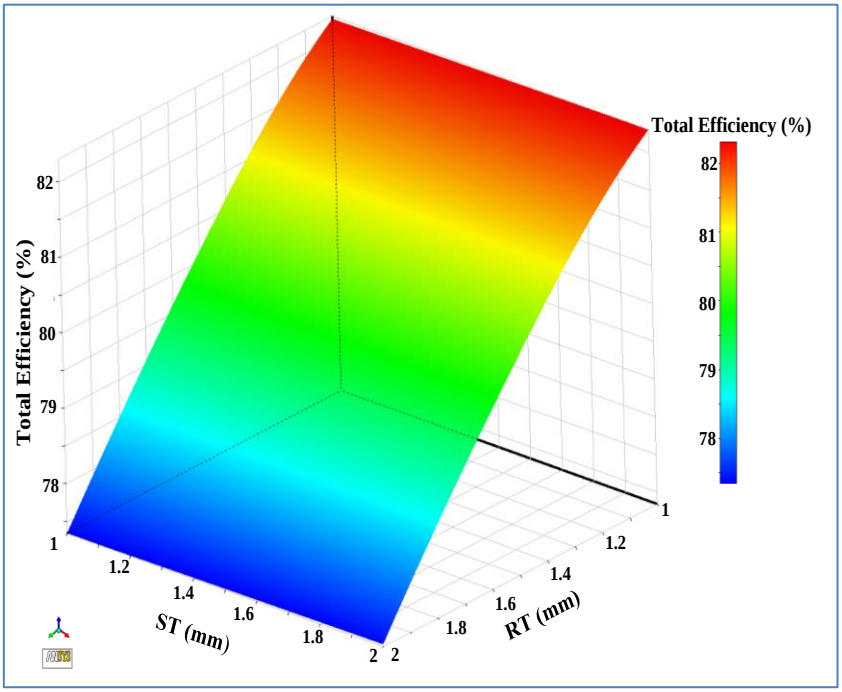

Figure 6-29 Effect of stator blade thickness (ST) and rotor blade thickness (RT) on total efficiency

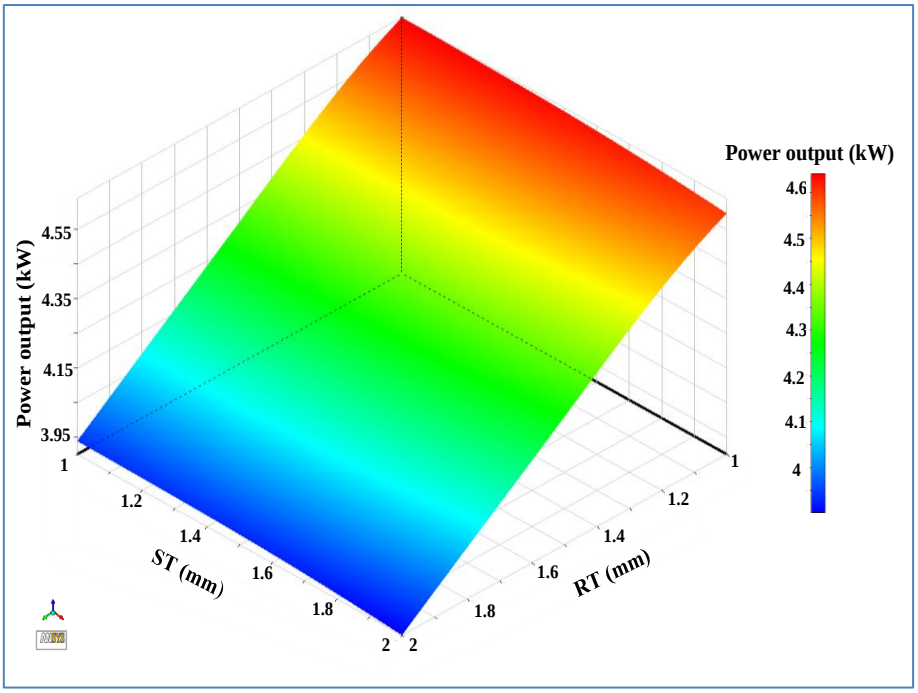

Figure 6-30 Effect of stator blade thickness (ST) and rotor blade thickness (RT) on output power

The first blade angle is another parameter that controls the inlet passage part of the blade. In Figure 6-31 and Figure 6-32 the effects of this angle for the stator and rotor on the turbine efficiency and output power are presented. It is evident from these figures that there is an optimum total efficiency of 80.6% and output power of 4.44 kW for the first blade angle in stator -10 degree and in the rotor -11.25 degree. The first blade angle is designed to match the flow direction with blade direction in a smooth way it follows that the mismatch between flow direction and blade direction will cause incidence losses [142]; thus there is always a need to find the optimum condition for this angle.

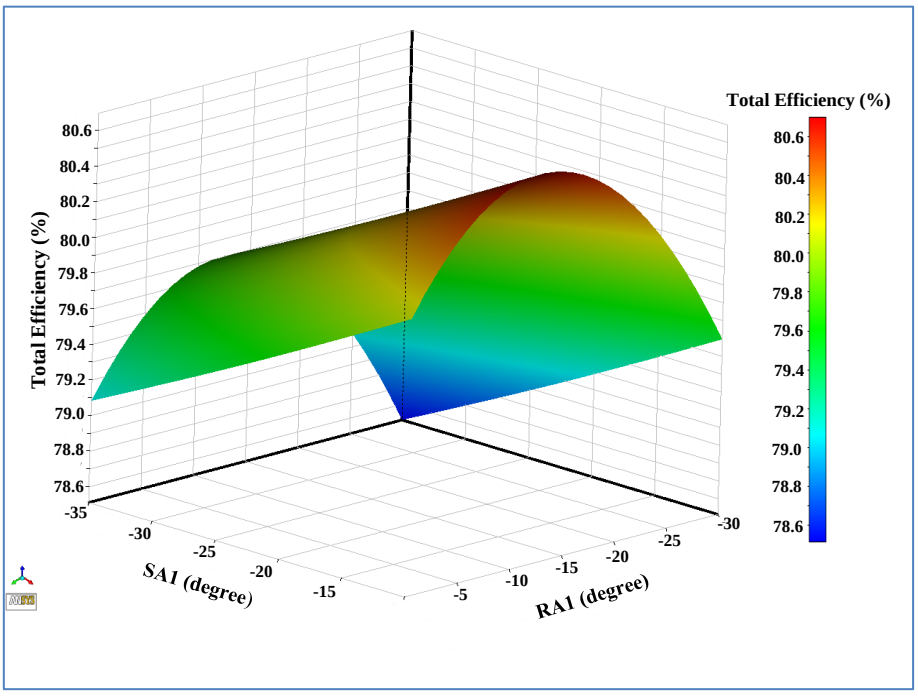

Figure 6-31 Effect of stator first angle (SA2) and rotor first angle (RA2) on total efficiency

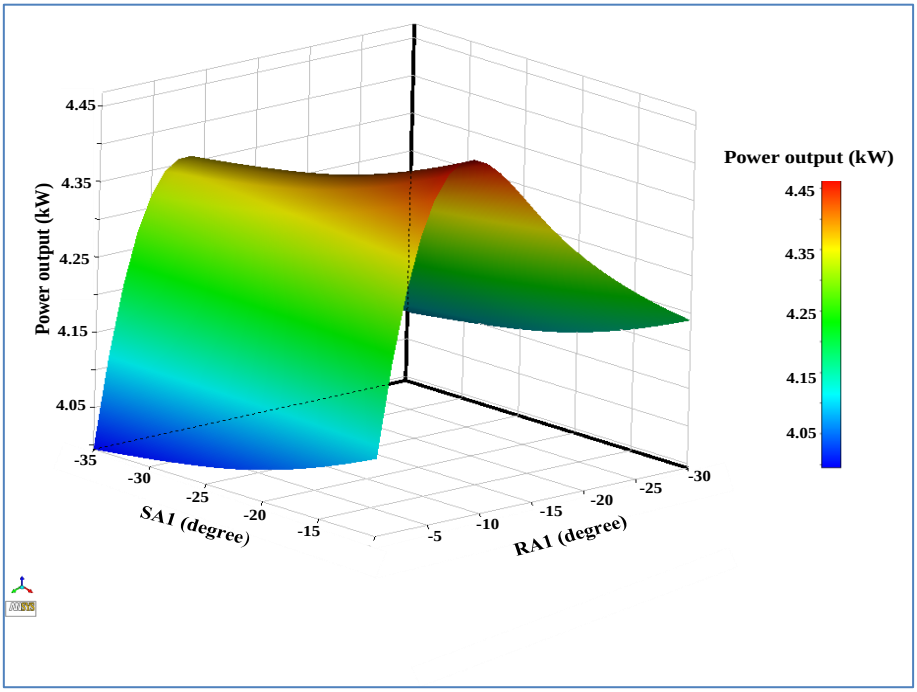

Figure 6-32 Effect of stator first angle (SA2) and rotor first angle (RA2) on total efficiency

The peak location for the blade camber line represents the point where the flow starts to change the direction from upstream to downstream or vice versa. Figure 6-33 and Figure 6-34 show the effects of this geometric length as a percentage of the total blade chord length on the total turbine efficiency and output power. It is obvious from these figures that increasing the rotor blade peak location from 25% to 50% will increase the total efficiency from 79.53% to 80.65% and power output from 3.95 kW to 4.53 kW. While the stator blade peak location does not have a significant impact on the turbine performance. As this parameter affects the blade lift characteristics, it is more effective with the rotor than the stator.

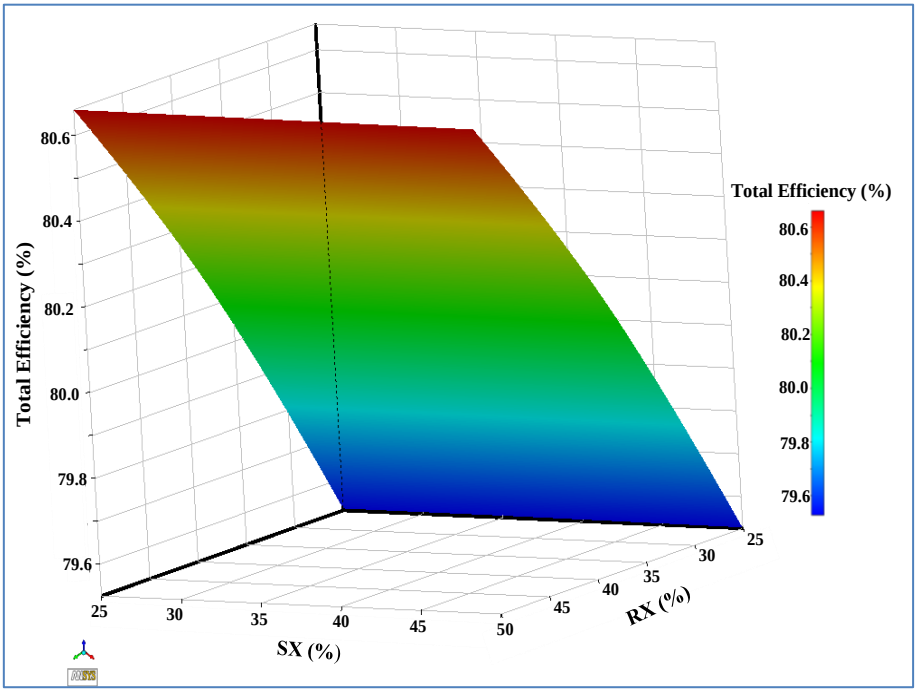

Figure 6-33 Effect of stator peak location (SX) and rotor peak location (RX) on total efficiency

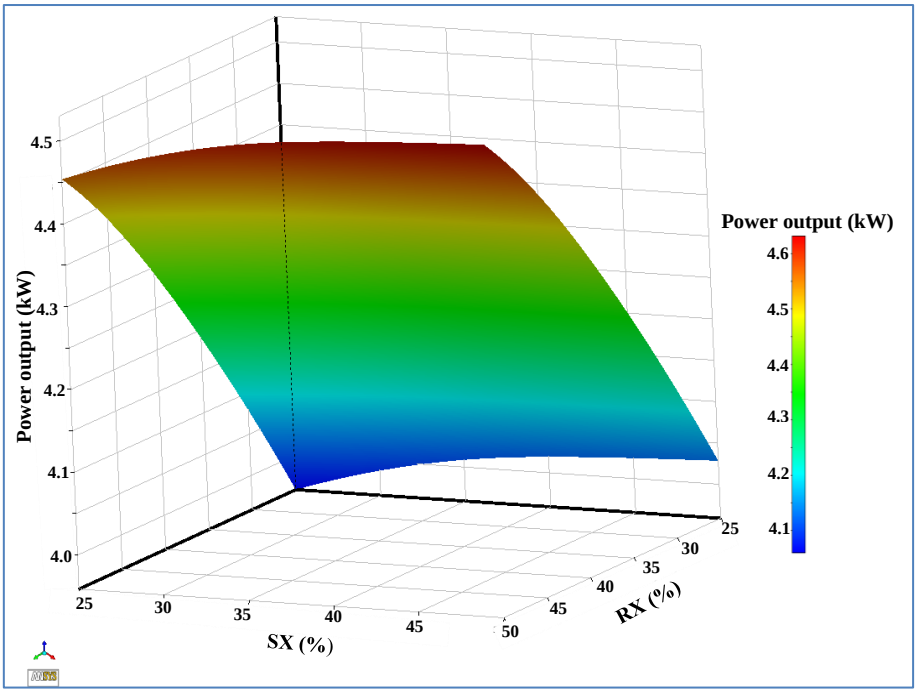

Figure 6-34 Effect of stator peak location (SX) and rotor peak location (RX) on power output

6.4.2 Optimization (MOGA) Results:

The optimization method (MOGA) uses the response surface relationships which connects input geometrical parameters with output performance parameters like turbine efficiency and output power to reach the optimum design. The comparison between the base-line and the optimum blade profile designs for the rotor and stator is clarified in Figure 6-35. It can be seen from this figure that the optimum rotor and stator blades have larger chord lengths and lower blade thicknesses compared to the base-line blade profile. More detailed comparison between base-line and optimum turbine blade design are shown in Table 6-4, which shows how the developed optimization procedure enhanced the turbine performance for total efficiency from 78.3% to 84.88% and power output from 4.6 kW to 5.3 kW.

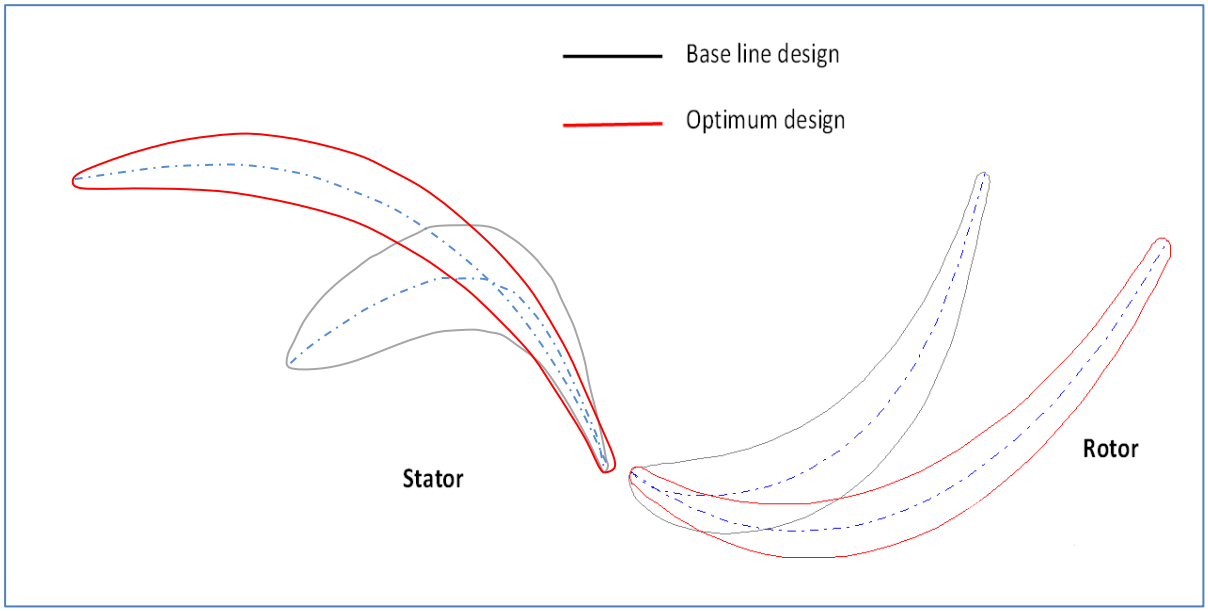

Figure 6-35 Comparison between base-line and optimum blade profile for turbine stator and rotor

Table 6-4 Blade profile results of base-line and optimum design for turbine stator and rotor

Design Parameters	Unit	Base line Value	Optimum value
Stator chord length (SC)	mm	9	15.2
rotor chord length (RC)	mm	8	12.1
stator first angle (SA1)	degree	-30	-10.83
rotor first angle (RA1)	degree	-40	-29.29
stator second angle (SA2)	degree	70	63.46
rotor second angle (RA2)	degree	70	53.7
stator blade thickness (ST)	mm	2.35	1
rotor blade thickness (RT)	mm	1.454	1
stator blade peak location (SX)	%	20	25
rotor blade peak location (RX)	%	56.7	30.57
stator number of blades (SN)	-	31	37
rotor number of blades (RN)	-	26	42
Total efficiency	%	78.3	84.88
Power output	kW	4.6	5.3

Figure 6-36 to Figure 6-38 show more details for the improvement in the turbine performance after optimization. Figure 6-36 demonstrates a comparison for blade loading between the base-line and the optimum blade designs cases, which comparison was carried out for both passages in the stator and rotor. It is obvious that the blade loading for both rotor and stator in the optimum blades design are lower than those in the base-line design. Moreover, in the optimum design case the loading is distributed along the blade streamwise in a more smooth way. It is worth pointing out here that despite the lower loading for the optimum blade case, it is still producing higher power output than the base-line blade design, and that because of the longer blade chord than that of the base-line design.

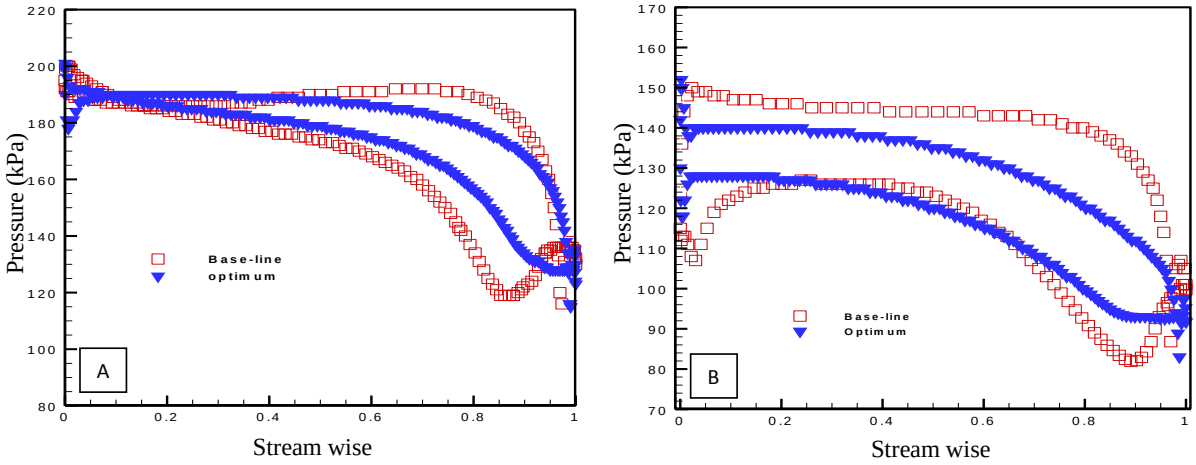

Figure 6-36 Blade loading comparison between base-line blade design and optimum blade design for (A) stator blade and (B) rotor blade at span 50%

Figure 6-37 depicts the comparison for the 3D streamline velocity through turbine flow passages between the base-line and the optimum turbine. It is evident from these figures how homogeneous the velocity distribution along the blade stream-wise in the optimum design. It is also clear that the velocity in the optimum design is lower than that in the baseline design.

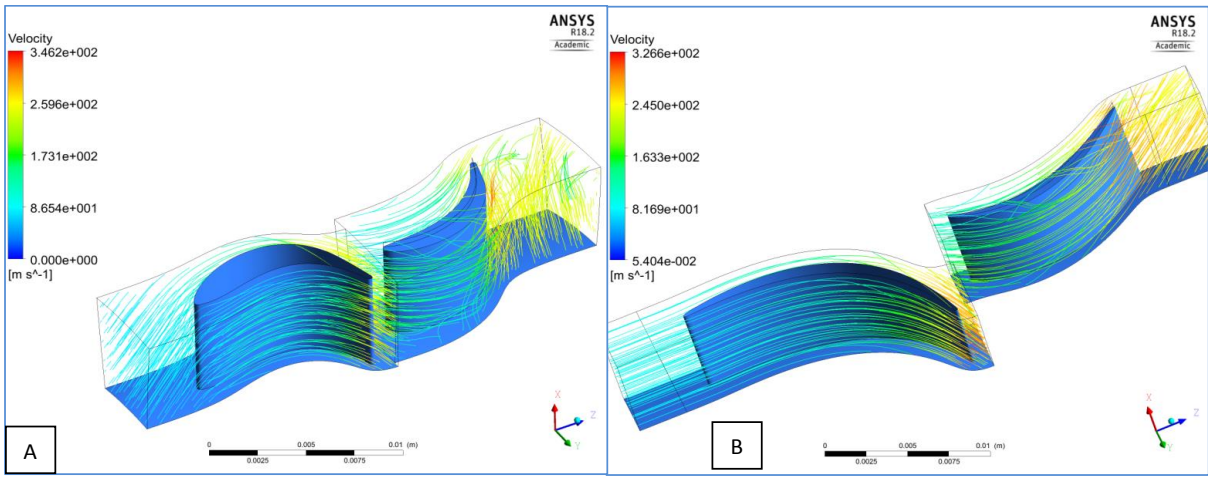

Figure 6-37 3D velocities streamline through turbine passage comparison between (A) base-line turbine and (B) optimum turbine

Figure 6-38 compares the static entropy generation for the base-line blade with optimum blade designs, where the base-line blade has secondary losses resulted in a considerable entropy generation in the suction side which developed downstream. Hence causing a reduction in the turbine efficiency, while in the optimum blade design there is significant overall reduction in the entropy generation.

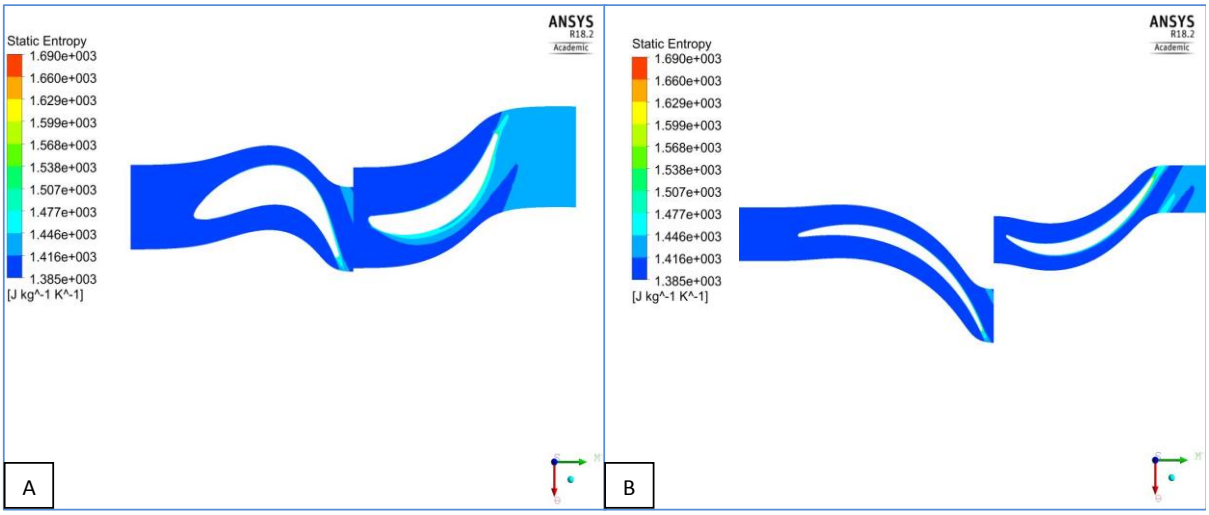

Figure 6-38 Static entropy contours at 50% span of (A) base-line turbine, (B) optimum turbine

6.5 Advanced Blade Configuration Analysis Results:

The use of advanced blade configurations to enhance the turbine performance is another approach developed in this study to investigate the effect of these configurations on a turbine with small blade span. Using Ansys CFX software a parametric study was carried out on four different blade configurations (twist, lean, bow, and sweep) for three case studies: (Stator) when the configuration change was applied to the stator blade only, (Rotor) when the configuration change was applied to the rotor blade only, and (StatorRotor) when the configuration change was applied to the stator and rotor blades at the same time. Results from this investigation are shown in Figure 6-39 to Figure 6-56.

6.5.1 Sweep Blade Configuration Results:

Figure 6-39 and Figure 6-40 show the effects of various rotor and stator sweep angle on the total efficiency and power output. It can be noticed that increasing negative sweep angle decreases the total efficiency and power output for all cases. Increasing positive sweep angle increases the total efficiency and power in the (Stator) case while it does not have a significant effects in the (Rotor) case. However, in the case (Stator) and sweep angle of 30 degree the turbine produces maximum turbine efficiency and output power of 82.4 % and 5185.23W respectively. Figure 6-41 shows blade loading comparison at the stator, rotor and the turbine passages for two cases, the base-line (no sweep just straight blade) and the (Stator) case sweep 30 degrees. Figure 6-41A shows that the stator blade in sweep turbine has a higher acceleration at the end of the blade than that of the base-line turbine stator. Figure 6-41B shows that the rotor blade of (Stator) case sweep 30 degree has higher and more distributed blade loading compared with the base-line rotor. Positive sweep angle increases the blade axial path from a maximum at the blade tip to the original length at the blade hub which efficiently re-distributes the blade loading as clarified by these figures [7] .

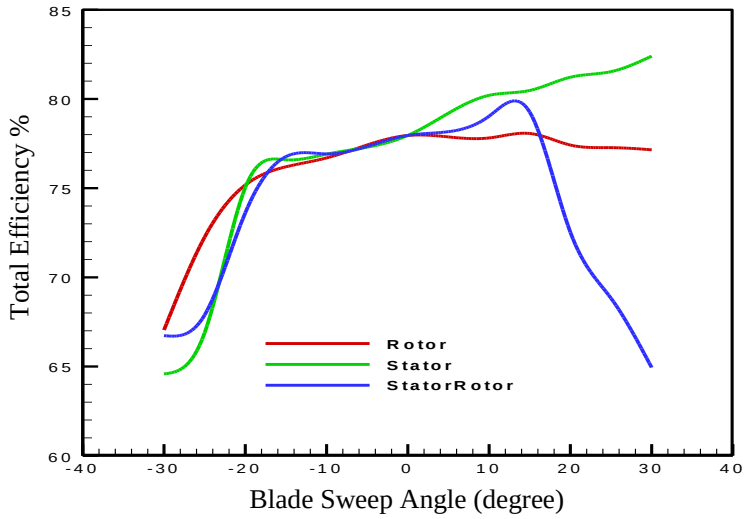

Figure 6-39 Effect of the stator and rotor blade sweep angle on total efficiency

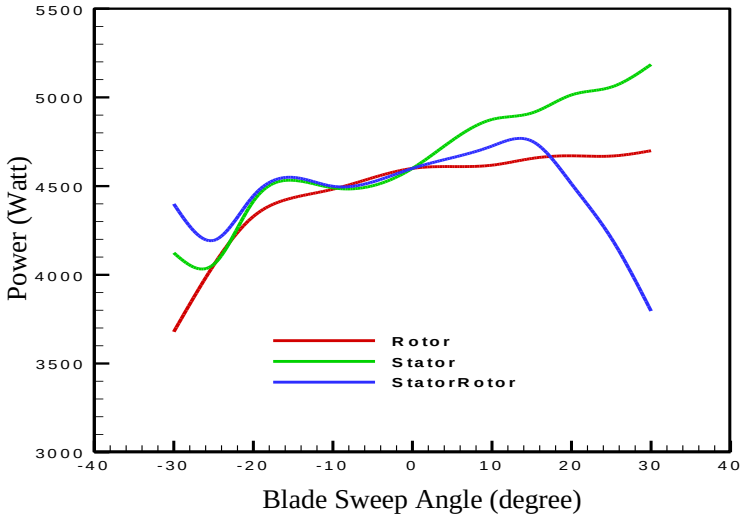

Figure 6-40 Effect of the rotor and stator blade sweep angle on power output [7]

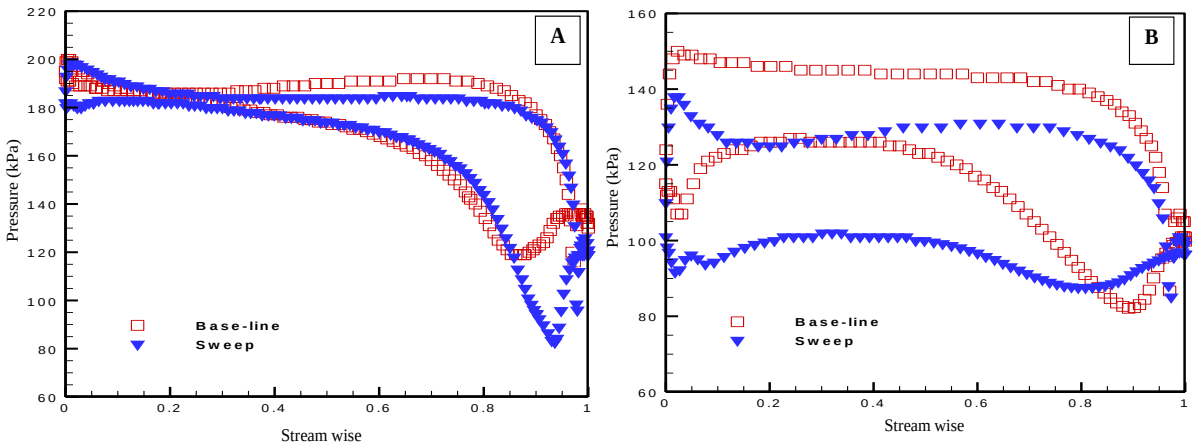

Figure 6-41 Blade loading comparison between the straight blade and sweep blade(Stator case 30 degrees) for (A) stator blade and (B) rotor blade at span 50% [7]

Figure 6-42, A and B compares the 3D streamline velocity through turbine passage between turbine sweep case (Stator) 30 degree and the base-line turbine case. It can be seen from this figure how the homogeneous velocity distribution varies along the blades stream-wise direction in the straight blade and in the sweep blade configuration and further how the flow acceleration in sweep blade is greater than that of the straight blade [7].

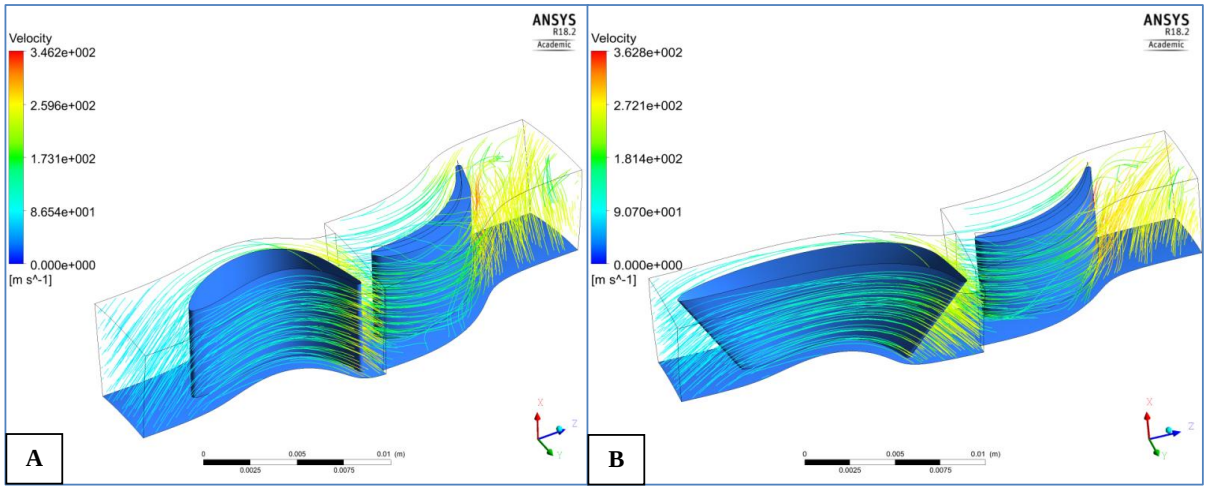

Figure 6-42 3D velocities streamline through turbine passage comparison between (A) base-line turbine and (B) sweep turbine (Stator case 30 degrees)

Figure 6-43 shows the static entropy contours at span 50% for base-line turbine blades and for sweep turbine (Stator case 30 degree). From this figure, it can be noticed that the entropy generated by stator and rotor of the sweep turbine is less than that generated by the base-line turbine which in turn means less losses.

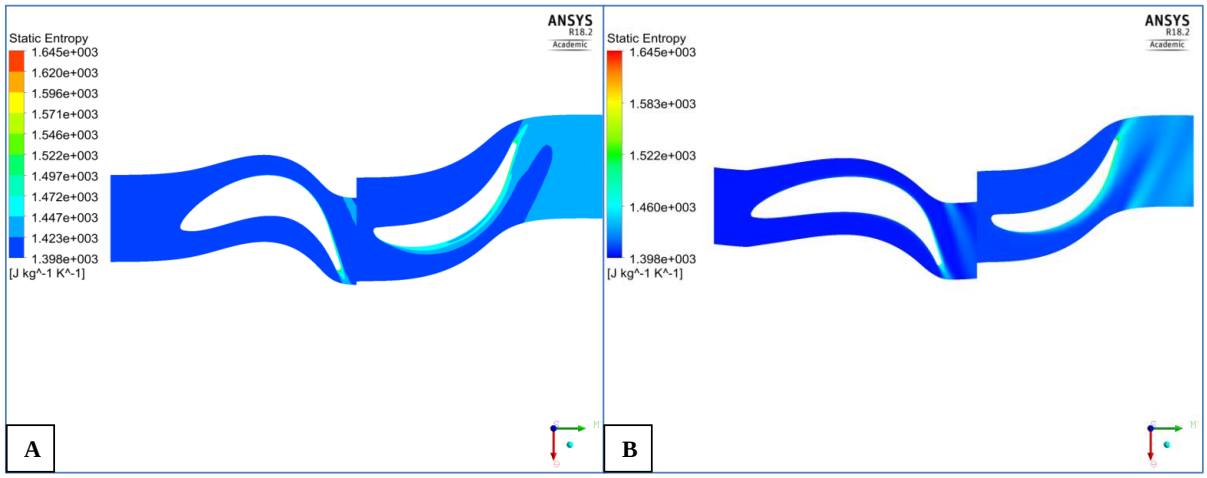

Figure 6-43 Static entropy contours at 50% span of (A) base-line turbine, (B) sweep turbine(Stator case 30 degrees) [7]

6.5.2 Lean Blade Configuration Results:

The blade lean is another blade configuration that affects the turbine performance, thus it has been investigated and the results are depicted in Figure 6-44 and Figure 6-45. These figures explain the effect of blade lean angle ranging from -20 degree to 20 degrees on the turbine efficiency and output power for three cases (Stator, Rotor, and Stator-Rotor). It is worth mentioning here that in the figures for the (Stator-Rotor) the lean angle refers to the stator and rotor where they are in the same direction. From Figure 6-44 it is clear that decreasing the blade lean angle from 0 to -20 degree will decrease the total efficiency for (Stator and Stator-Rotor) cases, while decreasing it for the (Rotor) case will increase the total efficiency to reach a maximum value of 78.75 at a lean angle of -7.5 degrees**.** On the contrary to the negative lean angle, increasing the positive lean angle from 0 to 20 degree increases the total efficiency of the cases (Stator and Stator-Rotor) until maximum values of 78.94% and 79.8% respectively at blade lean angle of 10 degrees, while in the case of (Rotor) the total efficiency decreases. Figure 6-45 shows a similar trend for the power output to that of the efficiency at negative lean angles apart from the Rotor case which is not significantly affected. The rotor negative lean will unload the tip region which reduces the tip leakage effect, while the positive stator lean will unload the hub region which reduces the hub trailing edge blocking effect [7].

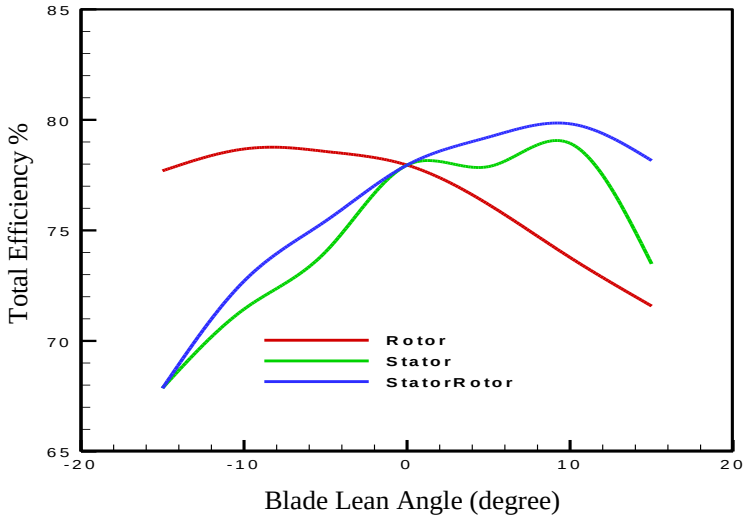

Figure 6-44 Effect of the stator and rotor blade lean angle on total efficiency [7]

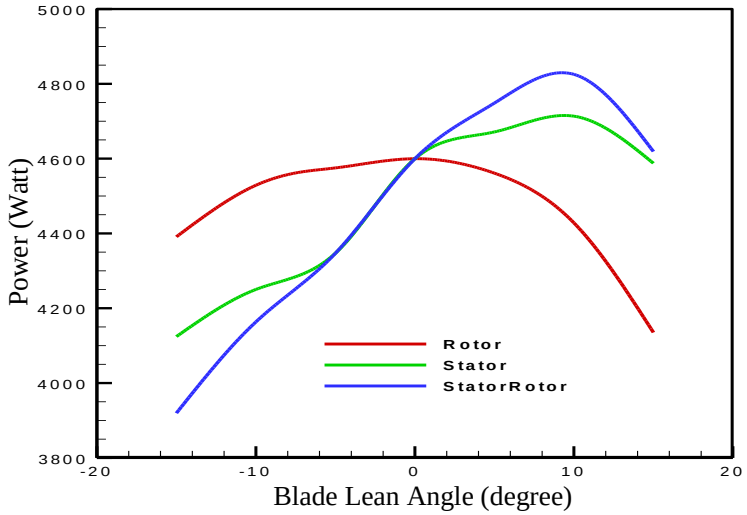

Figure 6-45 Effect of the rotor and stator blade lean angle on power output [7]

Figure 6-46 compares blade loading for two cases the base-line or straight blade and the (Stator-Rotor) case lean 10 degrees which produces better performance in lean cases, for both turbine passages stator and rotor. It can be seen from Figure 6-46A that a leaning stator blade suction side has higher pressure than the base-line stator blade but less loading at the hub

region where blade loading results from the pressure difference between suction and pressure sides.

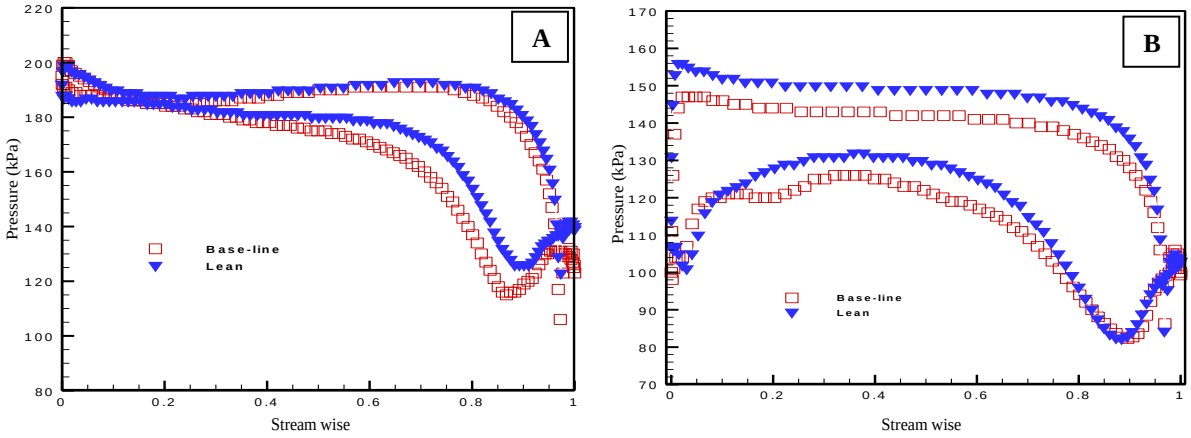

Figure 6-46 Blade loading comparison between the straight blade and lean blade(StatorRotor case 10 degrees) for (A) stator blade and (B) rotor blade at span 25% [7]

Figure 6-47 A and B compare the 3D streamline velocity through turbine passage for the base-line turbine and the lean turbine case (Stator-Rotor) by 10 degrees. It can be noticed from these figures the homogeneous velocity distribution along the blades in stream-wise direction in the base-line blade and in the lean blade configuration, and further how the flow acceleration in the leaning blade is greater than the base-line [7].

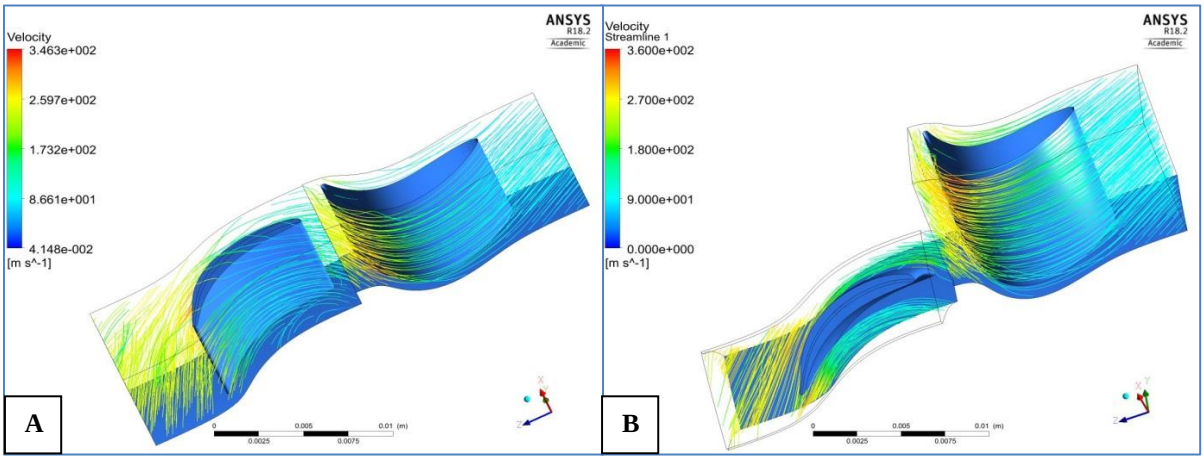

Figure 6-47 3D velocities streamline through turbine passage comparison between (A) base-line turbine and (B) lean turbine (StatorRotor case 10 degrees)

Figure 6-48 shows the static entropy contour at span 25% for base line turbine blades and for leaning turbine (Stator-Rotor) case by 10 degrees. From this figure, it is obvious that the entropy generated by the leaning rotor at span 25% is lower compared with base-line rotor which in turn means more generated power and lower losses**.**

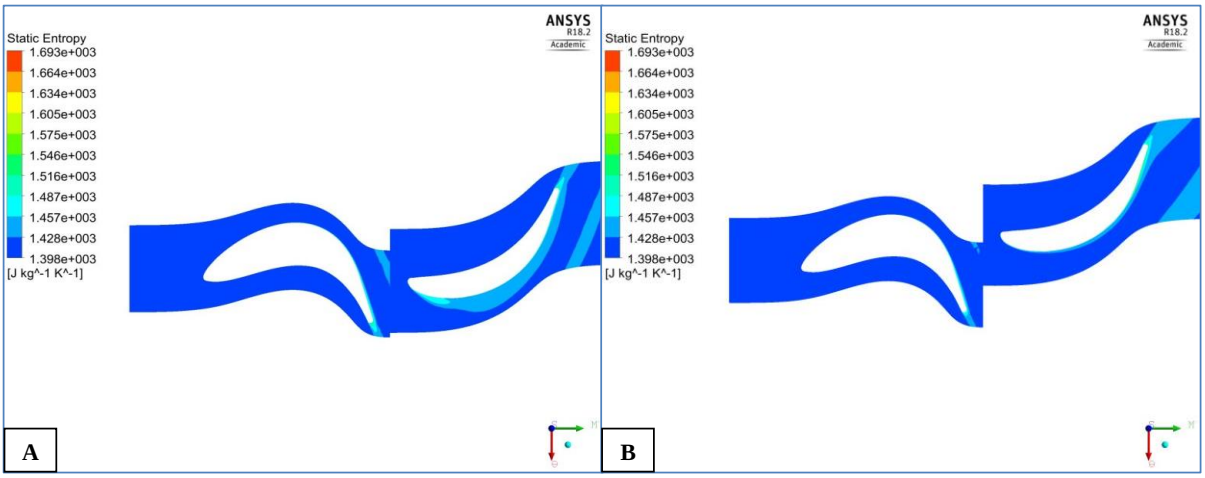

Figure 6-48 Static entropy contours at 25% span of (A) base-line turbine, (B) lean turbine (StatorRotor case 10 degrees) [7]

6.5.3 Twist Blade Configuration Results:

Twisting blade from hub cross section until tip section is an important 3D blade configuration which can be used to improve the blade aerodynamic performance as shown in Figure 6-49 and Figure 6-50. In these figures, the impact of varying the blade twist angle from -30 to 30 degree on the turbine efficiency and output power are explained. From Figure 6-49 it is clear that decreasing the blade twist angle from 0 to -30 degrees decreases the turbine efficiency and output power for all cases, while increasing the blade twist angle from 0 to 30 degrees increases the turbine efficiency and output power until the maximum value for cases (Stator) and (Stator-Rotor). The maximum values for efficiency and output power for the case (Stator) are 80.4 % and 4727.68 W respectively, and for the case (Rotor-Stator) are 78.8 % and 4607

W respectively at blade twist angle 10 degrees. The (Rotor) case does not show significant change with increasing positive twist angle. The positive twist produces better performance because the blade section near to tip area becomes flatter, which accelerates the flow in the axial direction which in turn leads to reduced tip leakage [7].

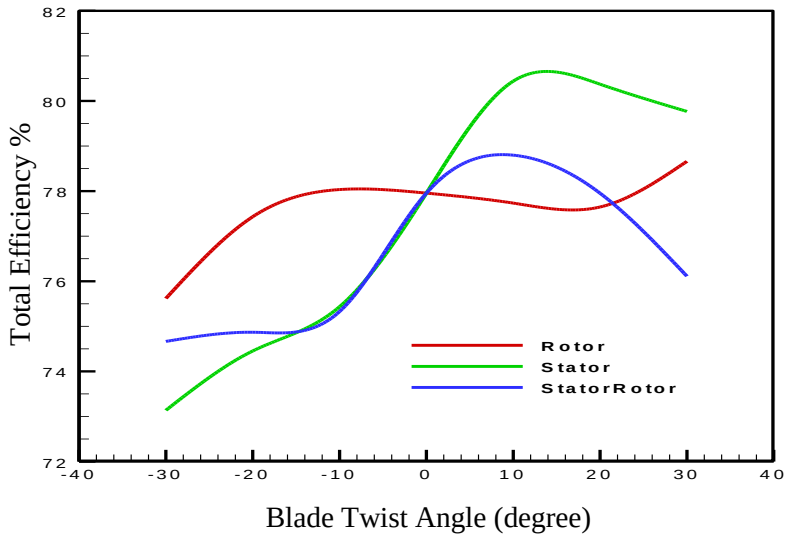

Figure 6-49 Effect of the stator and rotor blade twist angle on total efficiency [7]

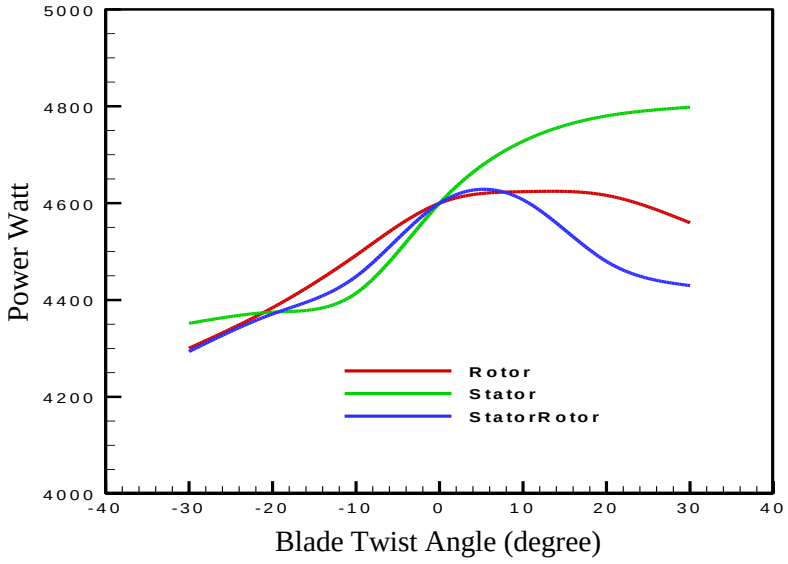

Figure 6-50 Effect of the rotor and stator blade twist angle on power output [7]

Figure 6-51 presents a comparison for blade loading between two cases: the base-line blade and the (Stator) case twist 10 degrees, which produces better performance among twist cases. The comparison was made for both turbine passages stator (A) and rotor (B). It can be noticed from Figure 6-51A that the stator twist blade has better loading distribution along streamwise direction compared to the base-line stator blade. It is evident from Figure 6-51B that the pressure in both pressure and suction sides in twist turbine is higher and the loading is less compared to the base-line blade. Figure 6-52A and B compare the 3D streamline velocity through turbine passage between the base-line turbine and the twist turbine case (Stator) 10 degrees. These figures show the homogeneous velocity distribution along the blades stream-wise in the base-line blade and in the twist blade configuration and they further show how the flow acceleration in twist blade is greater than the base-line [7].

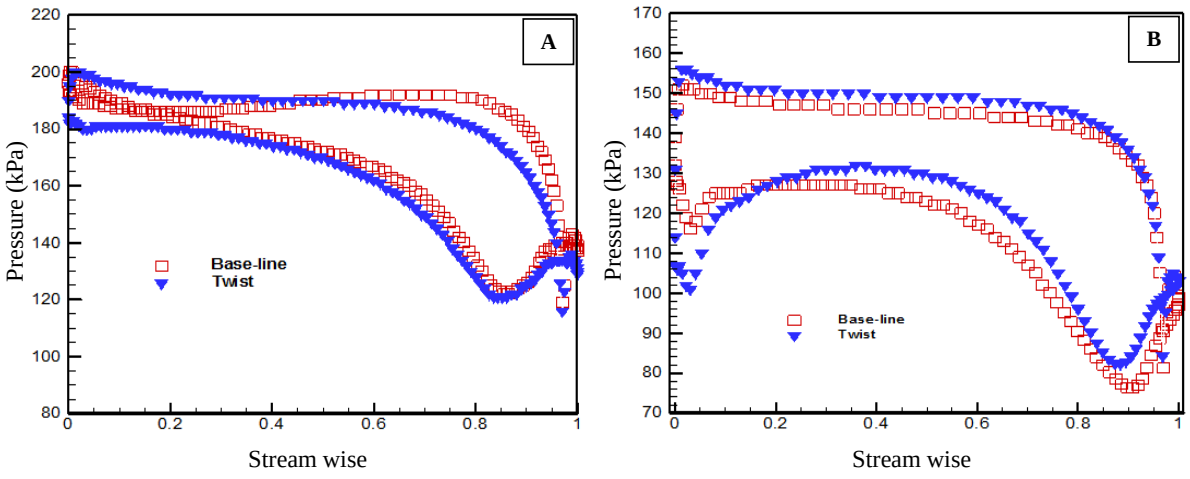

Figure 6-51 Blade loading comparison between the straight blade and twist blade(Stator case 10 degrees) for (A) stator blade and (B) rotor blade at span 75% [7]

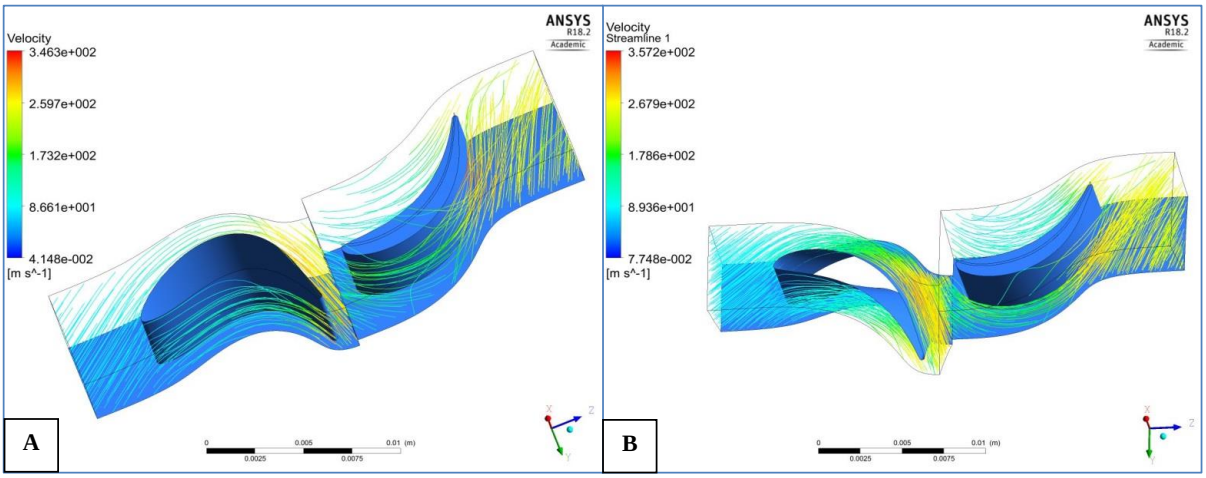

Figure 6-52 3D velocities streamline through turbine passage comparison between (A) base-line turbine and (B) twist turbine (Stator case 10 degrees)

Figure 6.53 shows that the twist has an effect on the tip section, and the static entropy contour at span 75% for base line turbine blades and twist turbine (Stator) case 10 degree. It can be noticed that the generated entropy by twisted stator turbine blade is less than the base-line one, especially at the rotor suction side which means less flow separation at this region.

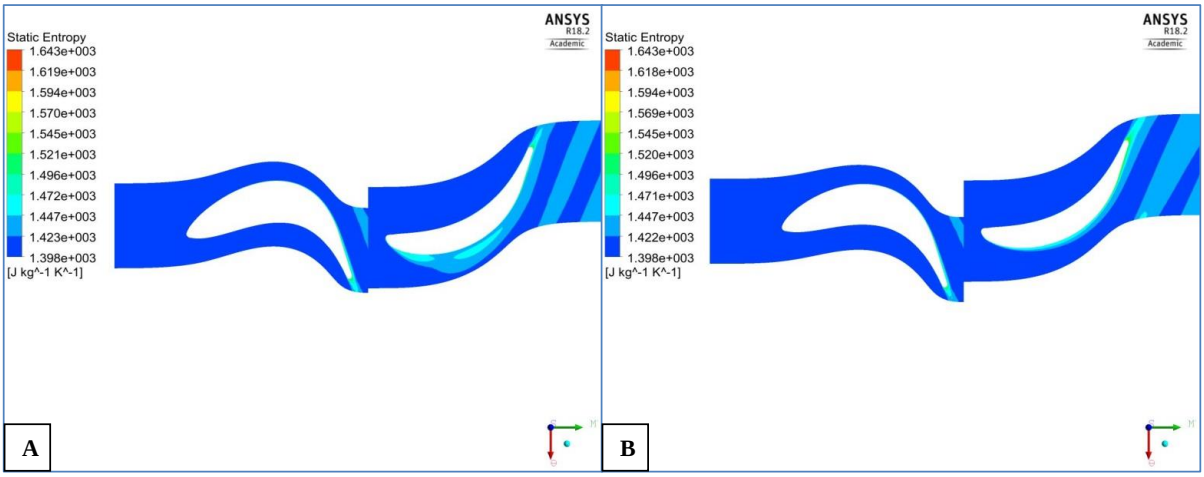

Figure 6-53 Static entropy contours at 75% span of (A) base-line turbine, (B) twist turbine (Stator case 10 degrees)

6.5.4 Bow Blade Configuration Results:

Figure 6-54 and Figure 6-55 clarify the effects of changing the blade bow angles for the rotor and stator from 1.4 degrees to 4.5 degrees on small scale axial turbine total efficiency and output power. It can be noticed that the bow blade configuration degrades the power output and total efficiency for all cases, with the (Stator) case having the worst performance while the Rotor case suffers lower effect. In the bow configuration, the mid-span section will be more loaded due to its higher skew compared to end walls sections [7]. The mid-span static entropy comparison between base-line turbine and bow blade turbine case (Stator-Rotor) 4.5 degree is shown in Figure 6-56. This figure clarifies how the entropy generation by bowed turbine rotor blade is larger than the base-line case especially at the outlet region on the suction side of the blades.

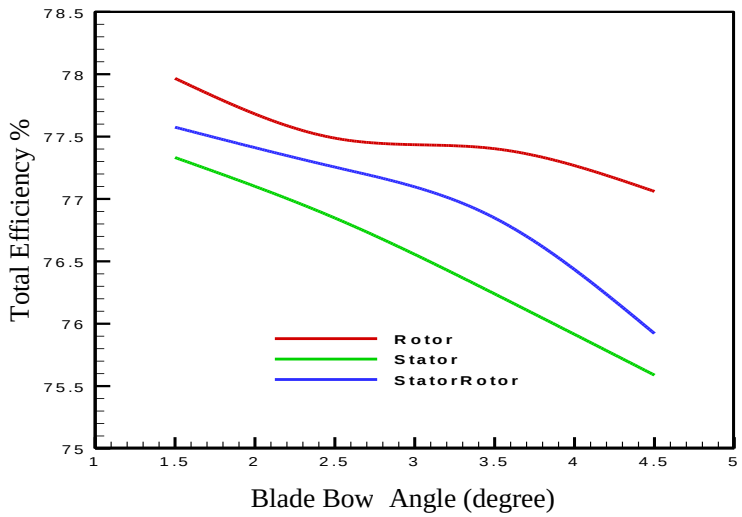

Figure 6-54 Effect of the rotor and stator blade bow angle on total efficiency [7]

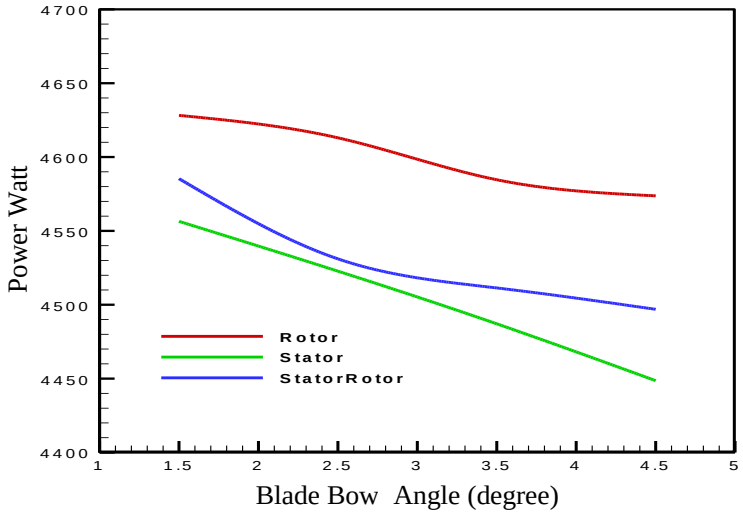

Figure 6-55 Effect of the stator and rotor blade bow angle on output power [7]

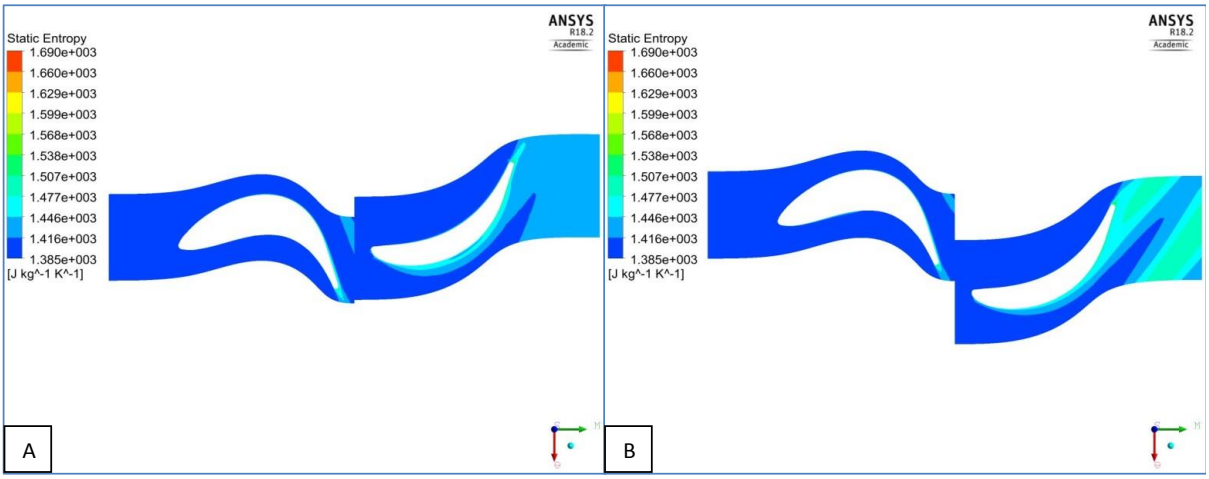

Figure 6-56 Static entropy contours at 50% span of (A) base-line turbine, (B) bow turbine (StatorRotor case 4.5 degree) [7]

6.6 Dual-Stage Small-Scale Axial Turbine Results:

Part of work in this section has been published by the author [55].

In the previous sections, the expansion ratio for turbine was 2 but to increase the cycle efficiency as presented in chapter 3 the expansion ratio needs to be increased. Such increase in the expansion ratio requires increasing the turbine number of stages. Therefore this section investigates the development of non-repeated dual-stage axial small-scale turbine for a nitrogen cryogen hybrid Rankine system. The same turbine design methodology used in the previous sections including the mean-line 1D analysis integrated with 3-D ANSYS CFD analysis has been used in this investigation. The outputs in terms of isentropic turbine efficiency and output power of comparative parametric study for three turbine types: single stage, two repeated stages and two non-repeated stages at design and off-design boundary conditions such as expansion ratios, rotational velocity and mass flow rate are presented in Figure 6-57 to Figure 6-66 [55]. The second stage blade profile for the two repeated stages are designed just same as first stage while the two non-repeated stages are designed according to suitable flow directions.

Figure 6-57 depicts the effect of turbine expansion ratio on turbine efficiency and power output for the three turbine types at turbine expansion ratios ranging from 1.5 to 3. Figure 6-57A shows that increasing expansion ratio increases the efficiency in both two-stage configurations, but decreases the efficiency in the single-stage turbine due to the over-speed occurring in the single-stage rotor. The isentropic efficiency for the single-stage is higher than that for the two-stage turbines for expansion ratios less than value of 2 because the flow of nitrogen is very slow in the two-stage turbines with low expansion ratios. It is important to point out here that the study [153] did not include low expansion ratios where axial single-stage turbines have an advantage. After the expansion ratio increased above the value of 2 the

performance of the two-stage non-repeated annular area becomes better than the other two types [55]. At the highest expansion ratio of 3, the efficiencies of the single-stage, two-stage repeated annular area, and two-stage non-repeated annular area are 74.6%, 78.2%, and 81.4% respectively [55]. Figure 6-57B shows approximatley a linear relationship between power output and expansion ratio for all three turbine configurations. The gradient of the line representing the linear relationship for the two-stage non-repeated annular area is higher than that for the other two configurations. This is because the line commences at a relatively low power output (1.3 kW, equal to that of the two-stage repeated annular area) at an expansion ratio of 1.5 but increases to a relatively high value (8.5 kW, equal to that of the single-stage) at an expansion ratio of 3. The single-stage turbine has a higher power rate because increasing the expansion ratio increases the flow rate in the single-stage higher than that of the other two-stage arrangements, as shown in Figure 6-58. This figure indicates that at a high expansion ratio (=3) the single-stage has a higher flow rate of 0.18 kg/s, and so is not as efficient as the two-stage non-repeated annular area where the flow rate is 0.15 kg/s. However, both arrangements produce the same power output of 8.5 kW [55]. The effect of configuration on the flow rate has not been included in former studies such as [153].

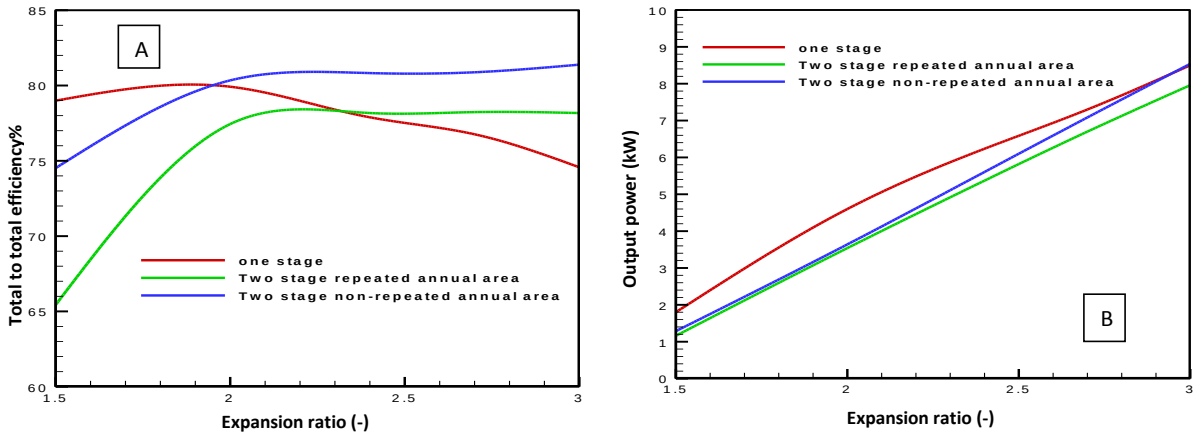

Figure 6-57 Effect of the expansion ratio on efficiency and output power: (A) total efficiency; (B) output power [55]

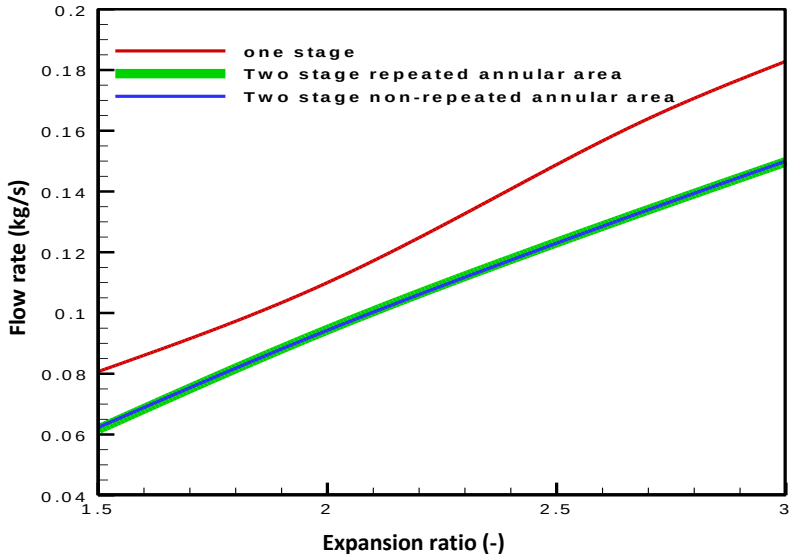

Figure 6-58 Effect of the expansion ratio on the turbine flow rate (kg/s) [55]

Figure 6-59 gives an indication of the distribution of power output between first and second stages of the two-stage repeated and non-repeated annular area axial turbines at rotational speeds ranging from 20k to 100k RPM. For the two-stage repeated annular area turbine (Figure 6-59A) the difference between first and second stage is high. Both bars show the same rising trend up to about 50k RPM, at which the power output of the first stage reaches about 45% of the power output of the second stage [55]. Above the 50k RPM the bars diverge and the power output of the first stage decreases while the power output of the second stage continues to increase, at least up to 80k RPM. However, the difference in power output between the stages increases with rotational after 50k RPM, and at 80k RPM the first stage produces about 20% of the power output of the second stage, which affects the performance. In the two-stage non-repeated annular area turbine shown in Figure 6-59 B, the difference between the first and second stage power output averages approximately 14%. It is clear that the two-stage non-repeated annular area turbine gives more balanced and stable performance at higher speeds than the two-stage repeated annular area turbine [55].

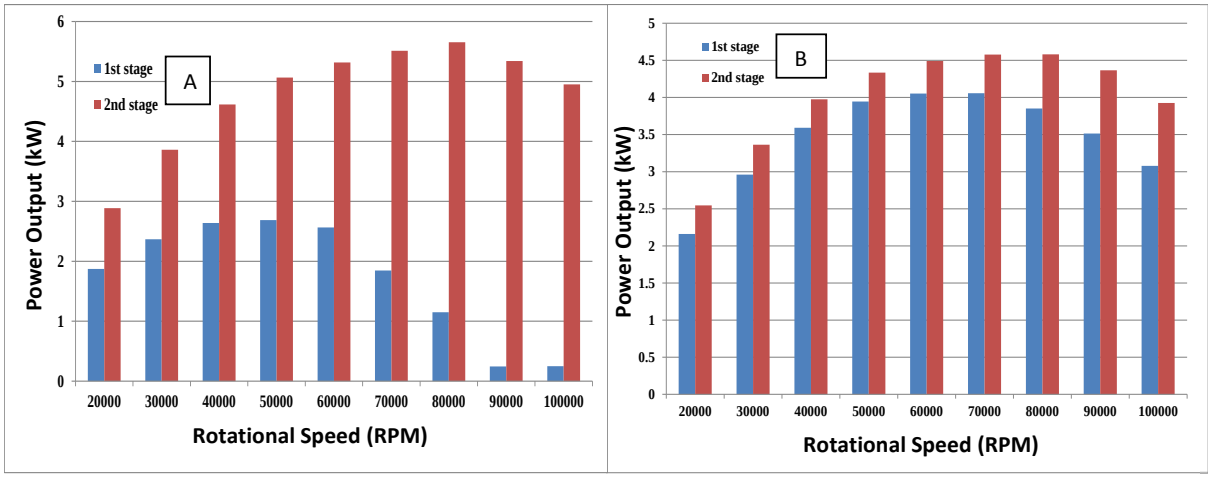

Figure 6-59 Power output of each stage at a different rotational speed of turbines (A) repeated stages (B) non-repeated stages [55]

Figure 6-60 shows details of rotor blade loading for both pressure sides (PS) and suction side (SS) for all three turbines configurations through a non-dimensional stream-wise meridional coordinate at an expansion ratio of 3 and 50% span. The area bounded by the two curves PS and SS represents the amount of work produced by the rotor blade which increases with increasing expansion ratio [55]. The difference between SS load curve and PS varies stream-wise from the inlet to the outlet and from being low at the beginning of the blade to a maximum at the end section of the blade. The maximum loading in the single-stage occurs at streamline location of 0.98 while in both two stage configurations it is located at a streamline position of 0.87. Figure 6-60A shows that the single-stage is more loaded than the other configurations. Comparison between Figure 6-60B and C discloses that loading of the first stage of the two-stage repeated annular area increased by 123.7% in the second stage while in

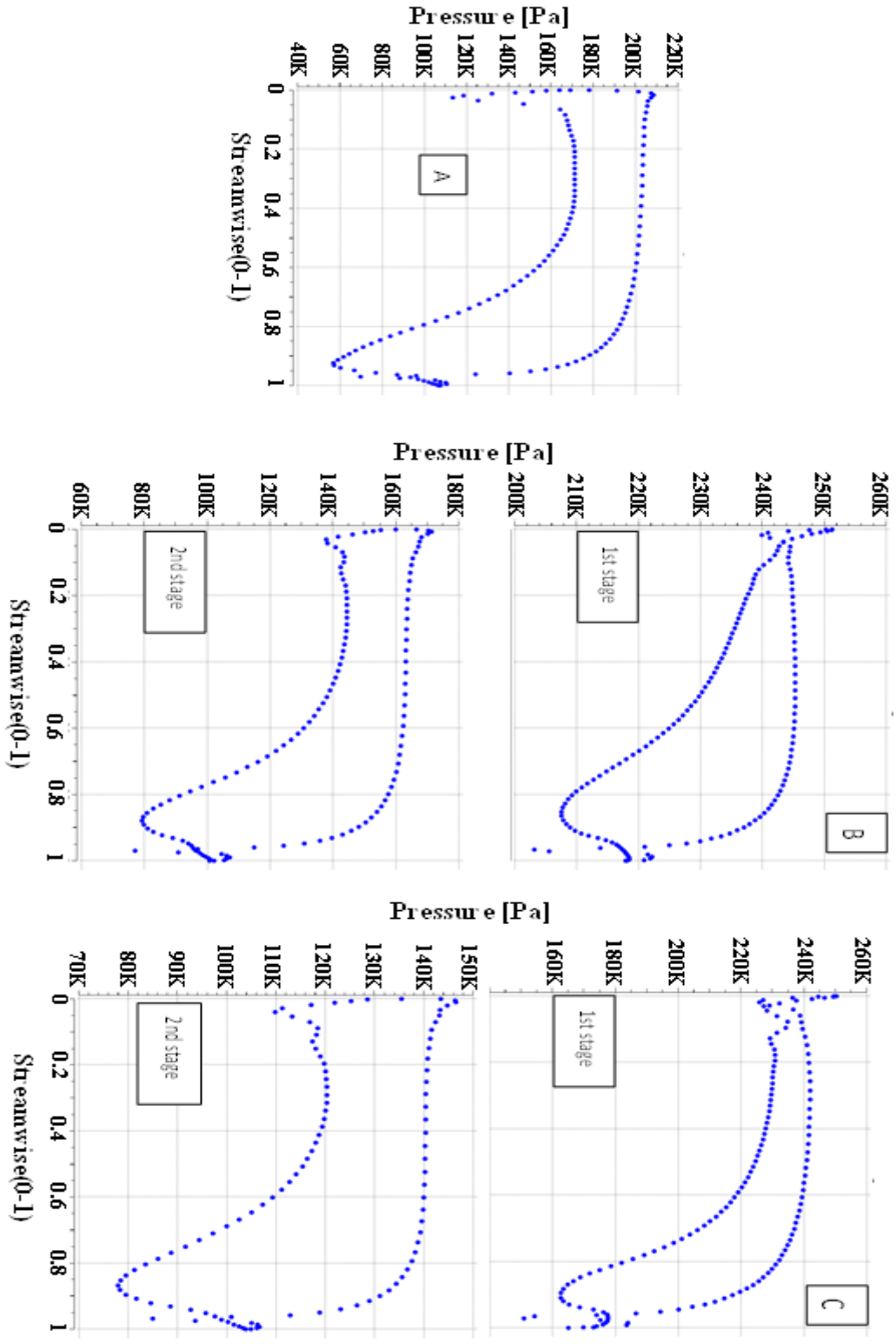

Figure 6-60 Turbines rotors blade load distribution at 50% span for (A) single stage, (B) repeated stages (C) non-repeated stages [55]

the two-stage non-repeated annular turbine it decreased by 18.7%, which indicates that the latter is more balanced and more stable [55]. Figure 6-61 presents the blade to blade pressure distribution across the three turbine configurations. It is noticeable that the maximum pressure is at the turbine inlet and is a minimum at the outlet. Figure 6-61 A shows that the pressure drops quickly in the single-stage, while in the other two configurations shown in Figure 6-61 B and Figure 6-61 C there are four recognizable regions of pressure drop [55]. The 3D velocity streamline distribution across the axial turbines stages for the three configurations are presented in Figure 6-62 A, B, and C. The flow in all three types is uniform only in the rotor shroud area where the tip clearance allows the fluid to move from rotor pressure side (high pressure) to the rotor suction side (low pressure). The single-stage rotor outlet has the maximum velocity while the second stage rotor outlet for the two-stage non-repeated annular area has the minimum [55].

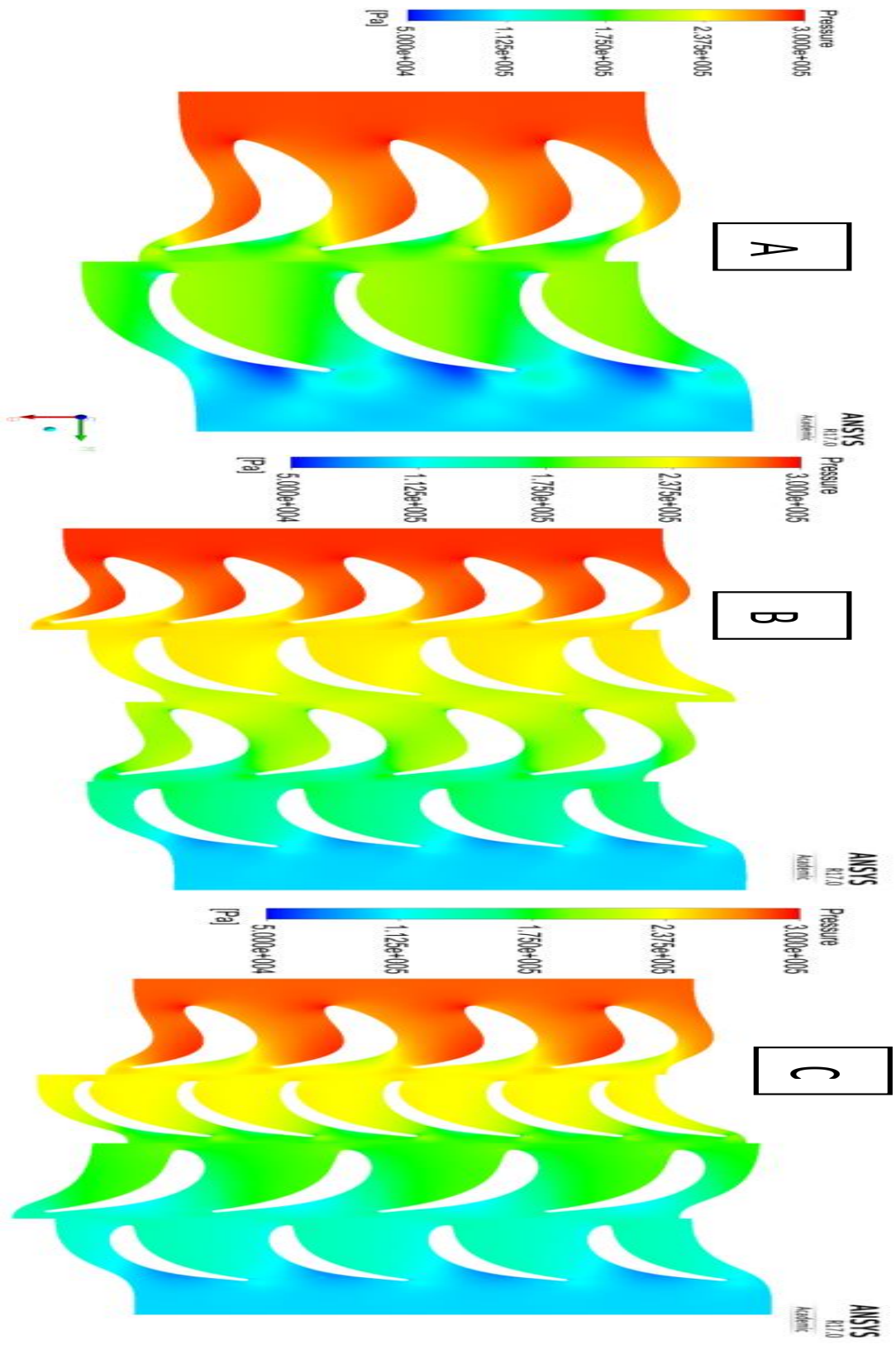

Figure 6-61 Turbines stage pressure contour distribution at span 50% for (A) single stage, (B) repeated stages (C) non-repeated stages [55]

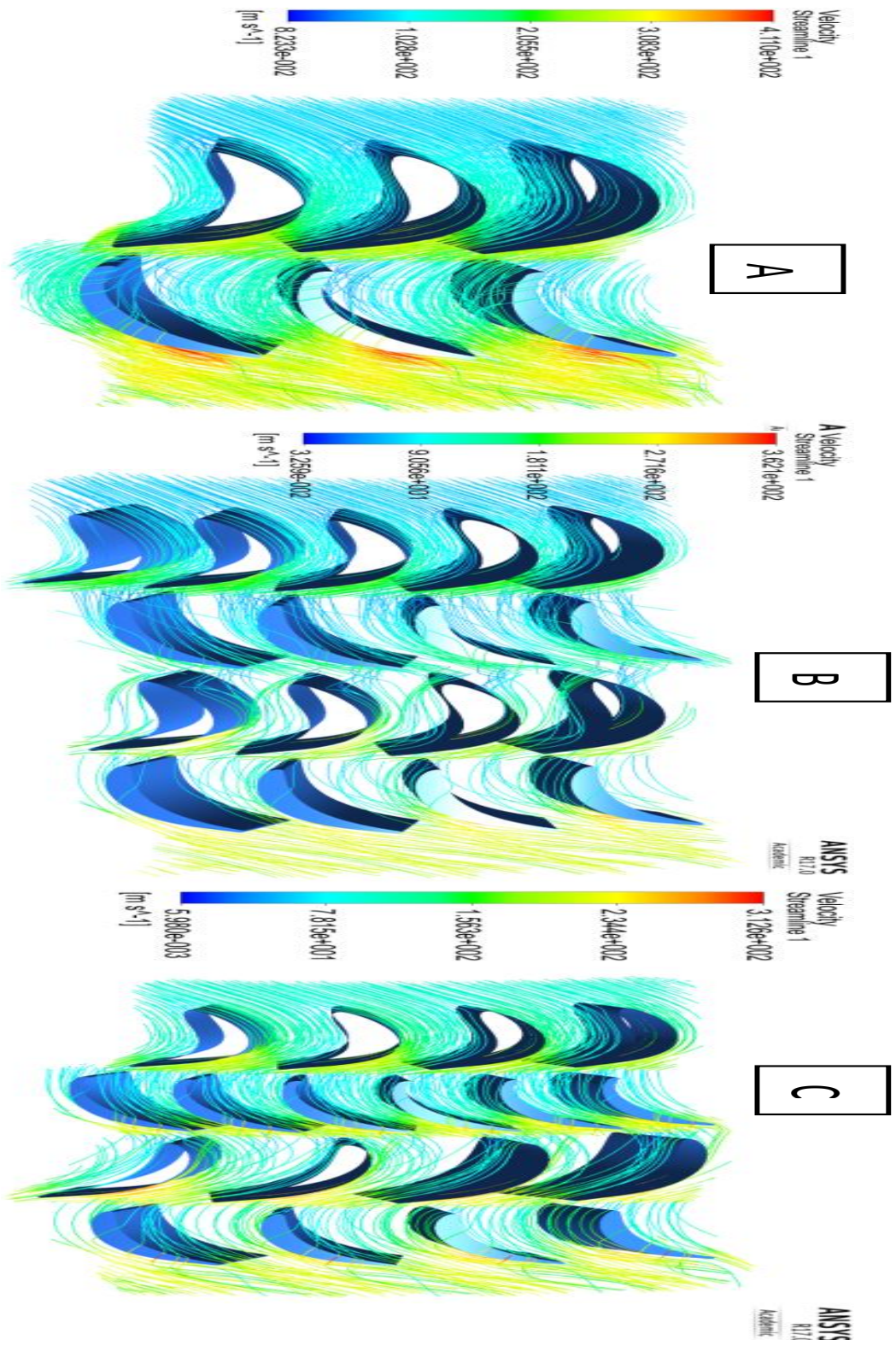

Figure 6-62 Turbines 3D velocity streamlines for (A) single stage, (B) repeated stages (C) non-repeated stages [55]

Figure 6-63 depicts the local Mach number distribution through the stages of the three axial turbine configurations. It can be noticed that at an expansion ratio of 3 the single-stage turbine has a supersonic Mach number reaching 1.4 at the rotor outlet as shown in Figure 6-63A. Similarly, for the two-stage repeated annular area turbine, the second stage presents a sonic flow of Mach number 1.1 at the rotor outlet, (see Figure 6-63B). In contrast, the Mach number of the two-stage non-repeated annular area for the second rotor stays within sonic flow limits ($M \leq 0.9$) as shown in Figure 6-63C. These show the advantages of the two-stage non-repeated annular area configuration, where losses generation by shock waves formation are avoided. Figure 6-64 presents a more detailed view of the acceleration development through the turbine stages, showing the stream-wise, area-averaged relative Mach number versus averaged normalized dimensionless distance from the inlet to the outlet of the entire turbine stage for all three configurations [55]. Figure 6-64A confirms the over-speed problem in the single-stage rotor due to high expansion ratio and high flow rate. The comparison between Figure 6-64B and Figure 6-64C show that there is unbalanced acceleration through the two repeated stages turbine. However, the two non-repeated stages turbine overcomes this unbalance problem and accelerates the flow smoothly within a sonic flow region. On the whole, during the expansion through the turbine stages, the fluid density decreases which in turn increases the flow velocity; so that in high expansion ratio the over-speed problem becomes noticeable in the single and the repeated turbines. With the two-stage non-repeated annular turbine the annular area increases from a minimum at the inlet to a maximum at the outlet in such a way that balances the decrease in the fluid density and overcomes the over-speed problem [55].

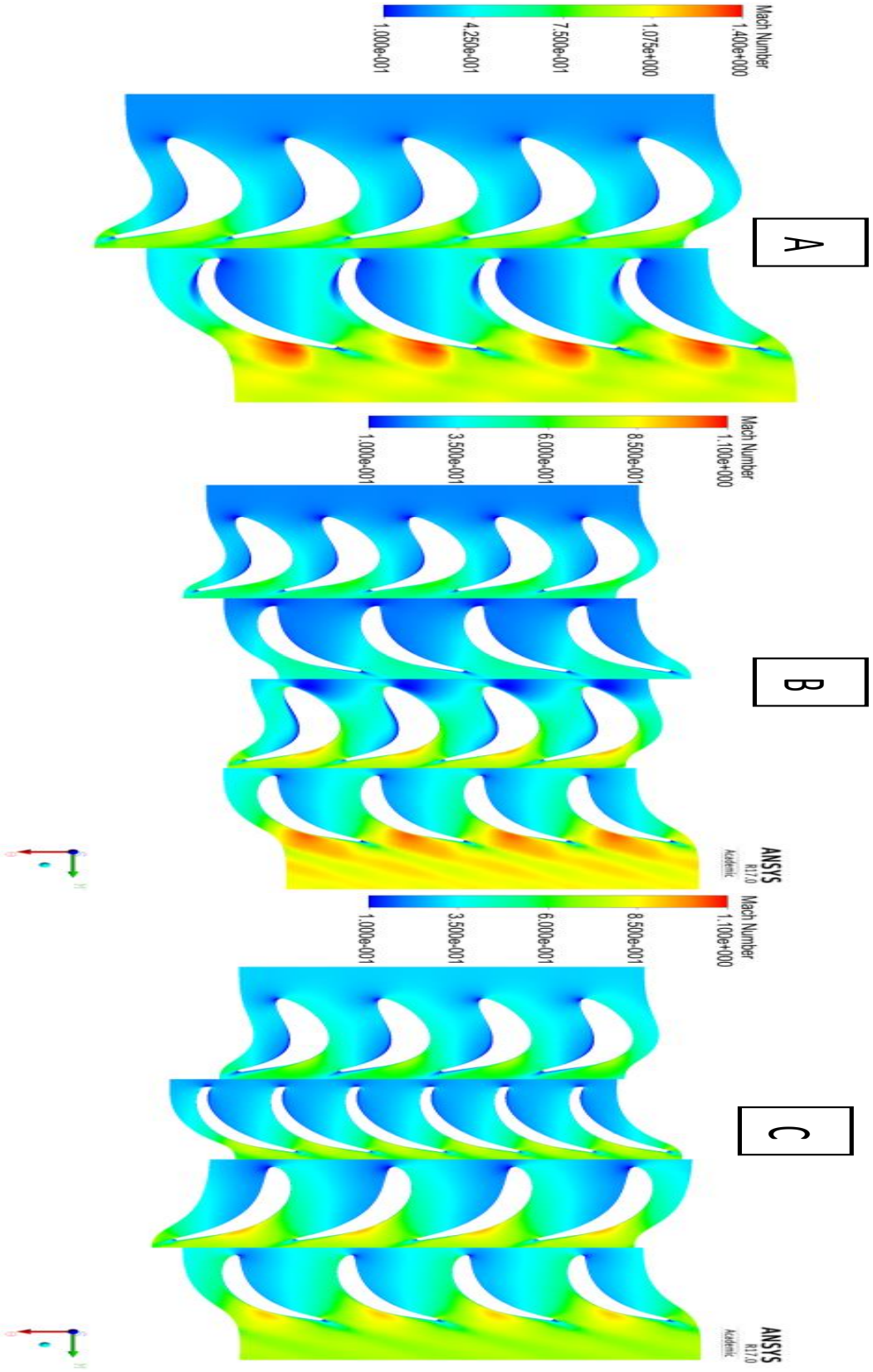

Figure 6-63 Turbines stages local Mach number distribution contour at expansion ratio 3 for (A) single stage, (B) repeated stages (C) non-repeated stages [55]

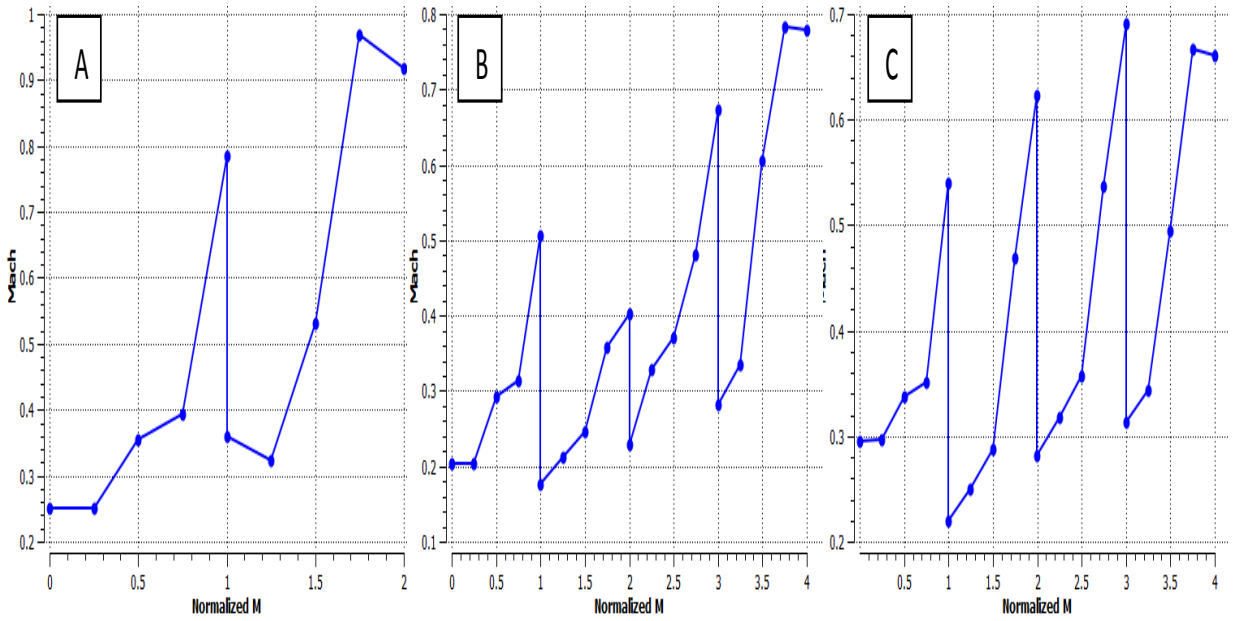

Figure 6-64 Stream-wise area averaged relative Mach number versus averaged normalized M from the inlet to the outlet of the full turbine stage for (A) single stage, (B) repeated stages (C) non-repeated stages [55]

Figure 6-65 shows the effect of changing the stream-wise slope on flow rate and turbine efficiency for the two-stage non-repeated annular area axial turbine at constant expansion ratio of 3. It can be seen that there is an optimum value for the slope (here this is 2^{o}), which gives the best acceleration balance and turbine performance to achieve an efficiency of 81.4% [55]. Increasing the slope will increase the mass flow rate because increasing the slope increases the annular area through the turbine passage. It is evident that for zero slope the second stage rotor will suffer from over-speed problems see Figure 6-66 A, while a large value of the slope reverses the over-speed problem to the first stage as shown in Figure 6-66 B. Thus, there is an optimum value for the slope which will balance the flow acceleration through the turbine stages [55].

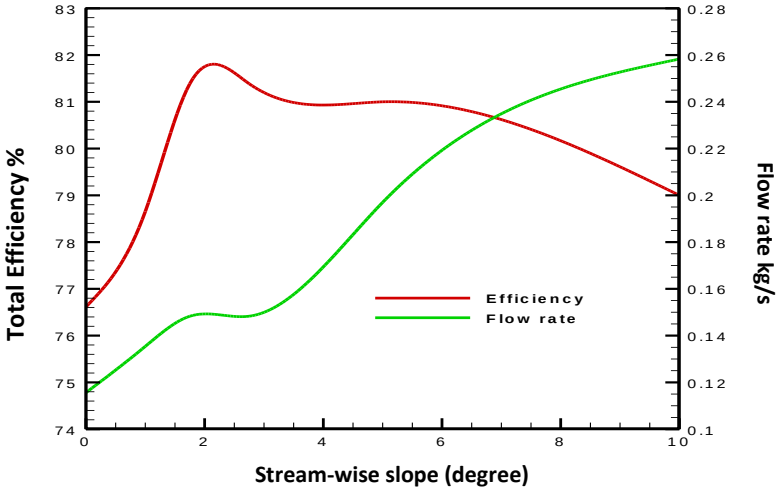

Figure 6-65 stream-wise slope versus total efficiency and flow rate for non-repeated stage turbine [55]

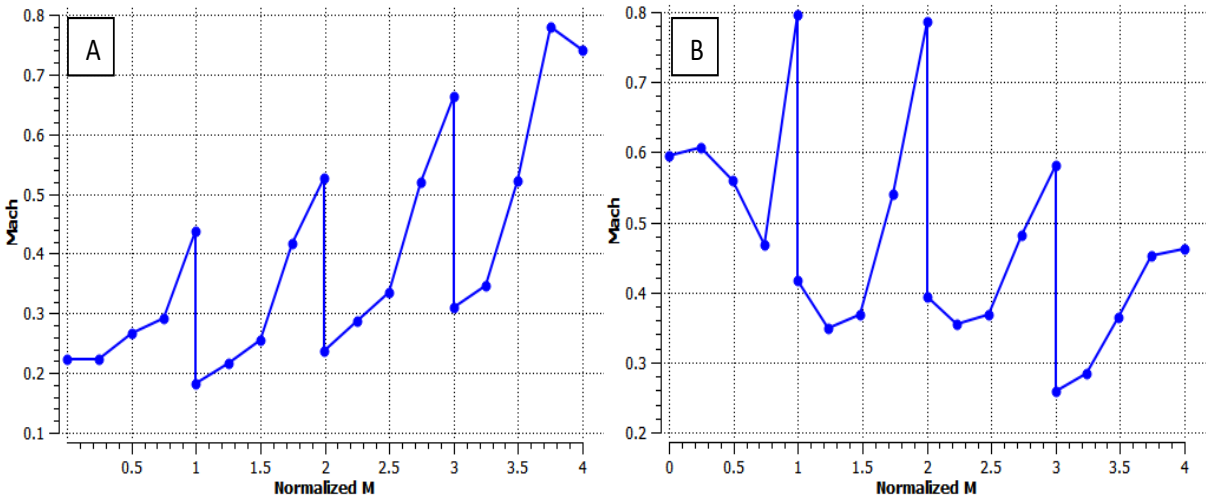

Figure 6-66 Stream-wise, area-averaged relative Mach number versus averaged normalized M from the inlet to the outlet of the two turbine stages for (A) Slope 0.0 degree, (B) Slope 10 degree [55]

6.7 Axial Turbine Experimental and CFD Model Validation Results:

The performance testing were carried out using the compressed air test rig explained in chapter 5 section 5.3 for the three manufactured single-stage axial turbines with three different blade heights. The blade height parameter is considered as one of the important design parameters in the small-scale turbine. Therefore, blade heights (4mm, 6mm, and 8mm) were used to achieve experimental parametric study for the axial small scale turbine and to validate CFD modelling and methodology. The small blade heights (4mm and 6mm) were used for the first time in small-scale experimental work; such data is very valuable in addressing the knowledge gap related to the minimum blade height that can be used in small-scale axial turbines.

6.7.1 CFD Validation Model:

With the objective of decreasing the hydraulic duct difference between the CFD model and the experimental prototype, the inlet reducer passage and the outlet manifold pipe domains were imported from SolidWorks to the ANSYS CFX to include them in the CFD model as shown in Figure 6-67. The measured inlet turbine temperature and pressure which are located at the reducer inlet while measured outlet temperature and pressure was located at the outlet manifold pipe. The CFD model setup features such as turbulence scheme, criteria of convergence, and the operation conditions arrangement used are same as in the methodology chapter 4 to ensure the validation accuracy. Figure 6-68 to Figure 6-70 show a sample of the CFD results for these integrated domains.

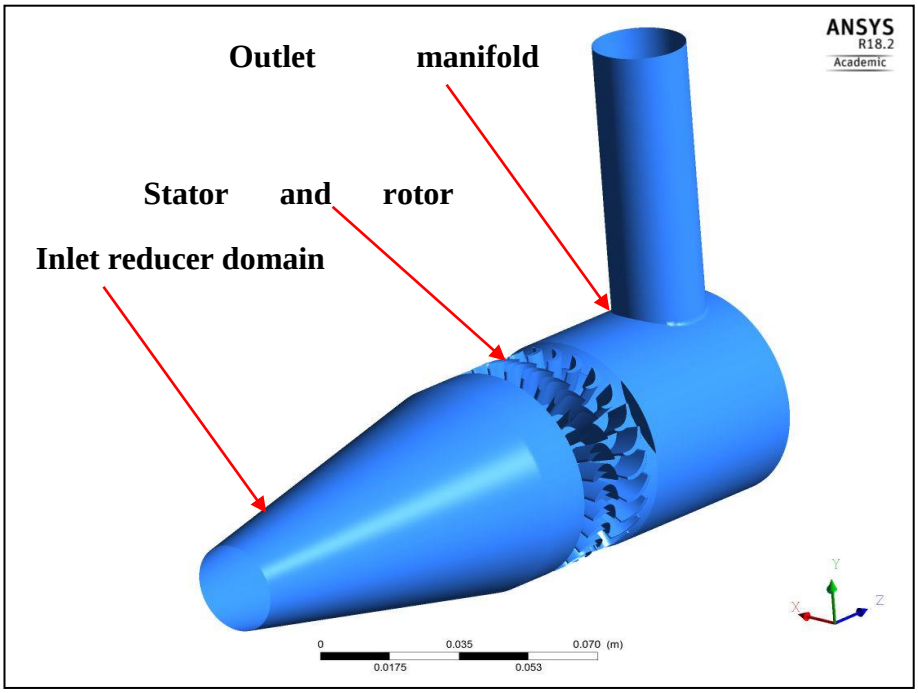

Figure 6-67 integrated geometry full domains for CFD model used in the validation

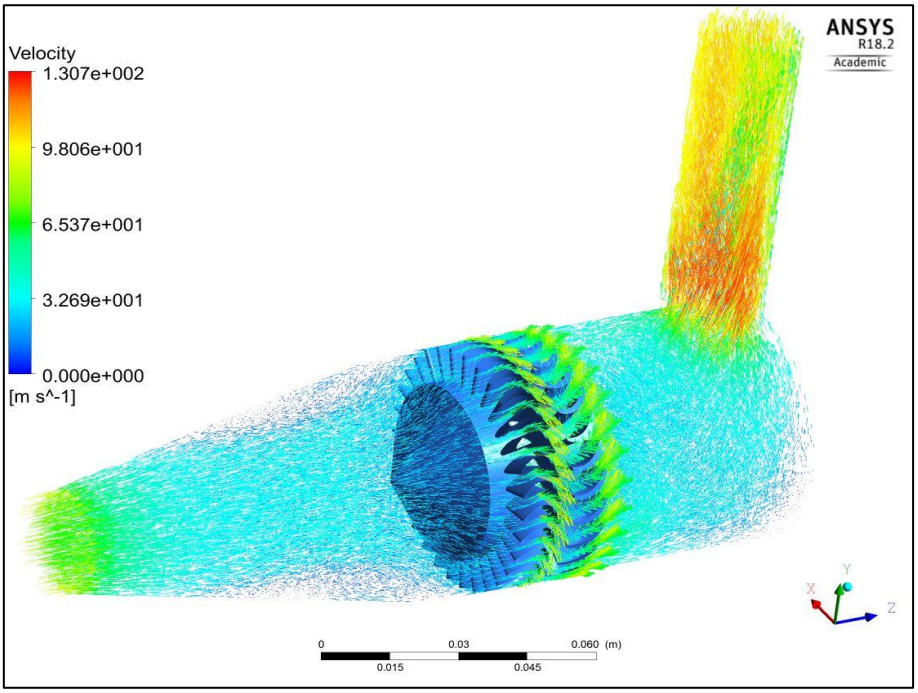

Figure 6-68 3D velocity vectors for full domains CFD validation model

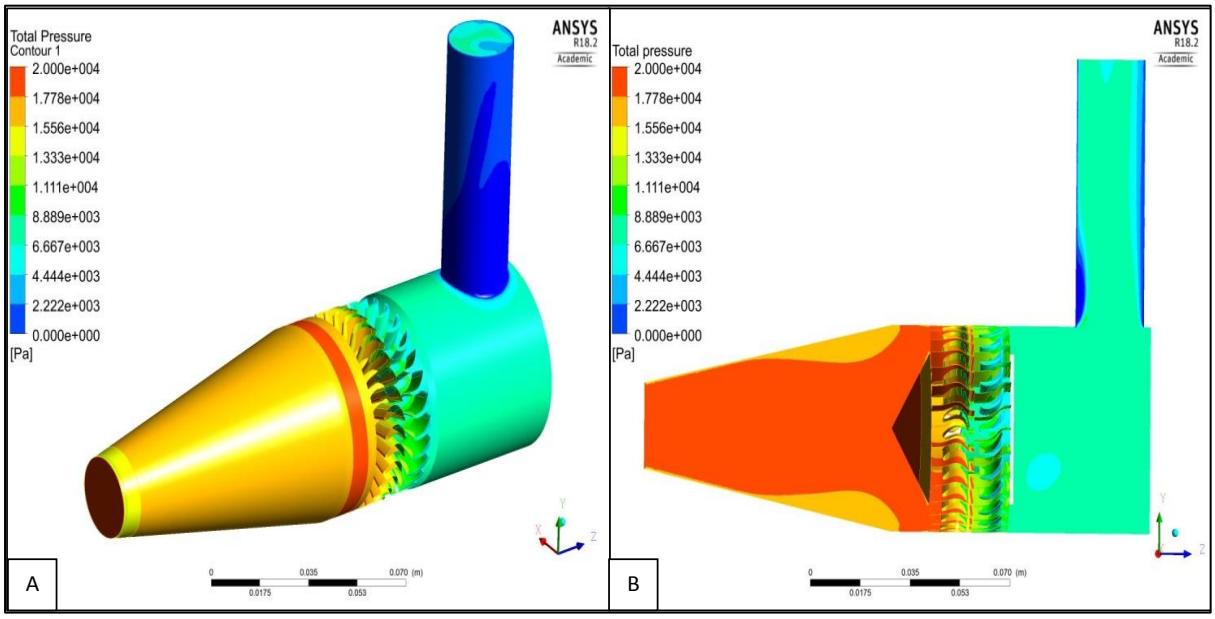

Figure 6-69 Gauge total pressure contour distribution through full CFD validation model for (A) 3D and (B) sectional domains

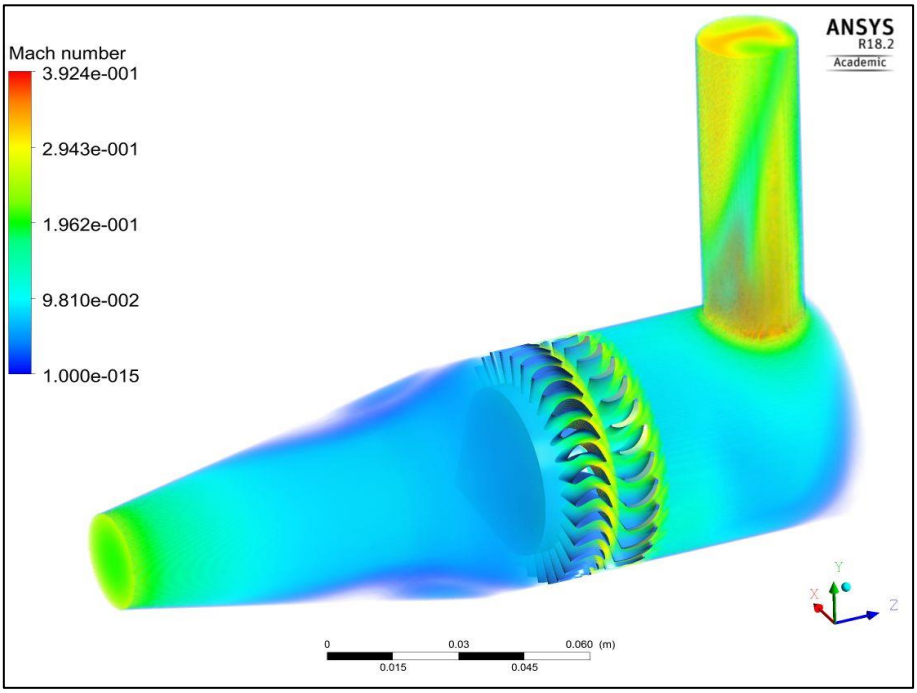

Figure 6-70 3D Mach number contour for full domains CFD validation model

6.7.2 Turbine Assembly FEA Results:

Prior to the manufacturing of the turbine, FE ANSYS structural analysis for the complete turbine assembly had been performed to ensure mechanical integrity of the stator, rotor, shaft and casing under the operating pressure and rotational velocity. The complete turbine assembly used in ANSYS structural analysis is demonstrated in Figure 6-71. The turbine shaft and ball bearing were manufactured from stainless steel which has the material tensile strength (505 MPa). The rest of the turbine parts were manufactured using the RGD 525 PolyJet material with a tensile strength of 60-70 MPa using 3D printing manufacturing technology. The simulation and the design process ensure that during the operating conditions the maximum stress in any part will not exceed its tensile strength, also the maximum deformation in the rotor blades needs to be lower than tip clearance of the rotor blade which is (0.5 mm). These design conditions were verified based on two parameters: total deformation and von-Mises stress. The integration between ANSYS CFX module and ANSYS structural analysis module is done by ANSYS software package to ensure that the ANSYS CFX aerodynamic solution outputs (pressure distribution and rotational speed) are used by ANSYS structural analysis module as input data. Figure 6-72 shows the overall distribution of Von-Mises equivalent stress on complete turbine assembly indicating that the maximum stress concentration is in the shaft which justifies using stainless steel material for the shaft to handle this stress levels. Figure 6-73 and Figure 6-74 depict the distribution of maximum total deformation for all turbine parts indicating a maximum deformation in the rotor blade less than 0.5 mm which is less than the rotor tip clearance. As the maximum deformation of the turbine case occurs at outlet pipe flange, the turbine inlet and outlet needs to be connected with high-pressure rubber flexible pipe to avoid any deformation consequences.

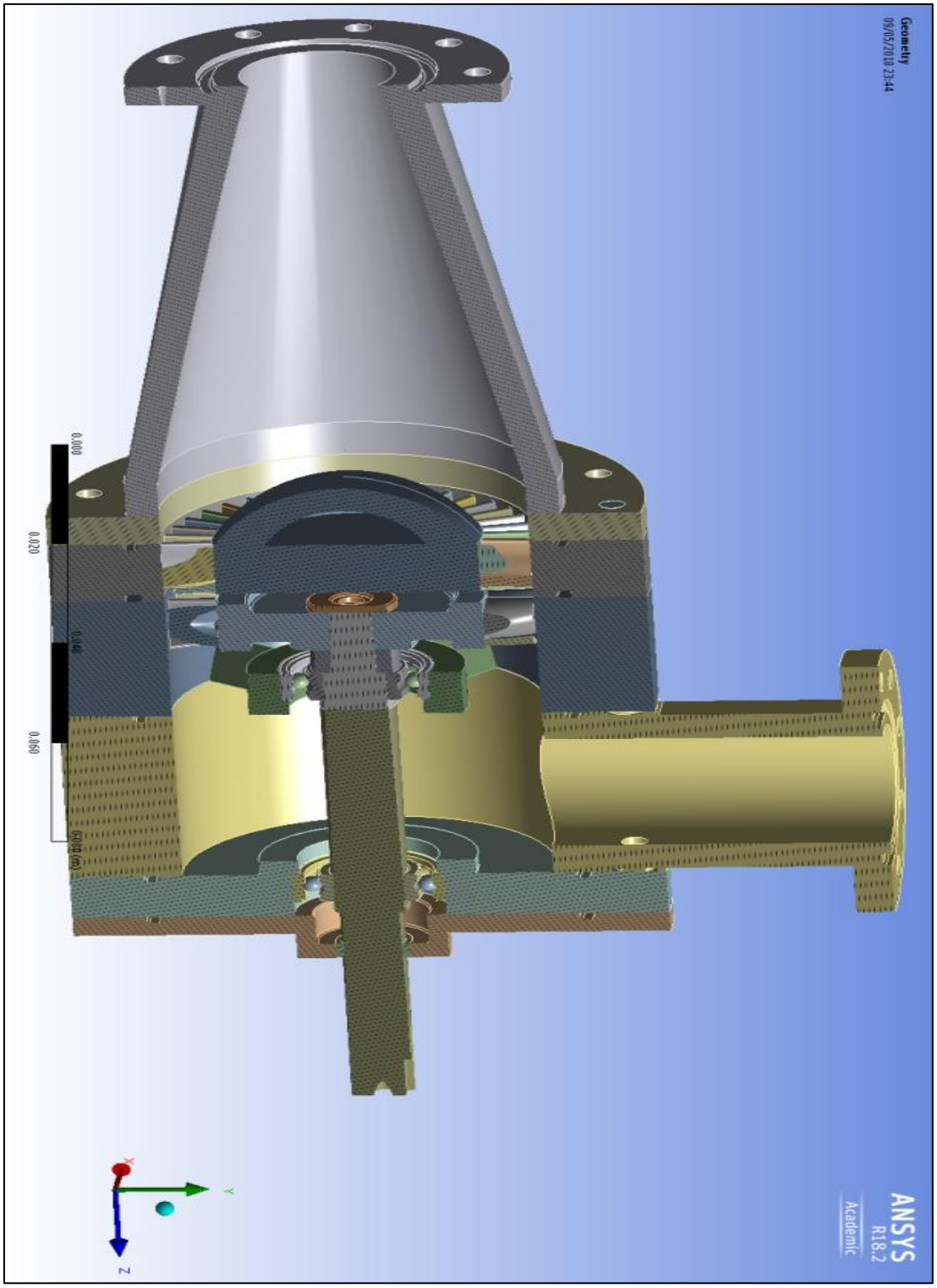

Figure 6-71 Complete turbine assembly 3D sectional geometry used in ANSYS structural analysis

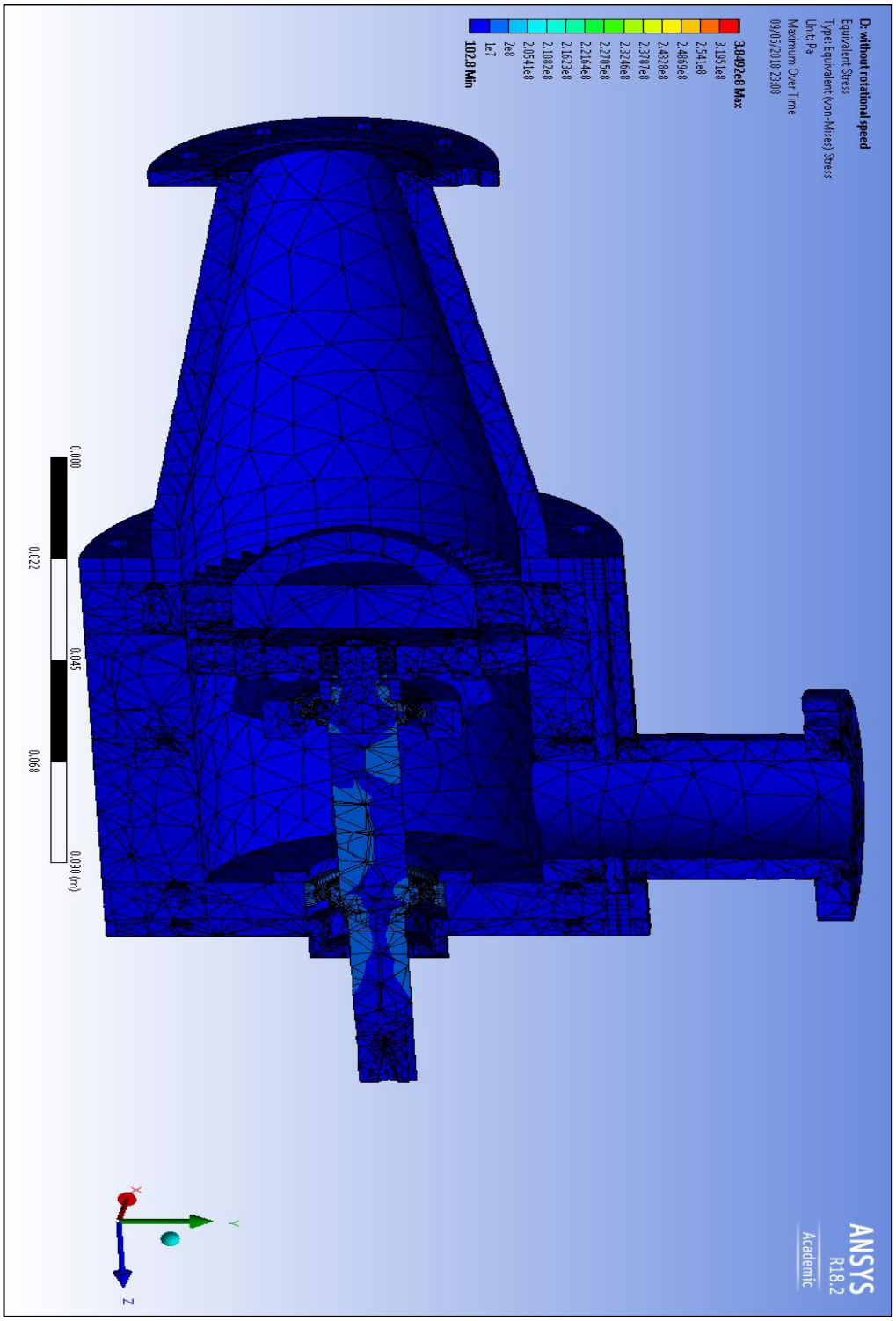

Figure 6-72 Von-Mises equivalent stress contour of complete turbine assembly

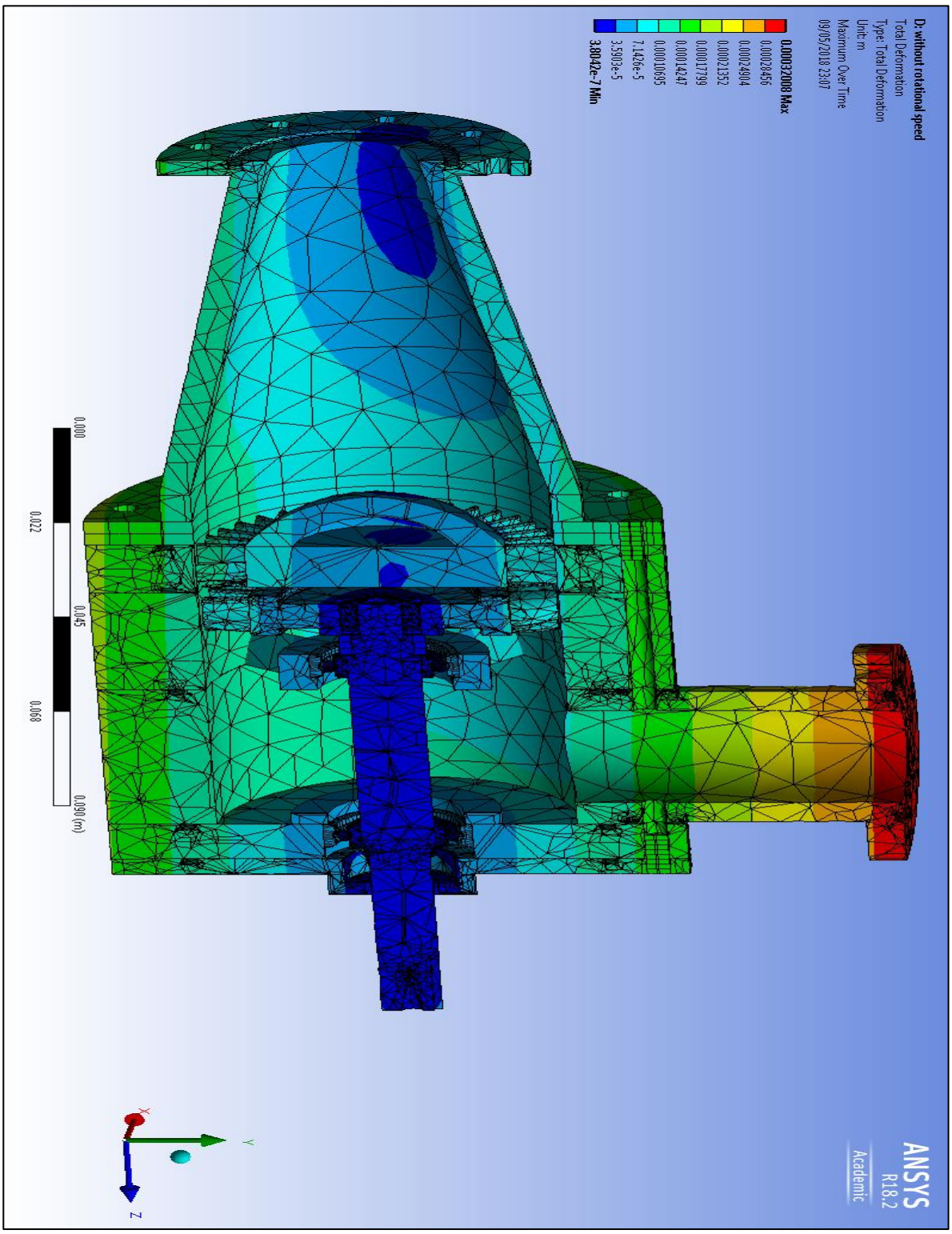

Figure 6-73 Total deformation contour of the complete turbine assembly

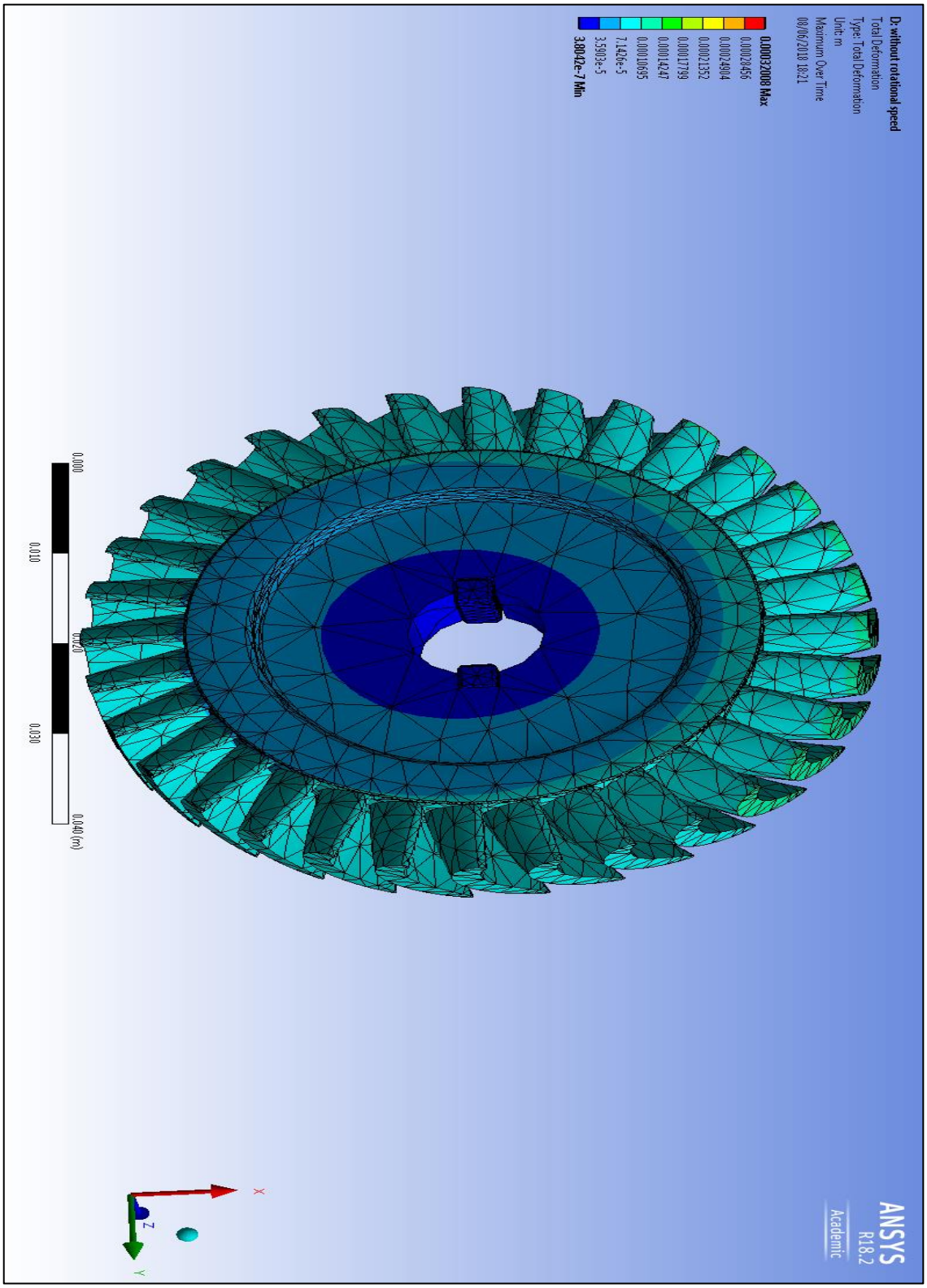

Figure 6-74 Total deformation contour of the turbine rotor

6.7.3 Experimental and Validation Results:

The three turbines with blade heights of (4mm, 6mm, and 8mm) were tested at a range of operating conditions such as inlet pressure, rotational speed, and flow rate. For each experiment set the temperature is fixed at the environmental temperature of around 16 ^{0}C as an average value while the other parameters changed according to the required range and apparatus limits. The inlet pressure for the turbine inlet was controlled using pressure regulator while the outlet turbine duct discharges to the environment, such variation of expansion ratios has created a series of design boundary conditions. Obviously, increasing the pressure energy will increase the rotor rotational speed, so to control this rise in rotational speed, the DC generator is adjusted with turbine and torque meter shaft. The load applied to the DC generator shaft is controlled by the electrical variable resistance which in turn controls the rotational speed of the turbine. This controlling technique allows creating maps of turbine constant expansion ratios while varying the rotational speeds for better performance description and validation purpose. The torque meter records the torque τ (Nm), and rotational speed ω (rad/sec) produced by the turbine through the connected shaft then calculates the actual shaft power output using the following equation:

$$Power = \tau * \omega \qquad 6\text{-}1$$

At the turbine outlet and inlet ducts the pressure and temperature are recorded at each experimental point, and then the recorded measurements are used to calculate the turbine efficiency using the following equation:

$$\eta_{turbine} = \frac{\Delta h_{actual}}{\Delta h_{ideal}} \qquad 6\text{-}2$$

Where the (h) is the enthalpy and(Δh_{actual}) is the actual work output due to actual expansion through the turbine while the ideal expansion represents the isentropic expansion at constant entropy or zero losses. These enthalpies were evaluated by developing MATLAB code integrated with reference fluid thermodynamic and transport properties database (REFPROP) software [197], with the measured temperatures and pressures used as input data. The main limitation for the torque meter is the inability of the torque meter to measure rotational speed higher than 16000 RPM. Therefore, the manufactured turbines were tested with off-design conditions which are lower than the design point operation conditions. The experiments were conducted at pressure ratio ranging from 1.2 to 1.75 and rotational speed ranging from 4000 RPM to 16000 RPM. The turbines inlet pressure was kept at a constant value by pressure regulator while the rotational speed was varied using the electrical resistance that generates a set of parametric study results shown in Figure 6-75 to Figure 6-80.

For all turbines types, Figure 6-75, Figure 6-77, and Figure 6-79 present the relationship between the expansion ratio and the actual power output, where increasing the expansion ratio increases the actual output power. From the experimental testing for turbines with blade heights of 4mm, 6mm, and 8mm, the maximum power produced at expansion ratio around 1.75 and rotational speed around 16000 RPM were 630.75 W, 694.1 W, and 796.89 W respectively. Figure 6-76, Figure 6-78, and Figure 6-80 present the relationship between expansion ratio and turbine efficiency, where the turbine efficiency is reduced by increasing the expansion ratio value through the turbine stage. More pressure drop means high fluid velocity which will lead to higher losses due to secondary losses in the turbine passages. It is noticeable from these figures that the efficiency of the turbine is affected by blade rotational speed more than stage expansion ratio, while the actual power is affected by both of them. It can also be noticed from the results for all developed turbine types that the deviation between

the experimental and CFD results increases as the expansion ratio and rotational speed increase. Such deviation can be explained by increasing pressure and velocity increasing the frictional losses in the turbine bearing which in turn increases the deviation between the CFD and experimental results.

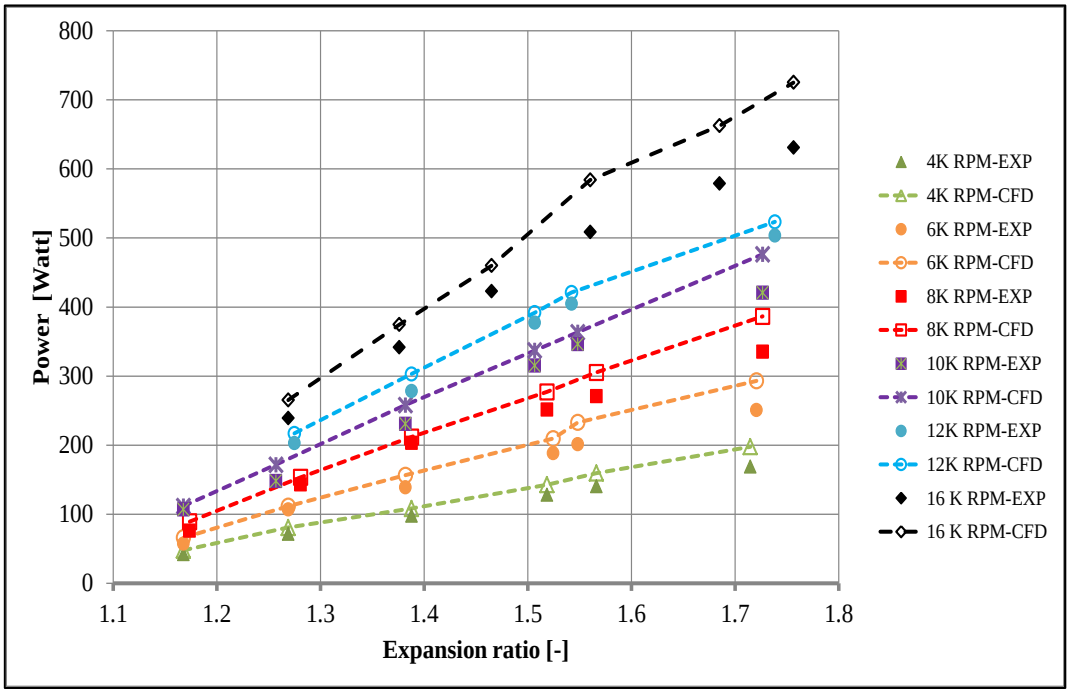

Figure 6-75 Turbine 4mm blade height CFD model validation for expansion ratio effect on power output with multi-rotational speeds

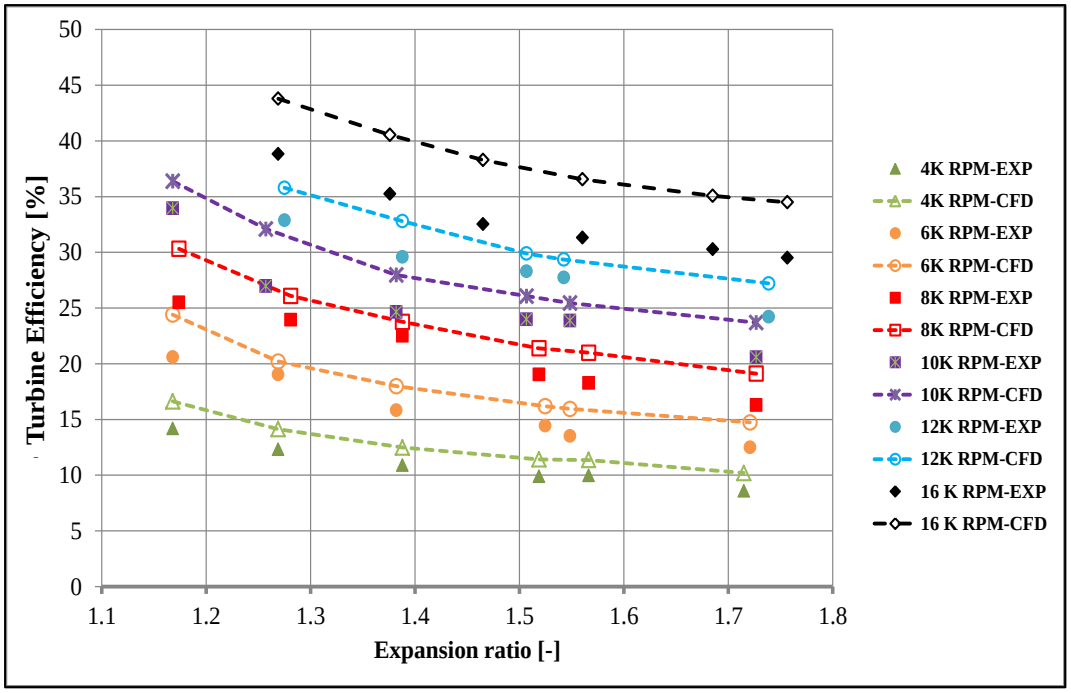

Figure 6-76 Turbine 4mm blade height CFD model validation for expansion ratio effect on the turbine efficiency with multi-rotational speeds

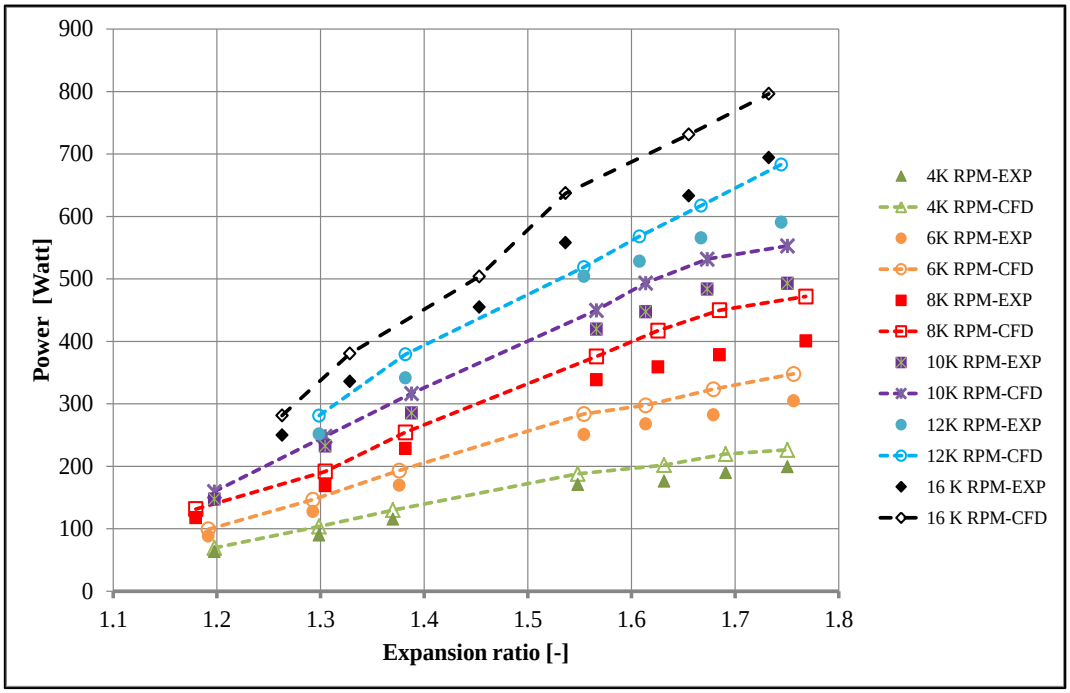

Figure 6-77 Turbine 6mm blade height CFD model validation for expansion ratio effect on power output with multi-rotational speeds

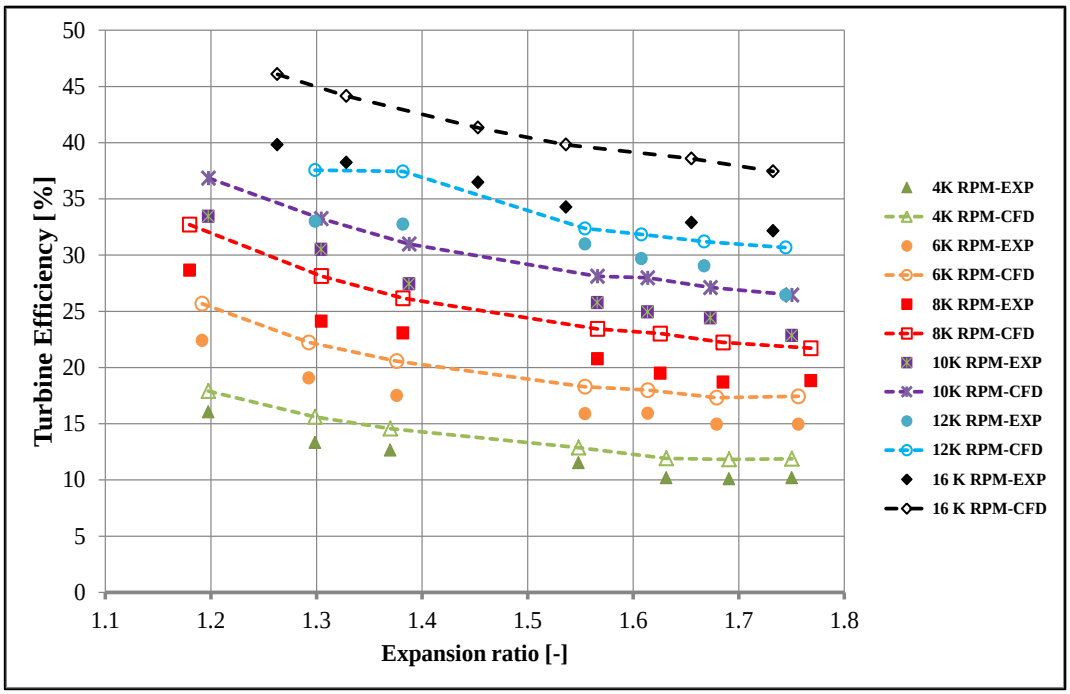

Figure 6-78 Turbine 6mm blade height CFD model validation for expansion ratio effect on turbine efficiency with multi-rotational speeds

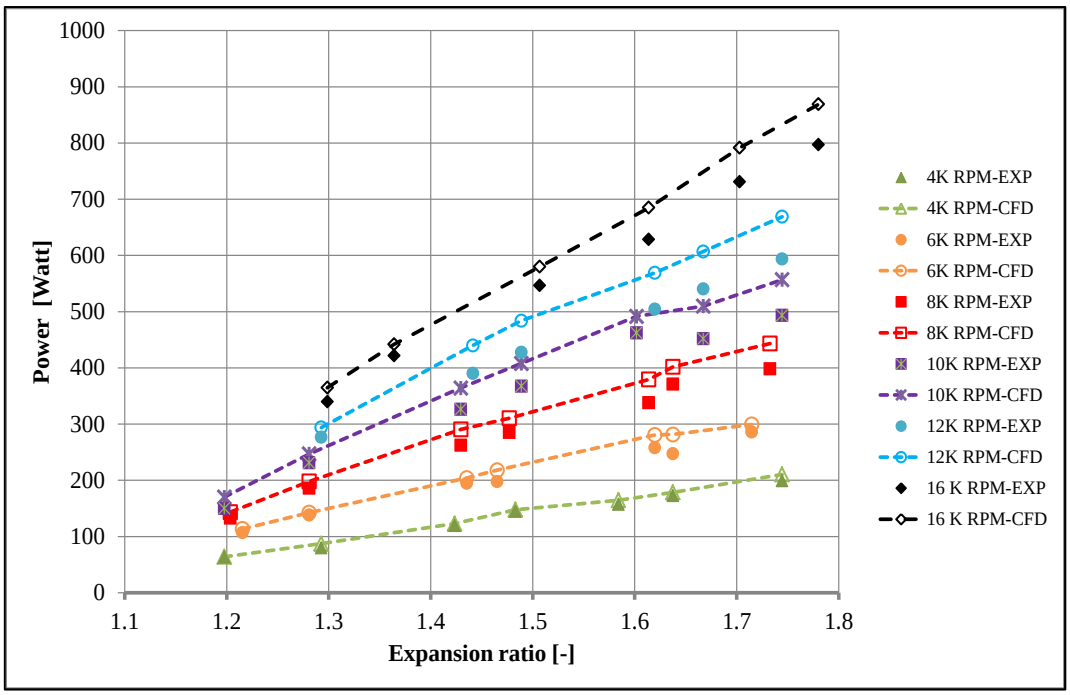

Figure 6-79 Turbine 8mm blade height CFD model validation for expansion ratio effect on power output with multi-rotational speeds

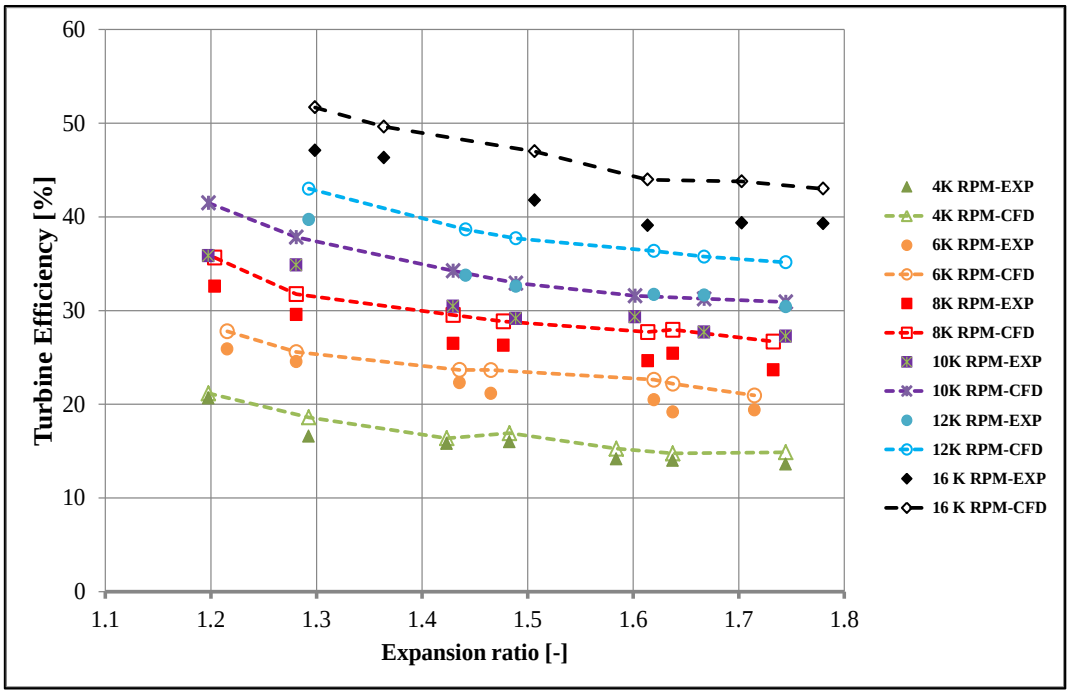

Figure 6-80 Turbine 8mm blade height CFD model validation for expansion ratio effect on turbine efficiency with multi-rotational speeds

Using experimental and CFD simulation results, Figure 6-81 to Figure 6-84 compare the effects of rotational speed on power output and turbine efficiency at two expansion ratios of 1.3 and 1.6 for the three turbines with blade heights of 4mm, 6mm, and 8mm. It is clear that increasing the rotor rotational speed increases the power output and turbine efficiency at both expansion ratios of 1.3 and 1.6. As noticed in Figure 6-81 and Figure 6-83 the power output for the 8mm and 6mm turbine are nearly the same up to rotational speed of 12000 RPM for expansion ratio of 1.3 and 10000 RPM for expansion ratio of 1.6. Above these RPM values the power output for the 8mm turbine becomes higher than that for the 6mm turbine, while the power output for the 4 mm turbine stays lower than the others for all rotational speeds. Also, as shown in Figure 6-82 and Figure 6-84 the turbine efficiency for the 8mm turbine is

higher than that for the other turbine types for all rotational speeds and both expansion ratios. Moreover the efficiency for the 6mm turbine is higher than that for the 4mm turbine, which means that the efficiency increases with the blade height increase. From these figures, the maximum efficiencies for the 4mm, 6mm, and 8mm turbines at pressure ratio 1.3 are: 47.1%, 39.8%, and 38.83% respectively. Increasing the blade height increases the turbine mass flow rate due to increasing passage annular area that in turn increases the power output and enhances turbine efficiency. These results show the high impact of the blade height on the output power and turbine efficiency for small-scale turbines.

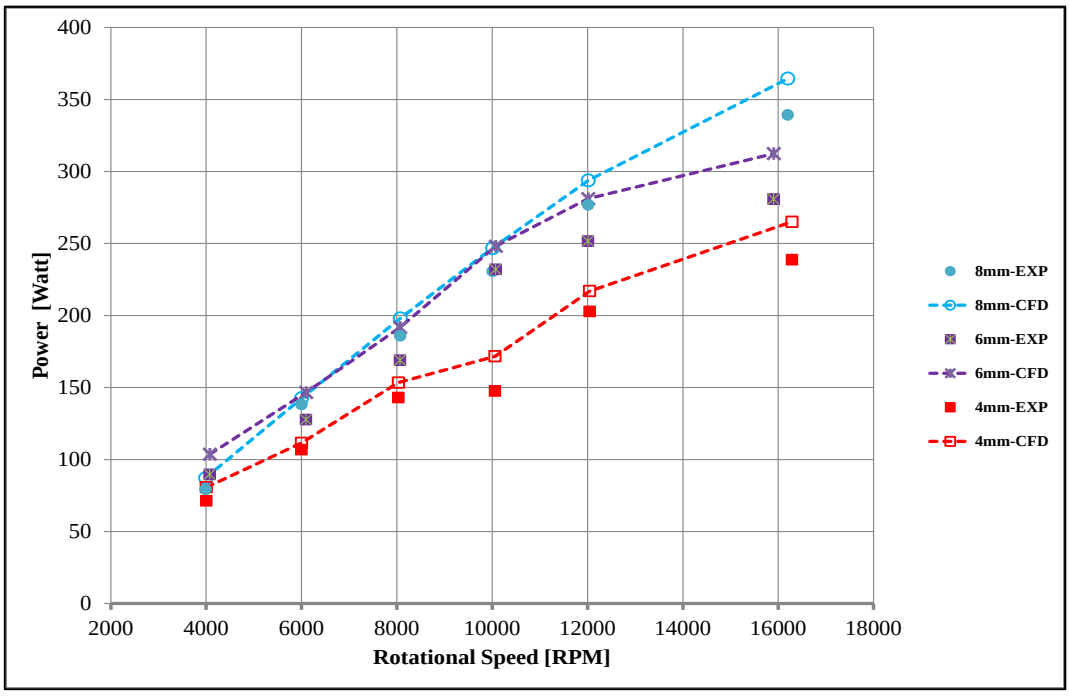

Figure 6-81 Turbines performance comparison for rotational speed effect on power output, CFD model validation with experimental data at expansion ratio 1.3

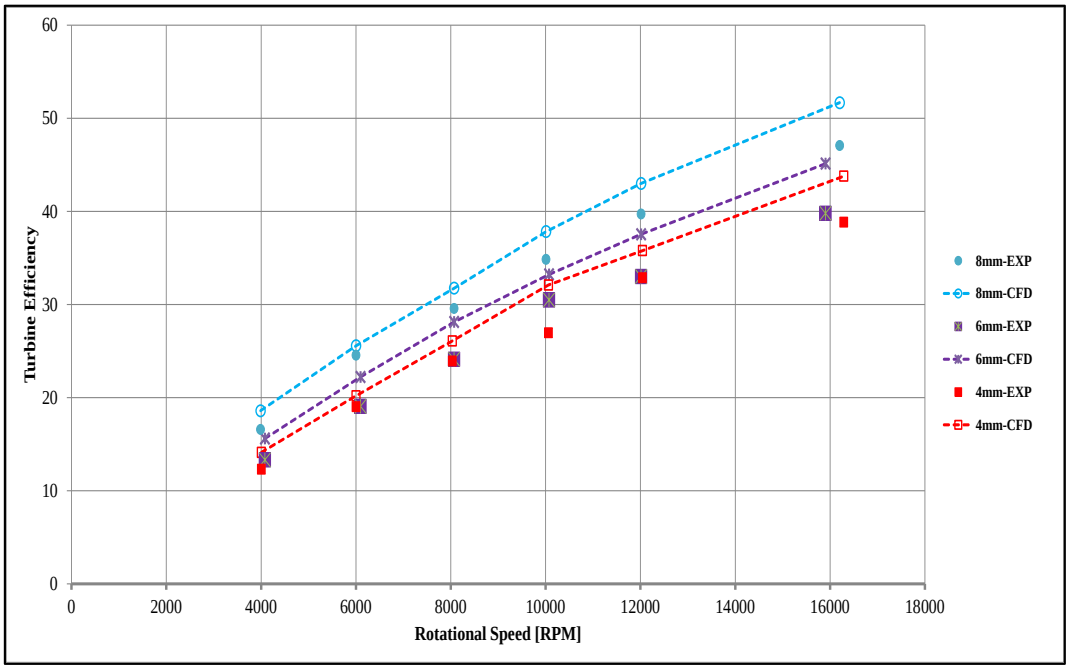

Figure 6-82 Turbines performance comparison for rotational velocity effect on the turbine efficiency, CFD model validation with experimental data at expansion ratio 1.3

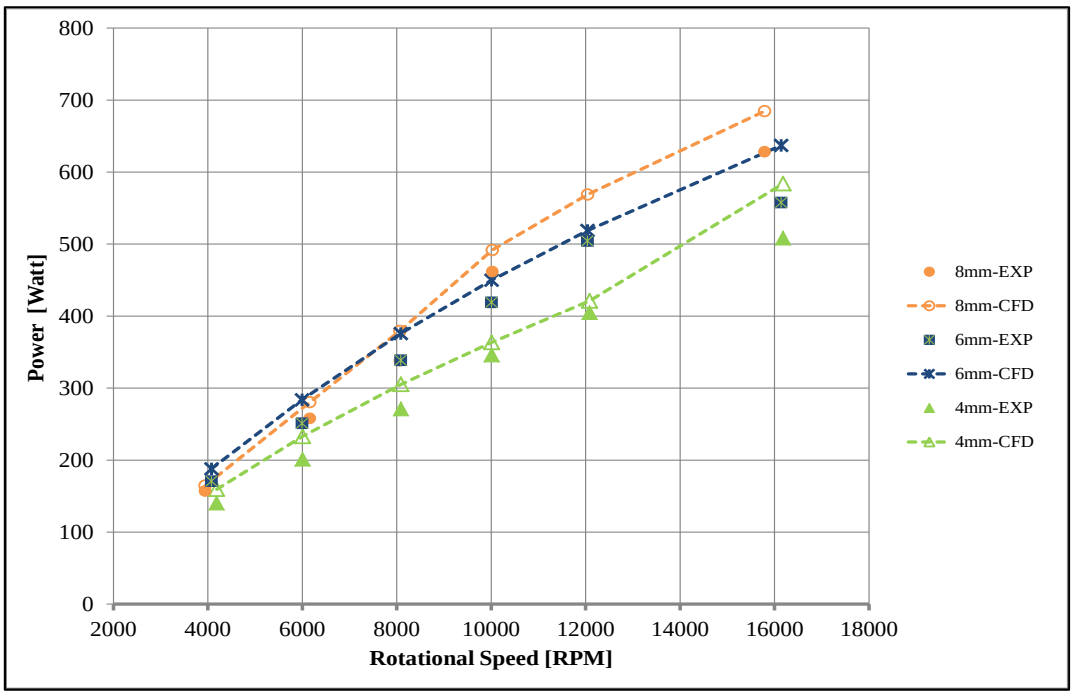

Figure 6-83 Turbines performance comparison for rotational speed effect on power output, CFD model validation with experimental data at expansion ratio 1.6

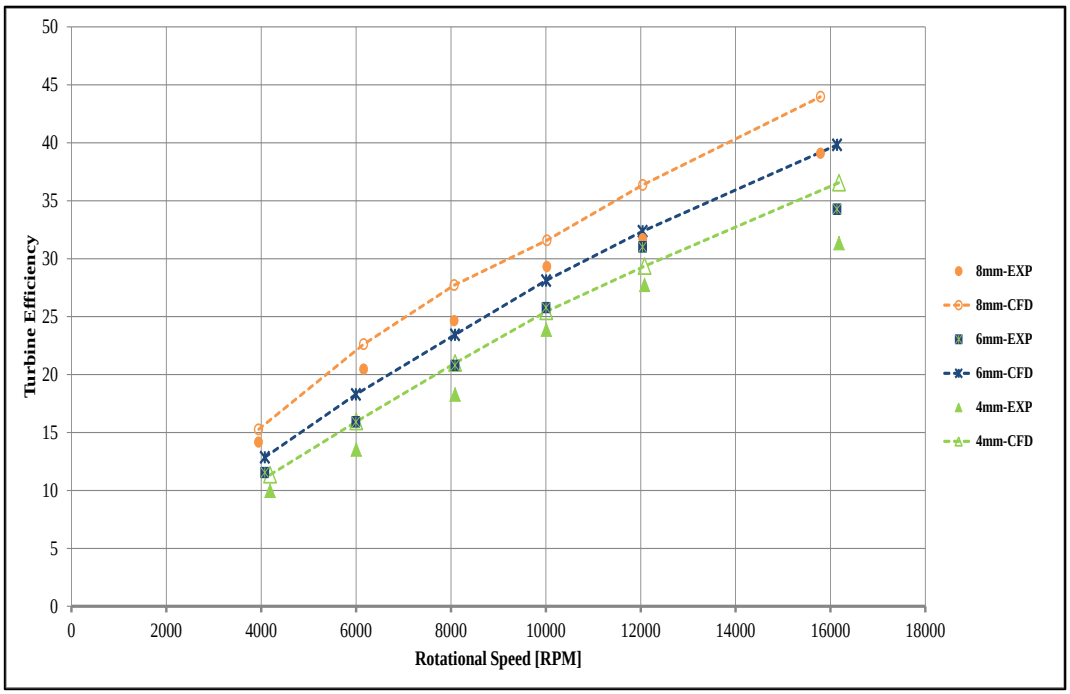

Figure 6-84 Turbines performance comparison for rotational velocity effect on the turbine efficiency, CFD model validation with experimental data at expansion ratio 1.6

In order to compare the results from the CFD model with experimental results for the developed three turbines (4mm, 6mm, and 8mm); both results were plotted on the same graph for both power output and turbine efficiency for each turbine type as shown in Figure 6-85 to Figure 6-90. The error edge lines were calculated using the following equation [198]:

$$Error\ percentage = \frac{CFD - Experimental}{CFD} * 100 \qquad 6\text{-}3$$

Since the aim of calculating this error percentage is to validate the CFD model results, therefore the CFD data are located at the denominator of equation 6-3.

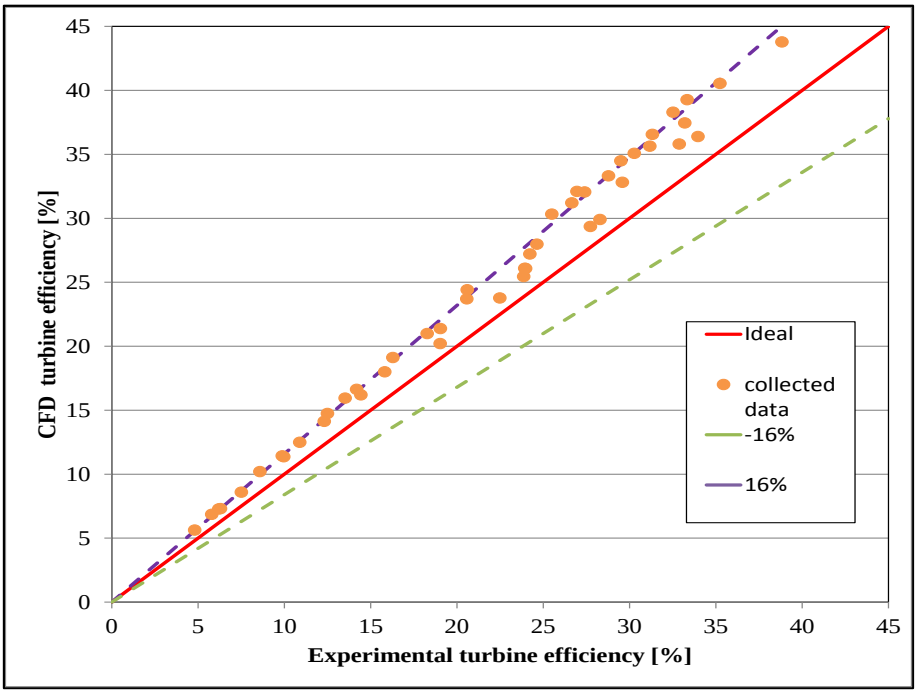

Figure 6-85 Turbine 4mm blade height turbine efficiency comparison between CFD model data and experimental data

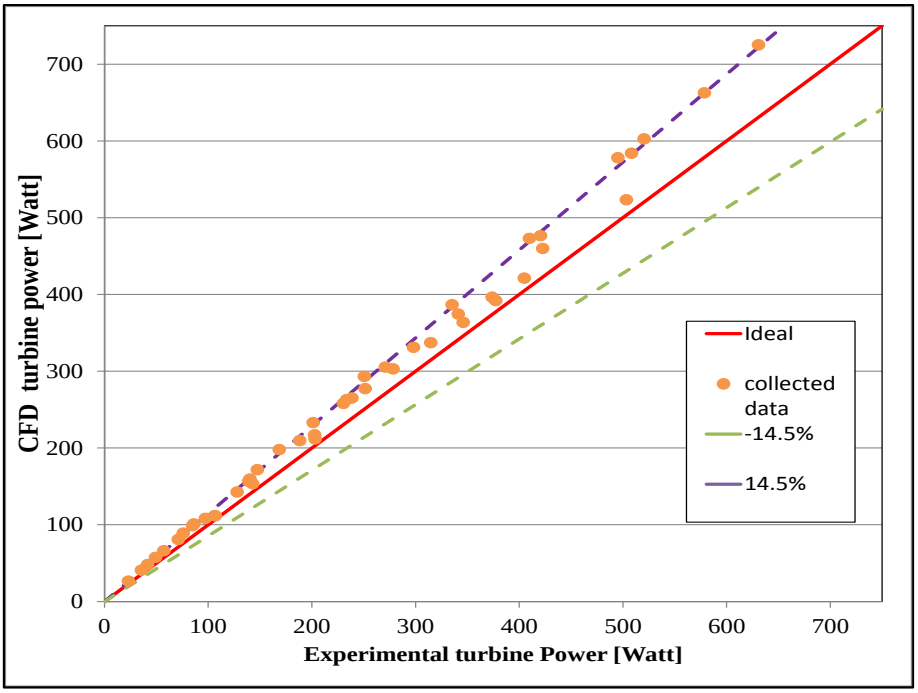

Figure 6-86 Turbine 4mm blade height power comparison between CFD model data and experimental data

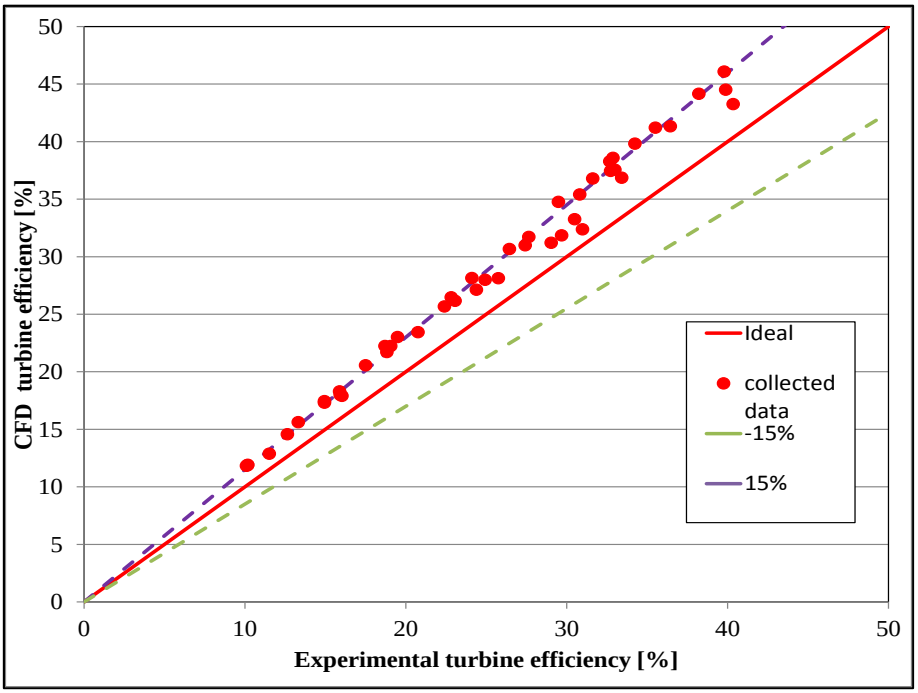

Figure 6-87 Turbine 6mm blade height turbine efficiency comparison between CFD model data and experimental data

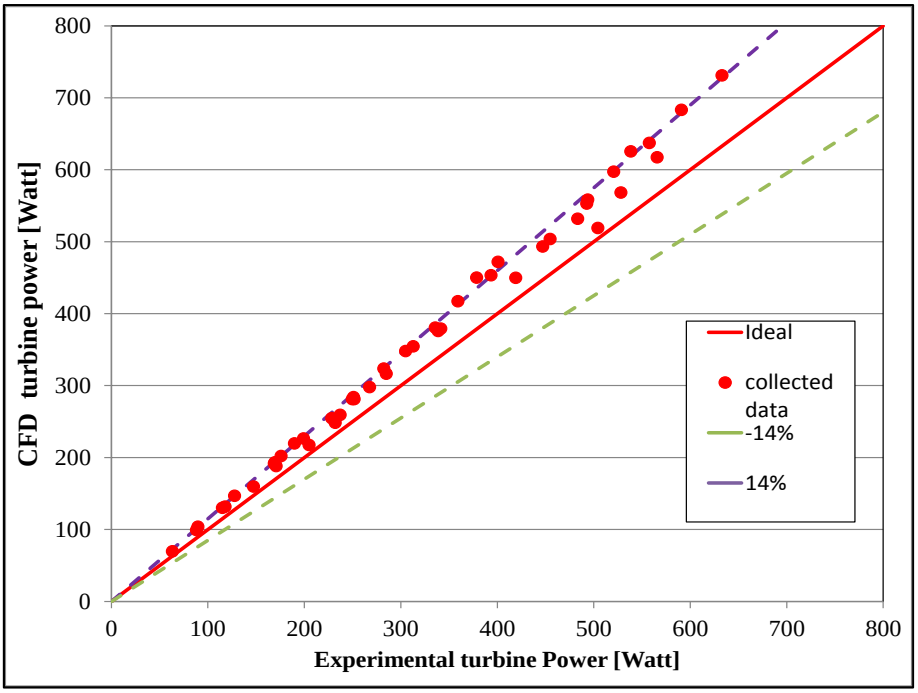

Figure 6-88 Turbine 6mm blade height power comparison between CFD model data and experimental data

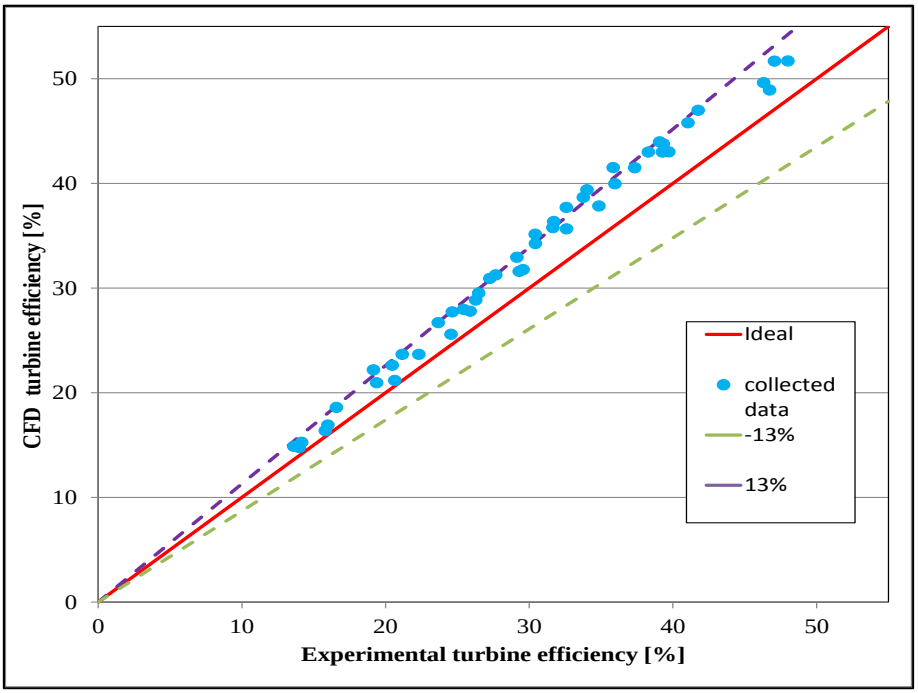

Figure 6-89 Turbine 8mm blade height turbine efficiency comparison between CFD model data and experimental data

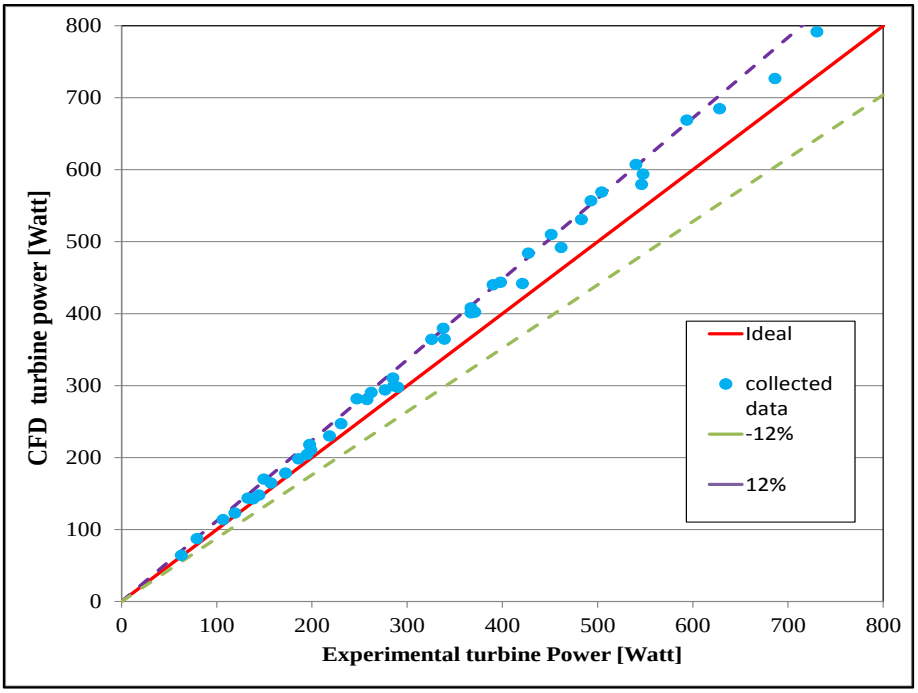

Figure 6-90 Turbine 8mm blade height power comparison between CFD model data and experimental data

Figure 6-85 and Figure 6-86 show that for the turbine with 4mm blade height the turbine efficiency CFD prediction for most of the data of experimental are in a range of +16%, while for the power output are in the range of +14.5%. Similarly, Figure 6-87 and Figure 6-88 show that for the turbine with 6mm blade height, the turbine efficiency CFD prediction for most of the experimental data are in the range of +15%, while for the power output data are in the range of +14%. Finally, Figure 6-89 and Figure 6-90 show that for the turbine with 8mm blade height turbine efficiency CFD prediction of most of the experimental data are in a range of +13%, while the power output data are in the range of +12%. This work reveals that the error gaps between experimental and CFD results increase with the decrease of blade height due to higher losses associated with small blade height. Also, for all developed turbines the power output with turbine efficiency of CFD simulations are overestimated compared to the experimental results. This overestimation can be attributed to many reasons such as: (1) The CFD simulation assumes steady state conditions while transient conditions take place in the experimental testing. (2) Surfaces are modeled as hydraulically smooth surfaces for the blades and turbine ducts, while the manufactured surfaces have certain levels of roughness. (3) The CFD model did not include bearing losses or shaft vibration effects in the aerodynamic CFX analysis. Another observation from the validation results is that for all developed turbines, the efficiency percentage errors are larger than the power output errors. This can be explained as the power output is measured directly by the torque meter while the efficiency is calculated using equation 6-2 which depends on the measured temperatures and pressures. The validation results indicate that developed CFD model could be used for predicting the axial turbine performances at various designs configurations and operating conditions and to further develop small-scale axial turbines.

6.8 Summary and Conclusions:

This chapter presented the developed small-scale axial turbines results for different designs and optimization methods with scientific discussion and analysis. The developed preliminary design method is used in a parametric study to develop the best initial turbine geometry that produces highest turbine total efficiency at the required operating conditions.

Results from the 1D preliminary design was used as input data to the ANSYS-CFX software to develop the 3D design model. The parametric study for 3D CFD model geometrical parameters was developed to choose the best design; the results of this study are presented, discussed and analyzed. The manual optimization of 3D CFD model design results are compared against mean-line preliminary design results to assess the reliability of the preliminary design model and at the same time, to provide an overall check for the 3D CFD model. The maximum difference in terms of efficiency was 9.5 %, power output and rotor outlet relative velocities were 7.9 % and 10.56 % respectively [55].

The novel parameterisation technique was developed to describe stator and rotor blades geometry using 12 parameters and it was used (MOGA) 3D optimization by ANSYS design exploration module. The performance was optimized according to maximizing the total efficiency and output power, while keeping the flowrate within the limits of 0.1 kg/s. The results from the standard response surface-full 2^{nd} order polynomials method as 3D surfaces, which connects two geometrical parameters and performance parameters, are presented; discussed and analyzed. The optimization process results revealed significant improvements in aerodynamic flow characteristics for the optimized design compared to the base-line design, where the total efficiency is enhanced from 78.3% to 84.88% and power output from 4.6 kW to 5.3 kW.

The small-scale turbine advanced blade configurations were developed using Ansys CFX software to enhance the turbine performance. The parametric study was carried out on four different blade configurations (twist, lean, bow, and sweep) for three cases: (Stator), (Rotor), and (Stator-Rotor). Results from this parametric study disclose that in the sweep angle of 30 degrees case (Stator) the efficiency and power output are enhanced to 82.4% and 5.18 kW; the optimum lean angle is 10 degrees for the case (Stator-Rotor) which produces total efficiency of 79.8%, while the same value of twist angle for case (Stator) produced a total efficiency of 80.4%. The blade bow configuration is found to not improve the performance of small-scale axial turbines.

The novel dual stage non repeated annular area small scale axial turbine was developed to handle higher expansion ratio of 3, which enhanced the cycle efficiency. Results from the comparative parametric study including three turbine types (single-stage, two repeated stage and two non-repeated stages) with a range of operating conditions like expansion ratio, mass flowrate and rotational speed based on efficiency and output power are presented. The results disclosed that the two non-repeated stages turbines has a higher total efficiency of 81.4% compared to the two repeated stages of 78.2% and single stage of 74.6%. Moreover, the two non-repeated stages turbine produces power output of 8.5kW using mass flow rate of 0.15kg/s, while the single stage needs 0.18kg/s to produce same power output.

Three manufactured axial turbines with different blade heights (4mm, 6mm, and 8mm) were designed manufactured and tested at various operating conditions to validate the CFD simulation, and the design methodology, and to investigate the effects of blade height on small scale axial turbines performance. Validation results show the validity of the developed CFD model, with maximum deviation between simulation and experimental results of +16%. These indicate the potentials of using the developed CFD methodology for further

investigations and development of small-scale axial turbine. The higher expansion ratio and rotational speed mean higher deviation between experimental and CFD results, more over the shorter blade heights add more losses on the flow domain.

CHAPTER 7

CONCLUSIONS AND FUTURE RECOMMENDATIONS

7.1 Introduction

The future challenges that face the world energy sector such as: reducing fossil fuel consumption, CO_2 emissions and improving the security of energy supply makes renewable energy sources a main solution to these challenges. Renewable energy sources are intermittent in nature, producing energy peaks at times when demands are low, thus energy storage systems are needed to store this surplus energy, smooth out energy production, reduce energy production cost, and increase the use of green power. Cryogenic energy storage (CES) is an innovative energy storage technology that has been developed as a low-temperature thermal energy storage system [7]. The integration between local small power generation and storage energy within smart girds has increased the development of innovative technologies such as micro or small turbines as power generation tools. Therefore this thesis has focused on the development of power generation cycles based on cryogenic energy storage and integrating that with the development of a nitrogen small-scale axial turbine as a key component of these cycles to achieve the best performance.

7.2 Conclusions

The present study is a comprehensive investigation of different power generation cryogenic energy storage cycles and different strategies for developing novel configurations for nitrogen small-scale axial turbines as the expanders for these cycles. These strategies include developing and integrating the 1D preliminary design, 3D CFD simulations, FEA analysis, and experimental testing to validate the analysis. Such strategies have also been used to develop 3D optimization techniques, advanced blade configurations, and dual stage axial turbine to achieve advanced nitrogen small-scale axial turbine designs.

The major findings and most important contributions of the present research can be summarised as follows:

- Four new cryogenic power generation cycles ranging from the simple basic cycle (open Rankine) to the complex combined one (combined power generation and cryogenic storage plant) were developed to evaluate the performance of a small scale power generation system. Full thermodynamic analysis and parametric studies have been conducted to specify the turbine design and operating conditions.
- The combined cycle (scheme2) predicted the best performance with round trip efficiency of 84.15% using air flow rate of 0.093kg/s. It highlighted the importance of the recovery part turbine efficiency where each 10% increase in the turbine efficiency had increased the round trip efficiency by 7.7 % [34]. The hybrid open-closed Rankine (HOCR) cycle has been chosen as the case study for further investigation of the nitrogen turbine since it represents the midway between simple OR cycle design and more advanced cycles in the integrated liquefaction and recovery schemes. Moreover, this cycle can handle the low input pressure between (1.5-3bar) which is

considered safe and convenient for small/medium buildings applications where the cycle thermal efficiency ranges from 15.45% to 24.72 %.

- A systematic comprehensive methodology for the integrated design of nitrogen small-scale axial turbine was developed by integrating 1-D preliminary (mean line method) and 3-D CFD simulations which were validated by experimental testing. Such methodology became an effective design tool for small scale axial turbine design which opens the way for further steps to develop small-scale power generation devices and cycles.
- Results from the 1D preliminary design were used as input data to the ANSYS-CFX software to develop the 3D design model. The parametric study for 3D CFD model geometrical parameters was developed to choose the best design of efficiency of 78.3% and output power of 4.6kW. The manual optimization of 3D CFD model design results were compared with the mean line preliminary design results to assess the reliability of the preliminary design model and at the same time to provide an overall check for the 3D CFD model. The maximum difference in terms of efficiency was 9.5 %, power output and rotor outlet relative velocities were 7.9% and 10.56 % respectively [55].
- The novel optimization parameterisation technique was developed to describe blade geometry by using only 6 parameters which were used this technique in (MOGA) 3D optimization through ANSYS design exploration module. The blade chord length included in the optimization parameters as important flow path parameter gave the optimization process more robustly and reliability. The performance was optimized accordingly to maximizing the efficiency and output power while keeping flow rate within the limits of 0.1 kg/s.

- It was noticeable from the 3-D CFD optimization result that aerodynamic characteristics of the flow were improved significantly for the optimized geometry compared with the baseline geometry where the total efficiency is enhanced from 78.3% to 84.88% and power output from 4.6 kW to 5.3 kW. This optimization procedure which is integrated with design methodology revealed that an efficient axial turbine can be developed by parameterisation technique which depends on blade thickness and angles for blade profile using a number of blade and chord length for flow path as qualitative parameters.
- The further modification based on the developed integrated methodology was small-scale turbine advanced blade configurations for the aim of enhancing turbine performance and investigating the effects of these configurations on the turbine performance. The parametric study was achieved on four different blades configurations (twist, lean, bow, and sweep) for three cases: (Stator), (Rotor), and (Stator-Rotor).
- Results from this parametric study disclosed that at sweep angle of 30 degree for the case (Stator), the efficiency and power output were enhanced to 82.4% and 5.18 kW; the optimum lean angle of 10 degrees for the case (Stator-Rotor) produced a total efficiency of 79.8%, while the same value of twist angle but for the case (Stator) produced a total efficiency of 80.4%. The blade bow configuration did not improve the performance of the small scale axial turbines.
- The novel dual stage non repeated annular area nitrogen small scale axial turbine was developed to handle a higher expansion ratio of 3, which enhanced the cycle efficiency. The integrated one dimensional preliminary design, and three dimensional CFD methodology have been adopted further which solved the over speed problems

that appeared in a second stage two stages axial turbine as reported in previous studies.

- Work on the dual stage non repeated annular area nitrogen small scale axial turbine involved comparative parametric study including three turbine types' single-stage, two repeated stage and two non-repeated stages with a range of operating condition like expansion ratio, mass flowrate and rotational speed based on isentropic efficiency and power output. The results disclosed that the two non-repeated stages turbine has higher total efficiency of 81.4% compared to the two repeated stages of 78.2% and the single stage of 74.6%. Moreover, the two non-repeated stages turbine produced power output of 8.5kW using a mass flowrate of 0.15kg/s, while the single stage needed mass flowrate of 0.18kg/s to produce the same power output.
- In order to study the effects of blade height on small-scale axial turbines performance and validate the CFD simulation and the design methodology, three axial turbines with different blade heights (4mm, 6mm, and 8mm) were designed, manufactured and tested at various operating conditions. The blade height is an important design parameter since it affects the passage annular area which in turn affects turbine flow rate and expansion ratio. Very limited work is reported in this field, therefore turbines with blade heights of 4mm and 6mm were manufactured and tested to contribute to the knowledge gap in this field and determine the minimum blade height that can be manufactured and tested for specific power output.
- The experimental results for turbines with blade heights of 4mm, 6mm, and 8mm, showed that with expansion ratio around 1.75 and rotational speed around 16000RPM the maximum produced powers were 630.75W, 694.1W, and 796.89W respectively. The maximum efficiencies for the 4mm, 6mm, and 8mm turbines at pressure ratio of 1.3 were: 47.1%, 39.8%, and 38.83% respectively. It can be concluded that

increasing the blade height increases the turbine mass flow rate due to increasing passage annular area that in turn will increase the power output and enhance turbine efficiency.

- The experimental validation results showed the validity of the developed CFD model for the 4mm, 6mm, and 8mm blade height turbines with deviation percentage in terms of efficiency were +16%, +15%,+13% respectively, while in terms of power output were +14.5%, +14%,+12% respectively. Such results reveal that the error gaps between experimental and CFD results increased with the decrease of the blade height due to higher losses associated with small blade height. They also show that for all developed turbines the power output and turbine efficiency from CFD simulations were overestimated compared to the experimental results. Another observation from the validation results is that for all developed turbines, the efficiency percentage errors are larger than the power output errors. This can be explained by the fact that the power output is measured directly by the torque meter while the efficiency is calculated by using measured temperatures and pressures. The validation results indicate that the developed CFD model could be used for predicting the performance of the axial turbine at various design configurations and operating conditions and can be used for further developments of small-scale axial turbines.

7.3 Future recommendations

Based on the results from this research work which focused on developing power cycles with cryogenic energy storage technology and nitrogen small-scale axial turbines, the future recommendation for more studies and investigations are summarised as follows:

- The cold and hot storage system in the integration of the liquefaction cycle with recovery cycle in storage power generation plant schemes needs to be investigated

with pebbles bed thermal storage system and compared with phase change material systems. The turbines in the recovery parts need be deeply investigated using the same methodology developed in this research.

- Developing the preliminary design approach to be suitable for partial admission axial turbine and supersonic stator arrangement for low flowrate and high expansion ratios operating conditions.
- Develop the unsteady flow analysis approach by using ANSYS CFD to catch the accurate interaction between stator fixed row and a rotor rotating row, and then compare the results with the current steady state results. And develop sonic and supersonic ANSYS CFD models to evaluate the shock wave losses by comparing the results with current steady state flow results.
- Use ANSYS CFD option to model the process of spraying the liquid droplets inside the axial turbine, this option will cancel the need for evaporation heat exchanger and can improve the turbine efficiency, since the expansion and evaporation will happen simultaneously.
- Develop the manufacturing process and the experimental testing for the non-repeated dual stage axial turbine, and compare the results with those for the single stage turbine developed in this study to provide more information and data regarding small-scale design concepts and analysis.

REFERENCE

1. Grübler, A., M. Jefferson, and N. Nakićenović, *Global energy perspectives: a summary of the joint study by the International Institute for Applied Systems Analysis and World Energy Council.* Technological Forecasting and Social Change, 1996. **51**(3): p. 237-264.
2. Masanet, E.R., *Energy Technology Perspectives 2017: Catalysing Energy Technology Transformations*. 2017: OECD.
3. Eller, A. and D. Gauntlett, *Energy storage trends and opportunities in emerging markets.* Energy storage trends Oppor. Emerg. Mark, 2017.
4. Yan, J., *Handbook of Clean Energy Systems.* Jonn Wiley & Sons Ltd, 2015. **5**.
5. Ackermann, T., G. Andersson, and L. Söder, *Distributed generation: a definition1*. Electric power systems research, 2001. **57**(3): p. 195-204.
6. Qiu, G., H. Liu, and S. Riffat, *Expanders for micro-CHP systems with organic Rankine cycle.* Applied Thermal Engineering, 2011. **31**(16): p. 3301-3307.
7. Khalil, K.M., et al., *Parametric analysis of blade configurations for a small-scale nitrogen axial expander with hybrid open-Rankine cycle.* Energy Conversion and Management, 2017. **142**: p. 82-94.
8. Chen, H., et al., *Progress in electrical energy storage system: A critical review.* Progress in Natural Science, 2009. **19**(3): p. 291-312.
9. Baker, J. and A. Collinson, *Electrical energy storage at the turn of the millennium.* Power Engineering Journal, 1999. **13**(3): p. 107-112.
10. Van der Linden, S., *Bulk energy storage potential in the USA, current developments and future prospects.* Energy, 2006. **31**(15): p. 3446-3457.
11. Akhil, A., S. Swaminathan, and R.K. Sen, *Cost analysis of energy storage systems for electric utility applications*. 1997, Sandia National Labs., Albuquerque, NM (United States).
12. Weinstock, I.B., *Recent advances in the US Department of Energy's energy storage technology research and development programs for hybrid electric and electric vehicles.* Journal of Power Sources, 2002. **110**(2): p. 471-474.
13. *Advanced electricity storage technologies programme.* Australian Greenhouse Office, 2005: p. 1–35.
14. Author, N., *Review of electrical energy storage technologies and systems and of their potential for the UK*. EA Technology, 2004. **1**: p. 34.
15. Ahearne, J., *Storage of electric energy, Report on research and development of energy technologies.* International Union of Pure and Applied Physics, 2004: p. 76-86.
16. Kondoh, J., et al., *Electrical energy storage systems for energy networks.* Energy Conversion and Management, 2000. **41**(17): p. 1863-1874.
17. Tafech, A., D. Milani, and A. Abbas, *Water storage instead of energy storage for desalination powered by renewable energy—king island case study*. Energies, 2016. **9**(10): p. 839.
18. IEA, *Technology Roadmap Energy storage.* International Energy Agency, 2014.
19. Miller, R., PE, *Opportunities in Pumped Storage Hydropower*. Power Engineering, Jun 2010. **114**(6).

20. Pérez-Díaz, J.I. and J. Jiménez, *Contribution of a pumped-storage hydropower plant to reduce the scheduling costs of an isolated power system with high wind power penetration.* Energy, 2016. **109**: p. 92-104.
21. Petrakopoulou, F., A. Robinson, and M. Loizidou, *Simulation and analysis of a stand-alone solar-wind and pumped-storage hydropower plant.* Energy, 2016. **96**: p. 676-683.
22. Pujades, E., et al., *Water chemical evolution in Underground Pumped Storage Hydropower plants and induced consequences.* Energy Procedia, 2017. **125**: p. 504-510.
23. Wang, J., et al., *Overview of Compressed Air Energy Storage and Technology Development.* Energies, 2017. **10**(7): p. 991.
24. He, W. and J. Wang, *Optimal selection of air expansion machine in Compressed Air Energy Storage: A review.* Renewable and Sustainable Energy Reviews, 2018. **87**: p. 77-95.
25. Kalhammer, F.R. and T.R. Schneider, *Energy storage.* Annual Review of Energy, 1976. **1**(1): p. 311-343.
26. Budt, M., et al., *A review on compressed air energy storage: Basic principles, past milestones and recent developments.* Applied Energy, 2016. **170**: p. 250-268.
27. Li, Y., et al. *Optimization model for the power system scheduling with wind generation and compressed air energy storage combination*. in *Automation and Computing (ICAC), 2016 22nd International Conference on*. 2016. IEEE.
28. Wang, J., et al., *Current research and development trend of compressed air energy storage.* Systems Science & Control Engineering, 2017. **5**(1): p. 434-448.
29. Mei, S., X. Xue, and L. Chen, *Discussion on compressed air energy storage technology and Its application.* Southern Power System Technology of China, 2016. **10**(3): p. 11-15.
30. He, Q., et al., *Thermodynamic analysis of a novel supercritical compressed carbon dioxide energy storage system through advanced exergy analysis.* Renewable Energy, 2018.
31. Tong, S., et al., *Developing a grid-connected power optimization strategy for the integration of wind power with low-temperature adiabatic compressed air energy storage.* Renewable Energy, 2018. **125**: p. 73-86.
32. Guanwei, J., et al., *Micron-sized water spray-cooled quasi-isothermal compression for compressed air energy storage.* Experimental Thermal and Fluid Science, 2018. **96**: p. 470-481.
33. Hamdy, S., T. Morosuk, and G. Tsatsaronis, *Cryogenics-based energy storage: Evaluation of cold exergy recovery cycles.* Energy, 2017. **138**: p. 1069-1080.
34. Khalil, K.M., et al., *Liquid air/nitrogen energy storage and power generation system for micro-grid applications.* Journal of cleaner production, 2017. **164**: p. 606-617.
35. Akhusrst, M., *Liquid Air in the energy and transport systems.* The Centre for Low Carbon Futures, 2013.
36. Abdo, R.F., et al., *Performance evaluation of various cryogenic energy storage systems.* Energy, 2015. **90**: p. 1024-1032.
37. Akhurst, M., et al., *Liquid Air in the energy and transport systems: Opportunities for industry and innovation in the UK.* 2013.
38. Park, J., et al., *Application of Cryogenic Energy Storage to Liquefied Natural Gas Regasification Power Plant*, in *Computer Aided Chemical Engineering*. 2017, Elsevier. p. 2557-2562.

39. Park, J., I. Lee, and I. Moon, *A Novel Design of Liquefied Natural Gas (LNG) Regasification Power Plant Integrated with Cryogenic Energy Storage System.* Industrial & Engineering Chemistry Research, 2017. **56**(5): p. 1288-1296.
40. Alyami, H.H. and R. Williams, *Study and Evaluation of Liquid Air Energy Storage Technology For a Clean and Secure Energy Future.*
41. Morgan, R., et al., *Liquid air energy storage–analysis and first results from a pilot scale demonstration plant.* Applied energy, 2015. **137**: p. 845-853.
42. Guizzi, G.L., et al., *Thermodynamic analysis of a liquid air energy storage system.* Energy, 2015. **93**: p. 1639-1647.
43. Kishimoto, K., K. Hasegawa, and T. Asano, *Development of generator of liquid air storage energy system.* Mitsubishi Juko Giho, 1998. **35**: p. 60-63.
44. Feifei, B. and Z. Zhang, *Integration of low-level waste heat recovery and liquefied nature gas cold energy utilization.* Chinese Journal of Chemical Engineering, 2008. **16**(1): p. 95-99.
45. Ameel, B., et al., *Thermodynamic analysis of energy storage with a liquid air Rankine cycle.* Applied Thermal Engineering, 2013. **52**(1): p. 130-140.
46. Li, Y., H. Chen, and Y. Ding, *Fundamentals and applications of cryogen as a thermal energy carrier: A critical assessment.* International Journal of Thermal Sciences, 2010. **49**(6): p. 941-949.
47. Li, Y., et al., *An integrated solar-cryogen hybrid power system.* Renewable energy, 2012. **37**(1): p. 76-81.
48. Chino, K. and H. Araki, *Evaluation of energy storage method using liquid air.* Heat Transfer—Asian Research: Co-sponsored by the Society of Chemical Engineers of Japan and the Heat Transfer Division of ASME, 2000. **29**(5): p. 347-357.
49. Li, Y., X. Wang, and Y. Ding, *A cryogen-based peak-shaving technology: systematic approach and techno-economic analysis.* International Journal of Energy Research, 2013. **37**(6): p. 547-557.
50. Kantharaj, B., S. Garvey, and A. Pimm, *Compressed air energy storage with liquid air capacity extension.* Applied Energy, 2015. **157**: p. 152-164.
51. Li, Y., et al., *Load shifting of nuclear power plants using cryogenic energy storage technology.* Applied Energy, 2014. **113**: p. 1710-1716.
52. Li, Y., et al., *An integrated system for thermal power generation, electrical energy storage and CO2 capture.* International Journal of Energy Research, 2011. **35**(13): p. 1158-1167.
53. Smith, E., *Storage of electrical energy using supercritical liquid air.* Proceedings of the Institution of Mechanical Engineers, 1977. **191**(1): p. 289-298.
54. Vandor, D., *System and method for liquid air production, power storage and power release*. 2010, Google Patents.
55. Khalil, K.M., S. Mahmoud, and R. Al-Dadah, *Development of innovative non-repeated annular area dual stage small-scale nitrogen axial turbine for hybrid open-closed Rankine cycle.* Energy Conversion and Management, 2018. **164**: p. 157-174.
56. Du, Y. and Y. Ding, *Feasibility of small-scale cold energy storage (CES) through carbon dioxide based Rankine cycle.* Journal of Energy Storage, 2016. **6**: p. 40-49.
57. Borri, E., et al., *A preliminary study on the optimal configuration and operating range of a "microgrid scale" air liquefaction plant for Liquid Air Energy Storage.* Energy Conversion and Management, 2017. **143**: p. 275-285.
58. El-Khattam, W. and M.M. Salama, *Distributed generation technologies, definitions and benefits.* Electric power systems research, 2004. **71**(2): p. 119-128.
59. Pepermans, G., et al., *Distributed generation: definition, benefits and issues.* Energy policy, 2005. **33**(6): p. 787-798.

60. Lopes, J.P., et al., *Integrating distributed generation into electric power systems: A review of drivers, challenges and opportunities.* Electric power systems research, 2007. **77**(9): p. 1189-1203.
61. Dondi, P., et al., *Network integration of distributed power generation.* Journal of power sources, 2002. **106**(1-2): p. 1-9.
62. Chambers, A., B. Schnoor, and S. Hamilton, *Distributed generation: a nontechnical guide*. 2001: PennWell Books.
63. IEA, *Distributed generation in liberalised electricity markets.* OECDPublishing. http://dx.doi.org/10.1787/9789264175976-en.
64. Borges, C.L. and D.M. Falcao, *Optimal distributed generation allocation for reliability, losses, and voltage improvement.* International Journal of Electrical Power & Energy Systems, 2006. **28**(6): p. 413-420.
65. *IEEE,InstituteofElectricalandElectronicsEngineers.* http://www.ieee.org.
66. Aste, N. and C. Del Pero. *Urban-scale distributed power generation—Forecast methods for the estimation of electricity exchange profiles for grid-connected solar photovoltaic (PV) systems*. in *Clean Electrical Power (ICCEP), 2013 International Conference on*. 2013. IEEE.
67. Ackermann, T., G. Andersson, and L. Soder. *Electricity market regulations and their impact on distributed generation*. in *Electric Utility Deregulation and Restructuring and Power Technologies, 2000. Proceedings. DRPT 2000. International Conference on*. 2000. IEEE.
68. Vivekanandan, K. and P. Prabu. *Distributed power generation for isolated loads using smart grid technology*. in *Information Communication and Embedded Systems (ICICES), 2014 International Conference on*. 2014. IEEE.
69. Wang, Y., et al., *Modelling and simulation of a distributed power generation system with energy storage to meet dynamic household electricity demand.* Applied thermal engineering, 2013. **50**(1): p. 523-535.
70. OECD/IEA, *Full report next generation wind and solar power from cost to value.* International Energy Agency, 2016.
71. Bruni, G., S. Cordiner, and V. Mulone, *Domestic distributed power generation: Effect of sizing and energy management strategy on the environmental efficiency of a photovoltaic-battery-fuel cell system.* Energy, 2014. **77**: p. 133-143.
72. Paliwal, P., N. Patidar, and R. Nema, *Planning of grid integrated distributed generators: A review of technology, objectives and techniques.* Renewable and sustainable energy reviews, 2014. **40**: p. 557-570.
73. Allan, G., et al., *The economics of distributed energy generation: A literature review.* Renewable and Sustainable Energy Reviews, 2015. **42**: p. 543-556.
74. Bloch, H.P. and C. Soares, *Turboexpanders and process applications*. 2001: Gulf Professional Publishing.
75. Khalil, K.M., et al., *Investigate a hybrid open-Rankine cycle small-scale axial nitrogen expander by a camber line control point parameterization optimization technique.* Applied Thermal Engineering, 2017. **127**: p. 823-836.
76. Weiß, A.P. *Volumetric expander versus turbine–which is the better choice for small ORC plants*. in *3rd ASME ORC Conference, Brussels (Belgium)*. 2015.
77. Bao, J. and L. Zhao, *A review of working fluid and expander selections for organic Rankine cycle.* Renewable and Sustainable Energy Reviews, 2013. **24**: p. 325-342.
78. Papes, I., J. Degroote, and J. Vierendeels, *New insights in twin screw expander performance for small scale ORC systems from 3D CFD analysis.* Applied Thermal Engineering, 2015. **91**: p. 535-546.

79. Nuramal, A., et al., *Experimental study of screw turbine performance based on different angle of inclination.* Energy Procedia, 2017. **110**: p. 8-13.
80. Shen, L., et al., *A study of clearance height on the performance of single-screw expanders in small-scale organic Rankine cycles.* Energy, 2018. **153**: p. 45-55.
81. Xiong, Y., et al., *A novel expander-depending natural gas pressure regulation configuration: Performance analysis.* Applied Energy, 2018. **220**: p. 21-35.
82. Bianchi, G., et al., *Numerical modeling of a two-phase twin-screw expander for Trilateral Flash Cycle applications.* International Journal of Refrigeration, 2018. **88**: p. 248-259.
83. Li, G., et al., *Influence of inlet pressure and rotational speed on the performance of high pressure single screw expander prototype.* Energy, 2018. **147**: p. 279-285.
84. Hsieh, J.-C., et al., *Design and preliminary results of a 20-kW transcritical organic Rankine cycle with a screw expander for low-grade waste heat recovery.* Applied Thermal Engineering, 2017. **110**: p. 1120-1127.
85. Ziviani, D., et al., *Employing a Single-Screw Expander in an Organic Rankine Cycle with Liquid Flooded Expansion and Internal Regeneration.* Energy Procedia, 2017. **129**: p. 379-386.
86. Shen, L., et al., *Theoretical and experimental analyses of the internal leakage in single-screw expanders.* International Journal of Refrigeration, 2018. **86**: p. 273-281.
87. *Liquid Air in the energy and transport systems: Opportunities for industry and innovation in the UK. Full Report.* Centre for Low Carbon Futures, 2013. **ISBN: 978-0-9575872-1-2**.
88. Tian, C.Z., G.J. Yuan, and G.J. Chen. *Cylinder flow simulation of liquid nitrogen engine based on STAR-CD*. in *Applied Mechanics and Materials*. 2013. Trans Tech Publ.
89. *Blower-scavenged, two-stroke-cycle engine with uniflow scavenging.* Encyclopædia Britannica, Inc. https://www.britannica.com/technology/gasoline-engine, 2007.
90. Mutumba, A., et al., *Design and development of a direct injection system for cryogenic engines.* Cryogenics, 2018. **91**: p. 77-86.
91. Morini, M., et al., *Analysis of a scroll machine for micro ORC applications by means of a RE/CFD methodology.* Applied Thermal Engineering, 2015. **80**: p. 132-140.
92. Garg, P., et al., *Development of a generic tool to design scroll expanders for ORC applications.* Applied Thermal Engineering, 2016. **109**: p. 878-888.
93. Kane, M., *Research, Development & Commercialization of ORC modules in Swithzerland.* Schweizer ORC Symposium, 2014.
94. Qiu, K., M. Thomas, and M. Douglas, *Investigation of a scroll expander driven by compressed air and its potential applications to ORC.* Applied Thermal Engineering, 2018. **135**: p. 109-115.
95. Luo, X., et al., *A New Scroll-Type Air Motor With Magnetic Spirals.* IEEE/ASME Transactions on Mechatronics, 2018. **23**(1): p. 459-468.
96. Lu, Y., et al., *Analysis of a 1 kW organic Rankine cycle using a scroll expander for engine coolant and exhaust heat recovery.* Frontiers in Energy, 2017. **11**(4): p. 527-534.
97. Zhang, X., et al., *Study on the performance and optimization of a scroll expander driven by compressed air.* Applied Energy, 2017. **186**: p. 347-358.
98. Chang, J.-C., et al., *Experimental study and CFD approach for scroll type expander used in low-temperature organic Rankine cycle.* Applied Thermal Engineering, 2014. **73**(2): p. 1444-1452.

99. Wang, H., R. Peterson, and T. Herron, *Experimental performance of a compliant scroll expander for an organic Rankine cycle*. 2009, SAGE Publications Sage UK: London, England.
100. Aparna, K. and K. Ramakrishna, *A Review on Mechanical Losses and Non-Uniform Expansion of Flu-id in A Scroll Expander.* Mechanical Engineering Research and Developments, 2018. **41**: p. 9-19
101. Mascuch, J., et al., *Towards development of 1-10 kW pilot ORC units operating with hexamethyldisiloxane and using rotary vane expander.* Energy Procedia, 2017. **129**: p. 826-833.
102. Imran, M., et al., *Volumetric expanders for low grade heat and waste heat recovery applications.* Renewable and Sustainable Energy Reviews, 2016. **57**: p. 1090-1109.
103. Kolasiński, P., P. Błasiak, and J. Rak, *Experimental and numerical analyses on the rotary vane expander operating conditions in a micro organic Rankine cycle system.* Energies, 2016. **9**(8): p. 606.
104. Subiantoro, A. and K.T. Ooi, *Comparison and performance analysis of the novel revolving vane expander design variants in low and medium pressure applications.* Energy, 2014. **78**: p. 747-757.
105. Vodicka, V., et al., *Impact of major leakages on characteristics of a rotary vane expander for ORC.* Energy Procedia, 2017. **129**: p. 387-394.
106. Lakshminarayana, B., *Fluid dynamics and heat transfer of turbomachinery*. 1995: John Wiley & Sons.
107. Zywica, G., T.Z. Kaczmarczyk, and E. Ihnatowicz, *A review of expanders for power generation in small-scale organic Rankine cycle systems: Performance and operational aspects.* Proceedings of the Institution of Mechanical Engineers, Part A: Journal of Power and Energy, 2016. **230**(7): p. 669-684.
108. Dixon, S.L. and C. Hall, *Fluid mechanics and thermodynamics of turbomachinery*. 2010: Butterworth-Heinemann.
109. Yahya, S., *Turbines compressors and fans*. 1987: Tata McGraw-Hill Education.
110. Azimian, M. and H.-J. Bart, *Computational analysis of erosion in a radial inflow steam turbine.* Engineering Failure Analysis, 2016. **64**: p. 26-43.
111. Persky, R. and E. Sauret, *Assessment of turbine performance variability in response to power block design decisions for SF 6 and CO 2 solar thermal power plants.* Energy Conversion and Management, 2018. **169**: p. 255-265.
112. Li, Z., et al., *Aerodynamic design method of micro-scale radial turbines considering the effect of wall heat transfer.* Applied Thermal Engineering, 2018. **138**: p. 94-109.
113. White, M.T. and A.I. Sayma, *A Generalised Assessment of Working Fluids and Radial Turbines for Non-Recuperated Subcritical Organic Rankine Cycles.* Energies, 2018. **11**(4): p. 800.
114. Cerdoun, M. and A. Ghenaiet, *Unsteady behaviour of a twin entry radial turbine under engine like inlet flow conditions.* Applied Thermal Engineering, 2018. **130**: p. 93-111.
115. Mounier, V., L.E. Olmedo, and J. Schiffmann, *Small scale radial inflow turbine performance and pre-design maps for Organic Rankine Cycles.* Energy, 2018. **143**: p. 1072-1084.
116. Kapoor, P., et al., *Adaptive Turbo Matching: Radial Turbine Design Optimization through 1D Engine Simulations with Meanline Model in-the-Loop.* SAE Technical Paper, 2018: p. 01-0974.
117. Alshammari, F., A. Karvountzis-Kontakiotis, and A. Pesyridis, *Effect of radial turbo-expander design on off-highway vehicle organic Rankine cycle system efficiency.* International Journal of Powertrains, 2018. **7**(1-3): p. 72-93.

118. He, W., J. Wang, and Y. Ding, *New radial turbine dynamic modelling in a low-temperature adiabatic compressed air energy storage system discharging process.* Energy Conversion and Management, 2017. **153**: p. 144-156.
119. Ke, C., et al., *Numerical and experimental study of the performance effects of varying vaneless space in high-speed micro turbine stators.* Cryogenics, 2017. **88**: p. 10-16.
120. Guillaume, L., et al., *Performance of a radial-inflow turbine integrated in an ORC system and designed for a WHR on truck application: An experimental comparison between R245fa and R1233zd.* Applied Energy, 2017. **186**: p. 408-422.
121. Kim, D.-Y. and Y.-T. Kim, *Preliminary design and performance analysis of a radial inflow turbine for organic Rankine cycles.* Applied Thermal Engineering, 2017. **120**: p. 549-559.
122. Heshmat, H., A. Hunsberger, and J.F. Walton. *Design of a Partial Admission Turbine for an Organic Rankine Cycle With Environmental Fluctuation Consideration*. in *ASME 2016 Power Conference collocated with the ASME 2016 10th International Conference on Energy Sustainability and the ASME 2016 14th International Conference on Fuel Cell Science, Engineering and Technology*. 2016. American Society of Mechanical Engineers.
123. Weiß, A.P., et al., *Experimental characterization and comparison of an axial and a cantilever micro-turbine for small-scale Organic Rankine Cycle.* Applied Thermal Engineering, 2018. **140**: p. 235-244.
124. Yue, C., D. Han, and W. Pu, *Design and Experimental Study of a 5-kW Organic Rankine Cycle with Axial-Flow Turbine for Low-Temperature Heat Recovery.* Journal of Energy Engineering, 2018. **144**(3): p. 04018034.
125. Dumont, O., *Experimental Investigation and Modelling of a 1.5 kW Axial Turbine for Waste Heat Recovery of a Gasoline Passenger Car through a Rankine Cycle*. 2018, SAE Technical Paper.
126. Adnan, F.P. and F. Hartono. *Design of Single Stage Axial Turbine with Constant Nozzle Angle Blading for Small Turbojet*. in *Journal of Physics: Conference Series*. 2018. IOP Publishing.
127. Di Battista, D. and R. Cipollone, *Experimental analysis of an organic rankine cycle plant bottoming a heavy-duty engine using axial turbine as prime mover.* SAE International Journal of Engines, 2017. **10**(2017-01-9279): p. 1385-1397.
128. Varma, A. and S. Soundranayagam, *Experimental study of a small partial admission axial turbine with low aspect ratio blade.* Proceedings of the Institution of Mechanical Engineers, Part G: Journal of Aerospace Engineering, 2014. **228**(1): p. 20-34.
129. Zhang, C., et al., *Performance optimization of low-temperature geothermal organic Rankine cycles using axial turbine isentropic efficiency correlation.* Journal of the Brazilian Society of Mechanical Sciences and Engineering, 2018. **40**(2): p. 61.
130. Bahr Ennil, A., *Optimization of small-scale axial turbine for distributed compressed air energy storage system*. 2017, University of Birmingham.
131. Pu, W., et al., *Experimental study on Organic Rankine cycle for low grade thermal energy recovery.* Applied Thermal Engineering, 2016. **94**: p. 221-227.
132. Sun, H., et al., *Performance evaluation of a partially admitted axial turbine using R245fa, R123 and their mixtures as working fluid for small-scale organic Rankine cycle.* Energy Conversion and Management, 2018. **171**: p. 925-935.
133. Zhou, Z., S. Chen, and S. Wang, *Aerodynamic optimisation of a winglet-cavity tip in a high-pressure axial turbine cascade.* Proceedings of the Institution of Mechanical Engineers, Part G: Journal of Aerospace Engineering, 2018. **232**(4): p. 649-663.
134. So, K., et al. *Aerodynamic Optimization of the Gas Outlet Casing of the Axial Turbine Stage in a Turbocharger With Experimental Validation*. in *ASME Turbo Expo 2015:*

Turbine Technical Conference and Exposition. 2015. American Society of Mechanical Engineers.
135. Marchukov, E.Y., et al. *Multidisciplinary Optimization of the Working Process of Uncooled Axial Turbine According to Efficiency and Strength Criteria*. in *ASME Turbo Expo 2017: Turbomachinery Technical Conference and Exposition*. 2017. American Society of Mechanical Engineers.
136. Asgarshamsi, A., A.H. Benisi, and A. Assempour, *Multi-objective optimum stator and rotor stagger angle distributions of an axial turbine stage.* Scientia Iranica. Transaction B, Mechanical Engineering, 2015. **22**(2): p. 448.
137. Meroni, A., et al., *Optimization of organic Rankine cycle power systems considering multistage axial turbine design.* Applied Energy, 2018. **209**: p. 339-354.
138. Li, Y., et al., *Aerodynamic optimisation of a low-pressure multistage turbine using the response-surface method.* Journal of Mechanical Science and Technology, 2013. **27**(8): p. 2537-2546.
139. Ennil, A.B., et al., *Minimization of loss in small scale axial air turbine using CFD modeling and evolutionary algorithm optimization.* Applied Thermal Engineering, 2016. **102**: p. 841-848.
140. Al Jubori, A., et al., *Three dimensional optimization of small-scale axial turbine for low temperature heat source driven organic Rankine cycle.* Energy conversion and management, 2017. **133**: p. 411-426.
141. Hazby, H., et al., *Effects of blade deformation on the performance of a high flow coefficient mixed flow impeller*. Journal of Turbomachinery, 2015. **137**(12): p. 121005.
142. Moustapha, H., et al., *Axial and radial turbines*. Vol. 2. 2003: Concepts NREC White River Junction, VT.
143. Asgarshamsi, A., et al. *Multi-point optimization of lean and sweep angles for stator and rotor blades of an axial turbine*. in *ASME Turbo Expo 2014: Turbine Technical Conference and Exposition*. 2014. American Society of Mechanical Engineers.
144. Shieh, T.-H., *Aerothermodynamic Effects and Modeling of the Tangential Curvature of Guide Vanes in an Axial Turbine Stage.* International Journal of Rotating Machinery, 2017. **2017**.
145. Karrabi, H. and M. Rezasoltani. *The effect of blade lean, twist and bow on the performance of axial turbine at design point*. in *ASME 2011 International Mechanical Engineering Congress and Exposition*. 2011. American Society of Mechanical Engineers.
146. D'Ippolito, G., V. Dossena, and A. Mora, *The influence of blade lean on straight and annular turbine cascade flow field.* Journal of Turbomachinery, 2011. **133**(1): p. 011013.
147. Bini, R. and D. Colombo, *Large multistage axial turbines.* Energy Procedia, 2017. **129**: p. 1078-1084.
148. Fuls, W., *Accurate stage-by-stage modelling of axial turbines using an appropriate nozzle analogy with minimal geometric data.* Applied Thermal Engineering, 2017. **116**: p. 134-146.
149. Surwilo, J., P. Lampart, and M. Szymaniak, *CFD analysis of fluid flow in an axial multi-stage partial-admission ORC turbine.* Open Engineering, 2015. **5**(1).
150. Ghenaiet, A. and K. Touil, *Characterization of component interactions in two-stage axial turbine.* Chinese Journal of Aeronautics, 2016. **29**(4): p. 893-913.
151. Ghoreyshi, S.M. and M.T. Schobeiri. *Numerical simulation of the multistage ultra-high efficiency gas turbine engine, UHEGT*. in *ASME Turbo Expo 2017:*

Turbomachinery Technical Conference and Exposition. 2017. American Society of Mechanical Engineers.
152. Jouybari, J., et al., *Analytical modeling of performance characteristics of axial flow two-stage turbine engine using pressure losses models and comparing with experimental results.* World Applied Sciences Journal, 2013. **21**(9): p. 1250-1259.
153. Al Jubori, A.M., R. Al-Dadah, and S. Mahmoud, *An innovative small-scale two-stage axial turbine for low-temperature organic Rankine cycle.* Energy Conversion and Management, 2017. **144**: p. 18-33.
154. Daabo, A.M., et al., *Numerical analysis of small scale axial and radial turbines for solar powered Brayton cycle application.* Applied Thermal Engineering, 2017. **120**: p. 672-693.
155. Kalogirou, S.A., *Solar thermal collectors and applications.* Progress in energy and combustion science, 2004. **30**(3): p. 231-295.
156. Van Erdeweghe, S., et al., *"Preheat-parallel" configuration for low-temperature geothermally-fed CHP plants.* Energy Conversion and Management, 2017. **142**: p. 117-126.
157. Kerry, F.G., *Industrial gas handbook: gas separation and purification*. 2007: CRC Press.
158. Venkatarathnam, G. and K. Timmerhaus, *Cryogenic mixed refrigerant processes*. Vol. 100. 2008: Springer.
159. Chiu, C.-H. and H. Kimmel. *Turbo-expander technology development for LNG plants*. in *LNG-13 Conference Seoul, Korea, May 2001*. 2001.
160. Darcovich, K., et al., *An international survey of electrical and DHW load profiles for use in simulating the performance of residential micro-cogeneration systems.* ECB Annex, 2014. **54**.
161. Whitfield, A. and N.C. Baines, *Design of radial turbomachines.* 1990.
162. Shepherd, D.G., *Principles of turbomachinery*. 1956: Macmillan.
163. Horlock, J.H., *Axial flow turbines*. 1966: Butterworth.
164. Buckingham, E., *On physically similar systems; illustrations of the use of dimensional equations.* Physical review, 1914. **4**(4): p. 345.
165. Japikse, D. and N. Baines, *Introduction to turbomachinery*. 1994.
166. Balje, O., *Turbomachines-A guide to design, selection, and theory*. 1981: John Wiley & Sons.
167. Wood, H.J. *Current technology of radial-inflow turbines for compressible fluids*. in *ASME 1962 Gas Turbine Power Conference and Exhibit*. 1962. American Society of Mechanical Engineers.
168. Glassman, A.J., *Computer code for preliminary sizing analysis of axial-flow turbines.* 1992.
169. Stewart, W.L., *A study of axial-flow turbine efficiency characteristics in terms of velocity diagram parameters*. 1961, national aeronautics and space administration washington dc.
170. Zweifel, O., *The spacing of turbo-machine blading, especially with large angular deflection.* Brown Boveri Rev., 1945. **32**(12): p. 436-444.
171. Ainley, D. and G.C. Mathieson, *A method of performance estimation for axial-flow turbines*. 1951, aeronautical research council london (united kingdom).
172. Dunham, J. and P. Came, *Improvements to the Ainley-Mathieson method of turbine performance prediction.* Journal of Engineering for Power, 1970. **92**(3): p. 252-256.
173. Kacker, S. and U. Okapuu, *A mean line prediction method for axial flow turbine efficiency.* Journal of engineering for power, 1982. **104**(1): p. 111-119.

174. MATLAB, M., *The language of technical computing. The MathWorks.* Inc http://www. mathworks.com, 2012.
175. *ANSYS TurboGrid Introduction.* Release 15.0, November 2013(ANSYS, Inc. is certified to ISO 9001:2008).
176. *ANSYS CFX-Solver Theory Guide.* Release 15.0, November 2013(ANSYS, Inc. is certified to ISO 9001:2008.).
177. Gatski, T. and C. Rumsey, *Linear and nonlinear eddy viscosity models.* Closure strategies for turbulent and transitional flows, 2002: p. 9-46.
178. Wilcox, D.C., *Multiscale model for turbulent flows.* AIAA journal, 1988. **26**(11): p. 1311-1320.
179. Carregal-Ferreira, J., et al., *Advanced CFD analysis of aerodynamics using CFX*. AEA Technology GmbH, Otterfing, 2002: p. 1-14.
180. Menter, F., E. Thomas, and V. Wolfgang. *Heat transfer predictions based on two-equation turbulence models*. in *ASME-JSME 2003 Thermal Engineering Joint Conference*. 2003.
181. *ANSYS Design Exploration User's Guide.* release 15, February 2014(ANSYS, Inc. is certified to ISO 9001:2008.).
182. Cornell, J.A., *The Basic References in Quality Contorol, Vol. 8, How to Apply Response Surface Methodology*. American Society for Quality, 1990. **51**.
183. Shyy, W., et al., *Global design optimization for aerodynamics and rocket propulsion components.* Progress in Aerospace Sciences, 2001. **37**(1): p. 59-118.
184. Dendaluce, M., et al. *Microcontroller implementation of a multi objective genetic algorithm for real-time intelligent control*. in *International Joint Conference SOCO'13-CISIS'13-ICEUTE'13*. 2014. Springer.
185. Han, W., et al. *Effects of leaning and curving of blades with high turning angles on the aerodynamic characteristics of turbine rectangular cascades*. in *ASME 1993 International Gas Turbine and Aeroengine Congress and Exposition*. 1993. American Society of Mechanical Engineers.
186. Wang, Z., et al., *The effect of blade leaning on cascade aerodynamic characteristics and the experimental study of mechanism of reducing secondary flow losses by leaned blades.* Journal of Engineering Thermophysics, 1988. **9**: p. 131-136.
187. Arabnia, M., *Aerodynamic shape optimization of axial turbines in three dimensional flow*. 2012, Concordia University.
188. Du, Q., et al., *Design performance evaluation and vortex structure investigation of different S-shaped intermediate turbine ducts.* Science China Technological Sciences, 2012. **55**(12): p. 3510-3520.
189. Gräsel, J., M. Pierré, and J. Demolis. *Parametric interturbine duct design and optimisation*. in *Proceedings of 25th international congress of the aeronautical sciences, ICAS*. 2006.
190. Liu, J., et al., *Effects of rising angle on upstream blades and intermediate turbine duct.* Journal of Thermal Science, 2016. **25**(4): p. 293-301.
191. Baskharone, E.A., *Principles of turbomachinery in air-breathing engines*. 2006: Cambridge University Press.
192. Moffat, R., *Contributions to the theory of single-sample uncertainty analysis.* Journal of Fluids Engineering, 1982. **104**(2): p. 250-258.
193. Cheatle, K., *Fundamentals of test measurement instrumentation*. 2006: ISA--Instrumentation, Systems, and Automation Society.
194. Stern, F., et al., *Summary of experimental uncertainty assessment methodology with example*. 1999, IIHR Report.
195. Logan Jr, E., *Handbook of turbomachinery*. 2003: CRC Press.

196. Tsakonas, S., W. Jacobs, and M. Ali, *Propeller Blade Pressure Distribution Due to Loading and Thickness Effects*. 1976, stevens inst of tech hoboken nj davidson lab.
197. LemmonE, W., M. Huber, and M. McLinder, *NIST reference database 23: reference fluid thermodynamic and transport properties-REFPROP, version 9.1 Natl.* Inst. Stand. Technol. Stand. Ref. Data Progr, 2013.
198. Rahbar, K., *Development and optimization of small-scale radial inflow turbine for waste heat recovery with organic rankine cycle*. 2016, University of Birmingham.

APPENDIX A

Uncertainties of Instruments

A-1: Thermocouples

The uncertainty in the thermocouples can be calculated by

$$U_{TC} = \pm\sqrt{(U_{st})^2 + (U_{curve\_fit})^2} \quad \text{A-1}$$

The uncertainties of thermocouples U_{TC},(U_{st}), and (U_{curve_fit}) are , total , standard and curve fit respectively. The standard uncertainty for thermometer is provided by the manufacturer $\pm 0.04^{o}$C. The uncertainty of the curve fit was calculated by mean deviation as below:

$$U_{curve\ fit} = t_{n-1,95\%} * \sigma_x \quad \text{A-2}$$

In summary the uncertainty for inlet thermocouple is shown in Table A-1 while the same procedure was followed for others thermocouples.

Table A-1 Calculation of uncertainty of inlet Thermocouple

Data point	Measurement of thermometer [˚C]	Measurement of thermocouple [˚C]	Curve fit equation y = 1.0057x + 0.3617	Deviation
1	23	23.88	23.167276	2.80E-02
2	25	25.86	25.147672	2.18E-02
3	30	30.52	29.808604	3.66E-02
4	35	35.48	34.769596	5.31E-02
5	40	40.85	40.14067	1.98E-02
6	50	50.52	49.812604	3.51E-02
7	60	60.84	60.134668	1.81E-02
8	70	70.7	69.99664	1.13E-05
9	80	80.73	80.028646	8.21E-04
Summation of deviation points				0.213379375
Degree of freedom				8
Standard deviation				0.163316937
Standard deviation of mean				0.05164535
Student distribution factor				2.306
Uncertainty curve fit				0.119094177
Overall uncertainty of thermocouple				0.125632094

A-2: Pressure sensors

Similar to the thermocouples uncertainties calculation the pressure sensors uncertainties are calculated by equation A-1. The standard uncertainty for the certified pressure gauge is ±0.0397 bars while the curve fit uncertainty for the pressure sensors was calculated by equation A-2. In summary the uncertainty for inlet total pressure sensor is showed in Table A-2 while the same procedure was followed for others sensors.

Table A-2 Calculation of uncertainty of inlet total pressure sensor

Data point	Guge pressure [bar]	Measurement of pressure [Voltag]	Curve fit equation y = 5.9447X - 2.4478	Deviation
1	0	0.401	-0.0639753	4.09E-03
2	0.5	0.498	0.5126606	1.60E-04
3	1	0.581	1.0060707	3.69E-05
4	1.5	0.665	1.5054255	2.94E-05
5	2	0.75	2.010725	1.15E-04
6	2.5	0.835	2.5160245	2.57E-04
7	3	0.919	3.0153793	2.37E-04
8	3.5	1.003	3.5147341	2.17E-04
9	4	1.084	3.9962548	1.40E-05
10	4.5	1.167	4.4896649	1.07E-04
11	5	1.252	4.9949644	2.54E-05
12	5.5	1.331	5.4645957	1.25E-03
13	6	1.422	6.0055634	3.10E-05
14	6.5	1.51	6.528697	8.24E-04
15	7	1.593	7.0221071	4.89E-04
16	7.5	1.677	7.5214619	4.61E-04
17	8	1.761	8.0208167	4.33E-04
18	8.5	1.844	8.5142268	2.02E-04
19	9	1.924	8.9898028	1.04E-04
20	9.5	2.008	9.4891576	1.18E-04
21	10	2.085	9.9468995	2.82E-03
Summation of deviation points				0.012025255
Degree of freedom				20
Standard deviation				0.02452066
Standard deviation of mean				0.007754114
Student distribution factor				2.086
Uncertainty curve fit				0.016175081
Overall uncertainty of thermocouple				0.042868674

APPENDIX B

Details of manufactured turbines drawings

This appendix shows the detailed drawings of the all turbine parts as listed in table B-1:

Table B-1 Turbines parts detailed drawings index table

No.	Part name	Figure number
1	Rotor 4mm	B-1
2	Rotor 6mm	B-2
3	Rotor 8mm	B-3
4	Stator 4mm	B-4
5	Stator 6mm	B-5
6	Stator 8mm	B-6
7	Turbine shaft	B-7
8	Rotor case	B-8
9	Outlet ring	B-9

10	Bearing house	B-10
11	Sealing house	B-11
12	Spacer	B-12
13	Disc	B-13
14	Shaft key	B-14

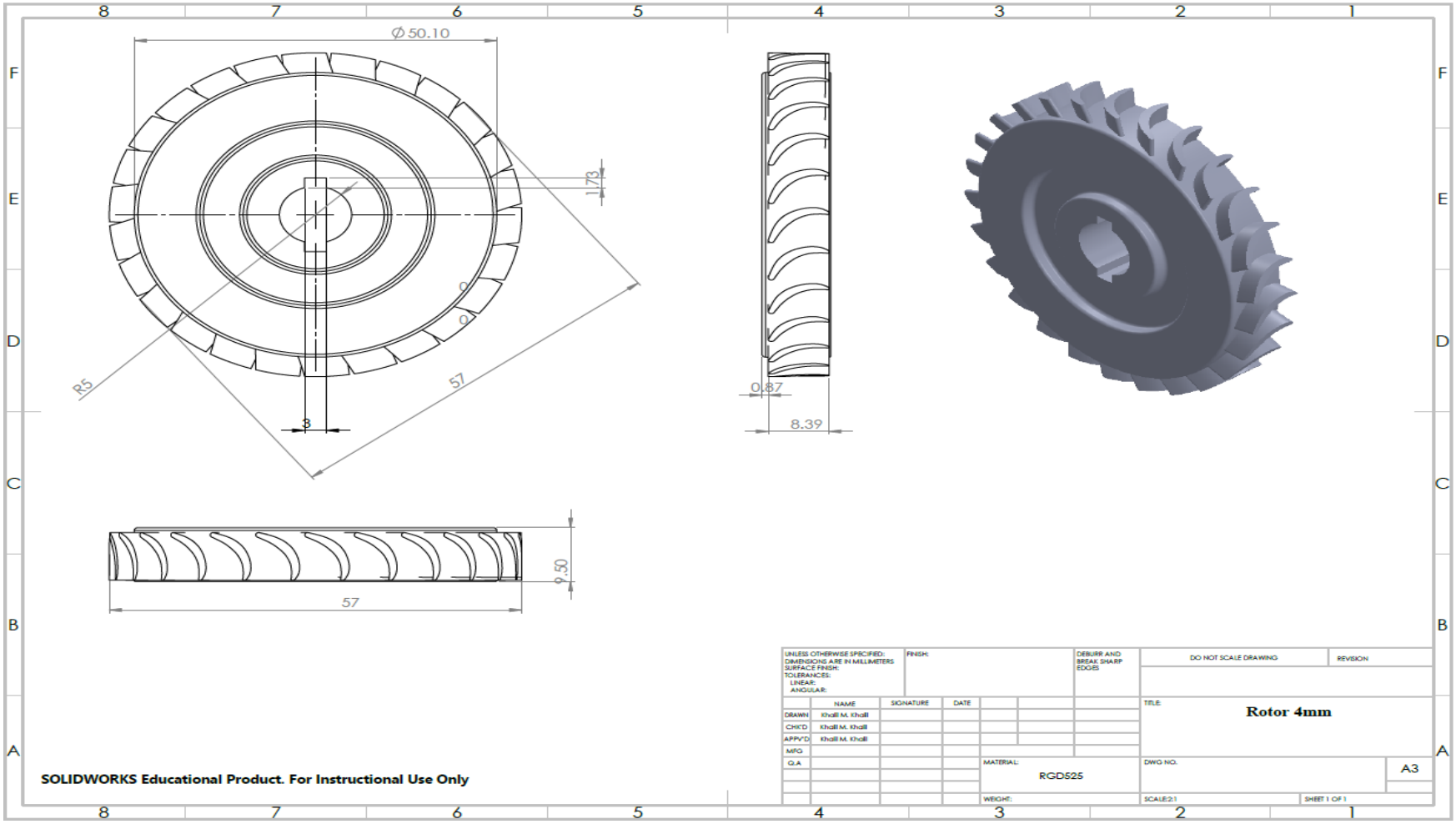

Figure B-1 Rotor 4mm blade height detailed drawing

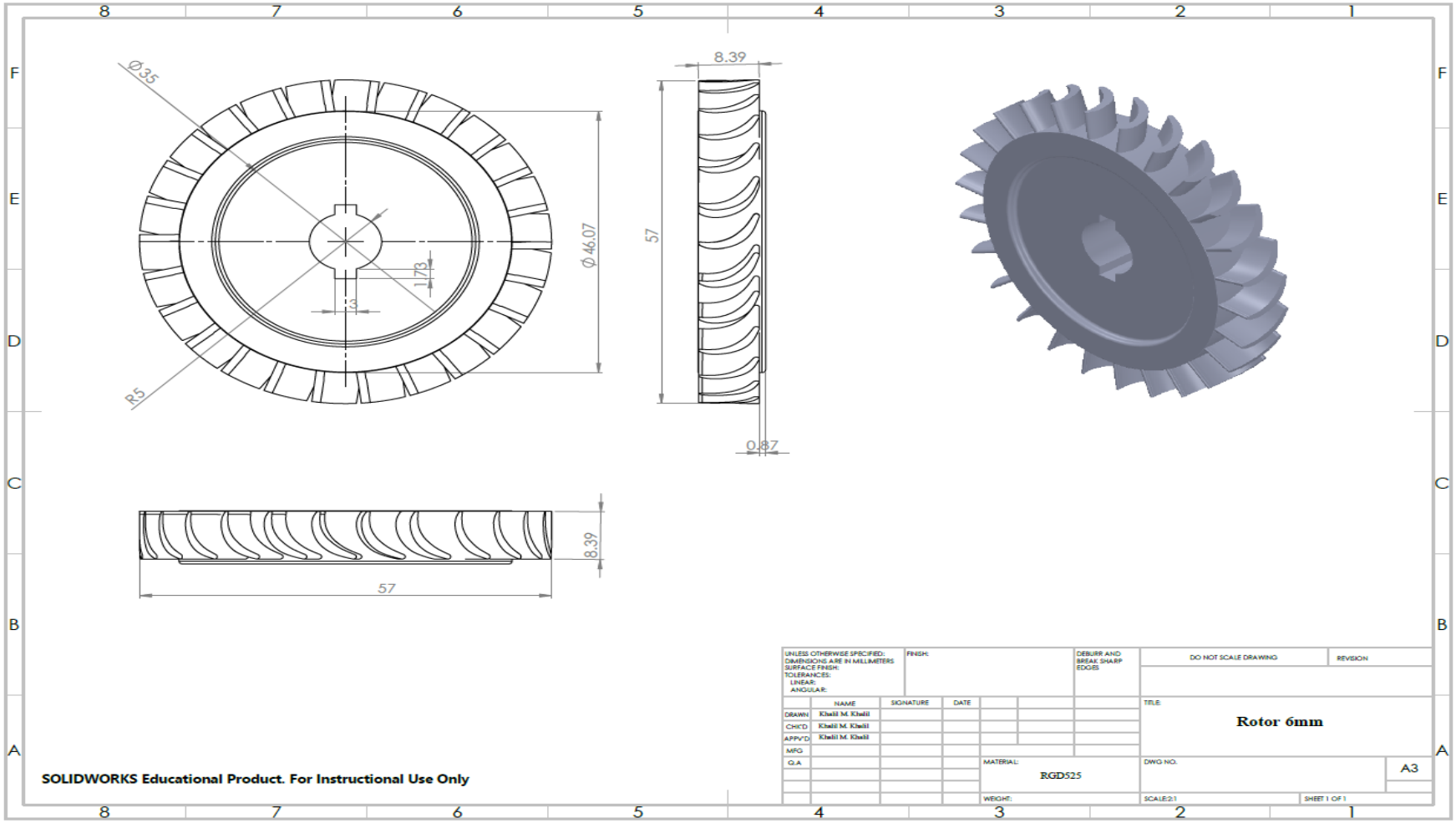

Figure B-2 Rotor 6mm blade height detailed drawing

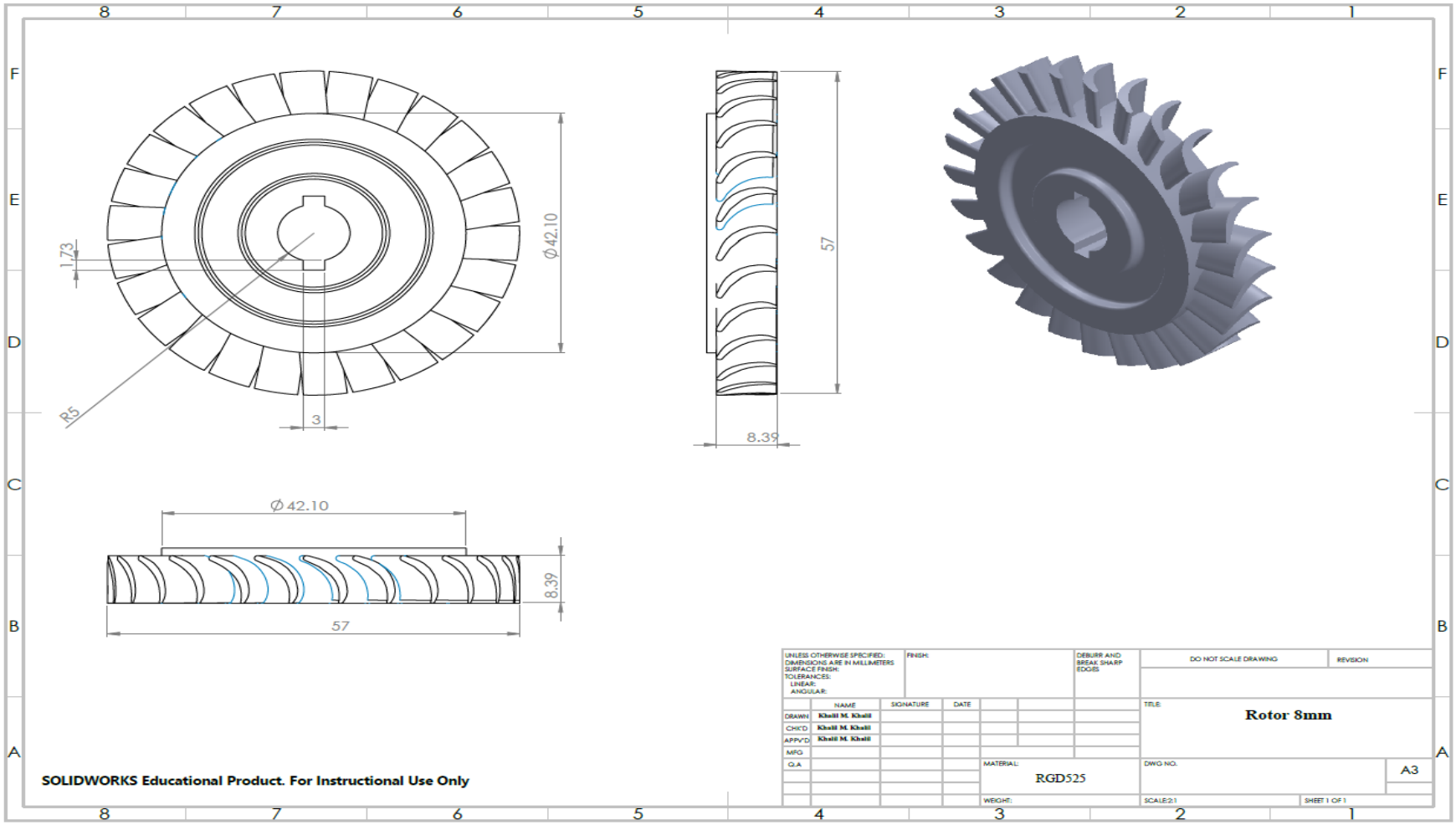

Figure B-3 Rotor 8mm blade height detailed drawing

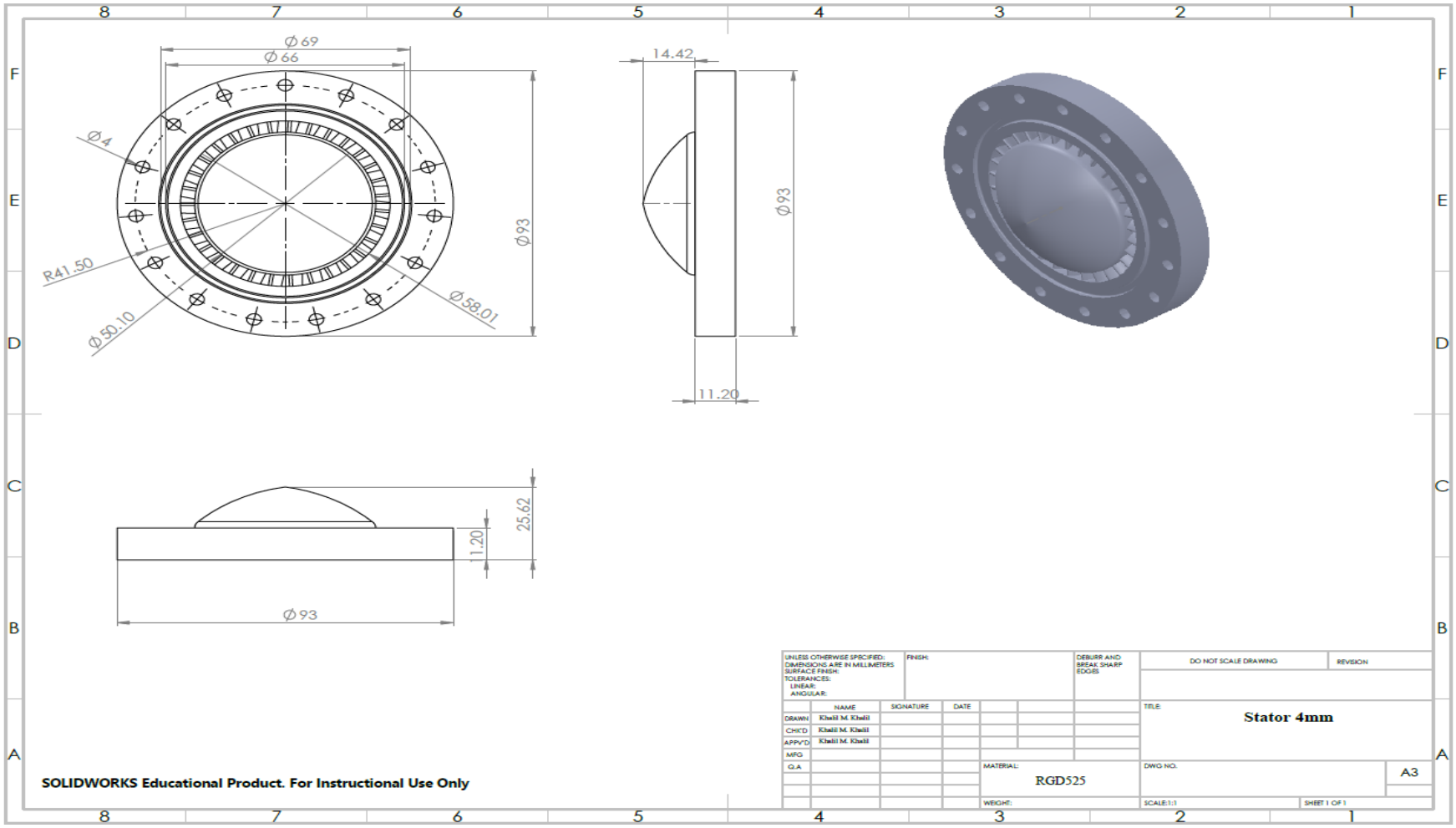

Figure B-4 Stator 4mm blade height detailed drawing

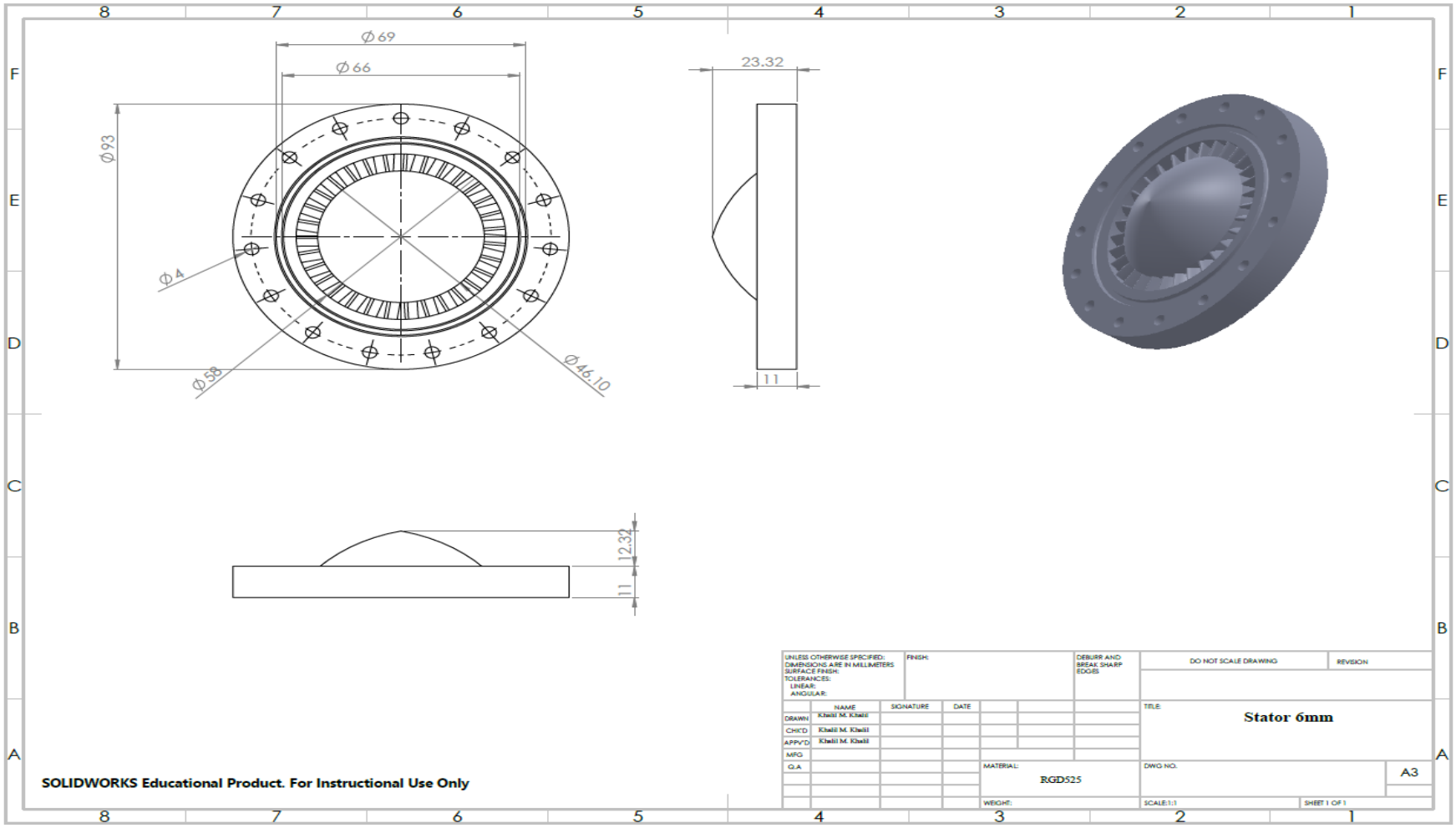

Figure B-5 Stator 6mm blade height detailed drawing

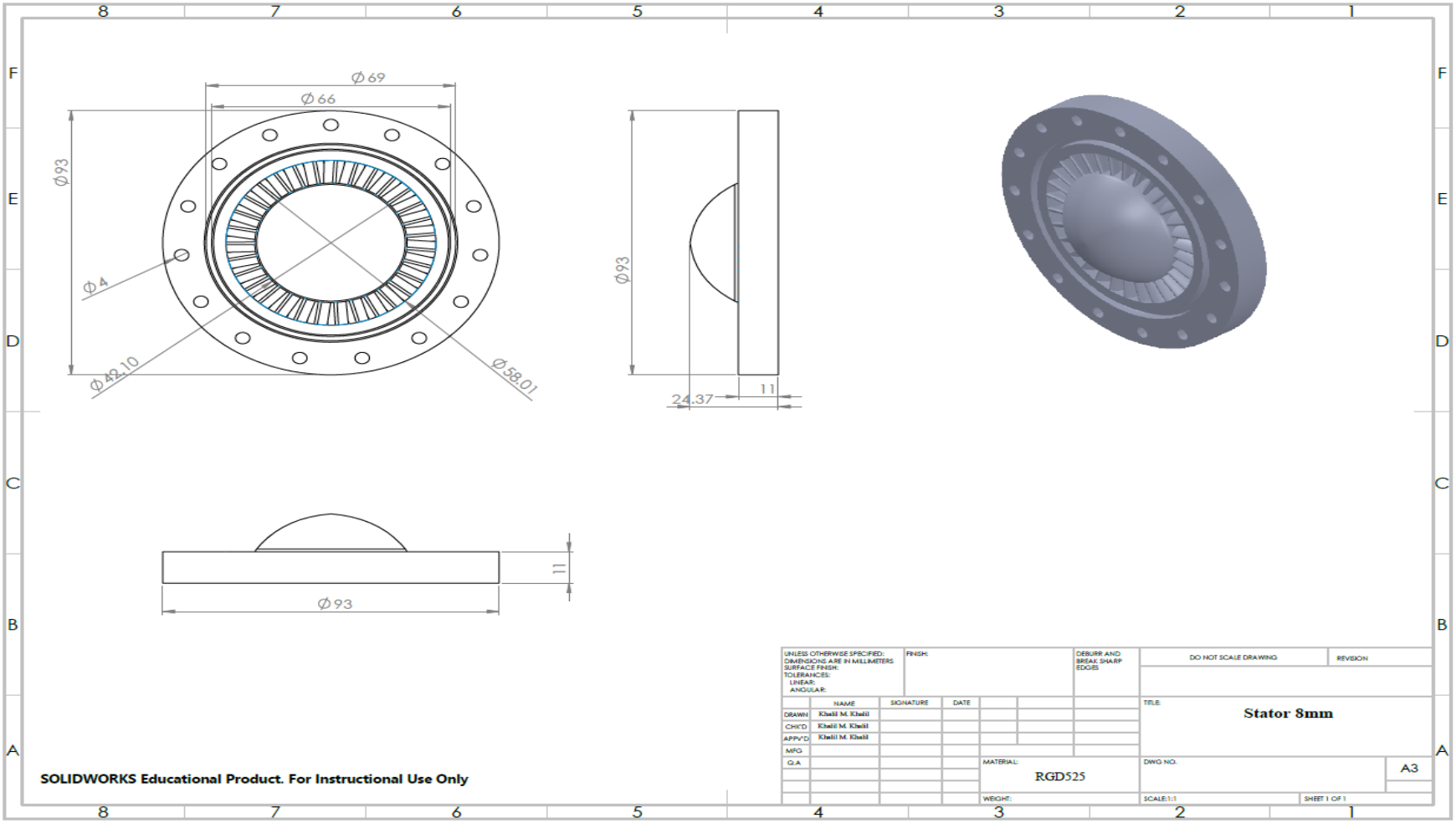

Figure B-6 Stator 8mm blade height detailed drawing

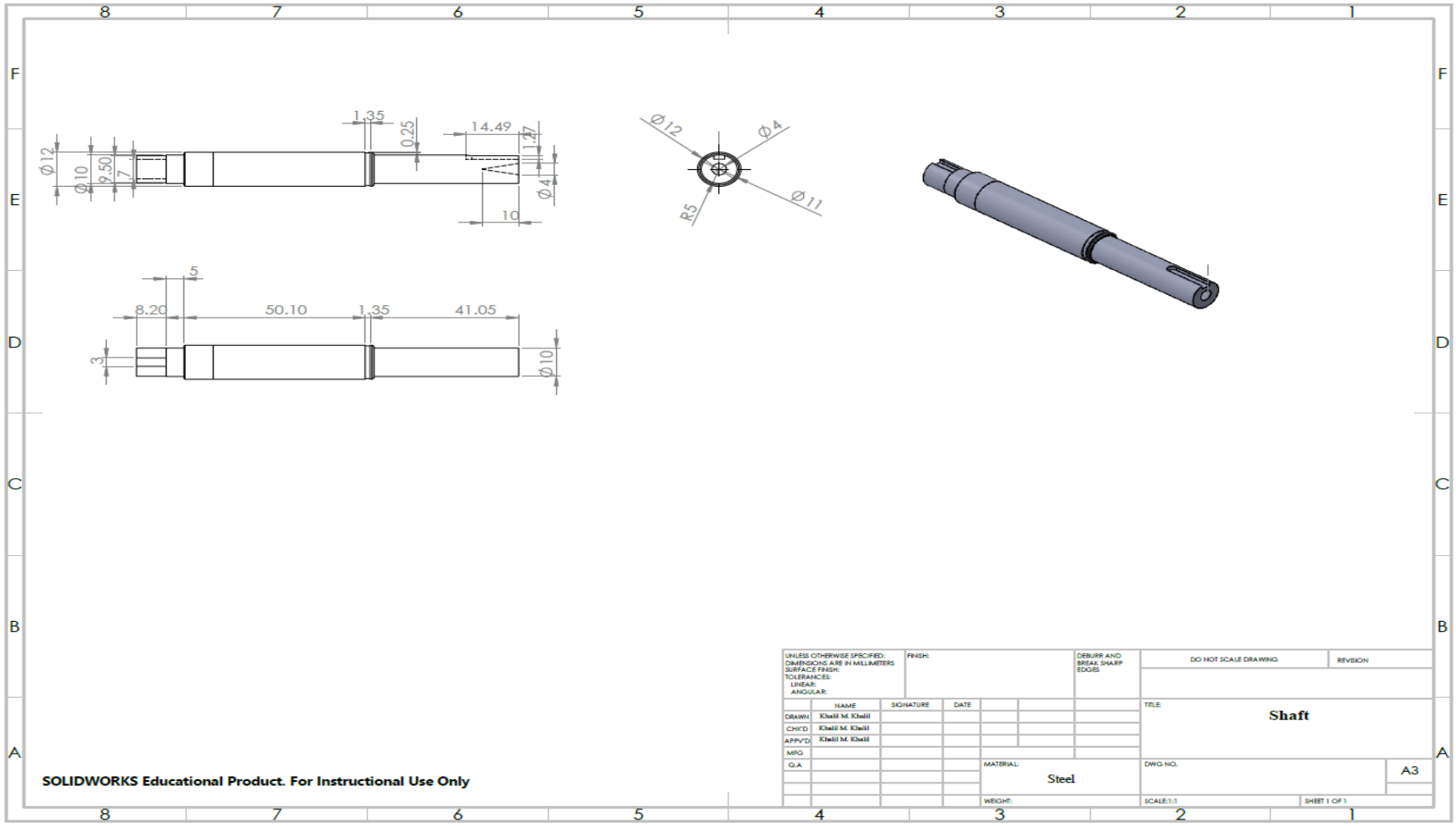

Figure B-7 turbine Shaft detailed drawing

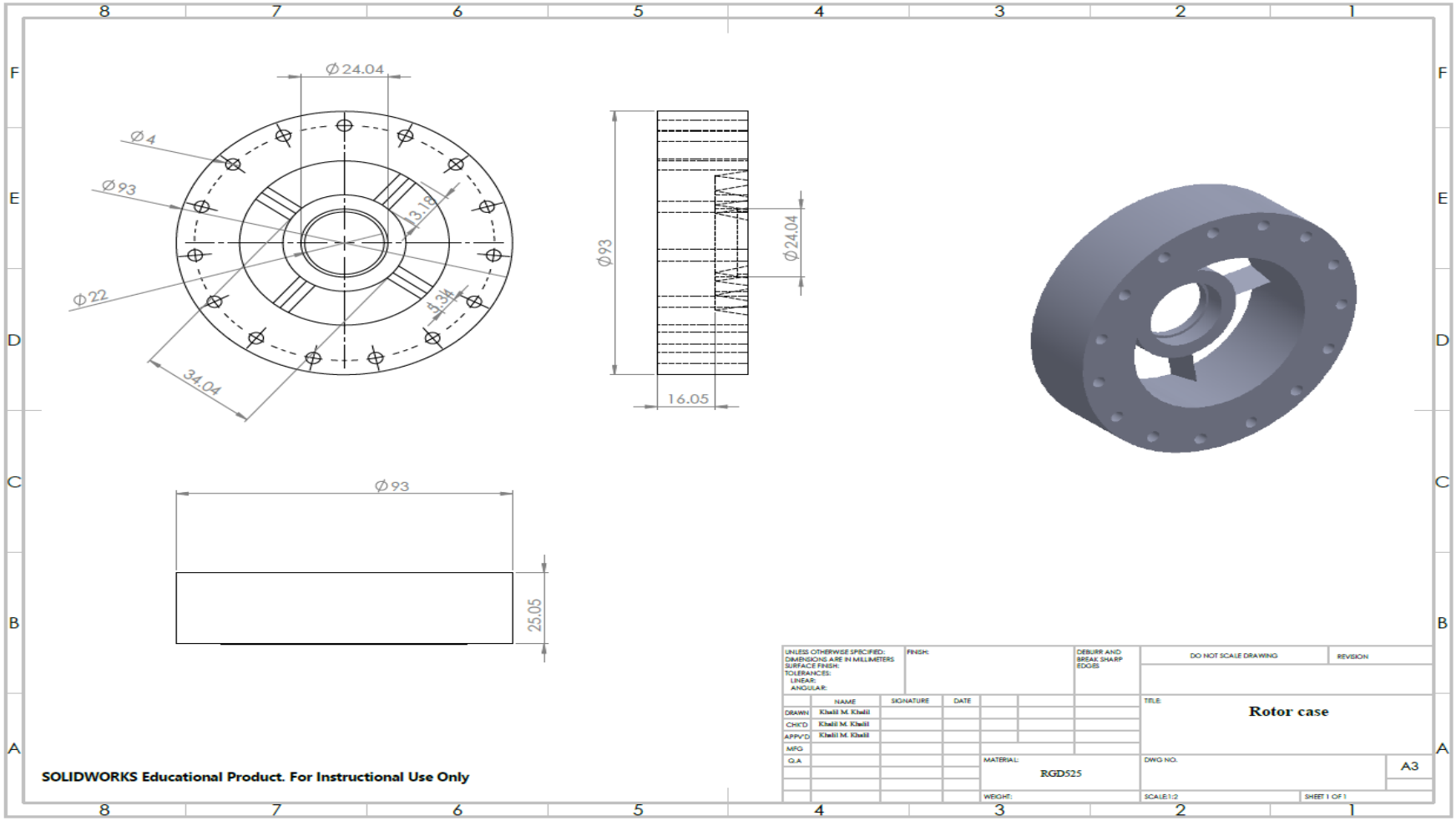

Figure B-8 Rotor case detailed drawing

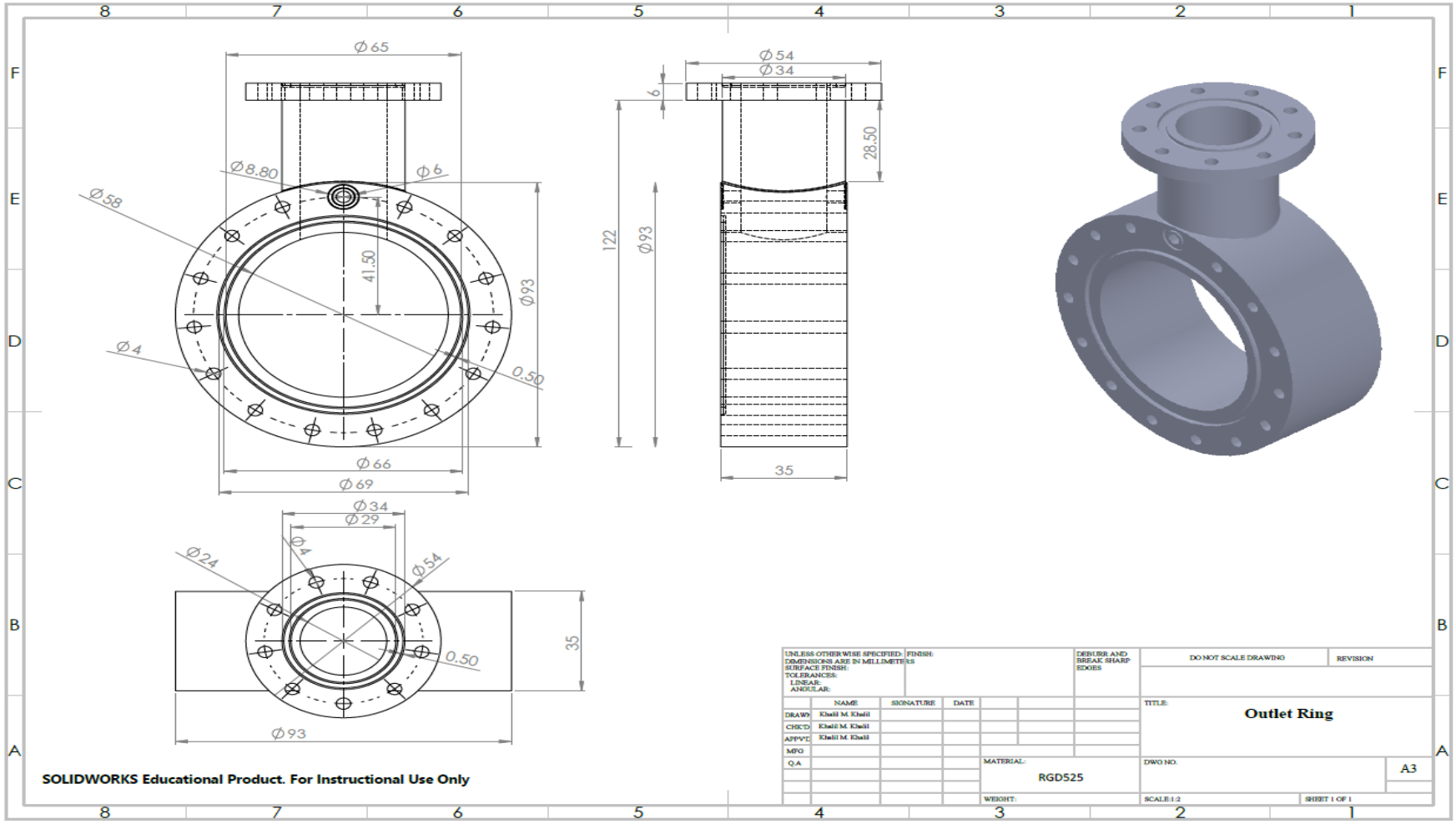

Figure B-9 outlet ring detailed drawing

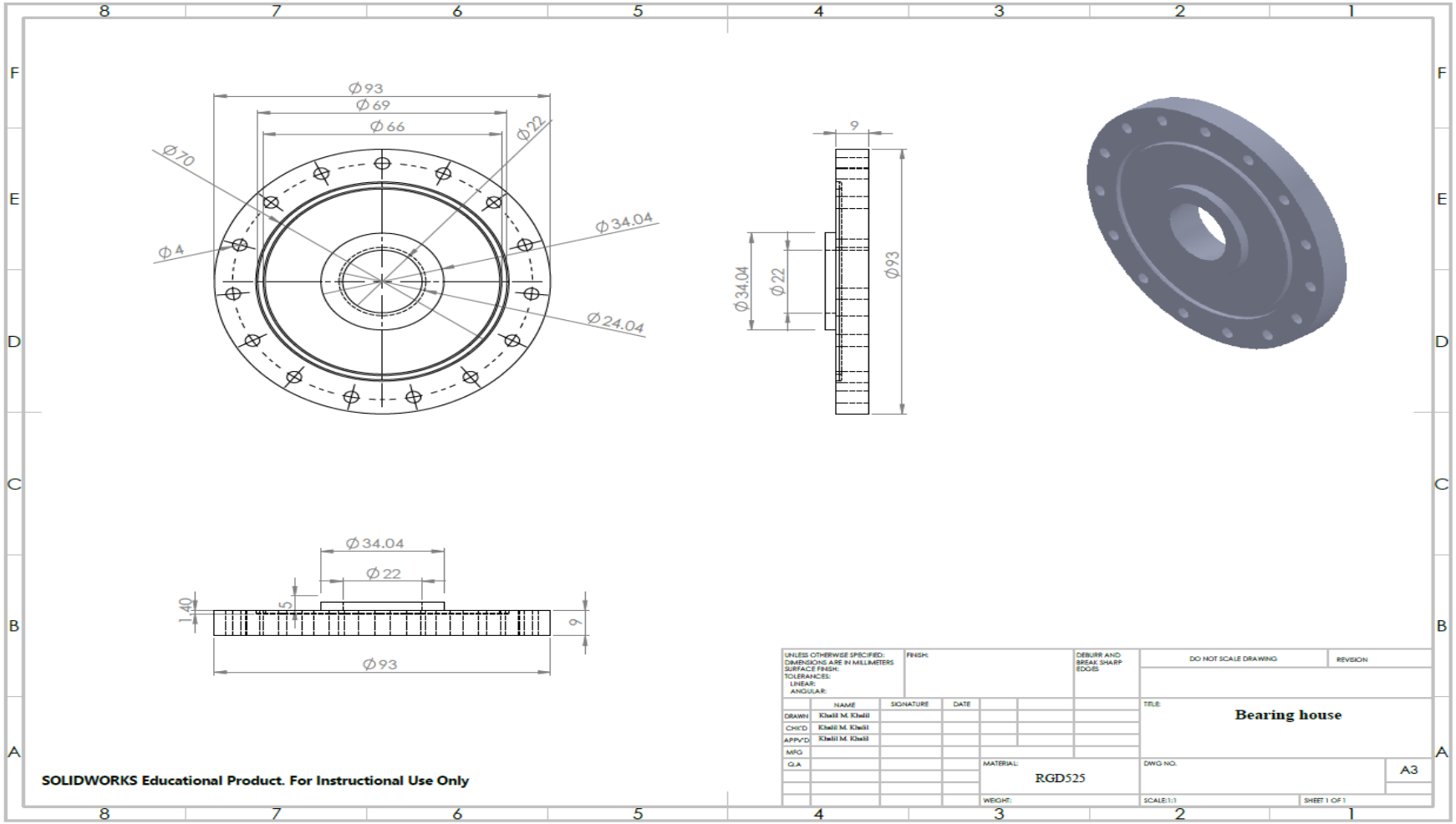

Figure B-10 Bearing house detailed drawing

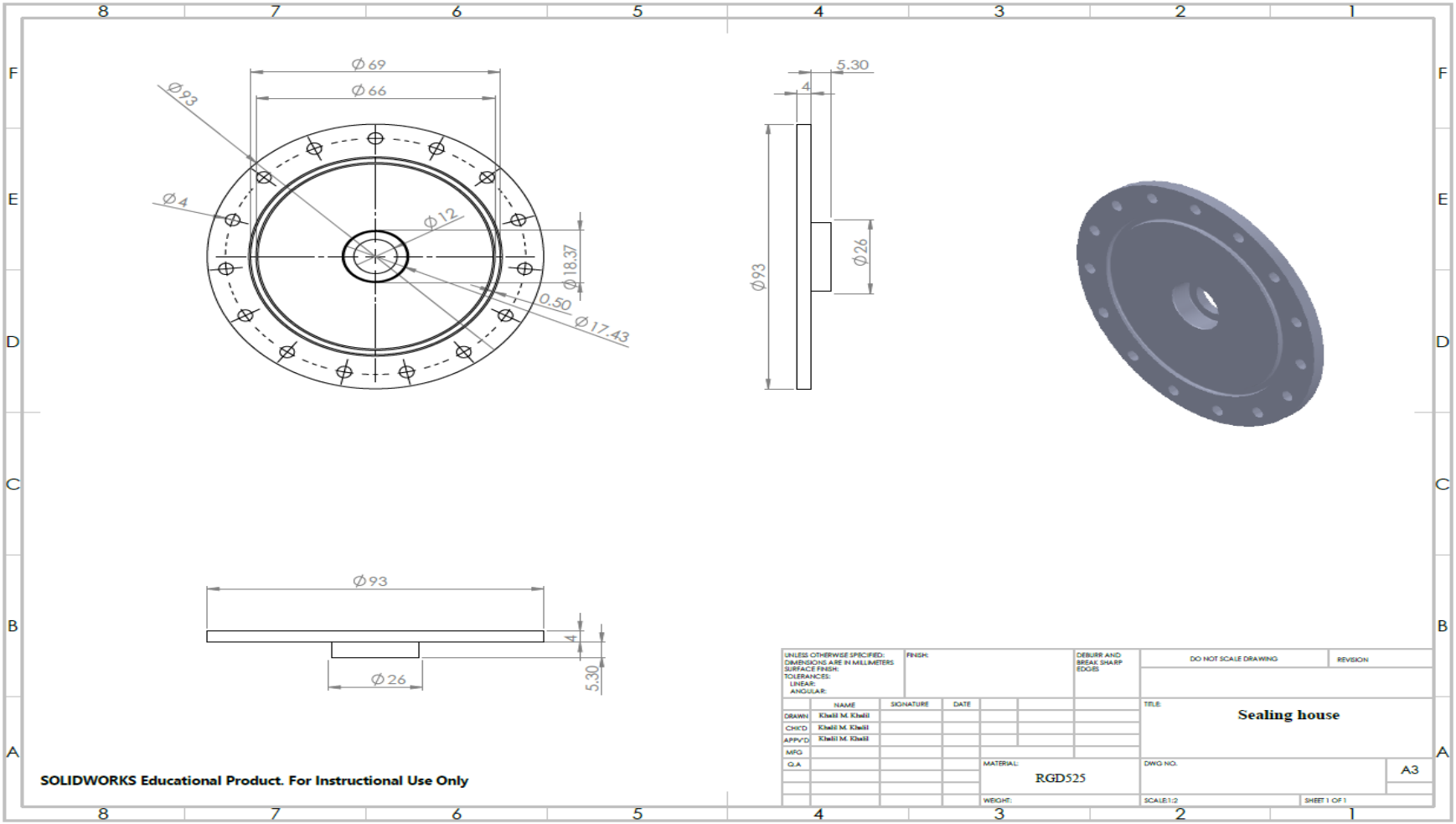

Figure B-11 Sealing house detailed drawing

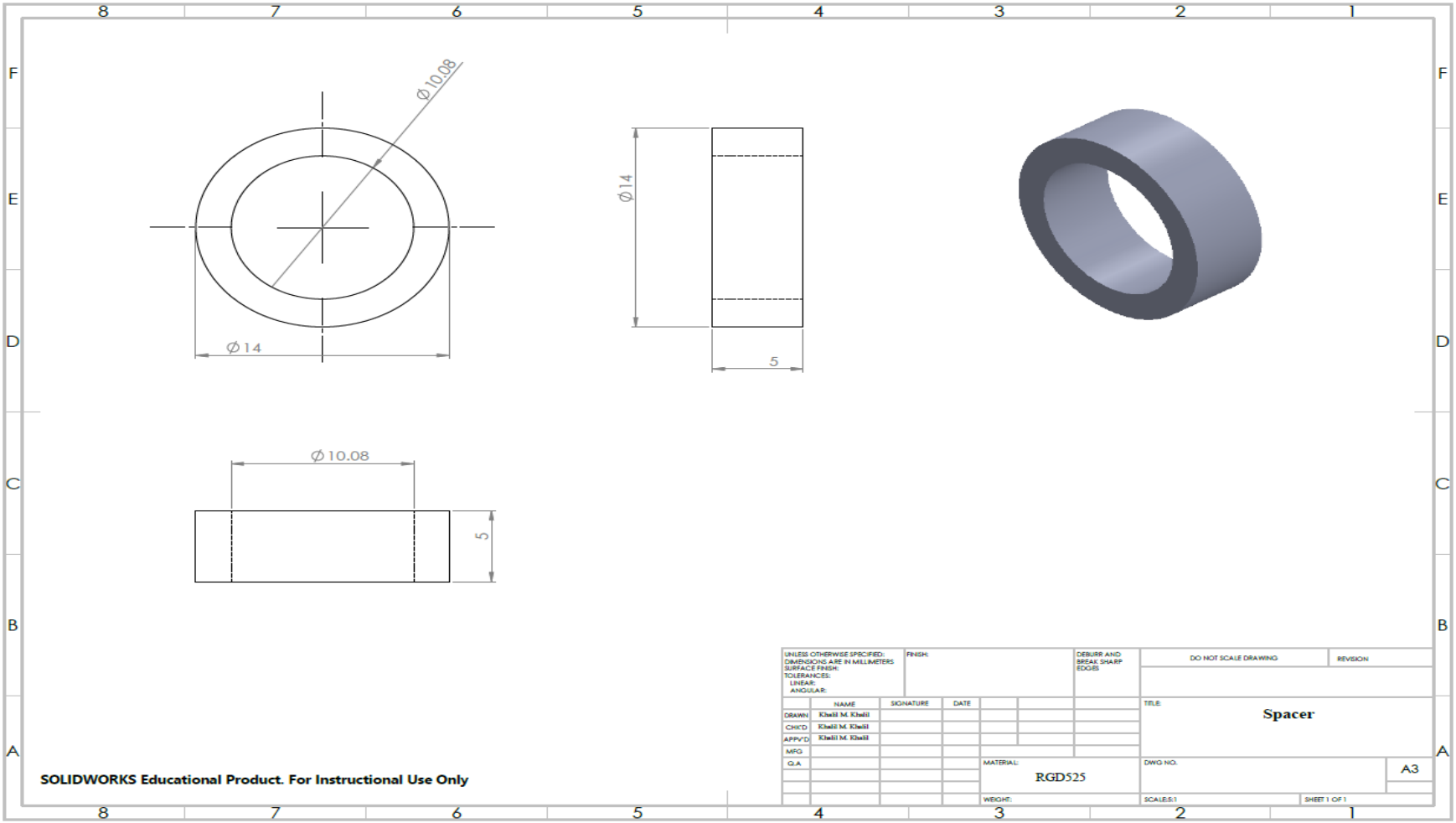

Figure B-12 Spacer detailed drawing

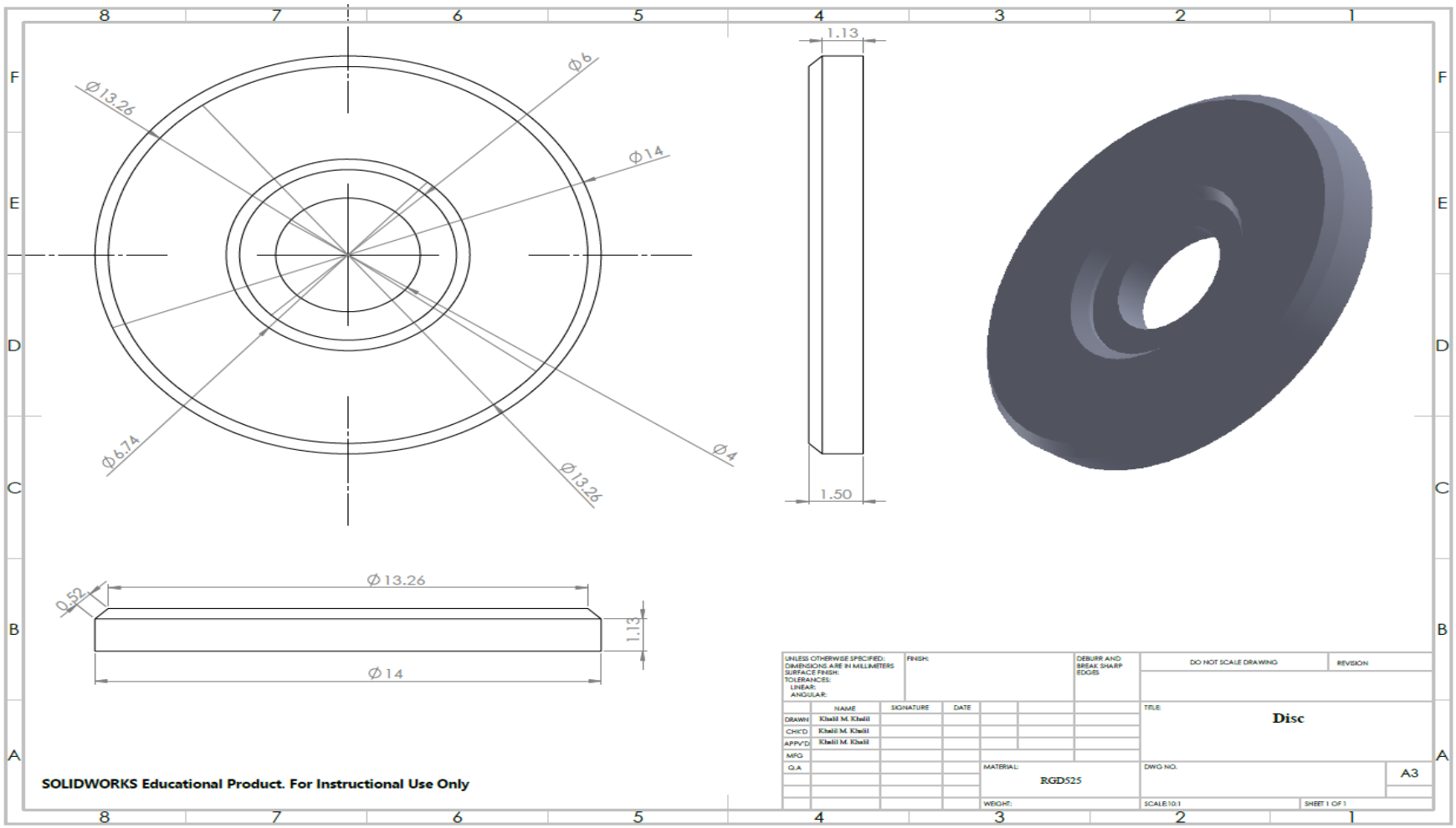

Figure B-13 Disc detailed drawing

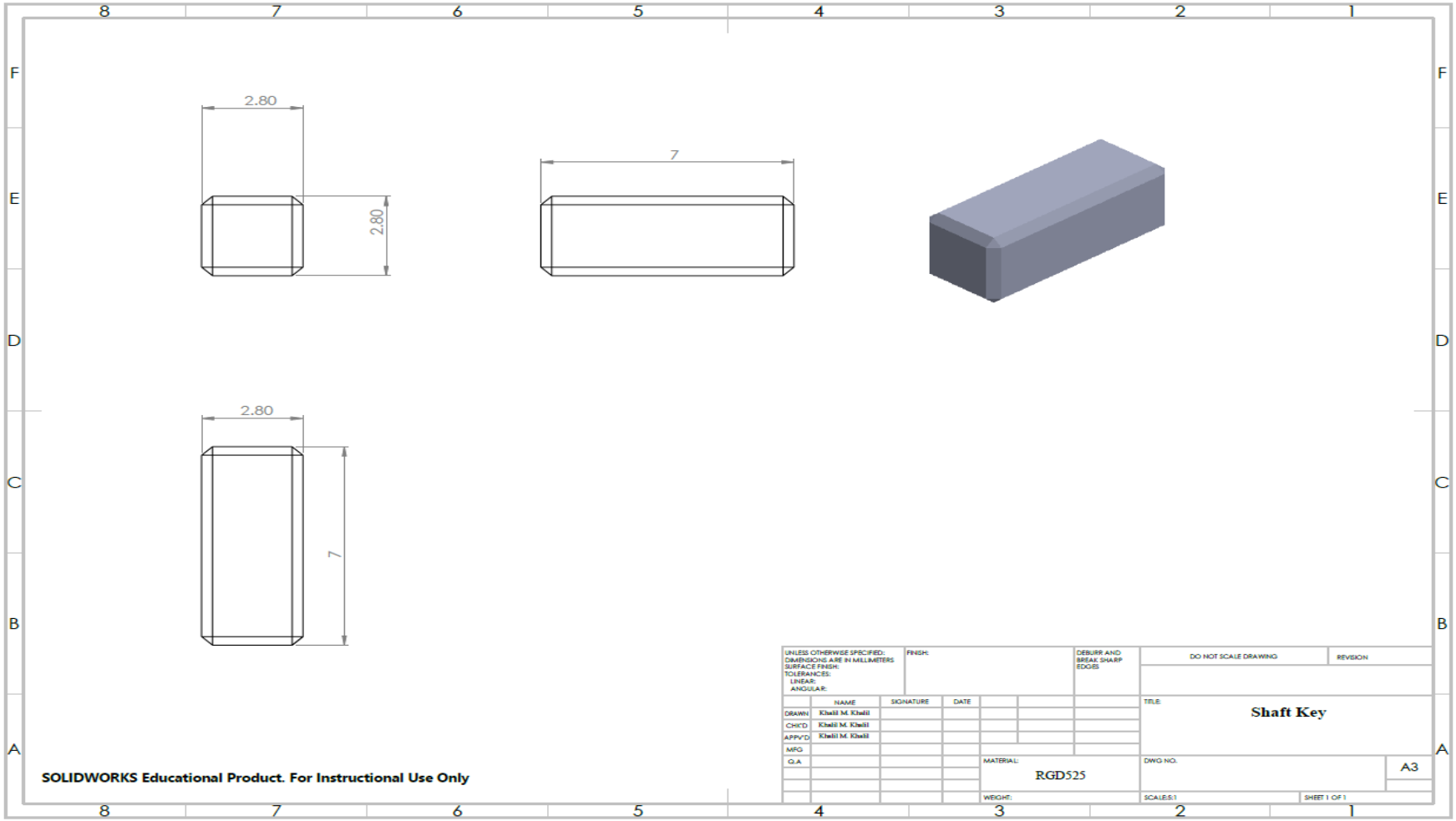

Figure B-14 Shaft key detailed drawing